Redundant Hybrid Cable-Driven Robots: Modeling, Control, and Analysis

by

Ronghuai Qi

A thesis
presented to the University of Waterloo
in fulfillment of the
thesis requirement for the degree of
Doctor of Philosophy
in
Mechanical and Mechatronics Engineering

Waterloo, Ontario, Canada, 2019

Examining Committee Membership

The following served on the Examining Committee for this thesis. The decision of the Examining Committee is by majority vote.

External Examiner:	Dr. Homayoun Najjaran Professor, School of Engineering, University of British Columbia
Supervisors:	Dr. Amir Khajepour and Dr. William Melek Professor, Dept. of Mechanical and Mechatronics Engineering, University of Waterloo
Internal Member:	Dr. Baris Fidan Associate Professor, Dept. of Mechanical and Mechatronics Engineering, University of Waterloo
Internal Member:	Dr. Soo Jeon Associate Professor, Dept. of Mechanical and Mechatronics Engineering, University of Waterloo
Internal-External Member:	Dr. Stephen L. Smith Associate Professor, Dept. of Electrical and Computer Engineering, University of Waterloo

Statement of Contributions

The following co-authors have contributed to the current work:

Prof. Amir Khajepour and Prof. William Melek supervised this Ph.D. thesis.

Dr. Mitch Rushton assisted with some preliminary tests of state estimation.

Abstract

Serial and Cable-Driven Parallel Robots (CDPRs) are two types of robots that are widely used in industrial applications. Usually, the former offers high position accuracy at the cost of high motion inertia and small workspace envelope. The latter has a large workspace, low motion inertia, and high motion accelerations, but low accuracy. In this thesis, redundant Hybrid Cable-Driven Robots (HCDRs) are proposed to harness the strengths and benefits of serial and CDPRs. Although the study has been directed at warehousing applications, the developed techniques are general and can be applied to other applications.

The main goal of this research is to develop integrated control systems to reduce vibrations and improve the position accuracy of HCDRs. For the proposed HCDRs, the research includes system modeling, redundancy resolution, optimization problem formulation, integrated control system development, and simulation and experimental validation.

In this thesis, first, a generalized HCDR is proposed for the step-by-step derivation of a generic model, and it can be easily extended to any HCDRs. Then, based on an in-plane configuration, three types of control architecture are proposed to reduce vibrations and improve the position accuracy of HCDR. Their performance is evaluated using several well-designed case studies. Furthermore, a stiffness optimization algorithm is developed to overcome the limitations of existing approaches.

Decoupled system modeling is studied to reduce the complexity of HCDRs. Control design, simulations, and experiments are developed to validate the models and control strategies. Additionally, state estimation algorithms are proposed to overcome the inaccurate limitation of Inertial Measurement Unit (IMU). Based on these state observers, experiments are conducted in different cases to evaluate the control performance.

An Underactuated Mobile Manipulator (UMM) is proposed to address the tracking and vibration- and balance-control problems. Out-of-plane system modeling, disturbance analysis, and model validation are also investigated. Besides, a simple but effective strategy is developed to solve the equilibrium point and balancing problem. Based on the dynamic model, two control architectures are proposed. Compared to other Model Predictive Control (MPC)-based control strategies, the proposed controllers require less effort to implement in practice. Simulations and experiments are also conducted to evaluate the model and control performance.

Finally, redundancy resolution and disturbance rejection via torque optimization in HCDRs are proposed: joint-space Torque Optimization for Actuated Joints (TOAJ) and joint-space Torque Optimization for Actuated and Unactuated Joints (TOAUJ). Compared to

TOAJ, TOAUJ can solve the redundancy resolution problem as well as disturbance rejection. The algorithms are evaluated using a Three-Dimensional (3D) coupled HCDR and can also be extended to other HCDRs.

Acknowledgements

First and foremost, I would like to express my sincere gratitude to my enthusiastic supervisors, Prof. Amir Khajepour and Prof. William Melek, for their continuous support, tremendous encouragement, and excellent guidance.

Besides my supervisors, I would like to thank the rest of my thesis committee: Prof. Homayoun Najjaran, Prof. Baris Fidan, Prof. Soo Jeon, and Prof. Stephen L. Smith, for their insightful comments and invaluable advice.

My sincere thanks go to the lab members, Dr. Mitchell Rushton, Dr. Hamed Jamshidianfar, Dr. Yanjun Huang, Dr. Chen Tang, Dr. Hong Wang, Dr. Yubiao Zhang, Mr. Jeff Graansma, Mr. Jeremy Reddekopp and so on, for the useful discussions, suggestions, and technical support.

Thanks are also due to the Beckhoff Technical Support Team in Canada and USA for providing me the technical instructions in hardware and software usage and development.

Additionally, I would like to knowledge the financial support of the Natural Sciences and Engineering Research Council of Canada (NSERC).

Last but not least, I would like to express my deepest gratitude to my family for their endless support and warm love.

Dedication

This thesis is dedicated to my family.

Table of Contents

List of Tables

List of Figures

Abbreviations

3D Three-Dimensional

CDPR Cable-Driven Parallel Robot

COM Center of Mass

DOF Degree of Freedom

DOR Degree of Redundancy

HCDR Hybrid Cable-Driven Robot

IMU Inertial Measurement Unit

MP Mobile Platform

MPC Model Predictive Control

PI Proportional-Integral

PID Proportional-Integral-Derivative

TOAJ Torque Optimization for Actuated Joints

TOAUJ Torque Optimization for Actuated and Unactuated Joints

UMM Underactuated Mobile Manipulator

Nomenclature

Generalized HCDR consists of an n-DOF ($\{n \in \mathbb{N} : n \leq 6\}$) mobile platform, N driven cables ($N \in \mathbb{N}$), and an m-DOF ($m \in \mathbb{N}$) robot arm, where the robot arm is mounted on the mobile platform and moves with the mobile platform. The mobile platform and driven cables constitute a CDPR. The generalized HCDR has $(n+m)$-DOFs and can move in the 3D space (shown in Figure 3.1).

HCDR-1 consists of a 3-DOF planar mobile platform (i.e., $n = 3$), a 2-DOF robot arm (i.e., $m = 2$), and 12 driven cables. HCDR-1 (shown in Figure 3.2) can only generate in-plane motion.

HCDR-2 consists of a 6-DOF mobile platform, two 1-DOF pendulums, and 12 driven cables. HCDR-2 (shown in Figure 3.3 and Figure 3.4) can realize in-plane motion and out-of-plane motion.

HCDR-3 consists of a 6-DOF mobile platform, two 1-DOF pendulums, a 1-DOF slider, and 12 driven cables. HCDR-3 (shown in Figure 3.6 and Figure 3.7) can realize in-plane motion and out-of-plane motion. The UMM (in Figure 3.6 and Figure 3.7), a subsystem of HCDR-3, can only realize out-of-plane motion.

HCDR-4 consists of a 6-DOF mobile platform, two 1-DOF pendulums, a 3-DOF robot arm, and 12 driven cables. HCDR-4 (shown in Figure 3.10) can realize in-plane motion and out-of-plane motion.

List of Symbols

$[x_{a0j}, y_{a0j}, z_{a0j}]^T$	Body-fixed position of the jth joint of the robot arm
$[x_{ac0j}, y_{ac0j}, z_{ac0j}]^T$	Body-fixed position of the jth COM (of the link) of the robot arm
$[x_{p0k}, y_{p0k}, z_{p0k}]^T$	Body-fixed position of the kth joint of the pendulum
$[x_{pc0k}, y_{pc0k}, z_{pc0k}]^T$	Body-fixed position of the kth COM of the pendulum
τ	Vector of forces/torques in generalized coordinates
$\tau_{\mathcal{A}}, \tau_{\mathcal{U}}$	Vectors of actuated joint torques and unactuated joint torques, respectively
$\{O\}$	Inertial coordinate frame of the robot
$\{O_m\}$	Coordinate frame of the mobile platform (located at the center of mass (COM))
A_m	Structure matrix
$C(q, \dot{q})$	Coriolis and centripetal matrix
EA_i	Product of the modulus of elasticity and cross-sectional area of the ith cable
g	Gravitational acceleration
$G(q)$	Gravitational vector
I	Identity matrix
K	Stiffness matrix

K_c	Cable stiffness matrix
K_E	Kinetic energy
K_k	Stiffness matrix as a product of cable stiffness
K_T	Stiffness matrix as a product of cable tensions
L	Vector of cable lengths
$M(q)$	Inertia matrix
p_{acj}, p_{aj}	The jth COM (of the link) position vector and joint position vector of the robot arm, respectively
p_{pck}	The kth COM position vector of the pendulum
$q_{\mathcal{A}}, \dot{q}_{\mathcal{A}}, \ddot{q}_{\mathcal{A}}$	Vectors of actuated joint coordinates, velocities, and accelerations, respectively
$q_{\mathcal{U}}, \dot{q}_{\mathcal{U}}, \ddot{q}_{\mathcal{U}}$	Vectors of unactuated joint coordinates, velocities, and accelerations, respectively
T	Vector of cable tensions
V_E	Potential energy
$(\cdot)^+$	Pseudo-inverse of the matrix $(\cdot)$
$(\cdot)^T$	Transposed matrix
$(\cdot)_{[i],[j]}$	Matrix indexed for some purpose
$(\cdot)_{[i]}$	Vector indexed for some purpose
$[a_{ix}, a_{iy}, a_{iz}]^T$	Position vector of the ith cable anchor point on the robot static frame with respect to the coordinate frame $\{O\}$, where $a_i := [a_{ix}, a_{iy}, a_{iz}]^T$
$[r_{ix}, r_{iy}, r_{iz}]^T$	Position vector of the ith cable anchor point on the mobile platform with respect to the body-fixed frame $\{O_m\}$, where $r_i := [r_{ix}, r_{iy}, r_{iz}]^T$
$[p_{mx}, p_{my}, p_{mz}]^T$	Position vector of the coordinate frame $\{O_m\}$ with respect to the coordinate frame $\{O\}$, where $p_m := [p_{mx}, p_{my}, p_{mz}]^T$

$\ddot{q}$	Vector of generalized accelerations
$\dot{p}_{mx}, \dot{p}_{my}, \dot{p}_{mz}$	Time-derivatives of $p_{mx},\ p_{my},$ and p_{mz}, respectively
$\dot{q}$	Vector of generalized velocities
$\mathbb{R}^{m\times n}$	The set of $m \times n$ real matrices
$\mathcal{SO}(n)$	The special orthogonal group of dimension n
$\operatorname{diag}(\cdot)$	Diagonal matrix of the matrix $(\cdot)$
$\operatorname{eig}(\cdot)$	Eigenvalues of the matrix $(\cdot)$
$\operatorname{rank}(\cdot)$	Rank of the matrix $(\cdot)$
τ_d	Vector of unknown bounded disturbances
$\\|(\cdot)\\|$	Norm of the vector $(\cdot)$ ($\\|(\cdot)\\|$ is equal to $\\|(\cdot)\\|_2$ by default)
F_e, M_e	External force and moment
J_e	Jacobian matrix of the HCDR
L_0	Vector of unstretched cable lengths
L_i	The ith cable length
m_m, I_m	Center of mass and moment of inertia of the mobile platform
m_{aj}, I_{aj}	Center of mass and moment of inertia of the jth link of the robot arm
m_{pk}, I_{pk}	Center of mass and moment of inertia of the kth pendulum
q	Vector of generalized coordinates
T_i	The ith cable tension
$v_{acj}, v_{aj}, \omega_{acj}$	The jth COM (of the link) linear velocity, joint linear velocity, and angle velocity of the robot arm, respectively
v_{pck}, ω_{pck}	The kth COM linear velocity and angle velocity of the pendulum, respectively
$\alpha_m, \beta_m, \gamma_m$	Euler angles of the mobile platform about X-, Y-, and Z-axes, respectively

$\dot{\alpha}_m, \dot{\beta}_m, \dot{\gamma}_m$	Time-derivative of $\alpha_m,\ \beta_m,$ and γ_m, respectively
$R_x(\theta)$	Rotation matrix for rotation of θ about the X-axis
$R_y(\theta)$	Rotation matrix for rotation of θ about the Y-axis
$R_z(\theta)$	Rotation matrix for rotation of θ about the Z-axis
v_m, ω_m	Linear velocity and angular velocity of the mobile platform, respectively

Chapter 1

Introduction

1.1 Motivation

Serial manipulators are one of the most common types of industrial robots, which consist of a base, a series of links connected by actuator-driven joints, and an end-effector. Usually, they have 6 DOFs and offer high position accuracy. They are commonly used in industrial applications; however, they have some key limitations, such as high motion inertia and limited workspace envelope [117]. CDPRs are another important type of industrial robots. Their configurations usually bear resemblance to parallel manipulators. For these robots, rigid links are replaced with cables. This reduces the robot weight since cables are almost massless. It also eliminates the need of these revolute joints. These features allow the mobile platform to reach high motion accelerations in large workspaces. However, they are not without some drawbacks, such as their low accuracy, high vibration, etc., all of which limit their applications [87]. To overcome the aforementioned shortages of serial and cable-driven parallel robots as well as aggregate their advantages, one approach is to combine these two types of robots to create a HCDR, i.e., a hybrid structure of CDPR(s) and serial robot(s). Compared to other hybrid robots such as mobile manipulators [123, 25, 68, 3], the benefits of HCDRs still hold (e.g., low motion inertia and large workspaces).

Additionally, the growth of automated warehousing solutions has been fueled by the e-commerce explosion in recent years [50]. By 2024, the market of global automated material handling equipment is predicted to no less than US$ 50.0 Billion with a Compound Annual Growth Rate (CAGR) of 8% [73, 72]. These increase of automated warehousing applications offers a unique opportunity for the development of cable robotics that is superior in, especially for HCDRs. Related research and applications have been reported in [107, 98, 97, 43, 28, 14, 44]. However, the literature shows that existing research and applications prefer to affix a robot arm upside down to the bottom of a CDPR's platform [9, 88, 14, 44, 5, 6, 98, 97] or mainly control the cable robot while treating the serial robot as a manipulation tool or an end-effector rather than a whole system [5, 6, 98, 97]. When a serial robot is mounted on a mobile platform, the two constitute a new coupled system. Only controlling the mobile platform (i.e., treating the serial robot as a manipulation tool) or the serial robot may not guarantee the position accuracy of the end-effector. For applications that use such a system, the main goal is to control the end-effector of the serial robot (e.g., its trajectories and vibrations) in order to accomplish tasks such as pick-and-place effectively. Another major challenge in the utilization of these systems is maintaining the appropriate cable tensions and stiffness for the robot. This requires the development of kinematic and dynamic models, stiffness optimization, and controllers for HCDRs.

Some research has been carried out to solve these problems: for kinematic and dynamic modeling, existing research mainly focuses on rigid serial robots [89], rigid/flexible parallel robots [62, 81, 112, 57, 102, 52], and wheeled rigid mobile vehicles carrying a rigid/flexible joint arm [68, 3]. In [62], a multilink manipulator model was developed, but this model applied to each link driven by cables. To solve the redundancy and stiffness optimization problems, some useful methods were studied, such as minimum 2-norm of cable tensions [57, 76] and stiffness maximization in the softest direction [52, 53]. However, their research focused on planar CDPRs, and the maximum of the system overall stiffness by using these approaches was not always guaranteed. Since the use of flexible cables reduces the overall stiffness of cable-driven robots, vibration control becomes a serious problem. Meanwhile, the moving robot arm also generates reaction forces acting on the mobile platform, resulting in mobile platform vibrations. Hence, it is challenging to achieve the goal of minimizing the vibrations and increasing the position accuracy of the end-effector simultaneously. To the best of the author's knowledge, limited studies address the modeling and control problems of flexible HCDRs, especially, when the redundancy and stiffness optimization problems are introduced, the control of trajectories and vibrations becomes more challenging.

This thesis will introduce contributions which solve the aforementioned problems for CDPRs with serial robotic arms in order to increase their accuracy and adoption in industrial or other potential applications (e.g., rehabilitation). To develop and implement these contributions, this thesis focuses on HCDRs, including modeling, control, and performance analysis.

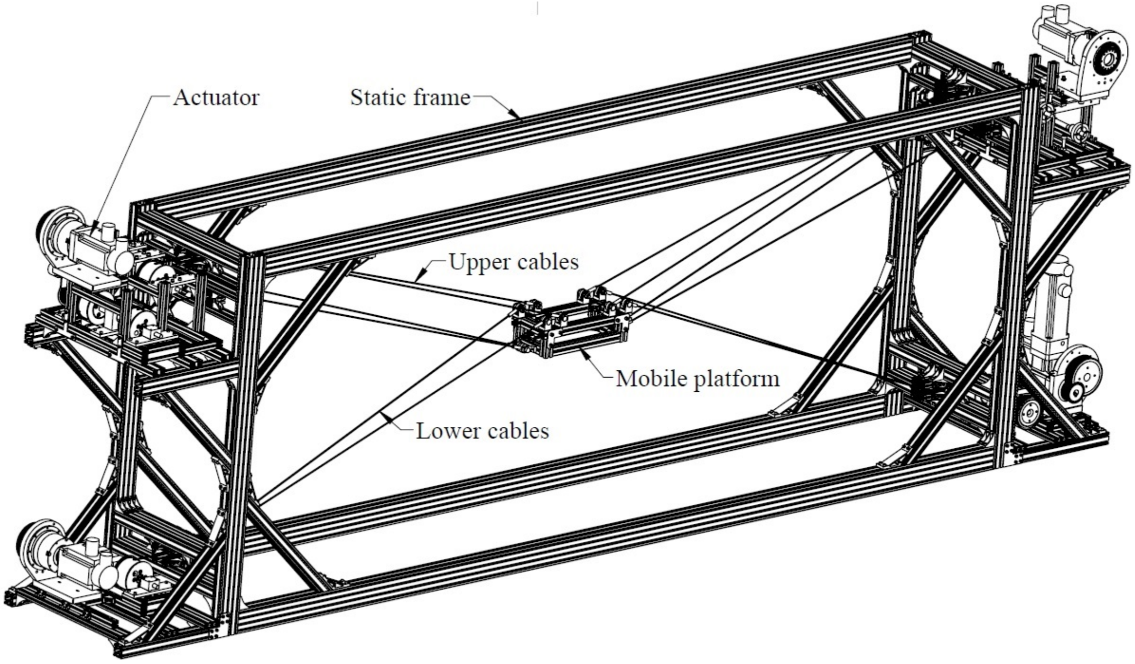

Figure 1.1: Main components of the existing planar CDPR [76].

1.2 Research Background

The research in thesis began in 2015, based on the existing planar CDPR (see Figure 1.1) [76]. In Figure 1.1, the mobile platform is driven by two sets of upper cables and two sets of lower cables. Jamshidifar [50] used this platform for studying the rigid body and in-plane vibration control of CDPR. Rushton [93] introduced two pendulums to eliminate out-of-plane vibrations. In this research, hybrid cable-driven robots (HCDRs) are proposed to overcome the shortcomings of CDPRs and serial robots as well as aggregate their advantages. The HCDR is defined as follows:

Definition 1.2.1. *A hybrid cable-driven robot (HCDR) is a robot that is composed of two or more heterogeneous mechatronic components, where at least one component is CDPR.*

Additionally, the following HCDRs are proposed (see below) to achieve the objectives shown in section 1.3: the generalized HCDR is used for the step-by-step derivation of a generic model for HCDRs. HCDR-1 is used as a simple in-plane configuration to help the reader understand the model. HCDR-2 is the decoupled configuration (with two pendulums) based on the existing HCDR prototype (the experimental setup). HCDR-3 includes an additional slider to extend out-of-plane motion and manipulation tasks. HCDR-4 is a 3-DOF arm on the mobile platform (with two pendulums).

- Generalized HCDR: It consists of an n-DOF ($\{n \in \mathbb{N} : n \leq 6\}$) mobile platform, N driven cables ($N \in \mathbb{N}$), and an m-DOF ($m \in \mathbb{N}$) robot arm, where the robot arm is mounted on the mobile platform and moves with the mobile platform. The mobile platform and driven cables constitute a CDPR. The generalized HCDR has $(n + m)$-DOFs and can move in the 3D space (shown in Figure 3.1).
- HCDR-1: It consists of a 3-DOF planar mobile platform (i.e., $n = 3$), a 2-DOF robot arm (i.e., $m = 2$), and 12 driven cables. HCDR-1 (see Figure 3.2) can only generate in-plane motion.
- HCDR-2: It consists of a 6-DOF mobile platform, two 1-DOF pendulums, and 12 driven cables. HCDR-2 (see Figure 3.3 and Figure 3.4) can realize in-plane motion and out-of-plane motion.
- HCDR-3: It consists of a 6-DOF mobile platform, two 1-DOF pendulums, a 1-DOF slider, and 12 driven cables. HCDR-3 (shown in Figure 3.6 and Figure 3.7) can realize in-plane motion and out-of-plane motion. An underactuated mobile manipulator (UMM) consists of the mobile platform, two pendulums, and the linear slider (see Figure 3.6 and Figure 3.7), a subsystem of HCDR-3, can only realize out-of-plane motion.
- HCDR-4: It consists of a 6-DOF mobile platform, two 1-DOF pendulums, a 3-DOF robot arm, and 12 driven cables. HCDR-4 (see Figure 3.10) can realize in-plane motion and out-of-plane motion.

1.3 Objectives

The main goal of this research is to develop integrated control systems to reduce vibrations and improve the position accuracy of HCDRs, including 1) development of generalized HCDR and system modeling, and then extending it to four types of hybrid robots: HCDR-1, HCDR-2, HCDR-3, and HCDR-4 for control design, simulations, and experiments, 2) developing trajectory and vibration control methods for the HCDRs, and 3) conducting effective simulations and experiments to validate the effectiveness of the proposed methods. To achieve these objectives, the following contributions are pursued:

1. For the objective of modeling and control of generalized flexible HCDR, the main contributions are as follows:

    (a) The derivation of the equations of motion and proof provide a very effective way to find items for generalized system modeling. Meanwhile, the proposed dynamic modeling approach avoids the drawback of traditional methods (e.g., [31]), and can be easily extended to other types of hybrid robots by changing the proposed structure matrix based on their desired configurations, e.g., robot arm(s) mounted on an aircraft platform [106, 90].

    (b) Three types of control architecture are proposed to reduce vibrations and improve the accuracy of the HCDR. Their performance is also evaluated using several well-designed case studies.

    (c) The proposed optimization problem and algorithm address the limitations of existing stiffness optimization approaches in [57, 76, 52, 53]. Meanwhile, they can be applied to not only CDPRs but also HCDRs.

2. Based on the proposed HCDR-2, the vibration control problems using MPC are tackled, including decoupled system modeling, control design with simulations, state estimation, and experimental validation of control performance. The unique contributions can be summarized as follows:

    (a) The whole-body model and decoupled model are developed for the HCDR. The latter is derived from the former for efficient use in practice. The proposed decoupled modeling method can be extended to other HCDRs or CDPRs based on their desired configurations.

    (b) Jamshidifar et al. studied vibration control of a planar (i.e., in-plane) CDPR [52, 53], while Rijk et al. only studied the out-of-plane system and its vibration control using a simple strategy (SMC) [30]. In SMC design, an accurate dynamic model is not essential (i.e., model-free SMC). Actually, the HCDR in Figure 3.3 is a coupled system. To achieve vibration control for the integrated system in real-time (no more than 0.01s in the experiments), especially using model-based control techniques, this research proposes to simplify the dynamic model while also ensuring satisfactory control performance (the experiments showed that the system might crash out if the coupled dynamic model is adopted, i.e., the CPU usage rate is beyond 90% (the maximum allowable value)). The proposed decoupled model for the integrated system can be implemented in real-time (the top CPU usage is reduced to 32%) and validated via experiments.

    (c) Based on the proposed decoupled dynamics form, model-based control architectures and observers are developed, and experimental results are satisfactory in different cases. The proposed state estimation is more robust than the state-of-art in [53]. The proposed control strategy can be generated to other CDPRs or HCDRs.

3. For the HCDR-2, the research focuses on decoupling the dynamics (i.e., in-plane and out-of-plane subsystems) based on the existing platform [76, 93]. For the proposed HCDR-3 (shown in Figure 3.6), since the motion of the slider mainly affects out-of-plane vibrations, in-plane motion is not considered in this case. The proposed subsystem is an underactuated mobile manipulator (UMM) (shown in Figure 3.6) which consists of a mobile platform, two pendulums, and a linear slider. Meanwhile, the control goal for this system focuses on minimizing the vibrations and increasing the position accuracy of the end-effector. The novelty and contributions can be summarized as follows:

    (a) Compared to the modeling and control objectives in [30], this thesis extends that configuration by introducing a coupled slider on the platform to enable execution of out-of-plane manipulation tasks such as pick-and-place. Accordingly, tracking and vibration- and balance-control problems must be considered, not only vibration control [30]. To develop the system dynamics, the equations of motion of the UMM, disturbance analysis, and model validation are carried out. Additionally, a simple but effective strategy is also proposed to solve the equilibrium point for control design and balance problem.

    (b) Jamshidifar et al. studied vibration control of a planar (i.e., in-plane) CDPR [52, 53], while Rijk et al. only studied the out-of-plane system and its vibration control using SMC [30]. In this thesis, based on the proposed dynamic model, two control architectures are developed: MPC with integral action and MPC+PI with integral action. Compared to other MPC-based control strategies, the proposed controllers are easier to implement in practice. The results of this thesis also offer noticeable improvements (in comparison with previous studies, such as PID [76], LPV [53], and SMC [30]), because the use of MPC enhances the control performance since the future steps from the reference trajectories are used to generate control laws.

    (c) Simulations, experiments, and robustness verification are conducted to validate the performance of the proposed methods.

    (d) Lyapunov-based stability analysis for the closed-loop systems is also proposed.

4. When kinematic redundancy occurs, existing research focuses on actuated joints (in joint-space), unactuated joints (e.g., disturbances applied to the unactuated joints may affect the motion of a robot) are not considered. To address this problem, the redundancy resolution and disturbance rejection via torque optimization in the 3D are studied by using the proposed HCDR-4, and the following contributions are highlighted:
    (a) Nonlinear whole-body dynamics equations of the HCDR are developed, and model reduction methods are proposed. Based on the reduced dynamic model, two new methods are proposed to solve redundancy resolution: joint-space torque optimization for actuated joints (TOAJ) and joint-space torque optimization for actuated and unactuated joints (TOAUJ). Compared to TOAJ, TOAUJ can solve the redundancy resolution problem as well as active satisfactory disturbance rejection.
    (b) Numerical results are introduced to evaluate the performance of TOAJ and TOAUJ. The corresponding results are also satisfactory by comparing with [55, 71, 38]. Additionally, a nonlinear controller is also proposed by applying the generated offline redundancy resolution data to evaluate the proposed methods.

In summary, the main contributions of this thesis are as follows:

- General system modeling for HCDRs.
- Redundancy resolution and optimization problems in HCDRs.
- Integrated control system development for HCDRs.

1.4 Thesis Outline

In this dissertation, motivation, objectives, and thesis outline are introduced in Chapter 1. The literature review and background knowledge are presented in Chapter 2. A generalized HCDR is introduced in Chapter 3. For the proposed HCDR, generalized system modeling is developed and then extended to four types of hybrid robots, namely, HCDR-1, HCDR-2, HCDR-3, and HCDR-4 for control design, optimization, and case studies (in Chapter 4), and experiments (in Chapter 5). In Chapter 4, different control strategies are developed based on HCDR-1, HCDR-2, and HCDR-3. Based on HCDR-4, the proposed methods for redundancy resolution and disturbance rejection are studied. The results are also evaluated using case studies in Chapter 4. In Chapter 5 experimental results are presented. Finally, in Chapter 6, the conclusions and future work are summarized.

Chapter 2

Literature Review and Background

2.1 Hybrid Cable-Driven Robots (HCDRs)

Serial manipulators are one of the most common types of industrial robots, which consist of a base, a series of links connected by actuator-driven joints, and an end-effector. Usually, they have 6 DOFs and offer high position accuracy. They are commonly used in industrial applications; however, they have some key limitations, such as high motion inertia and limited workspace envelope [117]. For example, the KUKA KR 60 HA (see Figure 2.1(a)) is a 6-DOF serial robotic manipulator with a high payload (60 kg) carrying capacity and repeatability of ±0.05 mm, but the maximum reach is 2033 mm [60]. CDPRs are another important type of industrial robots. Their configurations usually bear resemblance to parallel manipulators (e.g., Stewart platform [100]). The NIST RoboCrane [29, 4] is a typical CDPR with 6 DOFs (shown in Figure 2.1(b)), which is designed by utilizing the idea of the Stewart platform, and its unique feature is its use of six cables instead of linear actuators. For these robots, rigid links are replaced with cables. This reduces the robot weight since cables are almost massless. It also eliminates the use of revolute joints. These features allow the mobile platform to reach high motion accelerations in large workspaces. However, they are not without some drawbacks, such as their low accuracy, high vibration, etc., all of which limit their applications [87]. To overcome the aforementioned shortages of serial and cable-driven parallel robots as well as aggregate their advantages, one approach is to combine these two types of robots to create a HCDR, i.e., a hybrid structure of CDPR(s) and serial robot(s).

Some research and applications are developed as follows: NIST developed a dual manipulator (see Figure 2.2(a)) [85], where a robot arm is fixed upside down to the bottom of

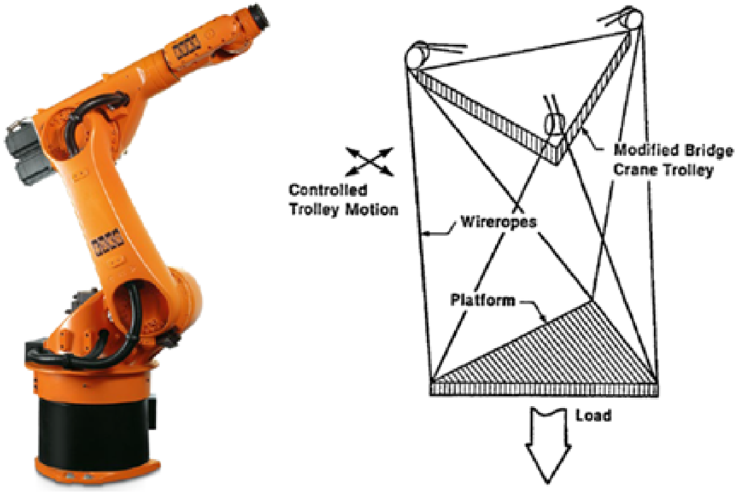

(a) (b)

Figure 2.1: Examples of serial robots and CDPRs. (a) KUKA KR 60 HA [60]; (b) NIST RoboCrane [29, 4].

the RoboCrane robot's platform, and the robot holds a retro-reflector as an off-board laser track. This experimental setup is used to measure the rigidity of the cable configuration. NIST also designed a Tetra work platform (shown in Figure 2.2(b)) [86], where a commercial robot arm is fixed to the bottom of the RoboCrane robot. The RoboCrane Tetra can be used to pick up and place a steel beam in a stanchion. In Figure 2.2(c), a CDPR carries a robot arm to paint large surfaces. The demonstration showed that vibrations were obvious and large [107]. In addition, cable-driven camera systems (e.g., Spidercam SC250 Field shown in Figure 2.2(d)) [98] and Skycam [97] are another type of cable-driven robots, which can move the camera in different poses for overhead filming (e.g., in football games). Gouttefarde [43] developed a CDPR (called CoGiRo CSPR, see Figure 2.2(e)) with the onboard Yaskawa-Motoman SIA20 robot arm for contactless and interacting applications (e.g., spray painting and metal cutting), but this project still had the main problems of low stiffness of the CDPR. CUHK C3 Robotics Laboratory (see Figure 2.2(f)) [28] also introduced a CDPR with the onboard UR3 robot arm, called SpiderArm robot. The CDPR and UR3 robot arm were powered by two independent motion control systems, and the demonstration showed that the CDPR vibrated while the UR3 was moving.

The literature shows that existing research and applications prefer to affix a robot arm upside down to the bottom of a CDPR's platform [9, 88, 14, 44, 5, 6, 98, 97] or mainly control the cable robot while treating the serial robot as a manipulation tool or an end-

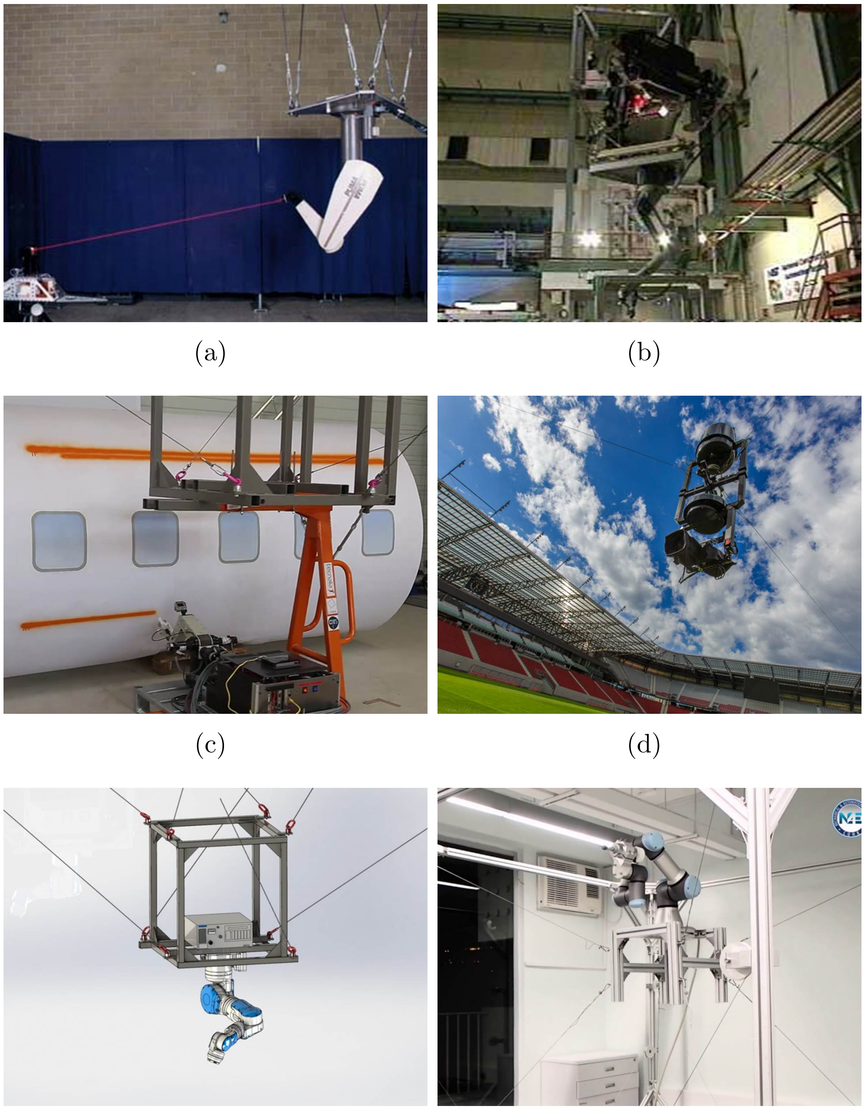

(a) (b) (c) (d) (e) (f)

Figure 2.2: Some existing HCDRs. (a) RoboCrane based dual manipulator [85]; (b) RoboCrane based Tetra work platform [86]; (c) CDPR attached a robot arm for large surface painting [107]; (d) Spidercam SC250 Field [98]; (e) CoGiRo CSPR with the on-board Yaskawa-Motoman SIA20 robot arm [43]; (f) SpiderArm robot [28].

effector rather than a whole system [5, 6, 98, 97]. When a serial robot is mounted on a mobile platform, they constitute a new coupled system. Only controlling the mobile platform (i.e., treating the serial robot as a manipulation tool) or the serial robot may not guarantee the position accuracy of the end-effector. For applications that use such a system, the main goal is to control the end-effector of the serial robot (e.g., its trajectories and vibrations) in order to accomplish tasks such as pick-and-place effectively. Another major challenge in the utilization of these systems is maintaining the appropriate cable tensions and stiffness for the robot. This requires the development of kinematic and dynamic models, stiffness optimization, and controllers for HCDRs.

2.2 Kinematics and Redundancy Resolution

As one of important topics in robotics, kinematics is concerned with the motion of the robot's joints in relation to the motion of the robot's end-effector, including forward kinematics and inverse kinematics. For a CDPR, calculating the mobile platform (end-effector) by the given cable lengths represents forward kinematics; computing the cable lengths by the given the mobile platform position denotes inverse kinematics. For a serial robot, forward kinematics is used to calculate the position and orientation of the end-effector when the joint angles are provided; inverse kinematics is used to compute the joint angles (the position and orientation of the end-effector are given. While for a HCDR, it includes the above two types of kinematic problems (e.g., the proposed redundant HCDR shown in Figure 3.10).

For cable-based robots, kinematic models are carried by simplifying non-stretchable and straight lines for cables [7, 111, 77]. Vafaei [110] proposed another method by considering the cables as linear springs and measuring the cable lengths using an encoder and a string pot. In these studies, CCDs and laser trackers are two popular devices [13, 84] used to measure the trajectories (e.g., position and velocity) of the moving platforms. For serial robots, commonly, DH (Denavit and Hartenberg) parameters need to be configured, and then transformation matrices [27] are calculated to find the forward kinematics. However, solving inverse kinematics problems is not always easy since there may be no solutions, multiple solutions, infinite solutions, or no closed-form solutions. Generally, geometric or algebraic methods can be utilized to find analytical solutions (closed-form solutions), and use approximate approaches (e.g., [65, 120, 115]) to find numerical solutions.

Redundancy resolution is another important topic in kinematics and has existed for years. One may fix this problem regarding the category of robots first: under-actuated robots and fully-actuated robots [108, 10, 67] (their strict definitions are provided in [108]).

The under-actuation represents the Degree of Freedom (DOF) of a robot n is more than the number of driven cables/independent joint driven actuators N, i.e., $n > N$; the fully-actuation denotes the DOF of a robot n is no more than the number of driven cables/independent joint driven actuators N, i.e., $n \leq N$. Then, the value of $N - n$ represents the Degree of Redundancy (DOR). When the redundancy problem exists, there are infinite solutions for inverse kinematics. Generally, approximate methods can be utilized to find numerical solutions, such as Jacobian pseudoinverse [65], Jacobian transpose [120], cyclic coordinate descent [115], damped least squares [113, 65, 83], and quasi-Newton and conjugate gradient [115, 132] approaches.

Some studies have tried to find the optimal redundancy resolutions: Barrette [15] used the inequality and equality constraints to find a redundancy resolution. Bruckmann [22] utilized different optimization objective functions to solve redundancy problems. In the past few years, researchers also attempted to use the below optimization methods: for instance, minimum energy [130], minimum norm at acceleration level [38], minimum infinity-norm at velocity level [104, 128], inertia-inverse weighted torque [129, 131], minimum torque norm [38, 129, 131], and minimization infinity-norm torque [127, 46, 105]. Additionally, Flacco [38] developed a discrete-time redundancy resolution by minimizing the norm of joint acceleration or joint torque. One of the advantages of the minimum weighted torque norm reported in [55, 71, 38] was that the motions of robot joints normally stayed bounded.

However, the existed research focus on actuated joints (in joint-space), unactuated joints (e.g., disturbances applied to the unactuated joints may affect the motion of a robot) are not considered. Although [38] mentioned torque optimization methods to find the redundancy resolution on actuated joints; they did not give a detailed study on it.

Furthermore, the singularity is another problem in robotic kinematics. When a robot moves into a singularity area, it cannot be controlled (e.g., for a CDPR, cable tensions cannot hold [47]), so the robot should not work within the singularity area. Some contiguous research, such as Dino et al. [32] have proposed a method to solve the Jacobian singularity problems; Gosselin and Angeles [42] used closed-loop chains to analyze the singularity, and Zlatanov et al. [134] developed a more generalized categorization method to solve several singularity problems.

2.3 Dynamics

Robot dynamics is required to build the relationship between the robot joint forces/torques and the produced accelerations, which includes forward dynamics (i.e., given forces/torques and calculate accelerations) and inverse dynamics (i.e., given accelerations and compute the forces/torques). Generally, to obtain robot's dynamic equations, two approaches can be used: the Newton-Euler equations and the Lagrange's equation. These equations describe the relationship between the input joint torques and the output motions. The Newton-Euler equations are derived from Newton's Second Law of Motion to describe a dynamic system in terms of force and momentum. In the Lagrange's equation, a dynamic system is described in terms of work and energy. Generally, the Lagrangian formulation is more systematic than the Newton-Euler formulation [119, 99].

For CDPRs' dynamics, the Newton-Euler formulation and Lagrangian formulation are utilized in different studies. For example, some research simplifies the dynamic models by ignoring the mass and elasticity of cables or mainly considering the cables' dynamics [87, 62, 103]. Bedoustani et al. [17] show that the elasticity and damping of cables are important factors in the dynamics. Some research has studied more complex dynamic behaviors, such as using a lumped mass-spring model with a finite number of elements [24], a discretized finite element model [34], variable stiffness coefficients [12], and damping elements to a lumped mass-spring model [78]. For hybrid robots' dynamics, some research has focused on the mobile manipulators (e.g., a robot arm with a mobile wheel) [123, 68] and flexible joints [63] using the Lagrangian formulation. In addition, the Lagrange-d'Alembert formulation is another approach to producing a dynamic model, shown by Chung et al. [25], who derived dynamic equations for a redundant mobile manipulator using this method.

Moreover, existing research mainly focuses on rigid serial robots [89], rigid/flexible parallel robots [62, 81, 112, 57, 102, 52], and wheeled rigid mobile vehicles carrying a rigid/flexible joint arm [68, 3]. In [62], a multilink manipulator model was developed, but this model applied to each link driven by cables. To solve the redundancy and stiffness optimization problems, some useful methods were studied, such as minimum 2-norm of cable tensions [57, 76] and stiffness maximization in the softest direction [52, 53]. However, their research focused on planar CDPRs, and the maximum of the system overall stiffness by using these approaches was not always guaranteed. Since the use of flexible cables reduces the overall stiffness of cable-driven robots, vibration control becomes a serious problem. Meanwhile, the moving robot arm also generates reaction forces to the mobile platform, resulting in the mobile platform vibrating. Hence, it is challenging to achieve the goal of minimizing the vibrations and increasing the position accuracy of the end-effector. To the best of the author's knowledge, limited studies address the modeling and control problems of flexible HCDRs. Especially when the redundancy and stiffness optimization problems are introduced, the control of trajectories and vibrations becomes more challenging.

2.4 Stiffness, Natural Frequency, and Stability

The stiffness, natural frequency, and stability of HCDRs are important issues, because driven cables are flexible, which will reduce the overall stiffness of the robots (compared to rigid cables) and produce undesired vibrations. When a HCDR or CDPR moves, driven cables should maintain enough tensions to reduce vibrations, i.e., keeping enough stiffness of the robot [18].

Regarding the stiffness problem, some research has been developed: Behzadipour and Khajepour [18] have proposed an equivalent four-spring model to express the stiffness matrices of a CDPR. They also used a simulation example to verify this model. Azadi et al. [12] introduced variable stiffness elements using antagonistic forces. Gosselin [41] analyzed the stiffness mapping for parallel manipulators by considering the internal forces; conversely, Griffis and Duffy [45] modeled the global stiffness of a class of compliant couplings but without considering the internal forces.

Widnall [118] defines the natural frequency as "the frequency at which the system will oscillate unaffected by outside forces." In cable-driven robots, methods that maximize the minimum natural frequency are studied and applied in [76, 33].

Stability is generally defined as follows: when an equilibrium point is given, the end-effector of a robot will be affected by an external disturbance [21]. It holds for cable-driven robots, i.e., a robot will be stable, if the end-effector of the robot can stay in the desired pose under an external force. Wei et al. [117] utilized the eigenvalues of the stiffness matrix to analyze the stability of a CDPR. Svinin et al. [101] proved that the positive definiteness of the stiffness matrix determines a parallel robot's stability. Carricato and Merlet [23] analyzed that the equilibrium configuration will be feasible only if the cable tensions are positive and the equilibrium is stable. In addition, Behzadipour and Khajepour [18] also proved that a static cable-driven robot is stable if the stiffness matrix is positive definite, i.e., they showed the sufficient stability conditions, using an equivalent four-spring model.

2.5 Control Strategies

The goal of control strategies for cable-driven robots includes rigid body motion control (position and orientation) and vibration control. Generally, maximizing position and orientation accuracy (i.e., minimizing tracking errors) and reducing vibrations (for flexible joints or cables) are the desired objectives. To achieve this goal, one of the effective approaches is to develop different control strategies. For example, a robust PID controller was proposed by Kawamura et al. [54] to control a rigid planar CDPR. Xu et al. [122] designed Proportional-Derivative (PD) controllers for a cable-driven multi-segment continuum manipulator and showed that the position errors of the end-effector were acceptable. Feedforward control and computed torque control were also applied to cable-driven robots: for instance, Kino et al. [58] designed a feedforward controller to solve the gravitational compensation and positioning problems. Alikhani et al. [7] utilized a computed torque controller to study a constrained CDPR. Additionally, linear control theory based methods were developed: for example, Pole Placement Controller (PPC) [64], Linear-Quadratic Regulator (LQR) [74], gain scheduling pole placement controller [51], and linear optimal controller [61] were used to achieve the rigid body motion control and vibration control. Abdolshah and Barjuei [1] developed a linear quadratic optimal controller for cable-driven parallel robots. ElMaraghy et al. [35] designed a robust linear controller for a flexible joint robot, and the results showed that the performance of the tracking and regulation was acceptable. Athans [11] proposed the role and use of the stochastic Linear-Quadratic-Gaussian problem in control system design. Other control strategies also have been used to control CDPRs, such as robust sliding mode controller [8], chattering-free sliding mode controller [126], fuzzy controller [133], linear parameter-varying (LPV) controller [53, 80], and non-collocated controller [24]. Moreover, as one of the optimal control approaches, MPC is mainly used for process control. Some recent research applied this method to other applications, such as energy-saving [48], battery optimal charging [135], navigation of autonomous vehicles [116], overhead travelling cranes [39], and robot control [40, 94].

The above control strategies are available for cable-driven and serial robots. However, when the redundancy, singularity, stiffness of flexible cables, and stability problems are introduced, control problems (e.g., vibration) become more complex. Another major problem is in maintaining cable tensions for sufficient stiffness for the robot. Some researchers have tried to solve these problems by controlling the minimal guarantees of trajectory tracking using a lower bound task stiffness [125] and minimizing the linear and quadratic cable tensions [79]. However, these methods focused on improving the cable-tension problems. Hence, these existing problems make the research and applications incomplete.

Additionally, for the related work on the planar CDPR [76, 52, 53], the authors studied planar vibration control and ignored nonplanar (i.e., out-of-plane) vibrations. Actually, because of disturbances and mechanical limitations, out-of-plane vibrations were existed and could not be eliminated well by only using cables (e.g., controlling cable lengths or tensions). [93, 94, 95, 30] introduced two pendulums (called multiaxis reaction system) and mounted them to the planar CDPR to eliminate out-of-plane vibrations. Based on the pendulums, the authors showed the pendulums were effective in eliminating out-of-plane vibrations using sliding mode control (SMC) [30]. In [92], the decoupled modeling (in-plane and out-of-plane subsystems) for a hybrid of planar CDPR and pendulums was studied. However, these studies focused on vibration control and could not handle some applications such as increasing pick-and-place workspace and improving end-effector accuracy. To solve these problems, a rigid linear slider is proposed in this thesis by mounting it on the mobile platform (shown in Figure 3.6). The coupled slider, however, will lead to a new problem: the moving slider generates reaction forces to the mobile platform resulting in mobile platform vibrations. Researchers in [107] showed a CDPR carrying a robot arm for painting large surfaces, but vibrations were obvious and large based on their demonstration.

2.6 Summary

In conclusion, the literature shows that existing research and applications prefer to affix a robot arm upside down to the bottom of a CDPR's platform or mainly control the cable robot while treating the serial robot as a manipulation tool or an end-effector rather than a whole system. When a serial robot is mounted on a mobile platform, they constitute a new coupled system. Only controlling the mobile platform (i.e., treating the serial robot as a manipulation tool) or the serial robot may not guarantee the position accuracy of the end-effector. For applications that use such a system, the main goal is to control the end-effector of the serial robot (e.g., its trajectories and vibrations) in order to effectively accomplish tasks such as pick-and-place. Another major challenge in the utilization of these systems is maintaining the appropriate cable tensions and stiffness for the robot. This requires the development of kinematic and dynamic models, redundancy resolution, stiffness optimization, and controllers for HCDRs.

Additionally, since the use of flexible cables reduces the overall stiffness of cable-driven robots, vibration control becomes a serious problem. The moving robot arm also generates reaction forces to the mobile platform, resulting in the mobile platform vibrating. Hence, it is challenging to achieve the goal of minimizing the vibrations and increasing the position accuracy of the end-effector. To the best of the author's knowledge, limited studies address the modeling and control problems of flexible HCDRs. Especially when the redundancy and stiffness optimization problems are introduced, the control of trajectories and vibrations becomes more challenging.

This thesis is motivated by the need to solve the aforementioned problems for CDPRs with serial robot arms in order to increase their accuracy and adoption in industrial or other potential applications (e.g., rehabilitation). To implement this motivation, this thesis focuses on HCDRs, including modeling, control, and analysis.

Chapter 3

System Modeling

In this chapter, a generalized flexible HCDR is first introduced in section 3.1. For this HCDR, generalized system modeling is developed and then extended to four types of hybrid robots, namely, HCDR-1, HCDR-2, HCDR-3, and HCDR-4, corresponding to different motion models: in-plane system modeling, decoupled system modeling, out-of-plane system modeling, and 3D coupled system modeling, respectively. These hybrid robots will be used for control design, optimization and case studies (Chapter 4), and experiments (Chapter 5).

In section 3.2, HCDR-1 is a planar coupled system and in-plane controllable. To extend the study of generalized HCDR both in in-plane and out-of-plane motions, and simplify system modeling so that one can easier carry out in experiments, HCDR-2 is proposed in section 3.3. The proposed HCDR-3 in section 3.4 extends the configuration of HCDR-2 (in section 3.3) by introducing a coupled slider on the platform to enable execution of out-of-plane manipulation tasks such as pick-and-place. Accordingly, tracking, and vibration- and balance-control problems must be considered. In section 3.5, the proposed HCDR-4 is a more complicated system and its in-plane and out-of-plane motions are coupled. HCDR-4 is used to study the redundancy resolution and disturbance rejection via joint-space torque optimization methods (shown in Chapter 4).

3.1 Generalized System Modeling

Consider a generalized $(n+m)$-DOF HCDR in the 3D space (shown in Figure 3.1) with an n-DOF ($\{n \in \mathbb{N} : n \leq 6\}$) cable-driven parallel robot (referred to herein as a mobile platform) and an m-DOF ($m \in \mathbb{N}$) robot arm, where the robot arm is mounted on the mobile platform and moves with it. To simplify system modeling, all the driven cables are assumed massless, straight, and stretchable.

As a coupled system, developing an analytical model for the system in Figure 3.1 is much harder by comparison to just parallel robot or serial robot arm, especially, when flexible parts are introduced (e.g., flexible cables). To develop the model of the hybrid system, first, one can derive the equations of motion of the n-DOF CDPR (in subsection 3.1.1); then, utilize the formulations developed in subsection 3.1.1 to derive the equations of motion of the $(n+m)$-DOF HCDR (in subsection 3.1.2).

3.1.1 Equations of Motion of CDPR

In Figure 3.1, the inertial coordinate frame $\{O\}$ is assumed fixed on the base/ground. Coordinate frame $\{O_m\}$ is located at the center of mass (COM) of the mobile platform. By assuming the Euler angles $[\alpha_m, \beta_m, \gamma_m]^T \in \mathbb{R}^3$ (the orientations of the mobile platform about X-, Y-, and Z-axes, respectively), the rotation matrix (e.g., $X \to Y' \to Z''$) is computed as

$$R_g^m = R_x(\alpha_m) R_{y'}(\beta_m) R_{z''}(\gamma_m) \in \mathcal{SO}(3). \tag{3.1}$$

Then, the cable-length vector is calculated as

$$\begin{aligned}\vec{L}_i =& [p_{mx}, p_{my}, p_{mz}]^T + R_g^m [r_{ix}, r_{iy}, r_{iz}]^T \\ &-[a_{ix}, a_{iy}, a_{iz}]^T, \ \{\forall\, i \in \mathbb{N} : 1 \le i \le N\}\end{aligned} \tag{3.2}$$

where $\vec{L}_i \in \mathbb{R}^3$ denotes the position vector from the ith cable anchor point on the robot static frame to the ith cable anchor point on the mobile platform; $p_m := [p_{mx}, p_{my}, p_{mz}]^T \in \mathbb{R}^3$ represents the position vector of the coordinate frame $\{O_m\}$ with respect to the coordinate frame $\{O\}$; $r_i := [r_{ix}, r_{iy}, r_{iz}]^T \in \mathbb{R}^3$ denotes the position vector of the ith cable anchor point on the mobile platform with respect to the body-fixed frame $\{O_m\}$; $a_i := [a_{ix}, a_{iy}, a_{iz}]^T \in \mathbb{R}^3$ represents the position vector of the ith cable anchor point on the robot static frame with respect to the coordinate frame $\{O\}$; and N is the total number of cables. Then, the ith cable length $L_i \in \mathbb{R}$ is computed as

$$\begin{aligned}L_i =& \| [p_{mx}, p_{my}, p_{mz}]^T + R_g^m [r_{ix}, r_{iy}, r_{iz}]^T \\ &-[a_{ix}, a_{iy}, a_{iz}]^T \|.\end{aligned} \tag{3.3}$$

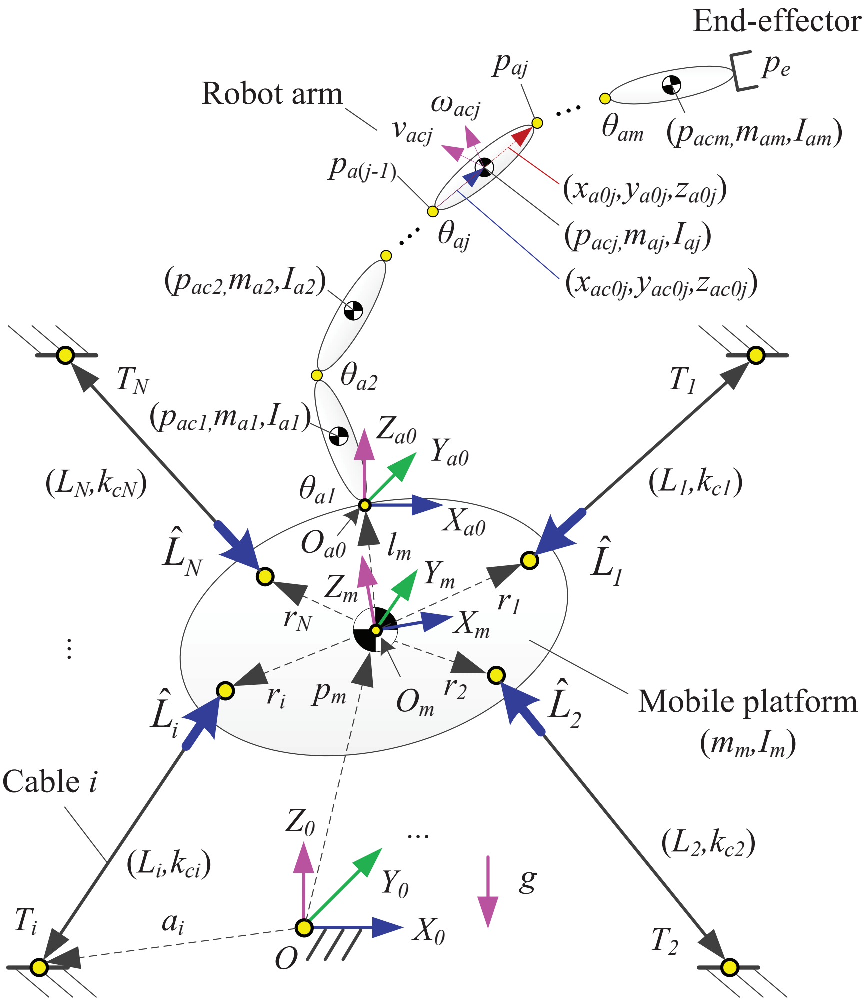

Figure 3.1: Configuration of a generalized $(n+m)$-DOF HCDR with an n-DOF CDPR and an m-DOF robot arm, where the robot arm is mounted on the CDPR.

In addition, the derivative of (3.2) is rearranged as

$$\dot{L}_i = \hat{L}_i^T v_m + (R_g^m [r_{ix}, r_{iy}, r_{iz}]^T \times \hat{L}_i)^T \omega_m \tag{3.4}$$

where $\dot{L}_i \in \mathbb{R}^3$ denotes the ith cable length velocity, $\hat{L}_i := \frac{\vec{L}_i}{L_i} = [\hat{L}_{ix}, \hat{L}_{iy}, \hat{L}_{iz}]^T \in \mathbb{R}^3$ represents the unit cable position vector, and $v_m, \omega_m \in \mathbb{R}^3$ are the linear and angular velocities of the coordinate frame $\{O_m\}$, respectively. Then, (3.4) can be expanded in matrix form as

$$
[\dot{L}_1, \dot{L}_2, \cdots, \dot{L}_N]^T = \underbrace{\begin{bmatrix} \hat{L}_1 & \cdots & \hat{L}_N \\ R_g^m \begin{bmatrix} r_{1x} \\ r_{1y} \\ r_{1z} \end{bmatrix} \times \hat{L}_1 & \cdots & R_g^m \begin{bmatrix} r_{Nx} \\ r_{Ny} \\ r_{Nz} \end{bmatrix} \times \hat{L}_N \end{bmatrix}^T}_{=:A_m} \begin{bmatrix} v_m \\ \omega_m \end{bmatrix} \tag{3.5}
$$

where A_m represents a structure matrix, determined by the position and orientation of the mobile platform. The linear velocity v_m and angular velocity ω_m are calculated as

$$
\left[\begin{array}{c} v_m \\ \hline \omega_m \end{array}\right] = (A_m^T)^+ [\dot{L}_1, \dot{L}_2, \cdots, \dot{L}_N]^T \tag{3.6a}
$$

$$
= \left[\begin{array}{c} [\dot{p}_{mx}, \dot{p}_{my}, \dot{p}_{mz}]^T \\ \hline [R_g^m]^T [\dot{\alpha}_m, 0, 0]^T + [R_{m\beta}^{m\gamma}]^T [R_{m\alpha}^{m\beta}]^T \\ [0, \dot{\beta}_m, 0]^T + [R_{m\beta}^{m\gamma}]^T [0, 0, \dot{\gamma}_m]^T \end{array}\right] \tag{3.6b}
$$

where $(\cdot)^+$ is the pseudo-inverse of the matrix $(\cdot)$, rotation matrices $R_{m\alpha}^{m\beta} = R_{y'}(\beta_m) \in \mathcal{SO}(3)$ and $R_{m\beta}^{m\gamma} = R_{z''}(\gamma_m) \in \mathcal{SO}(3)$ are obtained using (3.1). Eqs. (3.6a) and (3.6b) are two expressions to compute v_m and ω_m. $\dot{p}_{mx}, \dot{p}_{my}, \dot{p}_{mz}, \dot{\alpha}_m, \dot{\beta}_m$, and $\dot{\gamma}_m$ are the time-derivative of $p_{mx}, p_{my}, p_{mz}, \alpha_m, \beta_m$, and γ_m, respectively.

For the CDPR dynamics, the Newton-Euler equations of motion are used because they can describe the system in Figure 3.1 in terms of cable tensions directly, i.e.,

$$
\begin{bmatrix} m_m \dot{v}_m \\ I_m \dot{\omega}_m + \omega_m \times (I_m \omega_m) \end{bmatrix} + \begin{bmatrix} m_m [0, 0, g]^T + F_e \\ M_e \end{bmatrix} = \begin{bmatrix} \sum\limits_{i=1}^{N} (T_i \hat{L}_i) \\ \sum\limits_{i=1}^{N} [T_i (R_g^m [r_{ix}, r_{iy}, r_{iz}]^T \times \hat{L}_i)] \end{bmatrix} = A_m T \tag{3.7}
$$

where $T_i \in \mathbb{R}$ denotes the ith cable tension; $\hat{L}_i \in \mathbb{R}^3$ represents the unit vector of ith cable position; $F_e, M_e \in \mathbb{R}^3$ are the external forces and moments (e.g., the interaction forces and torques from the mounted robot arm affecting the mobile platform) applied to the coordinate frame $\{O_m\}$; $m_m \in \mathbb{R}$ is the mass of the mobile platform; $I_m \in \mathbb{R}^{3\times 3}$ denotes the moment of inertia of the mobile platform; $v_m, \dot{v}_m, \omega_m, \dot{\omega}_m \in \mathbb{R}^3$ represent the linear velocity, linear acceleration, angular velocity, and angular acceleration the mobile platform, respectively; and g is the gravitational acceleration.

Suppose the cable stiffness matrix is $K_c = \operatorname{diag}\left(k_{c1}, k_{c2}, \cdots, k_{cN}\right) \in \mathbb{R}^{N\times N}$, where $k_{ci} = \frac{EA_i}{L_{0i}}$ represents the ith cable stiffness, EA_i is the product of the modulus of elasticity and cross-sectional area of the ith cable, and L_{0i} denotes ith unstretched cable length. Then, the cable tension vector is calculated as

$$T = K_c\left(L - L_0\right) \tag{3.8}$$

where $T \in \mathbb{R}^N$ denotes the cable tension vector, $L \in \mathbb{R}^N$ represents the cable length vector, and $L_0 \in \mathbb{R}^N$ denotes the vector of unstretched cable lengths. The directions of T are shown in Figure 3.1.

Finally, by considering a vector of unknown bounded disturbances τ_{md}, (3.7) and (3.8) can be combined and rewritten as

$$\begin{aligned} &\underbrace{\begin{bmatrix} m_m I & \mathbf{0} \\ \mathbf{0} & I_m \end{bmatrix}}_{=:M_m(q_m)} \underbrace{\begin{bmatrix} \dot{v}_m \\ \dot{\omega}_m \end{bmatrix}}_{=:\ddot{q}_m} + \underbrace{\begin{bmatrix} \mathbf{0} \\ [\omega_m] I_m \end{bmatrix}}_{=:C_m(q_m,\dot{q}_m)} \underbrace{\begin{bmatrix} v_m \\ \omega_m \end{bmatrix}}_{=:\dot{q}_m} \\ &+ \begin{bmatrix} \underbrace{m_m[0,0,g]^T}_{=:G_m(q_m)} + F_e \\ M_e \end{bmatrix} + \tau_{md} = A_m T =: \tau_m \end{aligned} \tag{3.9}$$

where $[\omega_m] := \begin{bmatrix} 0 & -\omega_{mz} & \omega_{my} \\ \omega_{mz} & 0 & -\omega_{mx} \\ -\omega_{my} & \omega_{mx} & 0 \end{bmatrix}$ and $I \in \mathbb{R}^{3\times 3}$ is the identity matrix. $M_m(q_m)$, $C_m(q_m, \dot{q}_m)$, and $G_m(q_m)$ denote the inertia matrix, Coriolis and centripetal matrix, and gravitational vector, respectively. q_m, $\dot{q}_m$, $\ddot{q}_m$, and τ_m represent the vectors of generalized coordinates, velocities, accelerations, and joint forces/torques, respectively. Related background about CDPR modeling is introduced in [57, 52, 76, 18, 93, 95]. However, the derivation of equations of motion of the CDPR in this section provides a convenient closed form to simplify HCDR modeling in subsection 3.1.2.

3.1.2 Equations of Motion of HCDR

For the $(n+m)$-DOF HCDR shown in Figure 3.1, the jth ($\{\forall\, j \in \mathbb{N} : 0 \leq j \leq m\}$) COM (of the link) position vector p_{acj} and joint position vector p_{aj} are computed as

$$
\begin{aligned}
p_{acj} =& [p_{mx}, p_{my}, p_{mz}]^T + \underbrace{R_g^m R_m^{a0}}_{=:R_g^{a0}} [x_{a00}, y_{a00}, z_{a00}]^T \\
&+ \underbrace{R_g^m R_m^{a0} R_{a0}^{a1}}_{=:R_g^{a1}} [x_{a01}, y_{a01}, z_{a01}]^T + \cdots \\
&+ \underbrace{R_g^m R_m^{a0} R_{a0}^{a1} R_{a1}^{a2} \cdots R_{a(j-1)}^{aj}}_{=:R_g^{aj}} [x_{ac0j}, y_{ac0j}, z_{ac0j}]^T \\
=& [p_{mx}, p_{my}, p_{mz}]^T + R_g^{a0} [x_{a00}, y_{a00}, z_{a00}]^T + \\
& R_g^{a1} [x_{a01}, y_{a01}, z_{a01}]^T + \cdots + R_g^{aj} [x_{ac0j}, y_{ac0j}, z_{ac0j}]^T \\
=& [p_{mx}, p_{my}, p_{mz}]^T + R_g^{aj} [x_{ac0j}, y_{ac0j}, z_{ac0j}]^T + \\
& \sum_{k=0}^{j} \left\{ R_g^{a(j-1)} [x_{a0(j-1)}, y_{a0(j-1)}, z_{a0(j-1)}]^T \right\}
\end{aligned}
\tag{3.10}
$$

and

$$
\begin{aligned}
p_{aj} =& [p_{mx}, p_{my}, p_{mz}]^T + R_g^m R_m^{a0} [x_{a00}, y_{a00}, z_{a00}]^T \\
&+ R_g^m R_m^{a0} R_{a0}^{a1} [x_{a01}, y_{a01}, z_{a01}]^T + \cdots \\
&+ R_g^m R_m^{a0} R_{a0}^{a1} R_{a1}^{a2} \cdots R_{a(j-1)}^{aj} [x_{a0j}, y_{a0j}, z_{a0j}]^T \\
=& [p_{mx}, p_{my}, p_{mz}]^T + R_g^{a0} [x_{a00}, y_{a00}, z_{a00}]^T + \\
& R_g^{a1} [x_{a01}, y_{a01}, z_{a01}]^T + \cdots + R_g^{aj} [x_{a0j}, y_{a0j}, z_{a0j}]^T \\
=& [p_{mx}, p_{my}, p_{mz}]^T + \sum_{k=0}^{j} \left\{ R_g^{aj} [x_{a0j}, y_{a0j}, z_{a0j}]^T \right\}
\end{aligned}
\tag{3.11}
$$

where $m_{aj} \in \mathbb{R}$ is the mass of link j and $I_{aj} \in \mathbb{R}^{3\times 3}$ denotes the moment of inertia of link j. $[x_{ac0j}, y_{ac0j}, z_{ac0j}]^T$ and $[x_{a0j}, y_{a0j}, z_{a0j}]^T$ are body-fixed positions of the jth COM and joint, respectively. Also, for the jth revolute joint, a rotation matrix from frame $j-1$ to j is defined as

$$
R_{a(j-1)}^{aj} = \begin{cases} R_x(\theta_{aj}), & \text{revolute joint about } X\text{-axis} \\ R_y(\theta_{aj}), & \text{revolute joint about } Y\text{-axis} \\ R_z(\theta_{aj}), & \text{revolute joint about } Z\text{-axis} \end{cases}
\tag{3.12}
$$

and for the jth prismatic joint, the corresponding parameters of the revolute joint are replaced with

$$\begin{cases} R_{a(j-1)}^{aj} = I_{3\times 3} & \\ x_{ac0j} = x_{ac0j} + \theta_{aj}, & \text{prismatic joint about } X\text{-axis} \\ x_{a0j} = x_{a0j} + \theta_{aj}, & \text{prismatic joint about } X\text{-axis} \\ y_{ac0j} = y_{ac0j} + \theta_{aj}, & \text{prismatic joint about } Y\text{-axis} \\ y_{a0j} = y_{a0j} + \theta_{aj}, & \text{prismatic joint about } Y\text{-axis} \\ z_{ac0j} = z_{ac0j} + \theta_{aj}, & \text{prismatic joint about } Z\text{-axis} \\ z_{a0j} = z_{a0j} + \theta_{aj}, & \text{prismatic joint about } Z\text{-axis.} \end{cases} \tag{3.13}$$

The linear velocities of the jth COM (of the link) and joint are the time-derivative of positions in (3.10) and (3.11), respectively. Then,

$$v_{acj} = \dot{p}_{acj} \tag{3.14}$$

$$v_{aj} = \dot{p}_{aj}. \tag{3.15}$$

Additionally, the jth angle velocities are computed as

$$\omega_{acj} = \omega_{aj} = [R_m^{a0} R_{a0}^{aj}]^T \omega_m + \sum_{k=0}^{j} \left\{ [R_{ak}^{aj}]^T \vec{\dot{\theta}}_{ak} \right\}. \tag{3.16}$$

The proof of (3.16) is provided in Lemma 3.1.1. (3.16) is a simplified and very useful result for generalized dynamic modeling, e.g., calculating the kinetic energy.

Lemma 3.1.1. *Let* $\vec{\dot{\theta}}_{ak} \in \mathbb{R}^3$ *be the vector of joint velocity about its body-fixed axis. Then the* j*th angle velocity vector is equal to* $\omega_{acj} = [R_m^{a0} R_{a0}^{aj}]^T \omega_m + \sum_{k=0}^{j} \left\{ [R_{ak}^{aj}]^T \vec{\dot{\theta}}_{ak} \right\}$*, where* $\{\forall\, j, k \in \mathbb{N} : 0 \le j \le m,\ 0 \le k \le j\}$.

Proof. The jth angle velocity vector ω_{acj} can be derived as follows:

$$
\begin{aligned}
\omega_{acj} =& [\underbrace{R_g^{m\alpha} R_{m\alpha}^{m\beta} R_{m\beta}^{m\gamma}}_{R_g^m} R_m^{a0} \underbrace{R_{a0}^{a1} R_{a1}^{a2} \cdots R_{a(j-1)}^{aj}}_{R_{a0}^{aj}}]^T [\dot{\alpha}_m, 0, 0]^T \\
& + [R_{m\alpha}^{m\beta} R_{m\beta}^{m\gamma} R_m^{a0} R_{a0}^{a1} R_{a1}^{a2} \cdots R_{a(j-1)}^{aj}]^T [0, \dot{\beta}_m, 0]^T \\
& + [R_{m\beta}^{m\gamma} R_m^{a0} R_{a0}^{a1} R_{a1}^{a2} \cdots R_{a(j-1)}^{aj}]^T [0, 0, \dot{\gamma}_m]^T + \\
& \underbrace{[R_{a0}^{a1} R_{a1}^{a2} \cdots R_{a(j-1)}^{aj}]}_{R_{a0}^{aj}}{}^T \dot{\vec{\theta}}_{a1} + \underbrace{[R_{a1}^{a2} \cdots R_{a(j-1)}^{aj}]}_{R_{a1}^{aj}}{}^T \dot{\vec{\theta}}_{a2} \\
& + \cdots + \underbrace{[R_{a(j-2)}^{a(j-1)} R_{a(j-1)}^{aj}]}_{R_{a(j-2)}^{aj}}{}^T \dot{\vec{\theta}}_{a(j-1)} + [R_{a(j-1)}^{aj}]^T \dot{\vec{\theta}}_{0j} \\
=& [R_g^m R_m^{a0} R_{a0}^{aj}]^T [\dot{\alpha}_m, 0, 0]^T + [R_{m\alpha}^{m\beta} R_{m\beta}^{m\gamma} R_m^{a0} R_{a0}^{aj}]^T \\
& [0, \dot{\beta}_m, 0]^T + [R_{m\beta}^{m\gamma} R_m^{a0} R_{a0}^{aj}]^T [0, 0, \dot{\gamma}_m]^T + [R_{a0}^{aj}]^T \dot{\vec{\theta}}_{a1} \\
& + \cdots + [R_{a(j-2)}^{aj}]^T \dot{\vec{\theta}}_{a(j-1)} + [R_{a(j-1)}^{aj}]^T \dot{\vec{\theta}}_{aj} \\
=& [R_m^{a0} R_{a0}^{aj}]^T [R_g^m]^T [\dot{\alpha}_m, 0, 0]^T + [R_m^{a0} R_{a0}^{aj}]^T [R_{m\beta}^{m\gamma}]^T \\
& [R_{m\alpha}^{m\beta}]^T [0, \dot{\beta}_m, 0]^T + [R_m^{a0} R_{a0}^{aj}]^T [R_{m\beta}^{m\gamma}]^T [0, 0, \dot{\gamma}_m]^T \\
& + [R_{a0}^{aj}]^T \dot{\vec{\theta}}_{a1} + \cdots + [R_{a(j-2)}^{aj}]^T \dot{\vec{\theta}}_{a(j-1)} + [R_{a(j-1)}^{aj}]^T \dot{\vec{\theta}}_{aj} \\
=& [R_m^{a0} R_{a0}^{aj}]^T \underbrace{\left\{ \begin{array}{l} [R_g^m]^T [\dot{\alpha}_m, 0, 0]^T + [R_{m\beta}^{m\gamma}]^T [R_{m\alpha}^{m\beta}]^T \\ {[0, \dot{\beta}_m, 0]^T} + [R_{m\beta}^{m\gamma}]^T [0, 0, \dot{\gamma}_m]^T \end{array} \right\}}_{\omega_m} \\
& + [R_{a0}^{aj}]^T \dot{\vec{\theta}}_{a1} + \cdots + [R_{a(j-2)}^{aj}]^T \dot{\vec{\theta}}_{a(j-1)} + [R_{a(j-1)}^{aj}]^T \dot{\vec{\theta}}_{aj} \\
=& [R_m^{a0} R_{a0}^{aj}]^T \omega_m + \sum_{k=0}^{j} \left\{ [R_{ak}^{aj}]^T \dot{\vec{\theta}}_{ak} \right\}
\end{aligned}
$$

where $\{\forall\, j, k \in \mathbb{N} : 0 \leq j \leq m,\ 0 \leq k \leq j\}$, $R_g^{m\alpha} = R_x(\alpha_m) \in \mathcal{SO}(3)$, $R_{m\alpha}^{m\beta} = R_{y'}(\beta_m) \in \mathcal{SO}(3)$, and $R_{m\beta}^{m\gamma} = R_{z''}(\gamma_m) \in \mathcal{SO}(3)$. □

Substituting the corresponding results in (3.14) and (3.16), the total kinetic energy is calculated as

$$
\begin{aligned}
K_E = & \frac{1}{2} m_m [\dot{p}_{mx}, \dot{p}_{my}, \dot{p}_{mz}] [\dot{p}_{mx}, \dot{p}_{my}, \dot{p}_{mz}]^T + \frac{1}{2} \omega_m^T I_m \omega_m \\
& + \frac{1}{2} \sum_{k=0}^{j} \left\{ m_{ak} v_{ack}^T v_{ack} + \omega_{ack}^T I_{ak} \omega_{ack} \right\}. \qquad (3.17)
\end{aligned}
$$

The total potential energy is computed as

$$
\begin{aligned}
V_E = & m_m g p_{mz} + \sum_{k=0}^{j} \left\{ m_{ak} g p_{ack}^T [0, 0, 1]^T \right\} \\
& + \frac{1}{2} (L - L_0)^T K_c (L - L_0) \qquad (3.18)
\end{aligned}
$$

where g represents the gravity acceleration, position vector p_{ack} is obtained using (3.10), and $\frac{1}{2}(L - L_0)^T K_c (L - L_0)$ denotes the cable elastic potential energy with its variables defined in (3.8).

Based on the computed kinetic energy K_E and potential energy V_E in (3.17) and (3.18), respectively, the Lagrangian dynamic equation of motion is calculated as

$$
L_E = K_E - V_E. \qquad (3.19)
$$

Then, the torque equations can be calculated as

$$
\begin{aligned}
\tau_j & = \frac{d}{dt} \left(\frac{\partial L_E}{\partial \dot{q}_j} \right) - \frac{\partial L_E}{\partial q_j} \\
& = \frac{d}{dt} \left(\frac{\partial K_E}{\partial \dot{q}_j} \right) - \frac{\partial K_E}{\partial q_j} + \frac{\partial V_E}{\partial q_j} \qquad (3.20)
\end{aligned}
$$

where τ_j represents the generalized force/torque applied to the dynamic system at joint j to drive link j.

Based on open-chain, (3.20) can be described using the following form:

$$
\tau_j = \left\{ \left[\nabla \left(\left(\nabla L_{E\dot{q}} \right)_j \right)_q \right]^T \dot{q} + \left[\nabla \left(\left(\nabla L_{E\dot{q}} \right)_j \right)_{\dot{q}} \right]^T \ddot{q} - \left(\nabla L_{Eq} \right)_j \right\} \qquad (3.21)
$$

where $\nabla(\cdot)_q$ and $\nabla(\cdot)_{\dot{q}}$ are defined as the gradient vectors of $(\cdot)$ with respect to the vectors q and $\dot{q}$, respectively. Compared with (3.20), (3.21) is easier to implement (i.e., programming). By arranging (3.21) and introducing a vector of unknown bounded disturbances $\tau_d \in \mathbb{R}^{n+m}$, the equations of motion of the HCDR can be derived as

$$M(q)\ddot{q} + C(q,\dot{q})\dot{q} + G(q) + \tau_d =: \tau = \begin{bmatrix} \tau_m \\ \tau_a \end{bmatrix} = \begin{bmatrix} A_m T \\ \tau_a \end{bmatrix} \tag{3.22}$$

where $q \in \mathbb{R}^{n+m}$, $\dot{q} \in \mathbb{R}^{n+m}$, and $\ddot{q} \in \mathbb{R}^{n+m}$ represent the vectors of generalized coordinates, velocities, and accelerations, respectively. $M(q) \in \mathbb{R}^{(n+m)\times(n+m)}$ denotes the combined inertia matrix, $C(q,\dot{q}) \in \mathbb{R}^{(n+m)\times(n+m)}$ represents the combined Coriolis and centripetal matrix, and $G(q) \in \mathbb{R}^{n+m}$ denote the gravitational vector, respectively. $\tau_d \in \mathbb{R}^{n+m}$ and $\tau \in \mathbb{R}^{n+m}$ denote the vector of unknown bounded disturbances and forces/torques in generalized coordinates, respectively. Eq. (3.22) is the inverse dynamics model of the HCDR.

Since the inertia matrix M is symmetric and positive definite [68], then the forward dynamics can be computed as

$$\ddot{q} = M^{-1}(q)\left(\begin{bmatrix} A_m T \\ \tau_a \end{bmatrix} - C(q,\dot{q})\dot{q} - G(q) - \tau_d\right) \tag{3.23}$$

where the cable tension T and robot arm joint torque τ_a are inputs.

Additionally, (3.22) can be arranged as

$$\begin{aligned} &\begin{bmatrix} M_{11}(q) & M_{12}(q) \\ M_{21}(q) & M_{22}(q) \end{bmatrix} \begin{bmatrix} \ddot{q}_m \\ \ddot{q}_a \end{bmatrix} + \begin{bmatrix} C_{11}(q,\dot{q}) & C_{12}(q,\dot{q}) \\ C_{21}(q,\dot{q}) & C_{22}(q,\dot{q}) \end{bmatrix} \\ &\begin{bmatrix} \dot{q}_m \\ \dot{q}_a \end{bmatrix} + \begin{bmatrix} G_m(q_m) \\ G_a(q_a) \end{bmatrix} + \begin{bmatrix} \tau_{md} \\ \tau_{ad} \end{bmatrix} = \begin{bmatrix} A_m T \\ \tau_a \end{bmatrix} \end{aligned} \tag{3.24}$$

where $(\cdot)_m \in \mathbb{R}^n$ and $(\cdot)_a \in \mathbb{R}^m$ represent the vector of the mobile platform variables and the robot arm variables, respectively. It is clear that this equation includes the dynamics of the CDPR and the mounted robot arm.

In summary, the key benefits of the proposed modeling method can be highlighted as follows: 1) The derivation of the equations of motion (e.g., (3.10)–(3.16) and (3.21)) and the proof of (3.16) provide a very effective way to formulate the generalized dynamics model. 2) Traditionally, based on the Standard Denavit-Hartenberg (DH) method [31], a revolute joint must rotate about its Z-axis. The proposed method relaxes this limiting condition, i.e., it is unnecessary to follow DH configurations, and can be applied to any coordinate frames (e.g., about X-axis, Y-axis, or Z-axis), including revolute and prismatic joints. 3) The above modeling approach in this section can be easily extended to other types of hybrid robots by changing structure matrix A_m in (3.5) based on the desired configurations, e.g., a robot arm(s) mounted on an aircraft platform [106, 90].

3.1.3 Redundancy Resolution

Cable-driven robots (as shown in Figure 3.1) can be categorized into one of two classes: under-actuated and fully-actuated robots [108, 10, 67]. The first class of robots denotes the number of driven cables N is less than the number of DOF of a robot n, i.e., $N < n$; the second class of robots represents the number of driven cables N is no less than the DOF of a robot n, i.e., $N \geq n$. Then, the value of $(N - n)$ represents the DOR. When redundancy exists, there are infinite solutions for inverse kinematics, which make the motion planning challenging [102]. Usually, redundancy resolution problems are more general for cable-driven robots and can be solved only using a pseudo-inverse approach [27], but the obtained solutions are not usually optimal. Some other approaches were also proposed, such as a combination of pseudo-inverse and null-space method [27, 76, 18], damped least-squares approach [65], and energy-based method [65]. In this chapter, the combined method in [27, 76, 18] is adopted to tackle the redundancy resolution problem.

When q_m, $\dot{q}_m$, and $\ddot{q}_m$ are given, $\tau_m = A_m T$ can be computed using (3.9) or (3.22). Then, the cable tension T is calculate as

$$T = A_m^+ \tau_m = A_m^T (A_m A_m^T)^{-1} \tau_m \tag{3.25}$$

where $A_m^+ = A_m^T (A_m A_m^T)^{-1}$ represents the pseudo-inverse of matrix A_m. In (3.25), the elements of the cable tension $T \in \mathbb{R}^N$ may be negative. However, in practice, they cannot drive the mobile platform if they are negative. The redundancy resolution of the cable tension T can then be formulated as

$$T = A_m^T (A_m A_m^T)^{-1} \tau_m + N_A \lambda \tag{3.26}$$

where $N_A \in \mathbb{R}^{N \times (N-n)}$ represents the null space of structure matrix A_m (A_m is calculated using (3.5)), and $\lambda \in \mathbb{R}^{N-n}$ is a vector of arbitrary values. In (3.26), $N_A\lambda$ belongs to the null space of A_m, since it can be described as $A_m (N_A \lambda) = (A_m N_A) \lambda = \mathbf{0}$. The expression $N_A\lambda$ denotes antagonistic cable tensions. The cable tension T increases if all the antagonistic cable tensions are positive. Hence, the vector λ can be optimized (e.g., using the stiffness optimization method in the next section) to ensure that all the cable tensions are positive.

3.1.4 Stiffness Optimization

To solve the above problem of selecting λ, a stiffness maximization method is proposed in this section. Consider the same condition as (3.25), the stiffness matrix K is defined as

$$\begin{aligned} K :=& \frac{d(A_m T)}{dP_m} = \frac{dA_m}{dP_m}T + A_m\frac{dT}{dP_m} = \frac{dA_m}{dP_m}T + A_m\left(\frac{dT}{dL}\right) \\ &\left(\frac{dL}{dP_m}\right) = \frac{dA_m}{dP_m}T + A_m K_c A_m^T =: K_T + K_k \end{aligned} \tag{3.27}$$

where $P_m := [p_{mx}, p_{my}, p_{mz}, \alpha_m, \beta_m, \gamma_m]^T \in \mathbb{R}^6$, T, and L represent the position and orientation of the center of mass of the mobile platform, cable tension vector, and cable length vector, respectively. Matrices K_T and K_k are a product of the cable tensions and cable stiffness, respectively, where $K_c = \frac{dT}{dL} = \operatorname{diag}(k_{c1}, k_{c2}, \cdots, k_{ci}, \cdots, k_{cN}) \in \mathbb{R}^{N\times N}$ and k_{ci} denotes the ith cable stiffness (same as (3.8)).

Usually, K is obtained at static condition for ease of stability. In this case, if (3.27) is expanded in terms of the kinematic parameters L_i, $\hat{L}_i$, and r_i, the matrices K_T and K_k can be described as [18]

$$\begin{aligned} K_T =& \sum_{i=1}^{N}\frac{T_i}{L_i}\begin{bmatrix} I-\hat{L}_i\hat{L}_i^T & (I-\hat{L}_i\hat{L}_i^T)[r_i]^T \\ [r_i](I-\hat{L}_i\hat{L}_i^T) & [r_i](I-\hat{L}_i\hat{L}_i^T)[r_i]^T \end{bmatrix} \\ & -\sum_{i=1}^{N} T_i \begin{bmatrix} \mathbf{0} & \mathbf{0} \\ \mathbf{0} & [\hat{L}_i][r_i] \end{bmatrix} \end{aligned} \tag{3.28}$$

and

$$K_k = \sum_{i=1}^{N} k_{ci}\begin{bmatrix} \hat{L}_i\hat{L}_i^T & \hat{L}_i\hat{L}_i^T[r_i]^T \\ [r_i]\hat{L}_i\hat{L}_i^T & [r_i]\hat{L}_i\hat{L}_i^T[r_i]^T \end{bmatrix} \tag{3.29}$$

where

$$[r_i] := \begin{bmatrix} 0 & -(R_g^m r_i)_{3,1} & (R_g^m r_i)_{2,1} \\ (R_g^m r_i)_{3,1} & 0 & -(R_g^m r_i)_{1,1} \\ -(R_g^m r_i)_{2,1} & (R_g^m r_i)_{1,1} & 0 \end{bmatrix} \tag{3.30a}$$

$$[\hat{L}_i] := -\begin{bmatrix} 0 & -\hat{L}_{iz} & \hat{L}_{iy} \\ \hat{L}_{iz} & 0 & -\hat{L}_{ix} \\ -\hat{L}_{iy} & \hat{L}_{ix} & 0 \end{bmatrix} \tag{3.30b}$$

with $r_i = [r_{ix}, r_{iy}, r_{iz}]^T, \hat{L}_i = [\hat{L}_{ix}, \hat{L}_{iy}, \hat{L}_{iz}]^T$, and I is the identity matrix. Eqs. (3.28) and (3.29) are equivalent to the results of the four-spring model proposed by Behzadipour and Khajepour [18]. They proved that a static cable-driven robot is stable if the stiffness matrix K is positive definite (sufficient condition). In addition, elements of K_k cannot be controlled, because they are the property of the cables. Hence, the stiffness of HCDR can only be changed by optimizing K_T.

Additionally, combining (3.26) and (3.27), one can get

$$\begin{aligned} K(\lambda) = &\left(\frac{dA_m}{dP_m} N_A \right) \lambda + \frac{dA_m}{dP_m} A_m^T (A_m A_m^T)^{-1} \tau_m \\ &+ A_m K_c A_m^T. \end{aligned} \tag{3.31}$$

Since K is positive definite (or positive semidefinite), the maximum stiffness is determined by its eigenvalues [66, 59, 41]. Hence, the optimization problem can be described as

$$\max_{\lambda} \qquad J_K = \mathrm{eig}(K(\lambda))^T H_\lambda \mathrm{eig}(K(\lambda)) \tag{3.32a}$$

$$\text{s. t.} \qquad M(q)\ddot{q} + C(q,\dot{q})\dot{q} + G(q) + \tau_d = \begin{bmatrix} A_m T \\ \tau_a \end{bmatrix} \tag{3.32b}$$

$$\begin{aligned} K(\lambda) = &\left(\frac{dA_m}{dP_m} N_A \right) \lambda + \frac{dA_m}{dP_m} A_m^T (A_m A_m^T)^{-1} \tau_m \\ &+ A_m K_c A_m^T \end{aligned} \tag{3.32c}$$

$$0 \le T_{i\,\min} \le T_i \le T_{i\,\max}, \; i = 1, 2, \cdots, N \tag{3.32d}$$

where T_i, $T_{i\,\min}$, and $T_{i\,\max}$ represent the ith cable tension, minimum and maximum allowable tensions, respectively. H_λ denotes the stiffness weighting matrix. To ensure the stability of a HCDR in practical applications, some alternative strategies can be adopted as follows: 1) optimizing its trajectory to keep all the eigenvalues of K positive and 2) limiting the maximum payload [18]. Compared to existing stiffness optimization approaches in [57, 76, 52, 53], (3.32a) is introduced by combining the eigenvalues of K and weighting matrix H_λ so that one can optimize the system stiffness based on specific needs (by tuning H_λ). Meanwhile, (3.32) can be applied to not only CDPRs but also HCDRs.

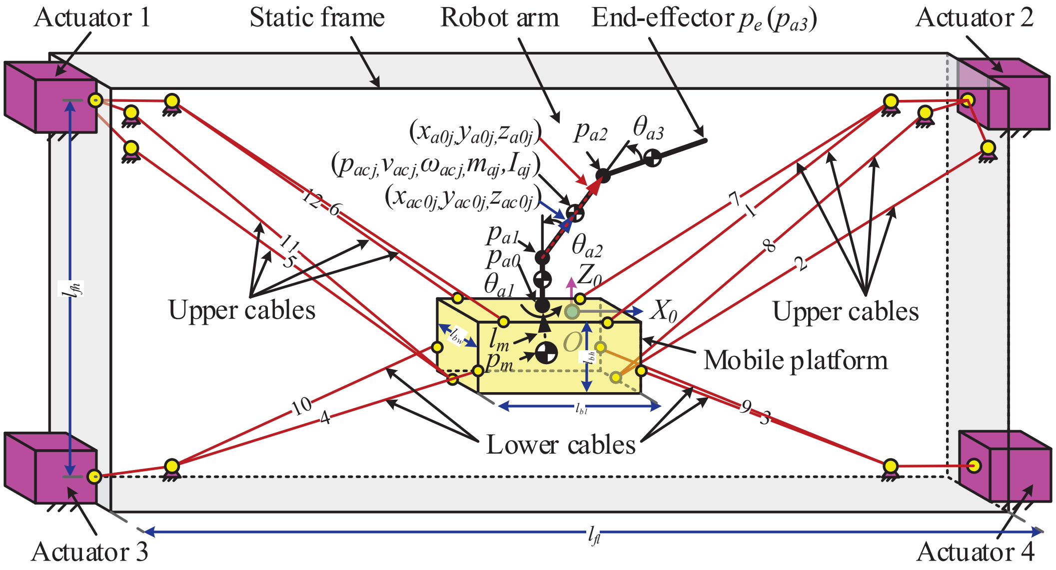

Figure 3.2: Configuration of the 9-DOF HCDR-1. The mobile platform is driven by four actuators with 12 cables; the robot arm has three joints with the first, second, and third joints rotating about Z_{a0}-, Y_{a1}-, and Y_{a2}-axis (i.e., the corresponding moving frames), respectively.

3.2 In-Plane System Modeling

3.2.1 Configuration and Kinematic Constraints

To analyze the generalized HCDR motion model in section 3.1 and study its control performance, a HCDR example, namely, HCDR-1 is given in Figure 3.2. The proposed full model of the HCDR-1 has 9 DOFs (the CDPR parameters come from [76, 93, 95]), which consists of a 3-DOF robot arm (i.e., $m = 3$), a 6-DOF mobile platform (i.e., $n = 6$), twelve cables, and four servo motors. The 3-DOF robot arm has three revolute joints, rotating about Z-axis (joint 1 frame), Y-axis (joint 2 frame), and Y-axis (joint 3 frame), respectively. The actuators are used to drive the cables to move the mobile platform. The robot arm is fixed on the mobile platform and moves with it. The twelve cables include four sets of cables: two sets of four-cable arrangement on the top and two sets of two-cable arrangement on the bottom. The driven cable mount locations the HCDR-1 are shown in Table 3.1. Each set of cables is controlled by one motor. In addition, the top actuators and bottom actuators control the upper cable lengths and lower cable tensions, respectively. The upper cables also restrict the orientation of the mobile platform, i.e., introduce kinematic constraints.

Table 3.1: Driven Cable Mount Locations of HCDR-1

N	a_{ix} (m)	a_{iy} (m)	a_{iz} (m)	r_{ix} (m)	r_{iy} (m)	r_{iz} (m)
1	1.500	0.000	0.500	0.153	-0.065	0.048
2	1.580	-0.065	0.404	0.233	0.000	-0.048
3	1.500	0.000	-0.500	0.223	-0.088	-0.017
4	-1.500	0.000	-0.500	-0.223	-0.088	-0.017
5	-1.580	-0.065	0.404	-0.233	0.000	-0.048
6	-1.500	0.000	0.500	-0.153	-0.065	0.048
7	1.500	0.000	0.500	0.153	0.065	0.048
8	1.580	0.065	0.404	0.233	0.000	-0.048
9	1.500	0.000	-0.500	0.223	0.088	-0.017
10	-1.500	0.000	-0.500	-0.223	0.088	-0.017
11	-1.580	0.065	0.404	-0.233	0.000	-0.048
12	-1.500	0.000	0.500	-0.153	0.065	0.048

In addition, the inertial coordinate frame $O\left\{x_0, y_0, z_0\right\}$ is located at the center of the static fixture.

Additionally, other HCDR-1 parameters are shown in Table 3.2, where m_m and I_m represent the mass and moment of inertia of the mobile platform, respectively. m_{aj} and I_{aj} ($\{\forall\ j \in \mathbb{N} : 1 \leq j \leq 3\}$) respectively denote the mass and moment of inertia of robot arm links. Also, $T_{i\,\min}$ and $T_{i\,\max}$ ($\{\forall\ i \in \mathbb{N} : 1 \leq i \leq 12\}$) represent the minimum and maximum allowable cable tensions, respectively. The sizes of the static fixture (e.g., l_{fl}) and mobile platform (e.g., l_{bl}), body-fixed positions (e.g., $[x_{a0j}, y_{a0j}, z_{a0j}]^T$), and etc. are also given in Table 3.2.

3.2.2 Equations of Motion

By applying the modeling method in section 3.1, the detailed equations of motion can be derived for the specific 9-DOF system (see Appendix A.1), where $q = [p_{mx}, p_{my}, p_{mz}, \alpha_m,$

Table 3.2: HCDR-1 Parameters

Symbol	Values	Symbol	Values
l_{fl}	3.160 m	l_{fh}	1.000 m
l_{bl}	0.365 m	l_{bw}	0.130 m
l_{bh}	0.096 m	l_m	$[0, 0, 0.048]^T$ m
m_{aj}	0.400 kg	I_{aj}	diag($[0.100, 0.100, 0.100]$) kg · m^2
$[x_{ac0j}, y_{ac0j}, z_{ac0j}]^T$	$[0, 0, 0.050]^T$ m	$[x_{a0j}, y_{a0j}, z_{a0j}]^T$	$[0, 0, 0.100]^T$ m
m_m	10.000 kg	I_m	diag($[0.0218, 0.1187, 0.1251]$) kg · m^2
EA_i	100 N	$[T_{i\min},\ T_{i\max}]$	$[5, 80]$ N
g	9.810 m/s^2		

$\beta_m, \gamma_m, \theta_{a1}, \theta_{a2}, \theta_{a3}]^T_{9\times 1} \in \mathbb{R}^{6+3}$, $\dot{q} \in \mathbb{R}^{6+3}$, $\ddot{q} \in \mathbb{R}^{6+3}$, $M(q) \in \mathbb{R}^{(6+3)\times(6+3)}$, $C(q, \dot{q}) \in \mathbb{R}^{(6+3)\times(6+3)}$, $G(q) \in \mathbb{R}^{6+3}, \tau_d \in \mathbb{R}^{6+3}, \tau_m \in \mathbb{R}^6, \tau_a \in \mathbb{R}^3, A_m \in \mathbb{R}^{6\times 12}$, and $T \in \mathbb{R}^{12}$. However, because of the kinematic constraints, the system is fully controllable in x_0z_0 plane, then the 9-DOF HCDR-1 is simplified as a 5-DOF in-plane system. The new control inputs are defined as $u := (u_m, u_a) := [T_3, T_4, \tau_{a2}, \tau_{a3}]^T \in \mathbb{R}^4$, where $u_m = [T_3, T_4]^T \in \mathbb{R}^2$ denote the lower cable tensions (two sets of two-cable arrangement on the bottom), i.e., T_3 (driven by actuator 3) represents cable tensions 4 and 10, and T_4 (driven by actuator 4) denotes cable tensions 3 and 9 (shown in Figure 3.2). $u_a = \tau_a = [\tau_{a2}, \tau_{a3}]^T \in \mathbb{R}^2$ represent input torques corresponding to the second and the third joints of the robot arm. For the simplified 5-DOF HCDR-1, the CDPR has more actuators (4 actuators) than the total DOFs (3 DOFs), and the robot arm has an equal number of actuators to its total DOFs (2 DOFs). Then, (3.23) can be expressed as

$$\dot{x}(t) = f(x(t), u(t), (L_{01}(t), L_{02}(t))),\ x(0) = x_0 \tag{3.33}$$

where $x := [p_{mx}, \dot{p}_{mx}, p_{mz}, \dot{p}_{mz}, \beta_m, \dot{\beta}_m, \theta_{a2}, \dot{\theta}_{a2}, \theta_{a3}, \dot{\theta}_{a3}]^T \in \mathbb{R}^{10}$ represents the state vector, $u \in \mathbb{R}^4$ denotes the control input vector, L_{01} and L_{02} represent the upper unstretched cable lengths (the two sets of four-cable arrangement on the top), respectively, i.e., L_{01} (driven by actuator 1) denotes unstretched cable lengths 5, 6, 11, and 12, and L_{02} (driven by actuator 2) represents unstretched cable lengths 1, 2, 7, and 8 (as shown in Figure 3.2). $x_0 \in \mathbb{R}^{10}$ is the initial state vector and $t \geq 0$.

By linearizing (3.33) around the reference states x_r and control inputs u_r, the continuous time state-space representation (Linear Time-Varying System (LTV)) can be described as

$$\begin{aligned}\dot{x}(t) &= A(t)x(t) + B(t)u(t) + B(t)w(t) \\ y(t) &= C(t)x(t),\ x(0) = x_0\end{aligned} \tag{3.34}$$

with the output vector $y(t) \in \mathbb{R}^{10}$, matrices $A(t) = \frac{\partial f(x,u)}{\partial x}\Big|_{x=x_r,u=u_r} \in \mathbb{R}^{10\times 10}$, $B(t) = \frac{\partial f(x,u)}{\partial u}\Big|_{x=x_r,u=u_r} \in \mathbb{R}^{10\times 4}$, and $C(t) = I \in \mathbb{R}^{10\times 10}$. $w(t) = (w_m(t), w_a(t)) \in \mathbb{R}^4$ are the white noise vector with zero mean Gaussian, where $w_m(t) \in \mathbb{R}^2$ and $w_a(t) \in \mathbb{R}^2$ are the noise vectors to the CDPR and robot arm, respectively.

Additionally, for the specific HCDR-1, the upper four cables are used for position control and the lower cables are used to set cable tensions. Hence, the specific stiffness matrices (3.28) and (3.29) can be rearranged as $K_T = \sum_{i=1}^{12}(\cdot)$ and $K_k = \sum_{i\in\{1,2,5,6,7,8,11,12\}}(\cdot)$, respectively.

3.3 Decoupled System Modeling[1]

3.3.1 System Setup

System modeling is based on the HCDR-2 platform [57, 76, 93, 95, 30] (shown in Figure 3.3), which consists of a mobile platform, twelve cables, four servo motors, and two 1-DOF pendulums. The HCDR-2 model corresponding to the actual system is shown in Figure 3.4. The actuators are used to drive the cables to move the mobile platform in the X-Y plane (i.e., in-plane moving). Twelve cables include four sets of cables: two sets of a four-cable arrangement on the top and two sets of a two-cable arrangement on the bottom. Two pendulums (which are mounted on the mobile platform and rotate about its body-fixed X-axis) are used to eliminate undesired out-of-plane moving. The driven cable mount locations of the CDPR are shown in Table 3.3, where $r_i := [r_{ix}, r_{iy}, r_{iz}]^T \in \mathbb{R}^3$ denotes the position vector of the ith cable anchor point on the mobile platform with respect to the body-fixed frame $\{O_m\}$; $a_i := [a_{ix}, a_{iy}, a_{iz}]^T \in \mathbb{R}^3$ represents the position vector of the ith cable anchor point on the robot static frame with respect to the coordinate frame $\{O\}$; and N is the total number of cables. Each set of cables is controlled by one motor. The top

---

[1] Parts of this section have been published in [92]. © 2019 Elsevier B.V.: "As the author of this Elsevier article, you retain the right to include it in a thesis or dissertation, provided it is not published commercially. Permission is not required, but please ensure that you reference the journal as the original source."

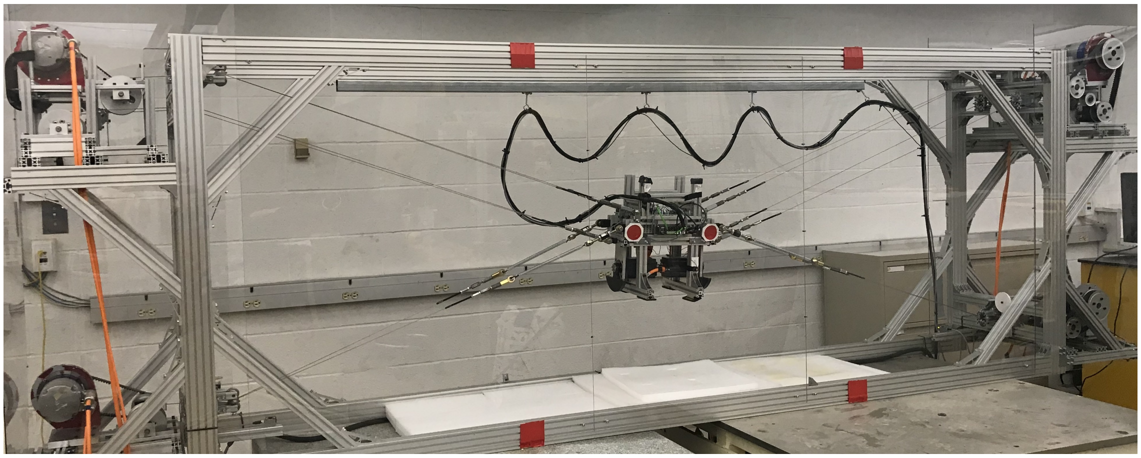

Figure 3.3: The prototype of HCDR-2. The mobile platform is driven by four actuators with 12 cables moving in X-Y plane (i.e., in-plane moving); two pendulums (mounted on the mobile platform and rotates about its body-fixed X-axis) are used to eliminate undesired out-of-plane moving (e.g., vibrations).

actuators and bottom actuators control the upper-cable lengths and lower-cable tensions, respectively. The upper cables also restrict the orientation of the mobile platform, i.e., the kinematic constraints. In addition, the inertial coordinate frame $O\{x_0, y_0, z_0\}$ is located at the center of the static fixture, coordinate frame $\{O_m\}$ is located at the center of mass (COM) of the mobile platform, and the pendulums' body-fixed X-axes are parallel to the X-axis of frame $\{O_m\}$ and located in the X-Y plane of frame $\{O_m\}$.

The main idea and benefits of actuating multi cables by means of a single motor are as follows: 1) increasing payload capability and mechanical strength (in comparison with a single cable) and 2) providing constraints to eliminate motions in specific directions (e.g., the mobile platform rotation about its Z-axis). More details about the cable-driven platform design are given in [57]. Optimization problems in design and workspace analysis (e.g., [2, 20]) are also talked in [57, 76].

Moreover, other HCDR-2 parameters are shown in Table 3.4, where m_m and I_m represent the mass and moment of inertia of the mobile platform, respectively. m_{pk} and I_{pk} ($\{\forall\ k \in \mathbb{N} : 1 \leq k \leq 2\}$) respectively denote the mass and moment of inertia of the pendulums. Also, $T_{i\,\text{min}}$ and $T_{i\,\text{max}}$ ($\{\forall\ i \in \mathbb{N} : 1 \leq i \leq 12\}$) represent the minimum and maximum allowable cable tensions, respectively. The sizes of the static fixture (e.g., l_{fl}) and mobile platform (e.g., l_{bl}), body-fixed positions (e.g., $[x_{p0k}, y_{p0k}, z_{p0k}]^T$, $[x_{pc0k}, y_{pc0k}, z_{pc0k}]^T$, $\{\forall\ k \in \mathbb{N} : 1 \leq k \leq 2\}$) and etc. are also given in Table 3.4.

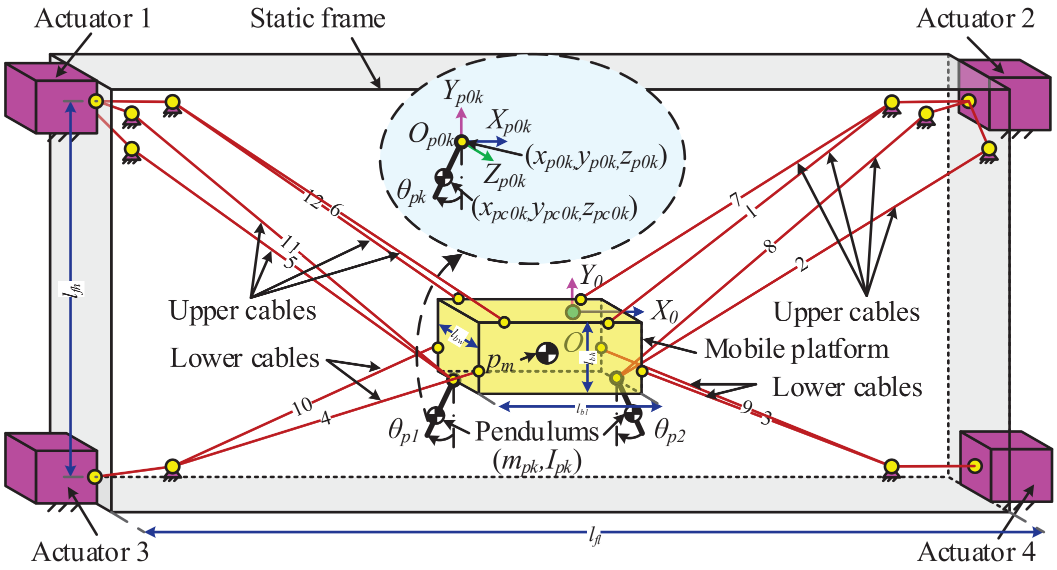

Figure 3.4: The schematic with frames assignment of the actual system in Figure 3.3.

3.3.2 Whole-Body System Modeling and Model Decoupling

Consider the HCDR-2 (in Figure 3.4) with a cable-driven parallel robot (mobile platform) and two 1-DOF pendulums. In this case, the general dynamic model can be described as

$$M\left(q\right)\ddot{q}+C\left(q,\dot{q}\right)\dot{q}+G\left(q\right)+\tau_d=\begin{bmatrix}\tau_m\\ \tau_p\end{bmatrix}=\begin{bmatrix}A_mT\\ \tau_p\end{bmatrix} \tag{3.35}$$

where $q=[p_{mx},p_{my},p_{mz},\alpha_m,\beta_m,\gamma_m,\theta_{p1},\theta_{p2}]^T\in\mathbb{R}^{6+2}$, $\dot{q}\in\mathbb{R}^{6+2}$, and $\ddot{q}\in\mathbb{R}^{6+2}$, represent the vector of generalized coordinates, velocities, and accelerations, respectively. $p_m:=[p_{mx},p_{my},p_{mz}]^T\in\mathbb{R}^3$ is the position vector of the coordinate frame $\{O_m\}$ with respect to the coordinate frame $\{O\}$, and $[\alpha_m,\beta_m,\gamma_m]^T\in\mathbb{R}^3$ (the orientations of the mobile platform about X-, Y-, and Z-axes, respectively) are Euler angles. $M\left(q\right)\in\mathbb{R}^{(6+2)\times(6+2)}$ denotes the combined inertia matrix, $C\left(q,\dot{q}\right)\in\mathbb{R}^{(6+2)\times(6+2)}$ represents the combined Coriolis and centripetal matrix, and $G(q)\in\mathbb{R}^{6+2}$ denote the gravitational vector, respectively. $\tau_d\in\mathbb{R}^{6+2}$, $\tau_m\in\mathbb{R}^6$, and $\tau_p\in\mathbb{R}^2$ are unknown bounded disturbances, forces/torques of the mobile platform, and forces/torques of the pendulums in generalized coordinates, respectively. $A_m\in\mathbb{R}^{6\times12}$ and $T\in\mathbb{R}^{12}$ represent the structure matrix and cable tensions, respectively.

Table 3.3: Driven Cable Mount Locations

N	$[a_{ix}, a_{iy}, a_{iz}]^T$ (m)	$[r_{ix}, r_{iy}, r_{iz}]^T$ (m)
1	$[1.500, 0.500, 0.000]^T$	$[0.153, 0.048, 0.065]^T$
2	$[1.580, 0.404, 0.065]^T$	$[0.233, -0.048, 0.000]^T$
3	$[1.500, -0.500, 0.000]^T$	$[0.223, -0.017, 0.088]^T$
4	$[-1.500, -0.500, 0.000]^T$	$[-0.223, -0.017, 0.088]^T$
5	$[-1.580, 0.404, 0.065]^T$	$[-0.233, -0.048, 0.000]^T$
6	$[-1.500, 0.500, 0.000]^T$	$[-0.153, 0.048, 0.065]^T$
7	$[1.500, 0.500, 0.000]^T$	$[0.153, 0.048, -0.065]^T$
8	$[1.580, 0.404, -0.065]^T$	$[0.233, -0.048, 0.000]^T$
9	$[1.500, -0.500, 0.000]^T$	$[0.223, -0.017, -0.088]^T$
10	$[-1.500, -0.500, 0.000]^T$	$[-0.223, -0.017, -0.088]^T$
11	$[-1.580, 0.404, -0.065]^T$	$[-0.233, -0.048, 0.000]^T$
12	$[-1.500, 0.500, 0.000]^T$	$[-0.153, 0.048, -0.065]^T$

In (3.35), A_m is determined by the position and orientation of the mobile platform:

$$A_m = \begin{bmatrix} \hat{L}_1 & \cdots & \hat{L}_{12} \\ R_g^m \begin{bmatrix} r_{1x} \\ r_{1y} \\ r_{1z} \end{bmatrix} \times \hat{L}_1 & \cdots & R_g^m \begin{bmatrix} r_{12x} \\ r_{12y} \\ r_{12z} \end{bmatrix} \times \hat{L}_{12} \end{bmatrix} \tag{3.36}$$

where the rotation matrix $R_g^m = R_x(\alpha_m) R_{y'}(\beta_m) R_{z''}(\gamma_m) \in \mathcal{SO}(3)$. Let the ith cable-length vector $\vec{L}_i = [a_{ix}, a_{iy}, a_{iz}]^T - [p_{mx}, p_{my}, p_{mz}]^T - R_g^m [r_{ix}, r_{iy}, r_{iz}]^T$, $\{\forall\ i \in \mathbb{N} : 1 \leq i \leq 12\}$, with $\vec{L}_i \in \mathbb{R}^3$ denotes the position vector from the ith cable anchor point on the robot static frame to the ith cable anchor point on the mobile platform. Then, the ith cable length $L_i = \|[a_{ix}, a_{iy}, a_{iz}]^T - [p_{mx}, p_{my}, p_{mz}]^T - R_g^m [r_{ix}, r_{iy}, r_{iz}]^T\|$. Finally, in (3.36), the ith unit cable-length vector $\hat{L}_i := \frac{\vec{L}_i}{L_i} = [\hat{L}_{ix}, \hat{L}_{iy}, \hat{L}_{iz}]^T \in \mathbb{R}^3$.

When the redundancy resolution and optimal stiffness problems are introduced, one

Table 3.4: HCDR-2 Parameters

Symbol	Values	Symbol	Values
l_{fl}	3.160 m	l_{fh}	1.000 m
l_{bl}	0.365 m	l_{bw}	0.130 m
l_{bh}	0.096 m	l_m	$[0, 0.048, 0]^T$ m
m_m	12.200 kg	I_m	$\mathrm{diag}([0.0218, 0.1187, 0.1251])$ kg · m^2
EA_i, for $i = 1, 2,$ $5, 6, 7, 8, 11, 12$	24900 N	$[T_{i\min},\ T_{i\max}]$, for $i = 3, 4, 9, 10$	$[5, 80]$ N
$m_{p1},\ m_{p2}$	0.640 kg	$I_{p1},\ I_{p2}$	$7.012e^{-4}$ kg · m^2
$[x_{p01}, y_{p01}, z_{p01}]^T$	$[-0.175, -0.100, 0]^T$ m	$[x_{p02}, y_{p02}, z_{p02}]^T$	$[0.175, -0.100, 0]^T$ m
$[x_{pc0k}, y_{pc0k}, z_{pc0k}]^T$	$[0, -0.050, 0]^T$ m	g	9.810 m/s^2

can get

$$\max_{\lambda} \quad J_K = \mathrm{eig}(K(\lambda))^T H_\lambda \mathrm{eig}(K(\lambda)) \tag{3.37a}$$

$$\text{s. t.} \quad M\left(q\right)\ddot{q} + C\left(q,\dot{q}\right)\dot{q} + G\left(q\right) + B_K\dot{q} + \tau_d = \begin{bmatrix} A_m T \\ \tau_p \end{bmatrix} \tag{3.37b}$$

$$\begin{aligned} K(\lambda) = & \left(\frac{dA_m}{dP_m}N_A\right)\lambda + \frac{dA_m}{dP_m}A_m^T(A_m A_m^T)^{-1}\tau_m \\ & + A_m K_c A_m^T \end{aligned} \tag{3.37c}$$

$$T_i = \begin{cases} \frac{EA_i}{L_{0i}}\left(L_i - L_{0i}\right), & \text{for } i = 1,2,5,6,7,8,11,12 \\ T_i, & \text{for } i = 3,4,9,10 \end{cases} \tag{3.37d}$$

$$0 \le T_{i\min} \le T_i \le T_{i\max},\ i = 1, 2, \cdots, 12 \tag{3.37e}$$

where T_i, $T_{i\min}$, and $T_{i\max}$ represent the ith cable tension, minimum and maximum allowable tensions, respectively. H_λ denotes the stiffness weighting matrix. EA_i is the product of the elastic modulus and cross-sectional area of the ith cable, and L_{0i} denotes the ith unstretched cable length. $T_i = T_i$, for $i = 3, 4, 9, 10$, indicates the direct input of lower-cable tensions. The actual viscous damping matrix [92, 30] is

$$B_K = \begin{bmatrix} 0 & 0 & 0 & 0 & 0 & 0 & 0 & 0 \\ 0 & 0 & 0 & 0 & 0 & 0 & 0 & 0 \\ 0 & 0 & 0 & 0 & 0 & 0 & 0 & 0 \\ 0 & 0 & 0 & 4 & 0 & 0 & 0 & 0 \\ 0 & 0 & 0 & 0 & 0.1 & 0 & 0.014 & 0.014 \\ 0 & 0 & 0 & 0 & 0 & 0.01 & 0 & 0 \\ 0 & 0 & 0 & 0 & 0 & 0 & 0.014 & 0 \\ 0 & 0 & 0 & 0 & 0 & 0 & 0 & 0.014 \end{bmatrix}. \tag{3.38}$$

More details about the derivation of (3.35) are provided in Appendix A.2. Eq. (3.37) shows the complete nonlinear dynamic model including constraints and optimization problems. To analyze and implement the model and control (e.g., via experiments in real time), one of the goals is to simplify the model (e.g., simplify inputs and decouple the higher dimensional model into lower ones). First, the control inputs are defined as (due to the kinematic constraints) $u := (u_m, u_p) := [T_3, T_4, \tau_{p1}, \tau_{p2}]^T \in \mathbb{R}^4$, where $u_m = [T_3, T_4]^T \in \mathbb{R}^2$ denote the lower-cable tensions (two sets of two-cable arrangement on the bottom), i.e., T_3 (driven by actuator 3) represents cable tensions 4 and 10, and T_4 (driven by actuator 4) denotes cable tensions 3 and 9 (shown in Figure 3.4). $u_p = \tau_p = [\tau_{p1}, \tau_{p2}]^T \in \mathbb{R}^2$ represents the input torques of the two pendulums. Hence, (3.35) or (3.37b) can be expressed as

$$\dot{x}(t) = f(x(t), u(t), (L_{01}(t), L_{02}(t))),\ x(0) = x_0 \in \mathbb{R}^{16} \tag{3.39}$$

where $x := [p_{mx}, \dot{p}_{mx}, p_{my}, \dot{p}_{my}, p_{mz}, \dot{p}_{mz}, \alpha_m, \dot{\alpha}_m, \beta_m, \dot{\beta}_m, \gamma_m, \dot{\gamma}_m, \theta_{p1}, \dot{\theta}_{p1}, \theta_{p2}, \dot{\theta}_{p2}]^T \in \mathbb{R}^{16}$ represents the state vector, $u \in \mathbb{R}^4$ denotes the control input vector, L_{01} and L_{02} represent the upper unstretched cable lengths (the two sets of four-cable arrangement on the top), respectively, i.e., L_{01} (driven by actuator 1) denotes unstretched cable lengths 5, 6, 11, and 12, and L_{02} (driven by actuator 2) represents unstretched cable lengths 1, 2, 7, and 8 (as shown in Figure 3.4). x_0 is the initial state vector, and $t \geq 0$. Additionally, the upper four cables are utilized for position control (i.e., given L_{01} and L_{02} directly) and the lower cables are used to set cable tensions (i.e., control T_3 and T_4).

Second, by linearizing the nonlinear system in (3.39) around the reference/nominal state vector x_r and control input vector u_r, the continuous time state-space representation can be described as

$$\begin{aligned} \dot{x}(t) &= A(t)x(t) + B(t)u(t) + B(t)w(t) \\ y(t) &= C(t)x(t),\ x(0) = x_0 \end{aligned} \tag{3.40}$$

with the output vector $y(t) \in \mathbb{R}^{16}$, matrices $A(t) = \frac{\partial f(x,u)}{\partial x}\Big|_{x=x_r,u=u_r} \in \mathbb{R}^{16\times 16}$, $B(t) = \frac{\partial f(x,u)}{\partial u}\Big|_{x=x_r,u=u_r} \in \mathbb{R}^{16\times 4}$, and $C(t) = I \in \mathbb{R}^{16\times 16}$. $w(t) = (w_m(t), w_p(t)) \in \mathbb{R}^4$ are process noise vectors, where $w_m(t) \in \mathbb{R}^2$ and $w_p(t) \in \mathbb{R}^2$ are noises to the mobile platform and pendulums, respectively.

Third, the cable-driven mobile platform shown in Figure 3.3 is a planar system, and the kinematic constraints and high stiffness of the cables result in small values for γ_m and β_m to be very small (i.e., close to zero). Also, the pendulums' body-fixed X-axes are parallel to the X-axis of frame $\{O_m\}$ and located in the X-Y plane of frame $\{O_m\}$, which indicates the motions of the pendulums have small impact on the motion in the X-Y plane. Hence, one can divide the 16 states (in (3.39)) into two parts: in-plane states ($x_{inp} := [p_{mx}, \dot{p}_{mx}, p_{my}, \dot{p}_{my}, \gamma_m, \dot{\gamma}_m]^T \in \mathbb{R}^6$) and out-of-plane states ($x_{outp} := [p_{mz}, \dot{p}_{mz}, \alpha_m, \dot{\alpha}_m, \beta_m, \dot{\beta}_m, \theta_{p1}, \dot{\theta}_{p1}, \theta_{p2}, \dot{\theta}_{p2}]^T \in \mathbb{R}^{10}$). Then, (3.40) can be rearranged as

$$\begin{aligned}
\begin{bmatrix} \dot{x}_{inp}(t) \\ \dot{x}_{outp}(t) \end{bmatrix} &= \bar{A}(t) \begin{bmatrix} x_{inp}(t) \\ x_{outp}(t) \end{bmatrix} + \bar{B}(t) \begin{bmatrix} u_{inp}(t) \\ u_{outp}(t) \end{bmatrix} + \bar{B}(t) \begin{bmatrix} w_{inp}(t) \\ w_{outp}(t) \end{bmatrix} \\
\begin{bmatrix} y_{inp}(t) \\ y_{outp}(t) \end{bmatrix} &= C(t) \begin{bmatrix} x_{inp}(t) \\ x_{outp}(t) \end{bmatrix}, \quad \begin{bmatrix} x_{inp}(0) \\ x_{outp}(0) \end{bmatrix} = \begin{bmatrix} x_{inp0} \\ x_{outp0} \end{bmatrix}
\end{aligned} \tag{3.41}$$

where in-plane and out-of-plane control inputs $u_{inp} = [T_3, T_4]^T \in \mathbb{R}^2$, $u_{outp} = [\tau_{p1}, \tau_{p2}]^T \in \mathbb{R}^2$, respectively.

For example, for an equilibrium point ($x_{inp} = \mathbf{0}$, $x_{outp} = \mathbf{0}$, $u_{inp} = [80, 80]^T$, $u_{outp} = [0, 0]^T$), the matrix $\bar{A}$ is computed as

$$\begin{aligned}
\bar{A} &= \left[\begin{array}{cccccc|cccccccccc}
0.0 & 1.0 & 0.0 & 0.0 & 0.0 & 0.0 & 0.0 & 0.0 & 0.0 & 0.0 & 0.0 & 0.0 & 0.0 & 0.0 & 0.0 & 0.0 \\
0.0 & 0.0 & 0.0 & 0.0 & 25.4 & 0.0 & 0.0 & 0.0 & 0.0 & 0.0 & 0.0 & 0.0 & 0.0 & 0.0 & 0.0 & 0.0 \\
0.0 & 0.0 & 0.0 & 1.0 & 0.0 & 0.0 & 0.0 & 0.0 & 0.0 & 0.0 & 0.0 & 0.0 & 0.0 & 0.0 & 0.0 & 0.0 \\
0.0 & 0.0 & 0.0 & 0.0 & 0.0 & 0.0 & 0.0 & 0.0 & 0.0 & 0.0 & 0.0 & 0.0 & 0.0 & 0.0 & 0.0 & 0.0 \\
0.0 & 0.0 & 0.0 & 0.0 & 0.0 & 1.0 & 0.0 & 0.0 & 0.0 & 0.0 & 0.0 & 0.0 & 0.0 & 0.0 & 0.0 & 0.0 \\
0.0 & 0.0 & 0.0 & 0.0 & -2237.3 & 0.0 & 0.0 & 0.0 & 0.0 & 0.0 & 0.0 & 0.0 & 0.0 & 0.0 & 0.0 & 0.0 \\
\hline
0.0 & 0.0 & 0.0 & 0.0 & 0.0 & 0.0 & 0.0 & 1.0 & 0.0 & 0.0 & 0.0 & 0.0 & 0.0 & 0.0 & 0.0 & 0.0 \\
0.0 & 0.0 & 0.0 & 0.0 & 0.0 & 0.0 & 0.0 & 0.0 & -0.7 & 0.0 & 0.0 & 0.0 & -0.3 & 0.0 & -0.3 & 0.0 \\
0.0 & 0.0 & 0.0 & 0.0 & 0.0 & 0.0 & 0.0 & 0.0 & 0.0 & 1.0 & 0.0 & 0.0 & 0.0 & 0.0 & 0.0 & 0.0 \\
0.0 & 0.0 & 0.0 & 0.0 & 0.0 & 0.0 & 0.0 & 0.0 & -3.9 & 0.0 & 0.0 & 0.0 & 4.0 & 0.0 & 4.0 & 0.0 \\
0.0 & 0.0 & 0.0 & 0.0 & 0.0 & 0.0 & 0.0 & 0.0 & 0.0 & 0.0 & 0.0 & 1.0 & 0.0 & 0.0 & 0.0 & 0.0 \\
0.0 & 0.0 & 0.0 & 0.0 & 0.0 & 0.0 & 0.0 & 0.0 & 0.0 & 0.0 & -0.0 & 0.0 & -4.3 & 0.0 & 4.3 & 0.0 \\
0.0 & 0.0 & 0.0 & 0.0 & 0.0 & 0.0 & 0.0 & 0.0 & 0.0 & 0.0 & 0.0 & 0.0 & 0.0 & 1.0 & 0.0 & 0.0 \\
0.0 & 0.0 & 0.0 & 0.0 & 0.0 & 0.0 & 0.0 & 0.0 & -137.0 & 0.0 & 0.0 & 0.0 & -161.0 & 0.0 & -3.8 & 0.0 \\
0.0 & 0.0 & 0.0 & 0.0 & 0.0 & 0.0 & 0.0 & 0.0 & 0.0 & 0.0 & 0.0 & 0.0 & 0.0 & 0.0 & 0.0 & 1.0 \\
0.0 & 0.0 & 0.0 & 0.0 & 0.0 & 0.0 & 0.0 & 0.0 & -137.0 & 0.0 & 0.0 & 0.0 & -3.8 & 0.0 & -161.0 & 0.0
\end{array}\right] \\
&= \begin{bmatrix} \bar{A}_{11} & \bar{A}_{12} \\ \bar{A}_{21} & \bar{A}_{22} \end{bmatrix}.
\end{aligned} \tag{3.42}$$

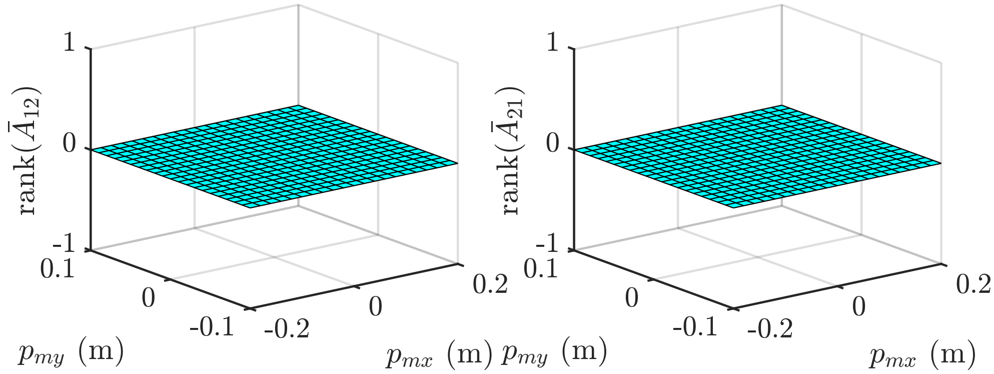

Figure 3.5: Ranks of $\bar{A}_{12}$ and $\bar{A}_{21}$ in a feasible region $\{-0.2 \text{ m} \leq p_{mx} \leq 0.2 \text{ m}, -0.1 \text{ m} \leq p_{my} \leq 0.1 \text{ m}\}$.

In (3.42), it is clear that both $\bar{A}_{12}$ and $\bar{A}_{21}$ are equal to zero (or very close to zero by using numerical computation); hence, (3.41) can be decoupled into in-plane model and out-of-plane model. A verified example provided in Figure 3.5 shows that the ranks of $\bar{A}_{12}$ and $\bar{A}_{21}$ are always zero (indicating they are zero matrices) in a feasible region $\{-0.2 \text{ m} \leq p_{mx} \leq 0.2 \text{ m}, -0.1 \text{ m} \leq p_{my} \leq 0.1 \text{ m}\}$. Furthermore, it can be easily verified that the two subsystems are fully controllable around the equilibrium point using (3.41) and (3.42). The proposed method (in the form of (3.41)) can also be extended to other HCDRs or CDPRs based on their specific configurations. In subsection 3.3.3 and subsection 3.3.4, one can develop the corresponding models, respectively.

3.3.3 Model Decoupling: In-Plane Kinematic Constraint Vibration Model

Suppose three in-plane states $p_{mx} = p_{mxr} + \delta p_{mx}, p_{my} = p_{myr+}\delta p_{my}$, and $\gamma_m = \gamma_{mr} + \delta\gamma_m$, where $p_{mxr}, p_{myr}, \gamma_{mr}$ represent reference/nominal states (rigid body motion), and $\delta p_{mx}, \delta p_{my}, \delta\gamma_m$ denote small changes or perturbations (vibration motion). γ_{mr} is equal to 0 (equilibrium point) due to the in-plane kinematic constraints. Using the first order Taylor series expansion [52, 53] to derive (3.37b), then the in-plane vibration model is obtained:

$$M_{inp}(q_{inpr})\delta\ddot{q}_{inp} + K_{inp}(q_{inpr}, T_{3opt}, T_{4opt})\delta q_{inp} = B_u(q_{inpr}) \begin{bmatrix} \delta T_3 \\ \delta T_4 \end{bmatrix} \tag{3.43}$$

with $\delta q_{inp} = [\delta p_{mx}, \delta p_{my}, \delta \gamma_m]^T$, $\delta \ddot{q}_{inp} = [\delta \ddot{p}_{mx}, \delta \ddot{p}_{my}, \delta \ddot{\gamma}_m]^T$, and $B_u(q_{inpr}) = A_{m[1,2,6][3,4]}$. $K_{inp}(q_{inpr}, T_{3opt}, T_{4opt})$ represents the optimal stiffness matrix (computed using (3.37c)). Then, the linearized in-plane vibration model can be described as $A_{inp} = \left.\frac{\partial f(x_{inp},u_{inp})}{\partial x_{inp}}\right|_{\substack{x_{inp}=x_{inpr}\\ u_{inp}=u_{inpr}}}$, $B_{inp} = \left.\frac{\partial f(x_{inp},u_{inp})}{\partial u_{inp}}\right|_{\substack{x_{inp}=x_{inpr}\\ u_{inp}=u_{inpr}}}$, and $C_{inp} = I \in \mathbb{R}^{6\times 6}$ with $\delta x_{inp} = [\delta p_{mx}, \delta \dot{p}_{mx}, \delta p_{my}, \delta \dot{p}_{my}, \delta \gamma_m, \delta \dot{\gamma}_m]^T$ and $\delta u_{inp} = [\delta T_3, \delta T_4]^T$.

3.3.4 Model Decoupling: Out-of-Plane Underactuated Dynamic Model

The decoupled out-of-plane model can be derived from (3.41) directly. Since two pendulums are used to eliminate undesired out-of-plane moving (e.g., disturbances) and kinematic constraints make the values of the out-of-plane states small, then the simplified state-space model can be obtained around the equilibrium point ($x_{outp} = \mathbf{0}$), i.e., $A_{outp} = \left.\frac{\partial f(x_{outp},u_{outp})}{\partial x_{outp}}\right|_{\substack{x_{outp}=\mathbf{0}\\ u_{outp}=\mathbf{0}}}$, $B_{outp} = \left.\frac{\partial f(x_{outp},u_{outp})}{\partial u_{outp}}\right|_{\substack{x_{outp}=\mathbf{0}\\ u_{outp}=\mathbf{0}}}$, and $C_{outp} = I \in \mathbb{R}^{10\times 10}$ with $x_{outp} = [p_{mz}, \dot{p}_{mz}, \alpha_m, \dot{\alpha}_m, \beta_m, \dot{\beta}_m, \theta_{p1}, \dot{\theta}_{p1}, \theta_{p2}, \dot{\theta}_{p2}]^T$ and $u_{outp} = [\tau_{p1}, \tau_{p2}]^T$. The out-of-plane model is an underactuated subsystem since it has a lower number of actuators (two 1-DOF pendulums) than the total DOFs (5 DOFs) of motion.

3.4 Out-of-Plane System Modeling

3.4.1 System Setup

The proposed HCDR-3 (shown in Figure 3.6) consists of a mobile platform, two 1-DOF pendulums, a 1-DOF slider, and 12 driven cables, and can realize in-plane motion and out-of-plane motion. The mobile platform and cable arrangements are the same as that of HCDR-2 shown in subsection 3.3.2.

The proposed underactuated mobile manipulator (UMM) (in Figure 3.6), a subsystem of HCDR-3, can only realize out-of-plane motion. Since the motion of the slider mainly affects out-of-plane vibrations, in-plane motion is not considered in this section. The UMM consists of a mobile platform, two pendulums, and a linear slider (with the schematic with frames assignment shown in Figure 3.7). Two pendulums (mounted on the mobile platform and rotates about its body-fixed X-axis) are used to eliminate undesired out-of-plane motion, and the linear slider (with load mass moving along its body-fixed Z-axis)

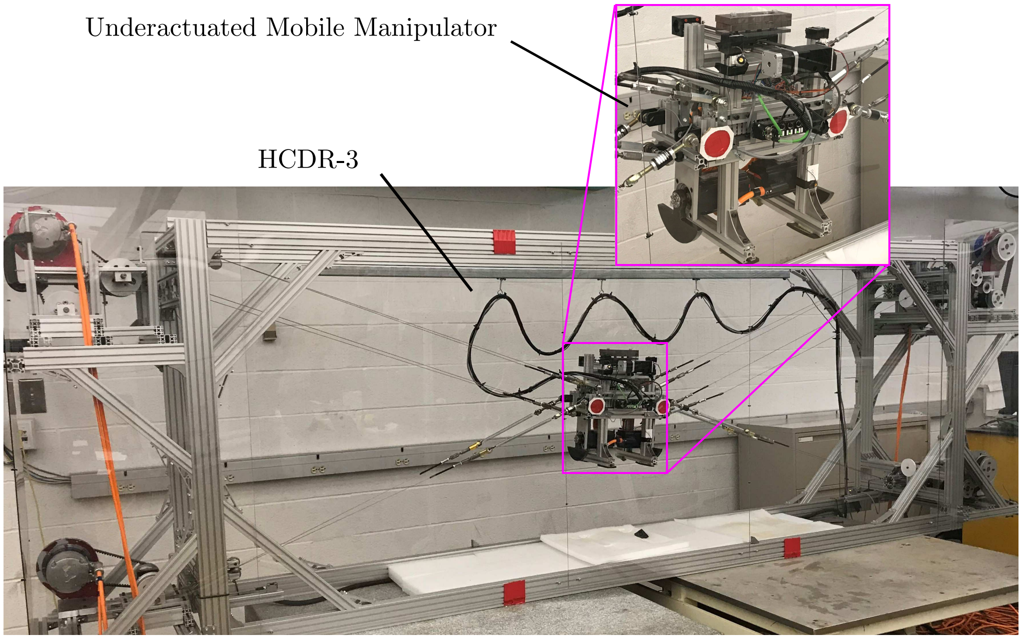

Figure 3.6: The proposed underactuated mobile manipulator (UMM) consists of a mobile platform (MP), two pendulums, and a linear slider. The mobile platform is driven by four actuators with 12 cables moving in the X-Y plane (i.e., in-plane moving); two pendulums (mounted on the mobile platform and rotates about its body-fixed X-axis) are used to eliminate undesired out-of-plane motion; and the linear slider (with load mass and moves along its body-fixed Z-axis) is used for operations. The above components constitute HCDR-3.

is used for operations such as pick-and-place. The slider is actuated by a stepper motor and the slider's actual position p_s is obtained in real-time by an optical encoder mounted on the motor shaft. Meanwhile, the stepper motor is commanded in speed control mode, i.e., the command to the stepper motor is velocity. The UMM (in Figure 3.6) motion for experiments utilizes a Beckhoff Embedded PC (CX2040).

In Figure 3.7, the inertial coordinate frame $O\{x_0, y_0, z_0\}$ is located at the center of the static fixture, coordinate frame $\{O_m\}$ is located at the center of mass (COM) of the mobile platform, and the pendulums' body-fixed X-axes are parallel to the X-axis of frame $\{O_m\}$ and located in the X-Y plane of frame $\{O_m\}$. The UMM parameters are given in Table 3.5, where m_m and I_m represent the mass and moment of inertia of the mobile platform, respectively. m_{pk} and I_{pk} ($\{\forall\ k \in \mathbb{N} : 1 \leq k \leq 2\}$) respectively denote the mass and moment of inertia of the pendulums. The sizes of the static fixture (e.g., l_{fl}) and

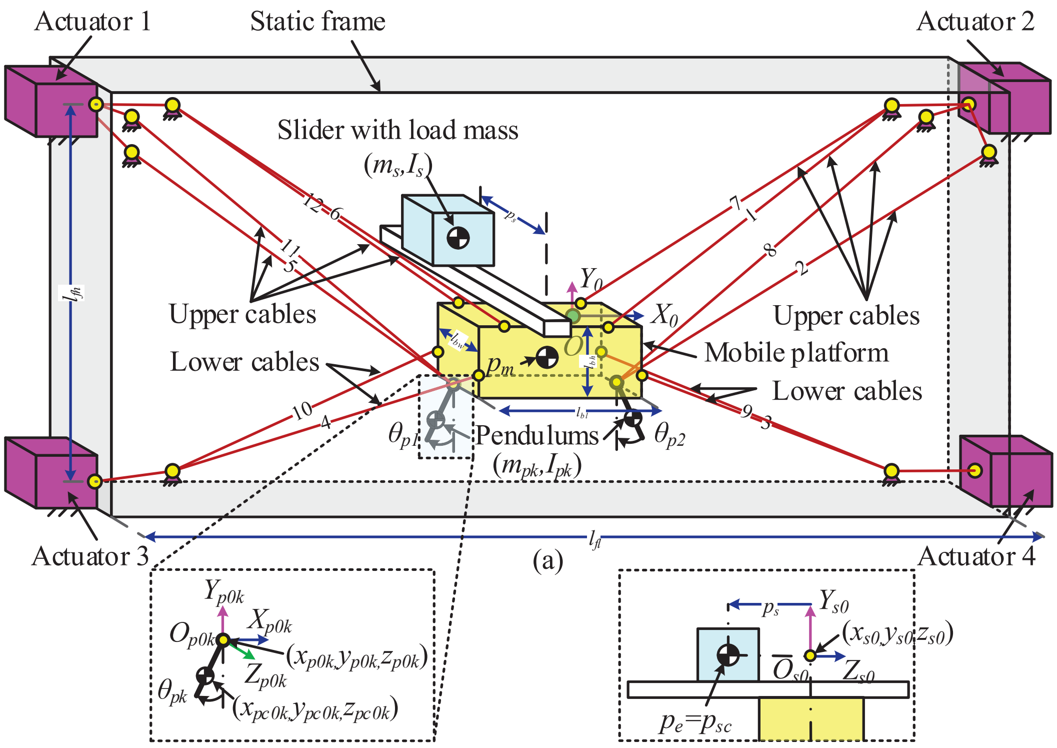

(a)

(b)

(c)

Figure 3.7: The schematic with frames assignment of the actual system in Figure 3.6. (a) The slider (with load mass) is mounted on the mobile platform; (b) zoom-in view of the pendulum; and (c) Y-Z view of the slider.

mobile platform (e.g., l_{bl}), body-fixed positions (e.g., $[x_{p0k}, y_{p0k}, z_{p0k}]^T$, $[x_{pc0k}, y_{pc0k}, z_{pc0k}]^T$, $[x_{s0}, y_{s0}, z_{s0}]^T$), etc. are also given in Table 3.5.

It is worth mentioning that the proposed UMM is an underactuated system since it has fewer actuators (two 1-DOF pendulums and a 1-DOF slider) than the total DOFs (6 DOFs) of motion.

3.4.2 Equations of Motion of the UMM

In Figure 3.7, the inertial coordinate frame $\{O\}$ is assumed fixed to the base/ground. Coordinate frame $\{O_m\}$ is located at the center of mass (COM) of the mobile platform. $p_m := [p_{mx}, p_{my}, p_{mz}]^T \in \mathbb{R}^3$ represents the position vector of the coordinate frame $\{O_m\}$

Table 3.5: Parameters of the UMM

Symbol	Values	Symbol	Values
l_{fl}	3.160 m	l_{fh}	1.000 m
l_{bl}	0.365 m	l_{bw}	0.130 m
l_{bh}	0.096 m	g	9.810 $\mathrm{m/s^2}$
m_m	12.200 kg	I_m	$\mathrm{diag}([0.1021, 0.167, 0.1251])$ $\mathrm{kg\,m^2}$
$m_{p1},\ m_{p2}$	0.640 kg	$I_{p1},\ I_{p2}$	$7.012e^{-4}$ $\mathrm{kg\,m^2}$
m_s	2.121 kg*	I_s	$\mathrm{diag}([0.1258\mathrm{e}^{-2}, 0.3818\mathrm{e}^{-2}, 0.3979\mathrm{e}^{-2}])$ $\mathrm{kg\,m^2}$
$[x_{p01}, y_{p01}, z_{p01}]^T$	$[-0.175, -0.100, 0]^T$ m	$[x_{p02}, y_{p02}, z_{p02}]^T$	$[0.175, -0.100, 0]^T$ m
$[x_{pc0k}, y_{pc0k}, z_{pc0k}]^T$	$[0, -0.050, 0]^T$ m	$[x_{s0}, y_{s0}, z_{s0}]^T$	$[0, 0.134, 0]^T$ m
K_z	1250 N/m	K_{α_m}	145 N m/rad
K_{β_m}	710 N m/rad	$K_{z\alpha_m}$	100 N m/rad
B_z	4 N s/m	B_{α_m}	0.1 N m s/rad
B_{β_m}	0.01 N m s/rad	B_p	0.014 N m s/rad
B_s	12.9625 N s/m	μ_{fs}	$1.6968\mathrm{e}^{-2}$

* The net mass of the slider and the load mass are equal to 0.778 kg and 1.343 kg, respectively.

with respect to the coordinate frame $\{O\}$. By assuming the Euler angles $[\alpha_m, \beta_m, \gamma_m]^T \in \mathbb{R}^3$ (the orientations of the mobile platform about X-, Y-, and Z-axes, respectively), the rotation matrix (e.g., $X \to Y' \to Z''$ order as below) is computed as

$$R_g^m = R_x(\alpha_m) R_{y'}(\beta_m) R_{z''}(\gamma_m). \tag{3.44}$$

The angular velocity ω_m of the frame $\{O_m\}$ is calculated as

$$\omega_m = [R_g^m]^T [\dot{\alpha}_m, 0, 0]^T + [R_{m\beta}^{m\gamma}]^T [R_{m\alpha}^{m\beta}]^T [0, \dot{\beta}_m, 0]^T + [R_{m\beta}^{m\gamma}]^T [0, 0, \dot{\gamma}_m]^T \tag{3.45}$$

where rotation matrices $R_{m\alpha}^{m\beta} = R_{y'}(\beta_m)$ and $R_{m\beta}^{m\gamma} = R_{z''}(\gamma_m)$ calculated from (3.44). $\dot{\alpha}_m, \dot{\beta}_m$, and $\dot{\gamma}_m$ are the time-derivatives of α_m, β_m, and γ_m, respectively. Eqs. (3.44) and (3.45) are obtained using (3.1) and (3.6b), respectively.

Then, the COM (of the links) positions are computed as

$$p_{pc1} = p_{p1_0} + R_g^m R_x(\theta_{p1}) [x_{pc01}, y_{pc01}, z_{pc01}]^T \tag{3.46a}$$

$$p_{pc2} = p_{p2_0} + R_g^m R_x(\theta_{p2}) [x_{pc02}, y_{pc02}, z_{pc02}]^T \tag{3.46b}$$

$$p_{sc} = [p_{mx}, p_{my}, p_{mz}]^T + R_g^m ([x_{s0}, y_{s0}, z_{s0}]^T + [0, 0, p_s]^T) =: p_e \tag{3.46c}$$

where the joint position vectors are described as $p_{p1_0} = [p_{mx}, p_{my}, p_{mz}]^T + R_g^m [x_{p01}, y_{p01}, z_{p01}]^T$ and $p_{p2_0} = [p_{mx}, p_{my}, p_{mz}]^T + R_g^m [x_{p02}, y_{p02}, z_{p02}]^T$. p_e denotes the position vector of the slider.

The COM linear velocities and angle velocities (of the links) are calculated as

$$v_{pc1} = \dot{p}_{pc1} \tag{3.47a}$$
$$v_{pc2} = \dot{p}_{pc2} \tag{3.47b}$$
$$v_{sc} = \dot{p}_{sc} \tag{3.47c}$$

and

$$\omega_{pc1} = (R_x(\theta_{p1}))^T \omega_m + [\dot{\theta}_{p1}, 0, 0]^T \tag{3.48a}$$
$$\omega_{pc2} = (R_x(\theta_{p2}))^T \omega_m + [\dot{\theta}_{p2}, 0, 0]^T \tag{3.48b}$$
$$\omega_{sc} = \omega_m \tag{3.48c}$$

where the corresponding parameters are shown in Figure 3.7 and Table 3.5. Substituting (3.46)–(3.48) into (3.49) and (3.50), the total kinetic and gravitational potential energies are calculated as

$$\begin{aligned} K_E = {} & \frac{1}{2} m_m [\dot{p}_{mx}, \dot{p}_{my}, \dot{p}_{mz}][\dot{p}_{mx}, \dot{p}_{my}, \dot{p}_{mz}]^T + \frac{1}{2}\omega_m^T I_m \omega_m \\ & + \frac{1}{2}\sum_{k=1}^{2} \left\{ m_{pk} v_{pck}^T v_{pck} + \omega_{pck}^T I_{pk} \omega_{pck} \right\} \\ & + m_s v_{sc}^T v_{sc} + \omega_{sc}^T I_s \omega_{sc} \end{aligned} \tag{3.49}$$

and

$$V_E = m_m g p_{my} + \sum_{k=1}^{2} \left\{ m_{pk} g p_{pck}^T [0,1,0]^T \right\} + m_s g p_{sc}^T [0,1,0]^T \tag{3.50}$$

where g represents the gravity acceleration.

The Lagrangian L_E is obtained by substituting (3.49) and (3.50) into (3.19). Then, the generalized force τ_j applied to the dynamic system at joint j to drive link j can be described as

$$\begin{aligned} \tau_j = \Bigg\{ & \left[\nabla\Big(\big(\nabla L_{E\dot{q}}\big)_j \Big)_q \right]^T \dot{q} + \left[\nabla\Big(\big(\nabla L_{E\dot{q}}\big)_j \Big)_{\dot{q}} \right]^T \ddot{q} \\ & - \big(\nabla L_{Eq}\big)_j \Bigg\}, \quad \{\forall\, j \in \mathbb{N} : 1 \leq j \leq 6\} \end{aligned} \tag{3.51}$$

where $\nabla(\cdot)_q$ and $\nabla(\cdot)_{\dot{q}}$ are defined as the gradient vectors of $(\cdot)$ with respect to the vectors q and $\dot{q}$, respectively. (3.51) can also be arranged into a general form:

$$M\left(q\right)\ddot{q} + C\left(q,\dot{q}\right)\dot{q} + G\left(q\right) + F_K + F_B + F_{fri} + \tau_d = \begin{bmatrix} \mathbf{0} \\ \tau_p \\ f_s \end{bmatrix} \tag{3.52}$$

where $q = [p_{mz}, \alpha_m, \beta_m, \theta_{p1}, \theta_{p2}, p_s]^T \in \mathbb{R}^6$, $\dot{q} \in \mathbb{R}^6$, and $\ddot{q} \in \mathbb{R}^6$ represent the vector of generalized coordinates, velocities, and accelerations, respectively. $M\left(q\right) \in \mathbb{R}^{6\times6}$ denotes the combined inertia matrix, $C\left(q,\dot{q}\right) \in \mathbb{R}^{6\times6}$ represents the combined Coriolis and centripetal matrix, and $G(q) \in \mathbb{R}^6$ denote the gravitational vector, respectively. $\tau_d \in \mathbb{R}^6$, $\tau_p \in \mathbb{R}^2$, and $f_s \in \mathbb{R}$ are bounded disturbances, input torques of the pendulums, and input force of the slider in generalized coordinates, respectively. The elastic force vector is

$$F_K = \begin{bmatrix} K_z p_{mz} \\ K_{\alpha_m}\alpha_m + K_{z\alpha_m} p_{mz} \\ K_{\beta_m}\beta_m \\ 0 \\ 0 \\ 0 \end{bmatrix}, \tag{3.53}$$

damping force vector is

$$F_B = \begin{bmatrix} B_z \dot{p}_{mz} \\ B_{\alpha_m}\dot{\alpha}_m + B_p\dot{\theta}_{p1} + B_p\dot{\theta}_{p2} \\ B_{\beta_m}\dot{\beta}_m \\ B_p\dot{\theta}_{p1} \\ B_p\dot{\theta}_{p2} \\ B_s\dot{p}_s \end{bmatrix}, \tag{3.54}$$

and friction vector is

$$F_{fri} = [0, 0, 0, 0, 0, \mu_{fs} m_s g \dot{p}_s]^T. \tag{3.55}$$

The parameters $K_z, K_{\alpha_m}, K_{\beta_m}, K_{z\alpha_m}, B_z, B_{\alpha_m}, B_{\beta_m}, B_p, B_s, \mu_{fs}$ (shown in Table 3.5) are defined in subsection 3.4.3.

In (3.52), the command to the slider is force f_s, while in the actual system (shown in Figure 3.6), the command to the stepper motor is velocity $v_{stepper}$, so a transfer function $H_s(s)$ of the slider is defined as

$$H_s(s) = \frac{v_{stepper}}{f_s} = \frac{1}{m_s s^2 + (B_s + \mu_{fs} m_s g)s}. \tag{3.56}$$

Additionally, in comparison with the system modeling in [30], this chapter extends the DOFs of the configuration by introducing a coupled slider on the platform. Consequently, tracking, and vibration- and balance-control problems must be considered (see the below sections, e.g., subsection 3.4.5 and section 4.3), not just vibration control [30]. In Appendix A.3, a scenario analysis about the disturbances τ_d (in (3.52)) is conducted.

3.4.3 Model Validation

To validate the nonlinear dynamic model (3.52), the following steps are taken:

1. Identification of geometrical and dynamic parameters: The geometrical, mass, and moment of inertia parameters shown in Table 3.5 came from the SolidWorks model (matched the actual system shown in Figure 3.6). After giving impulse torque inputs to the pendulums, the stiffness parameters $K_z, K_{\alpha_m}, K_{\beta_m}$ are identified using the system natural frequency-based method [30] (i.e., by measuring accelerations (using accelerometer ADXL335 and gyroscope ENC-03R) and then converting them into natural frequencies using the Fast Fourier Transform (FFT)). Stiffness $K_{z\alpha_m}$ and damping ratios $B_z, B_{\alpha_m}, B_{\beta_m}, B_p$ are obtained by matching the simulation and experimental responses [30]. Additionally, the slider damping ratio B_s and friction coefficient μ_{fs} are determined by applying an impulse velocity input, i.e., B_s and μ_{fs} are estimated using Trust-Region-Reflective and nonlinear least squares optimization algorithms (in Matlab Optimization Toolbox) [26] based on the simulation and measured experimental position data of the slider.

2. Validation of the model: Using the same impulse input as the previous step, the model validation results are shown in Figure 3.8. In Figure 3.8, although there are some discrepancies between the simulation and experimental responses, the proposed controllers discussed in section 4.3 can effectively handle the uncertainty of dynamics.

3.4.4 Linearization

Eq. (3.52) shows the complete nonlinear dynamic model of the UMM. To analyze and implement the model and associated control, (3.52) can be redefined as

$$\dot{x}(t) = f(t, x(t), u(t)),\ x(0) = x_0 \in \mathbb{R}^{12} \tag{3.57}$$

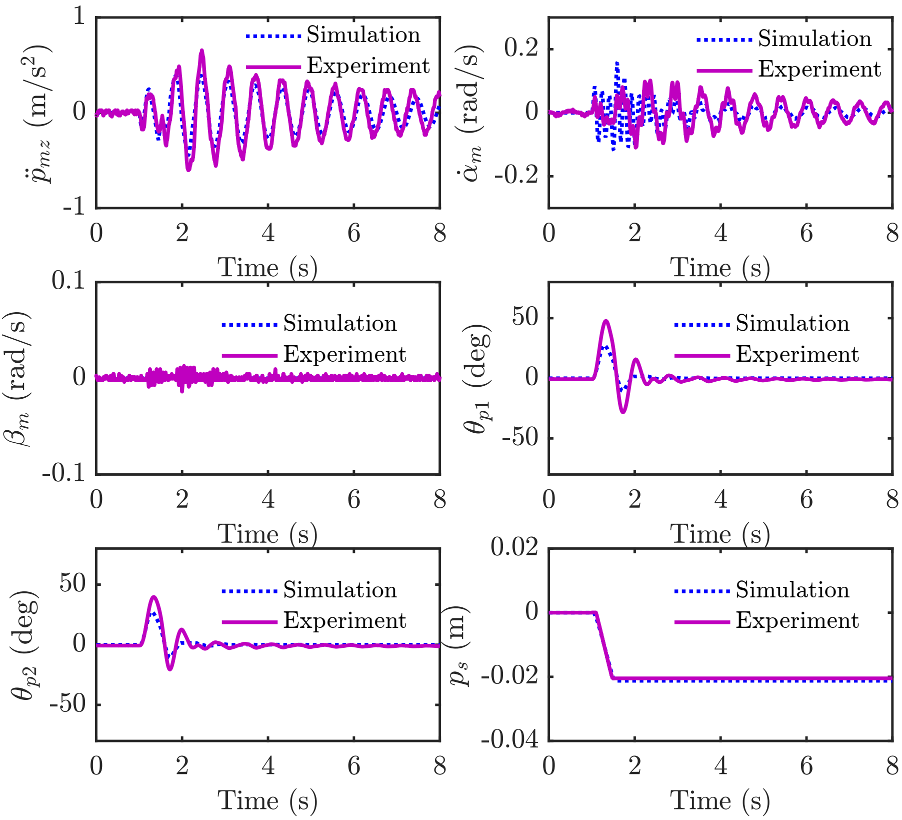

Figure 3.8: Model validation results of the UMM. The simulation and experimental responses are compared.

where $x := [p_{mz}, \dot{p}_{mz}, \alpha_m, \dot{\alpha}_m, \beta_m, \dot{\beta}_m, \theta_{p1}, \dot{\theta}_{p1}, \theta_{p2}, \dot{\theta}_{p2}, p_s, \dot{p}_s]^T \in \mathbb{R}^{12}$ and $u = [\tau_{p1}, \tau_{p2}, f_s]^T \in \mathbb{R}^3$ represent state and input variables, respectively. x_0 is the initial state vector and time $t \geq 0$.

By linearizing (3.57) around the reference/nominal states x_r and control inputs u_r, the continuous time state-space representation can be described as

$$\begin{aligned} \dot{x}(t) &= A(t)x(t) + B(t)u(t) + B(t)w(t) \\ y(t) &= Cx(t),\ x(0) = x_0 \end{aligned} \tag{3.58}$$

where the outputs $y(t) \in \mathbb{R}^3$, matrices $A(t) = \frac{\partial f(x,u)}{\partial x}\Big|_{x=x_r,u=u_r} \in \mathbb{R}^{12\times 12}$, $B(t) = \frac{\partial f(x,u)}{\partial u}\Big|_{x=x_r,u=u_r} \in \mathbb{R}^{12\times 3}$, and $C \in \mathbb{R}^{3\times 12}$. $w(t) \in \mathbb{R}^3$ is process noise. It is interesting to track the position (p_s) of the slider and angles (θ_{p1}, θ_{p2}) of the pendulums (to balance the COM offset of the slider), then $C := \begin{bmatrix} 0,0,0,0,0,0,1,0,0,0,0,0 \\ 0,0,0,0,0,0,0,0,1,0,0,0 \\ 0,0,0,0,0,0,0,0,0,0,1,0 \end{bmatrix}$.

Since the reference is not always zero, an augmented system form with integral action is introduced to solve this problem. Define an integral output vector $z(k+1) = z(k) + (r(k) - y(k))$ and substitute it into the discrete form of (3.58), an augmented state-space representation is described as

$$\begin{aligned} \begin{bmatrix} x(k+1) \\ z(k+1) \end{bmatrix} &= \begin{bmatrix} A(k) & \mathbf{0} \\ -C & I \end{bmatrix} \begin{bmatrix} x(k) \\ z(k) \end{bmatrix} + \begin{bmatrix} B(k) \\ \mathbf{0} \end{bmatrix} u(k) \\ &+ \begin{bmatrix} \mathbf{0} \\ I \end{bmatrix} r(k) + \begin{bmatrix} B(k) \\ \mathbf{0} \end{bmatrix} w(k) \\ y(k) &= \begin{bmatrix} C & \mathbf{0} \end{bmatrix} \begin{bmatrix} x(k) \\ z(k) \end{bmatrix} \end{aligned} \tag{3.59}$$

where $r(k) \in \mathbb{R}^3$ denotes the reference vector.

3.4.5 Equilibrium Point and Balance Problem

The linearized state-space model (3.58) is applicable around the reference state vector x_r and control input vector u_r. However, both of them are unknown. To find x_r and u_r, a typical pick-and-place scenario is considered as below, i.e., the slider (shown in Figure 3.7(c)) moves from the initial position 0 (i.e., $p_s = 0$) to a pick/place position p_{sr} (i.e., $p_{sr} = p_s \neq 0$) and stands still at p_{sr}.

The cable-driven mobile platform shown in Figure 3.6 is a planar system, and the kinematic constraints and high stiffness of the cables lead the state variables $p_{mz}, \dot{p}_{mz}, \alpha_m, \dot{\alpha}_m, \beta_m, \dot{\beta}_m$ having small magnitudes. Meanwhile, the two pendulums are used to eliminate undesired out-of-plane motion (e.g., vibrations) and also to balance the COM offset of the slider (i.e., $p_s \neq 0$). When the slider arrives at p_{sr}, the equilibrium point (instead of the reference) x_r and u_r are given as

$$x_r = \lim_{t \to \infty} x = [0,0,0,0,0,0,\theta_{p1r},0,\theta_{p2r},0,p_{sr},0]^T \tag{3.60a}$$

$$u_r = \lim_{t \to \infty} u = [\tau_{p1r}, \tau_{p2r}, 0]^T \tag{3.60b}$$

$$r = \lim_{t \to \infty} y = [\theta_{p1r}, \theta_{p2r}, p_{sr}]^T \tag{3.60c}$$

where $\theta_{p1r}, \theta_{p2r}, p_{sr}, \tau_{p1r}, \tau_{p2r}$ are the reference state and input variables of the pendulums.

To simplify computation, let $\theta_{p1} = \theta_{p2}$. The total moment about the frame $\{O_m\}$ is equal to zero, i.e.,

$$\begin{aligned}\sum \mathcal{M}_{O_m} = (K_{\alpha_m} - g(m_s y_{sc0} + 2m_{pk} y_{p0k} + 2m_{pk} y_{pc0k} \\ \cos(\theta_{pk})))\alpha_m - g(m_s p_{sr} + 2m_{pk} y_{pc0k} \\ \sin(\theta_{pk})) = 0.\end{aligned} \tag{3.61}$$

Substituting the corresponding parameters shown in Table 3.5 into (3.61), then

$$(143.4675 + 0.6278\cos(\theta_{pk}))\alpha_m - 20.8070 p_{sr} + 0.6278\sin(\theta_{pk}) = 0. \tag{3.62}$$

Clearly, $0.6278\cos(\theta_{pk}) \leq 0.6278 \ll 143.4675$ for an arbitrary angle θ_{pk}. Using (3.60), one can get $\lim_{t\to\infty} \alpha_m = 0$. However, in practice, $\alpha_m =: \epsilon_{\alpha_m}$ is a small angle. Hence, (3.61) can be simplified as

$$\begin{aligned}(K_{\alpha_m} - g(m_s y_{sc0} + 2m_{pk} y_{p0k}))\epsilon_{\alpha_m} - g(m_s p_{sr} \\ + 2m_{pk} y_{pc0k} \sin(\theta_{pk})) = 0,\end{aligned} \tag{3.63}$$

then,

$$\begin{aligned}\theta_{pkr} = \sin^{-1}\Big[\frac{(K_{\alpha_m} - g(m_s y_{sc0} + 2m_{pk} y_{p0k}))\epsilon_{\alpha_m}}{2m_{pk} g y_{pc0k}} \\ - \frac{m_s p_{sr}}{2m_{pk} y_{pc0k}}\Big],\ \theta_{pkr} \in (-\pi/2, \pi/2)\end{aligned} \tag{3.64}$$

with $\{\forall\, k \in \mathbb{N} : 1 \leq k \leq 2\}$. (3.64) has two input variables $(\epsilon_{\alpha_m},\ p_{sr})$ but ϵ_{α_m} is unknown and not unique, which results in more than one solution. Here, a simple linear equation is constructed as $\epsilon_{\alpha_m} = \zeta p_{sr}$, where $\zeta = 0.004$ is an evaluated value for experiments. Then, (3.64) is rearranged as

$$\theta_{pkr} = \sin^{-1}\Big[\frac{(\zeta K_{\alpha_m} - \zeta g(m_s y_{sc0} + 2m_{pk} y_{p0k}) - m_s)p_{sr}}{2m_{pk} g y_{pc0k}}\Big] \tag{3.65}$$

with $\theta_{pkr} \in (-\pi/2, \pi/2)$. The kth reference torque of the pendulum is computed as

$$\begin{aligned}\tau_{pkr} &= -m_{pk} g y_{pc0k}(\sin(\theta_{pkr}) + \epsilon_{\alpha_m}\cos(\theta_{pkr})) \\ &\approx -m_{pk} g y_{pc0k} \sin(\theta_{pkr})\end{aligned} \tag{3.66}$$

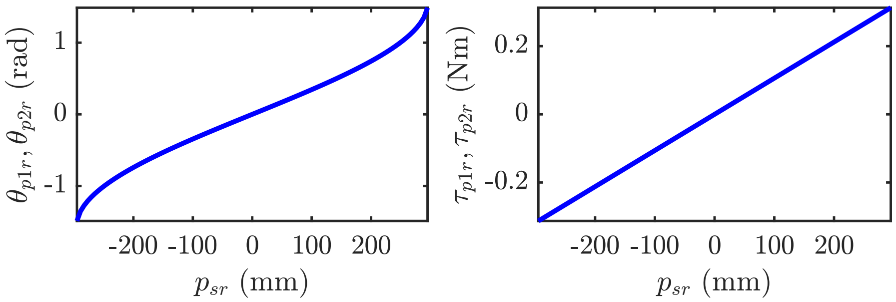

Figure 3.9: An example of the equilibrium point of the pendulums. The reference position of the slider is given as $-0.295\,\mathrm{m} \leq p_{sr} \leq 0.295\,\mathrm{m}$.

where the pendulum's reference angle θ_{pkr} is obtained using (3.65), m_{pk} and y_{pc0k} denote mass and body-fixed position of the pendulum (shown in Table 3.5), respectively.

An example of the equilibrium point of the pendulums is shown in Figure 3.9 is given to illustrate the results obtained by applying (3.65) and (3.66), where the reference position of the slider is given as $-0.295\,\mathrm{m} \leq p_{sr} \leq 0.295\,\mathrm{m}$.

3.5 3D Coupled System Modeling

3.5.1 System Setup

This section proposes a new redundant HCDR-4 (shown in Figure 3.10) which consists of a mobile platform, two 1-DOF pendulums, a 3-DOF robot arm, and 12 driven cables. The mobile platform and pendulums are based on the cable-driven platform in [76, 93, 95, 92]. Four actuators are used to drive the cables to move the mobile platform in the X-Y plane (i.e., in-plane moving). The mobile platform and cable arrangements are the same as that of HCDR-2 shown in subsection 3.3.2. Meanwhile, some Cartesian coordinate frames are defined as follows: the inertial coordinate frame $O\{x_0, y_0, z_0\}$ is located at the center of the static fixture, coordinate frame $\{O_m\}$ is located at the center of mass (COM) of the mobile platform. In addition, two pendulums (mounted on the mobile platform and rotate about their body-fixed X-axes) are used to eliminate undesired out-of-plane moving (e.g., vibrations). The robot arm (with its first, second, and third revolute joints rotating about the body-fixed Y-, Z-, and Z-axes, respectively) is mounted on the mobile platform and used for operations such as pick-and-place.

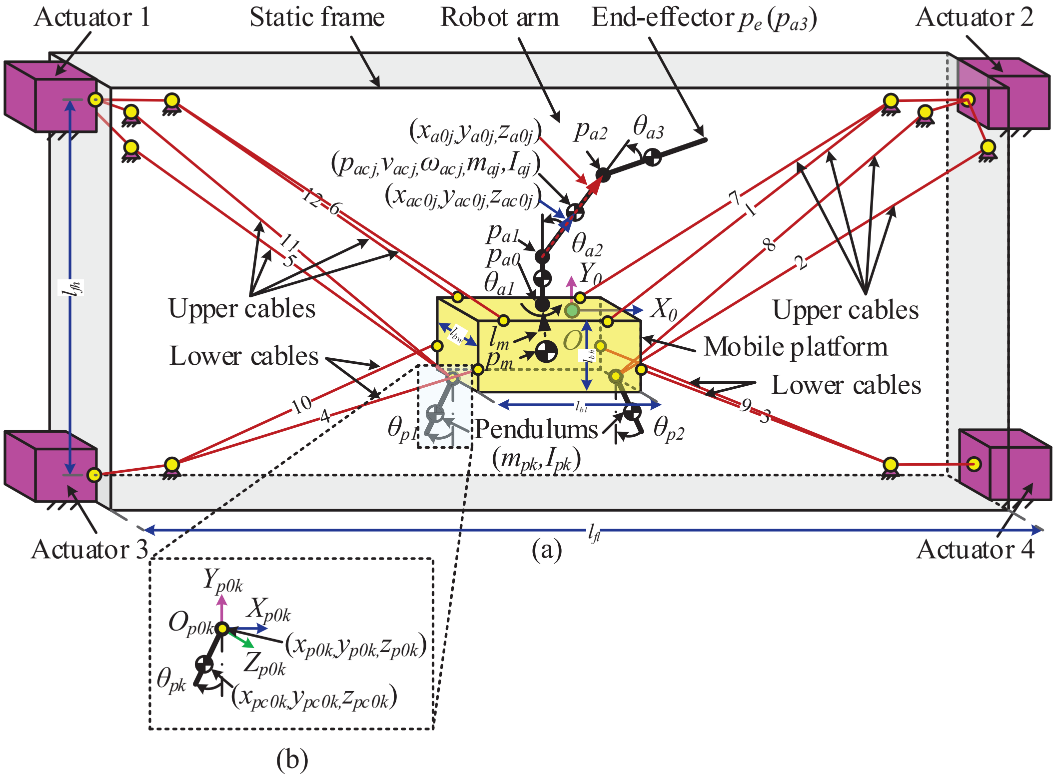

Figure 3.10: The proposed redundant hybrid cable-driven robot (HCDR-4) consists of a mobile platform, two 1-DOF pendulums, and a 3-DOF robot arm. (a) The overall structure of HCDR-4 and (b) enlarge view of the pendulum.

3.5.2 Nonlinear Whole-Body Dynamics

Consider the HCDR-4 shown in Figure 3.10 and define $p_m := [p_{mx}, p_{my}, p_{mz}]^T \in \mathbb{R}^3$ as the position vector of the coordinate frame $\{O_m\}$ with respect to the coordinate frame $\{O\}$ and $[\alpha_m, \beta_m, \gamma_m]^T \in \mathbb{R}^3$ (the orientations of the mobile platform about X-, Y-, and Z-axes, respectively) as the vector of Euler angles. $[\theta_{p1}, \theta_{p2}]^T \in \mathbb{R}^2$ and $[\theta_{a1}, \theta_{a2}, \theta_{a3}]^T \in \mathbb{R}^3$ represent the rotation angles of two 1-DOF pendulums and the 3-DOF robot arm, respectively. Other HCDR-4 parameters used for system modeling are shown in Table 3.6, where m_m and I_m represent the mass and moment of inertia of the mobile platform, respectively. m_{pk} and I_{pk} ($\{\forall\ k \in \mathbb{N} : 1 \leq k \leq 2\}$) respectively denote the mass and moment of inertia of the pendulums. The sizes of the static fixture (e.g., l_{fl}) and mobile platform (e.g., l_{bl}), body-fixed positions (e.g., $[x_{p0k}, y_{p0k}, z_{p0k}]^T$, $[x_{pc0k}, y_{pc0k}, z_{pc0k}]^T$, $\{\forall\ k \in \mathbb{N} : 1 \leq k \leq 2\}$,

Table 3.6: HCDR-4 Parameters

Symbol	Values	Symbol	Values
l_{fl}	3.160 m	l_{fh}	1.000 m
l_{bl}	0.365 m	l_{bw}	0.130 m
l_{bh}	0.096 m	l_m	$[0, 0.048, 0]^T$ m
m_m	12.200 kg	I_m	$\mathrm{diag}([0.1021, 0.167, 0.1251])$ kg m^2
$m_{p1},\ m_{p2}$	0.640 kg	$I_{p1},\ I_{p2}$	$7.012e^{-4}$ kg m^2
$[x_{p01}, y_{p01}, z_{p01}]^T$	$[-0.175, -0.100, 0]^T$ m	$[x_{p02}, y_{p02}, z_{p02}]^T$	$[0.175, -0.100, 0]^T$ m
$[x_{pc01}, y_{pc01}, z_{pc01}]^T$	$[0, -0.050, 0]^T$ m	$[x_{pc02}, y_{pc02}, z_{pc02}]^T$	$[0, -0.050, 0]^T$ m
m_{a1}	0.300 kg	I_{a1}	$\mathrm{diag}([6.76\mathrm{e}^{-5}, 6.76\mathrm{ee}^{-5}, 6.76\mathrm{ee}^{-5}])$ kg m^2
$m_{a2},\ m_{a3}$	0.300 kg	$I_{a2},\ I_{a3}$	$\mathrm{diag}([1.70\mathrm{e}^{-3}, 1.70\mathrm{e}^{-3}, 1.70\mathrm{e}^{-3}])$ kg m^2
$[x_{a01}, y_{a01}, z_{a01}]^T$	$[0, 0.026, 0]^T$ m	$[x_{ac01}, y_{ac01}, z_{ac01}]^T$	$[0, 0.013, 0]^T$ m
$[x_{a02}, y_{a02}, z_{a02}]^T$	$[0, 0.130, 0]^T$ m	$[x_{ac02}, y_{ac02}, z_{ac02}]^T$	$[0, 0.065, 0]^T$ m
$[x_{a03}, y_{a03}, z_{a03}]^T$	$[0, 0.130, 0]^T$ m	$[x_{ac03}, y_{ac03}, z_{ac03}]^T$	$[0, 0.065, 0]^T$ m
$[x_{a0}, y_{a0}, z_{a0}]^T$	$[0, 0.048, 0]^T$ m	$EA_1,\ EA_2$	24900 N
$T_{34\,\mathrm{max}}$	80 N	g	9.810 m/s^2

$[x_{a0j}, y_{a0j}, z_{a0j}]^T$, $[x_{ac0j}, y_{ac0j}, z_{ac0j}]^T$, $\{\forall\ j \in \mathbb{N} : 1 \leq j \leq 3\}$), etc. are also given in Table 3.6. Then, the total kinetic and potential energies are computed as

$$\begin{aligned} K_E = {} & \frac{1}{2} m_m [\dot{p}_{mx}, \dot{p}_{my}, \dot{p}_{mz}][\dot{p}_{mx}, \dot{p}_{my}, \dot{p}_{mz}]^T + \frac{1}{2}\omega_m^T I_m \omega_m \\ & + \frac{1}{2}\sum_{k=1}^{2}\left\{ m_{pk} v_{pck}^T v_{pck} + \omega_{pck}^T I_{pk} \omega_{pck} \right\} \\ & + \frac{1}{2}\sum_{j=1}^{3}\left\{ m_{aj} v_{acj}^T v_{acj} + \omega_{acj}^T I_{aj} \omega_{acj} \right\} \end{aligned} \tag{3.67}$$

and

$$\begin{aligned} V_E = {} & m_m g p_{my} + \sum_{k=1}^{2}\left\{ m_{pk} g p_{pck}^T [0, 1, 0]^T \right\} \\ & + \sum_{j=1}^{3}\left\{ m_{aj} g p_{acj}^T [0, 1, 0]^T \right\} \\ & + \frac{1}{2}(L - L_0)^T K_c \,(L - L_0) \end{aligned} \tag{3.68}$$

where the term $\frac{1}{2}(L-L_0)^T K_c (L-L_0)$ denotes the cable elastic potential energy. Details on how other terms in (3.67) and (3.68) are calculated are provided in Appendix A.4.

The Lagrangian equation is obtained by substituting (3.67) and (3.68) into $L_E = K_E - V_E$. Then, the equations of motion of the HCDR-4 can be derived from L_E and arranged as

$$M(q)\ddot{q} + C(q,\dot{q})\dot{q} + G(q) + \tau_d = \begin{bmatrix} \tau_m \\ \tau_p \\ \tau_a \end{bmatrix} = \begin{bmatrix} A_m T \\ \tau_p \\ \tau_a \end{bmatrix} \tag{3.69}$$

where $q = [p_{mx}, p_{my}, p_{mz}, \alpha_m, \beta_m, \gamma_m, \theta_{p1}, \theta_{p2}, \theta_{a1}, \theta_{a2}, \theta_{a3}\ ]^T \in \mathbb{R}^{11}$, $\dot{q} \in \mathbb{R}^{11}$, and $\ddot{q} \in \mathbb{R}^{11}$, represent the vectors of generalized coordinates, velocities, and accelerations, respectively. $M(q) \in \mathbb{R}^{11\times11}$ denotes the combined inertia matrix, $C(q,\dot{q}) \in \mathbb{R}^{11\times11}$ represents the combined Coriolis and centripetal matrix, and $G(q) \in \mathbb{R}^{11}$ denote the gravitational vector, respectively. $\tau_d \in \mathbb{R}^{11}$, $\tau_m \in \mathbb{R}^{6}$, and $\tau_p \in \mathbb{R}^{2}$ are unknown bounded disturbances, forces/torques of the mobile platform, and forces/torques of the pendulums in the generalized coordinates, respectively. $A_m \in \mathbb{R}^{6\times12}$ and $T \in \mathbb{R}^{12}$ represent the structure matrix and cable tensions, respectively. A_m can be computed using (3.36). In A_m, the rotation matrix R_g^m and the ith unit cable-length vector $\hat{L}_i$ are provided in Appendix A.4.

3.5.3 Model Reduction

Eq. (3.69) provides the complete nonlinear dynamic model with the 6-DOF mobile platform driven by 12 cables. One can simplify this model by considering the kinematic constraints of the HCDR-4 (shown in subsection 3.5.1). The mobile platform is actuated in the X-Y plane (in-plane motion) with the nominal angle γ_m is equal to zero. The twelve cable-driven platform is equivalent to a four cable-driven platform [92], i.e., by given L_{01}, L_{02}, T_3, and T_4, where L_{01} (driven by actuator 1) denotes unstretched cable lengths 5, 6, 11, and 12; L_{02} (driven by actuator 2) represents unstretched cable lengths 1, 2, 7, and 8; T_3 (driven by actuator 3) represents cable tensions 4 and 10; and T_4 (driven by actuator 4) denotes cable tensions 3 and 9. These cables are labeled in Figure 3.10. The inputs to the whole system are defined as $[L_{01}, L_{02}, T_3, T_4, \tau_{p1}, \tau_{p2}, \tau_{a1}, \tau_{a2}, \tau_{a3}]^T \in \mathbb{R}^9$ with $\tau_p = [\tau_{p1}, \tau_{p2}]^T \in \mathbb{R}^2$ denoting input torques of the two pendulums and $\tau_a = [\tau_{a1}, \tau_{a2}, \tau_{a3}]^T \in \mathbb{R}^3$ representing input torques of the 3-DOF robot arm.

Additionally, in (3.69), the redundancy resolution problem (i.e., $\tau_m = A_m T$) resulting from multi-cables can be solved as follows: since the equivalent four-cable planar CDPR has one DOR, then A_m (equals $A_{m[1,2,6][6,1,4,3]}$ in (3.69)) is redefined as a new 3×4 matrix.

One can restrict one of lower cable tensions T_i (for $i = 3, 4$) to the maximum allowable value $T_{34\text{max}}$. In this case, the redundancy resolution and optimal cable tensions T_{opt} are computed as

$$T_{\text{opt}} = \begin{cases} [\Gamma_1, \Gamma_2, T_{34\,\text{max}}, \Gamma_3]^T & \text{if } \Gamma_3 \geq T_{34\,\text{max}}, \\ [\Gamma_1, \Gamma_2, \Gamma_3, T_{34\,\text{max}}]^T & \text{otherwise}, \end{cases} \tag{3.70a}$$

$$\tau_{m[1,2,6]} = A_m \begin{bmatrix} T_{1\text{opt}} \\ T_{2\text{opt}} \\ T_3 \\ T_4 \end{bmatrix} = A_m \begin{bmatrix} \frac{EA_1}{L_{01}}(L_1 - L_{01}) \\ \frac{EA_2}{L_{02}}(L_2 - L_{02}) \\ T_{3\text{opt}} + \delta T_3 \\ T_{4\text{opt}} + \delta T_4 \end{bmatrix}, \tag{3.70b}$$

$$L_{01} = \frac{EA_1 L_1}{EA_1 + T_{1\text{opt}}}, L_{02} = \frac{EA_2 L_2}{EA_2 + T_{2\text{opt}}}, \tag{3.70c}$$

where

$$\Gamma = (\bar{A}_{mi})^{-1}([0, (m_m + m_{p1} + m_{p2} + m_{a1} + m_{a2} + m_{a3})g, 0]^T - A_{mi} T_{34\,\text{max}}), \tag{3.71a}$$

$$A_m = [A_{m1}, A_{m2}, A_{m3}, A_{m4}], \bar{A}_{m3} = [A_{m1}, A_{m2}, A_{m4}], \bar{A}_{m4} = [A_{m1}, A_{m2}, A_{m3}], \tag{3.71b}$$

$A_{mi} \in \mathbb{R}^3$, and $\bar{A}_{mi} \in \mathbb{R}^{3\times 3}$. $T_{34\,\text{max}}$ represents the maximum allowable tensions of lower cables (shown in Table 3.6). EA_1 and EA_2 are the product of the elastic modulus and cross-sectional area of the upper two cables (shown in Table 3.6). In comparison to [93], (3.70) provides a simpler and more effective method. Moreover, $\delta T_3, \delta T_4$ are control inputs of the CDPR denoting changes of lower cable tensions, and the control inputs of the HCDR-4 are defined as $u = [\delta T_3, \delta T_4, \tau_{p1}, \tau_{p2}, \tau_{a1}, \tau_{a2}, \tau_{a3}]^T \in \mathbb{R}^7$. Eqs. (3.69) and (3.70) provide the complete equations of motion of the HCDR-4.

3.6 Summary

In this chapter, first, a generalized HCDR is proposed. For the proposed HCDR, the system motion model is developed. The proposed dynamic modeling approach avoids the drawback of traditional methods, and can be easily extended to other types of hybrid robots by changing structure matrix A_m in (3.5) based on the desired configurations.

In addition, for the configuration of HCDR-2, whole-body model and decoupled model are developed, and the latter is derived from the former for control design and experiments.

Unlike the system modeling in [30], the proposed modeling extends the system configuration by introducing a coupled slider to achieve out-of-plane manipulation tasks. To develop the complete system dynamics, equations of motion of the UMM are derived, disturbance analysis is investigated, and model validation is carried out. A simple but effective strategy is also developed to solve the equilibrium point and balance problem.

Finally, for HCDR-4, nonlinear whole-body dynamics of the HCDR and model reduction are developed. Redundancy resolution and disturbance rejection via torque optimization will be studied in Chapter 4.

Chapter 4

Control Design, Optimization, and Case Studies

In this chapter, different control methods and optimization problems will be studies based on the system models in Chapter 3, and the results will also be evaluated using case studies.

To begin with, in section 4.1, to study the vibration control and trajectory tracking using different control methods, the proposed HCDR-1 is used since it is easier for control design. In this case, the objective is to develop effective control schemes to minimize vibration and improve the accuracy of the end-effector, i.e., the position-holding performance of the CDPR and the position accuracy performance of the end-effector relative to its reference trajectory. Three control structures are proposed: independent control, integrated control-I, and integrated control-II (fully integrated control). The control performance is evaluated using case studies. The results show that the integrated control-II (only using MPC) has better tracking performance than that of integrated control-I and independent control.

In section 4.2, MPC (an extension of the integrated control-II shown in section 4.1) and state estimation will be proposed for decoupled HCDRs in experiments. In this case, HCDR-2 is utilized to solve vibration control and regression problems. Additionally, the motivation of choosing an MPC-based controller is summarized as follows: some existed control techniques may be available for HCDRs, such as PID [76, 49, 56], SMC [30], linear parameter-varying (LPV) [53]. However, to the best of the author's knowledge, there are few studies using MPC, which can handle optimal control problems while satisfying constraints.

In section 4.2, the model decoupling (i.e., in-plane and out-of-plane subsystems) based on the existed platform [76, 93], in-plane vibration, and regression problems are studied using MPC. However, due to the limits of HCDR-2 (e.g., to achieve out-of-plane manipulation tasks) and the disadvantages of MPC (e.g., requiring an accurate enough dynamics model), in section 4.3, two practical control methods (MPC with integral action and MPC+PI with integral action) are proposed to handle vibration control and trajectory tracking problems based on the new system (shown in Figure 3.6). Since the motion of the slider mainly affects out-of-plane vibrations, then in-plane movements are not considered in this section. The proposed subsystem–UMM (shown in Figure 3.6) consists of a mobile platform, two pendulums, and a linear slider. Meanwhile, in section 4.3, the control goal based on the UMM is motivated by the need to minimize the vibrations and increase the position accuracy of the end-effector. Compared to other controllers, e.g., MPC with changes of input [48], the proposed controllers are easier to implement in practice.

Finally, in section 4.4, redundancy resolution and disturbance rejection via torque optimization (based on HCDR-4, a more complicated 3D coupled system) will be studied.

4.1 Vibration Control and Trajectory Tracking Using Multi Control Methods

For the configuration of the HCDR-1 shown in section 3.2, the eight upper cables, four lower cables, and robot arm are based on position control, force control, and torque control, respectively, i.e., their corresponding inputs are positions (cable lengths), forces, and joint torques. Furthermore, the flexible cables reduce the overall stiffness of the robot, so vibrations become a serious problem for precise control [18]. Another major problem is maintaining cable tensions to keep the desired stiffness of the robot, as mentioned above. In addition, since the driven cables are flexible, the position of the mobile platform or actual cable lengths cannot be computed directly from the measurements of encoders (embedded in the corresponding driven actuators). However, the upper unstretched (i.e., nominal) cable lengths (L_{01} and L_{02} in (3.33)) can be obtained using (3.33) when the reference trajectory $r(t) = x_r$ is given. Then, one can readjust lower cable tensions using (3.32). Hence, tracking the reference trajectory as well as optimizing the lower cable tensions to satisfy the required stiffness of the HCDR-1 should be included in control design.

Based on the above analysis, the proposed control structures of the HCDR-1 are shown in Figure 4.1(a-c). Additionally, because of the kinematic constraints, system (3.34) is fully controllable in x_0z_0 plane. The states and control inputs are simplified for the proposed vibration control.

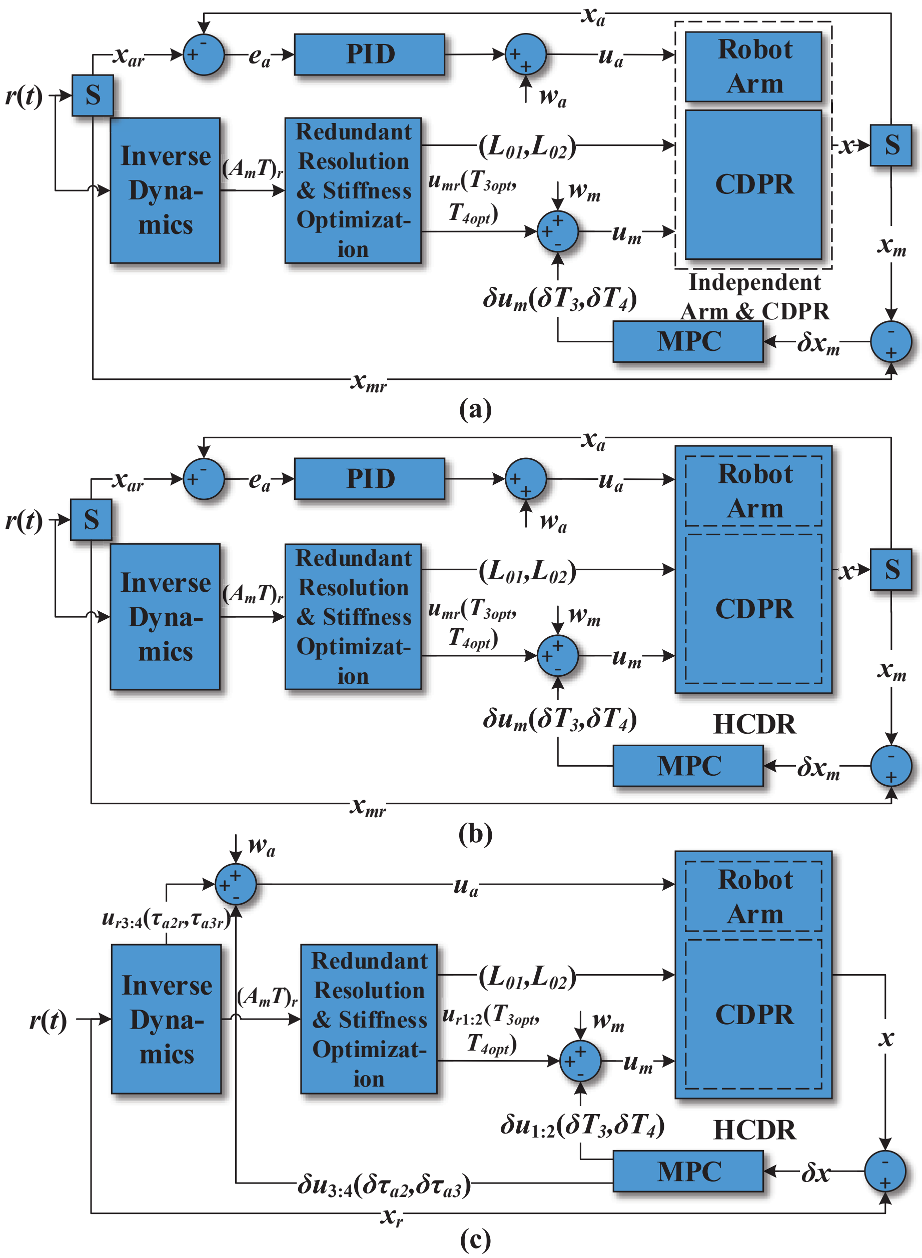

Figure 4.1: Three types of control architecture based on HCDR-1. (a) Independent control with the CDPR and the robot arm are decoupled; (b) integrated control-I with the CDPR and the robot arm are coupled; and (c) integrated control-II with the CDPR and the robot arm are coupled.

4.1.1 Independent Control

For the independent plant (i.e., the Independent Arm & CDPR block diagram shown in Figure 4.1(a)), it includes two independent subsystems: the flexible CDPR and the rigid robot arm. There is no coupled forces/torques between them. In this case, the dynamic model of the CDPR can be developed using (3.9) or by replacing (3.17) and (3.18) with $K_E = \frac{1}{2} m_m [\dot{p}_{mx}, \dot{p}_{my}, \dot{p}_{mz}][\dot{p}_{mx}, \dot{p}_{my}, \dot{p}_{mz}]^T + \frac{1}{2}\omega_m^T I_m \omega_m$ and $V_E = m_m g p_{mz} + \frac{1}{2}(L - L_0)^T K_c (L - L_0)$, respectively. The dynamic equations of the robot arm are derived by replacing (3.17) and (3.18) with $K_E = \frac{1}{2}\sum_{k=0}^{3}\left\{m_{ak} v_{ack}^T v_{ack} + \omega_{ack}^T I_{ak} \omega_{ack}\right\}$ and $V_E = \sum_{k=0}^{3}\left\{m_{ak} g p_{ack}^T [0, 0, 1]^T\right\}$, respectively. By substituting the new (3.17) and (3.18) into (3.19), the independent nonlinear dynamic equations of the CDPR and robot arm can be derived (in forms of (3.22) and (3.23)). The LTV model of the CDPR is expressed in form of (3.34). The block diagram S is used to select elements from input vector. It can be described as

$$\left[\begin{array}{c} x_m \\ \hline x_a \end{array}\right] = \underbrace{\left[\begin{array}{cc} I_{6\times 6} & \mathbf{0}_{6\times 4} \\ \hline \mathbf{0}_{4\times 6} & I_{4\times 4} \end{array}\right]}_{\text{Block diagram S}} \left[\begin{array}{c} x \\ \hline x \end{array}\right] \tag{4.1}$$

where I represents the identity matrix. x, x_m, and x_a denote the state vectors of the whole system, CDPR, and robot arm, respectively. In (4.1), x, x_m, and x_a can be replaced with reference state vectors x_r, x_{mr}, and x_{ar}, respectively.

When the reference trajectory $r(t) = x_r$ is given (in Figure 4.1(a)), Algorithm 1 is implemented to compute the optimal cable tensions T_{3opt} and T_{4opt}. By substituting T_{3opt} and T_{4opt} into (3.8), the upper unstretched cable lengths L_{01} and L_{02} are also calculated. A stiffness optimization example using Algorithm 1 is shown in Figure 4.2. Figure 4.2(a) shows that increasing T_3 and T_4 will rise up J_K (in Figure 4.2(b)). The corresponding eigenvalues of stiffness matrix K (in 4.2(c)) are always positive. Because of the constraints in (3.32), the maximum of J_K corresponds to the optimal values of T_3 and T_4, i.e., T_{3opt} and T_{4opt}, respectively.

Based on the computed values above (in this section), the proposed control approaches are then utilized to stabilize the system around its reference trajectories. For the independent control, Model Predictive Control (MPC) and Proportional-Integral-Derivative (PID) based control schemes are designed. The former is used to control the lower cable tensions $u_m(T_3, T_4)$, the latter is utilized to control the arm joint torques to minimize joint position errors. The main reason for using MPC-based controllers (see Figure 4.1) is that they can handle optimal control problems as well as satisfying constraints.

Algorithm 1 Computation of the optimal cable tensions T_{3opt} and T_{4opt}

```
Input: Reference trajectory $r(t) = x_r$.
Output: Optimal cable tensions $T_{3opt}$ and $T_{4opt}$.
1: Given $r(t)$ and calculate the nominal matrix $A_{mr}$ and torque $(A_m T)_r$ by using (3.5) and (3.32b), respectively;
2: Given the stiffness weighting matrix $H_\lambda$ (e.g., in all the case studies in this chapter, $H_\lambda$ is equal to the identity matrix $I$) and solve (3.32a) (which also subjects to (3.32c) and (3.32d)), then the optimal stiffness $K(\lambda)_{opt}$ and variable $\lambda_{opt}$ are obtained;
3: Resubstitute $K(\lambda)_{opt}$, $\lambda_{opt}$, $A_{mr}$, and $(A_m T)_r$ into (3.32c), the optimal cable tensions $T_{3opt}$ and $T_{4opt}$ are computed;
4: Return $T_{3opt}$ and $T_{4opt}$.
```

1) MPC Control Design (depicted as the MPC control block diagram in Figure 4.1(a)): As an optimization based control approach, the MPC cost function with constraints is defined below to minimize the vibration of the mobile platform:

$$
\begin{aligned}
\min \quad & \sum_{k=0}^{N_p-1} \Big(e_{x_m}(k)^T Q_p e_{x_m}(k) + e_{u_m}(k)^T R_p e_{u_m}(k) \Big) \\
& + e_{x_m}(N_p)^T P_p e_{x_m}(N_p) \qquad\qquad (4.2) \\
\text{s. t.} \quad & \delta x_m(k+1)_{6\times 1} = A(k)_{6\times 6} \delta x_m(k)_{6\times 1} \\
& + B(k)_{6\times 2} \delta u_m(k)_{2\times 1} + B(k)_{6\times 2} w_m(k)_{2\times 1} \\
& \delta y_m(k)_{6\times 1} = C(k)_{6\times 6} \delta x_m(k)_{6\times 1} \\
& \delta x_m(k)_{6\times 1} = x_m(k)_{6\times 1} - x_m(k-1)_{6\times 1} \\
& \delta u_m(k)_{2\times 1} = u_m(k)_{2\times 1} - u_m(k-1)_{2\times 1} \\
& \delta y_m(k)_{6\times 1} = y_m(k)_{6\times 1} - y_m(k-1)_{6\times 1} \\
& e_{x_m}(k)_{6\times 1} = x_{mr}(k)_{6\times 1} - x_m(k)_{6\times 1} \\
& e_{u_m}(k)_{2\times 1} = u_{mr}(k)_{2\times 1} - u_m(k)_{2\times 1} \\
& \delta x_{mL}(k)_{6\times 1} \le \delta x_m(k)_{6\times 1} \le \delta x_{mU}(k)_{6\times 1} \\
& \delta u_{mL}(k)_{2\times 1} \le \delta u_m(k)_{2\times 1} \le \delta u_{mU}(k)_{2\times 1}
\end{aligned}
$$

where the state-space model in (4.2) represents the independent CDPR. The error vector between the reference trajectory x_{mr} and actual states x_m is defined as

$$e_{x_m} = x_{mr} - x_m = [p_{mxr}, \dot{p}_{mxr}, p_{mzr}, \dot{p}_{mzr}, \beta_{mr}, \dot{\beta}_{mr}]^T - [p_{mx}, \dot{p}_{mx}, p_{mz}, \dot{p}_{mz}, \beta_m, \dot{\beta}_m]^T. \tag{4.3}$$

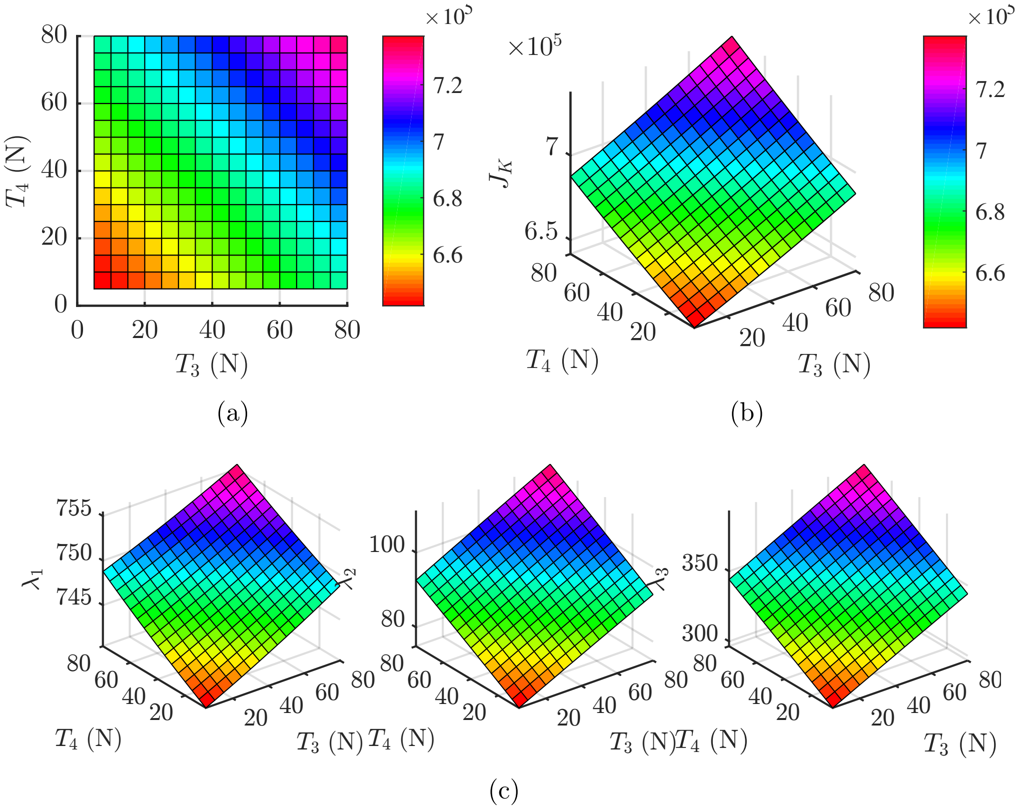

(a)

(b)

(c)

Figure 4.2: An stiffness optimization example using Algorithm 1, where the mobile platform is stationary (i.e., position-holding at $[p_{mx}, p_{mz}]^T = [0, 0]^T$) and the upper unstretched cable lengths are equal to $L_{01} = L_{02} = 1.005$ m. (a) X-Y view, (b) 3D view, and (c) eigenvalues of the stiffness matrix K.

The error vector between the reference inputs u_{mr} and actual inputs u_m is defined as

$$e_{u_m} = u_{mr} - u_m = [T_{3opt}, T_{4opt}]^T_{2\times 1} - [T_3, T_4]^T_{2\times 1}. \tag{4.4}$$

δx_{mL} and δx_{mU} denote the lower bound and upper bound of the states δx_m, respectively. δu_L and δu_U represent the lower bound and upper bound of the control inputs δu, respectively. $R_p \in \mathbb{R}^{2\times 2}$ ($R_p = R_p^T \succ \mathbf{0}$), $Q_p \in \mathbb{R}^{6\times 6}$ ($Q_p = Q_p^T \succeq \mathbf{0}$), and $P_p \in \mathbb{R}^{6\times 6}$ ($P_p = P_p^T \succeq \mathbf{0}$) are input, state, and terminal weighting matrices, respectively.

As an advanced control technique, MPC utilizes the state-space model in (4.2) to predict the systems behavior in the future, i.e., by minimizing the cost function (as well as handling constraints) to find the optimal control action. To carry out the MPC in (4.2), parameters (see Table 4.1 in subsubsection 4.1.4.1 for case studies) such as sampling time T_s, predictive horizon N_p, control horizon N_c, input weighting matrix R_p, state weighting matrix Q_p, terminal weighting matrix P_p, lower bound δx_{mL}, upper bound δx_{mU}, lower bound δu_{mL}, and upper bound δu_{mU} must be considered. Additionally, some key guidelines can help tuning MPC parameters such as set smaller N_p and $N_c \leq N_p$.

2) PID Control Design (shown in Figure 4.1(a)): For the mounted arm, the PID controller is designed as

$$\begin{aligned} u_a(\tau_{a2}, \tau_{a3}) = K_p[\theta_{a2r}(t) - \theta_{a2}(t), \theta_{a3r}(t) - \theta_{a3}(t)]^T \\ + K_i \int_0^t [\theta_{a2r}(\mathfrak{t}) - \theta_{a2}(\mathfrak{t}), \theta_{a3r}(\mathfrak{t}) - \theta_{a3}(\mathfrak{t})]^T d\mathfrak{t} \\ + K_d[\dot{\theta}_{a2r}(t) - \dot{\theta}_{a2}(t), \dot{\theta}_{a3r}(t) - \dot{\theta}_{a3}(t)]^T \end{aligned} \tag{4.5}$$

where K_p, K_i, and K_d are the proportional, integral, and derivative terms, respectively. θ_{a2r} and θ_{a3r} denote the reference angles of joint 2 and 3, respectively. θ_{a2} and θ_{a3} represent the actual angles of joint 2 and 3, respectively. $u_a(\tau_{a2}, \tau_{a3})_{2\times 1}$ denotes the control inputs to the robot arm.

4.1.2 Integrated Control-I

Regarding the integrated control-I, it is also based on hybrid MPC and PID controllers (shown in Figure 4.1(b)). In this case, a coupled plant (the HCDR-1 block diagram in Figure 4.1(b)) is adopted, i.e., the nonlinear model (3.33). The corresponding LTV representation of the CDPR is obtained by linearizing (3.33) around the reference states x_{mr} and inputs u_{mr}, which is used for MPC design (in the form of (4.2)) to damp vibrations. Meanwhile, the PID control design for the robot arm is expressed as (4.5).

Additionally, the implementation of integrated control-I is the same as the independent control (in subsection 4.1.1): when the reference trajectory $r(t)$ is given, the optimal cable tensions T_{3opt} and T_{4opt} and the upper unstretched cable lengths L_{01} and L_{02} are computed. By inputting these values and the outputs of MPC and PID into HCDR-1 to minimize vibration and improve the accuracy of the end-effector.

4.1.3 Integrated Control-II (Fully Integrated Control)

Integrated control-II is defined as a fully integrated control, which is only based on MPC (shown in Figure 4.1(c)). In this case, the coupled plant (the HCDR-1 block diagram in

Figure 4.1(c)) is the same as the one shown in Figure 4.1(b), but the corresponding LTV model is extended to all the states and inputs, i.e., in terms of (3.34).

The integrated control-II is designed to control lower cable tensions and the arm joint torques simultaneously to minimize the vibration of the overall system. Then, the MPC cost function with constraints is redefined as

$$
\begin{aligned}
\min \quad & \sum_{k=0}^{N_p-1} \Big(e_x(k)^T Q_p e_x(k) + e_u(k)^T R_p e_u(k) \Big) \\
& + e_x(N_p)^T P_p e_x(N_p) \qquad (4.6) \\
\text{s. t.} \quad & \delta x(k+1)_{10\times1} = A(k)_{10\times10} \delta x(k)_{10\times1} \\
& + B(k)_{10\times4} \delta u(k)_{4\times1} + B(k)_{10\times4} w(k)_{4\times1} \\
& \delta y(k)_{10\times1} = C(k)_{10\times10} \delta x(k)_{10\times1} \\
& \delta x(k)_{10\times1} = x(k)_{10\times1} - x(k-1)_{10\times1} \\
& \delta u(k)_{4\times1} = u(k)_{4\times1} - u(k-1)_{4\times1} \\
& \delta y(k)_{10\times1} = y(k)_{10\times1} - y(k-1)_{10\times1} \\
& e_x(k)_{10\times1} = x_r(k)_{10\times1} - x(k)_{10\times1} \\
& e_u(k)_{4\times1} = u_r(k)_{4\times1} - u(k)_{4\times1} \\
& \delta x_L(k)_{10\times1} \le \delta x(k)_{10\times1} \le \delta x_U(k)_{10\times1} \\
& \delta u_L(k)_{4\times1} \le \delta u(k)_{4\times1} \le \delta u_U(k)_{4\times1}
\end{aligned}
$$

where the error vector between the reference trajectory x_r and actual states x is described as

$$
\begin{aligned}
e_x = x_r - x = & [p_{mxr}, \dot{p}_{mxr}, p_{mzr}, \dot{p}_{mzr}, \beta_{mr}, \dot{\beta}_{mr}, \theta_{a2r}, \dot{\theta}_{a2r}, \theta_{a3r}, \dot{\theta}_{a3r}]^T_{10\times1} \\
& - [p_{mx}, \dot{p}_{mx}, p_{mz}, \dot{p}_{mz}, \beta_m, \dot{\beta}_m, \theta_{a2}, \dot{\theta}_{a2}, \theta_{a3}, \dot{\theta}_{a3}]^T_{10\times1}, \qquad (4.7)
\end{aligned}
$$

and the error vector between the reference inputs u_r and actual inputs u is expressed as

$$
e_u = u_r - u = [T_{3opt}, T_{4opt}, \tau_{a2r}, \tau_{a3r}]^T_{4\times1} - [T_3, T_4, \tau_{a2}, \tau_{a3}]^T_{4\times1}. \qquad (4.8)
$$

Compared to (4.2), other variables (e.g., δx_L, δx_U, δu_L, δu_U, R_p, Q_p, and P_p) are extended to higher dimensions. $R_p \in \mathbb{R}^{4\times4}$ ($R_p = R_p^T \succ \mathbf{0}$), $Q_p \in \mathbb{R}^{10\times10}$ ($Q_p = Q_p^T \succeq \mathbf{0}$), and $P_p \in \mathbb{R}^{10\times10}$ ($P_p = P_p^T \succeq \mathbf{0}$).

Moreover, when the reference trajectory $r(t)$ is given, the nominal variables T_{3opt}, T_{4opt}, L_{01}, L_{02}, τ_{a2r}, and τ_{a3r} are computed the same as integrated control-I (in subsection 4.1.2).

Theoretically, when the the same goal and conditions are given, the higher integrated control techniques (e.g., the integrated control-II in subsection 4.1.3) are easier lead to better performance, since the control performance indices are more guaranteed by balancing control gains, e.g., using the cost function in (4.6).

Additionally, the block diagrams (in Figure 4.1) of *Inverse Dynamics*, *Redundant Resolution & Stiffness Optimization*, *Independent Arm & CDPR* (or *HCDR-1*), *PID*, and *MPC* mainly correspond to (3.32b), Algorithm 1, (3.33), (4.5), and (4.2) (or (4.6)), respectively. In the next section, case studies will be proposed to evaluate the control performance.

4.1.4 Simulation Results

4.1.4.1 Case Study–Comparison of Three Control Structures

To evaluate the performance of the above three control strategies, many case studies can be implemented, e.g., applying different trajectories to the mobile platform and robot arm. However, when the robot arm moves, it generates reaction forces which result in vibration of the mobile platform even when the desired position of the mobile plat-

Table 4.1: Parameters of Three Control Structures

Control structures	MPC parameters	PID parameters
Independent control or integrated control-I	$T_s = 0.01$ s (sampling time); $N_p = 50$ (predictive horizon); $N_c = 50$ (control horizon); $R_p = 0.0001 I_{2\times 2}$ (input weighting matrix); $Q_p = I_{4\times 4}$ (state weighting matrix); $P_p = I_{4\times 4}$ (terminal weighting matrix); $\delta x_{mL} = -[\infty, \infty]^T$(lower bound); $\delta x_{mU} = [\infty, \infty]^T$(upper bound); $\delta u_{mL} = -[80, 80]^T$(lower bound); $\delta u_{mU} = [80, 80]^T$(upper bound).	$K_p = 400$; $K_i = 100$; $K_d = 10$.
Integrated control-II	$T_s = 0.01$ s; $N_p = 50$; $N_c = 50$; $R_p = 0.0001 I_{4\times 4}$; $Q_p = I_{10\times 10}$; $P_p = I_{10\times 10}$; $\delta x_L = -[\infty, \infty, \infty, \infty]^T$; $\delta x_U = [\infty, \infty, \infty, \infty]^T$; $\delta u_L = -[80, 80, 2, 2]^T$; $\delta u_U = [80, 80, 2, 2]^T$.	–

form is to remain unchanged. This case is quite important in pick-and-place applications. To illustrate the position-holding performance of the CDPR and the position accuracy performance of the end-effector relative to its reference trajectory, reference points $r(t) = x_r = [p_{mxr}, \dot{p}_{mxr}, p_{mzr}, \dot{p}_{mzr}, \beta_{mr}, \dot{\beta}_{mr}, \theta_{a2r}, \dot{\theta}_{a2r}, \theta_{a3r}, \dot{\theta}_{a3r}]^T$ are given as $\underset{t_0}{r_0} = \underset{t_A}{r_A} = [0.05, 0, 0.1, 0, 0, 0, 0, 0, 0, 0]^T \rightarrow \underset{t_B}{r_B} = [0.05, 0, 0.1, 0, 0, 0, 0, 0, 0.3(t_B - t_A), 0]^T \rightarrow \underset{t_C}{r_C} = [0.05, 0, 0.1, 0, 0, 0, 0.4(t_C - t_B), 0, 0.3(t_C - t_B), 0]^T \rightarrow \underset{t_{end}}{r_{end}} = [0.05, 0, 0.1, 0, 0, 0, 1.0(t_D - t_C), 0, 1.0(t_D - t_C), 0]^T$, where point-to-point (e.g., $r_B \rightarrow r_C$ from time t_B to t_C) movements are implemented using the 5th order polynomial trajectories, and $t_0 = 0$ s, $t_A = 1$ s, $t_B = 3$ s, $t_C = 5$ s, and $t_{end} = 6$ s.

In this case study, $r(t)$ are given in joint space, and they can be mapped to the end-effector positions $(x_e, 0, z_e) = p_e$ in Cartesian coordinates by using the equations in Appendix A.1. Then, the corresponding multi segment curves are generated: from the start point → point A → point B → point C → the end point as shown in Figure 4.3.

Furthermore, the control performance is evaluated using MATLAB 2015a (The MathWorks, Inc.) on a Windows 7 x64 desktop PC (Intel Core i7-4770, 3.4 GHz CPU and 8 GB RAM), and the quadratic programming problems ((4.2) and (4.6)) in the independent control, integrated control-I, and integrated control-II are solved using FiOrdOs [109]. The constraints and tuning parameters are given in Table 4.1.

Based on the desired end-effector trajectory and tuning parameters of three control structures, the responses are shown in Figure 4.3 and Figure 4.4. Figure 4.3 shows the end-effector trajectory in Cartesian coordinates. The aim of three controllers is to follow the desired curved path (dotted line). The independent control based tracking trajectory (dashed line), the integrated control-I based tracking trajectory (dash-dot line), and the integrated control-II based tracking trajectory (solid line) are all commanded from the same start point. It is clear that independent control cannot follow the desired path well. The main reason is that it doesn't consider the coupling forces/torques between the mobile platform and the robot arm. This leads to large tracking errors.

Additionally, from the start point → point A → point B, integrated control-I and integrated control-II show good trajectory tracking performance. However, from point B → point C → endpoint, tracking errors of the former is larger than the latter (always has an excellent tracking performance). Integrated control-II uses an optimized control scheme to handle dynamic coupling hence suppressing vibrations to satisfy (4.6).

Figure 4.4 shows the end-effector trajectory versus time. The time responses for three control structures have a similar tracking performance, as shown in Figure 4.3. In Figure 4.4, both the independent control (for the decoupled HCDR-1) and the integrated

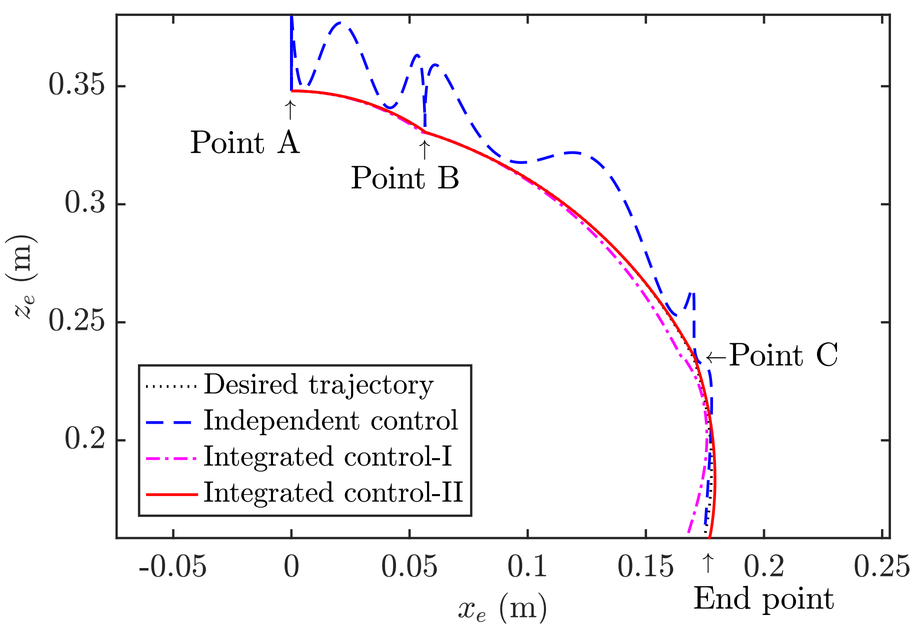

Figure 4.3: End-effector trajectory in Cartesian coordinates.

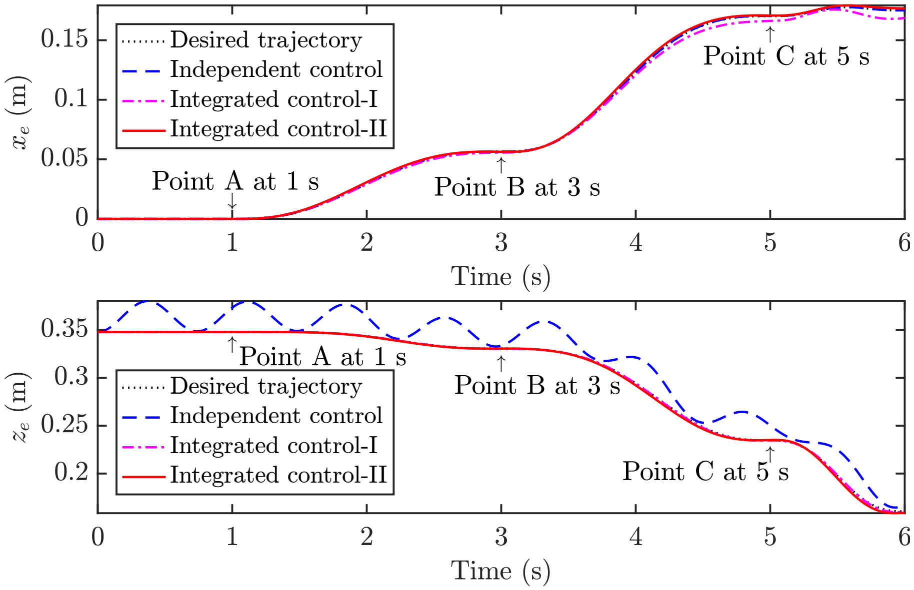

Figure 4.4: End-effector trajectory versus time.

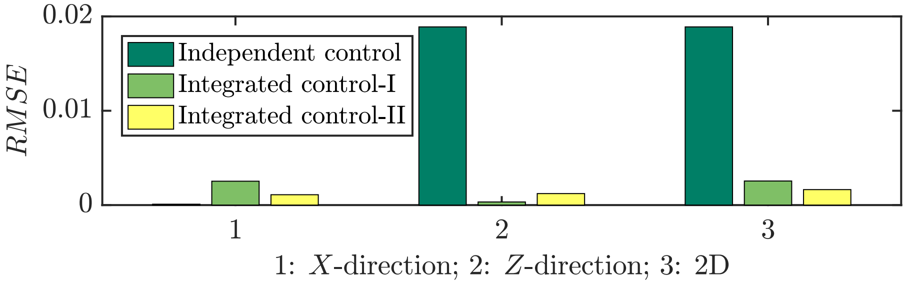

Figure 4.5: RMSE of the end-effector trajectory.

control-I (for the coupled HCDR-1) use the same controllers (MPC and PID) and tuning parameters (shown in Table 4.1). The integrated control-I shows good tracking performances in the X- and Z-directions, and the control inputs can handle the reaction forces between the CDPR and robot arm. However, for the independent control, the control inputs cannot effectively handle the decoupled HCDR-1 (i.e., the ignored reaction forces mainly coming from the gravity forces of the robot arm that cannot be overcome) in the Z-direction, resulting in vibrations and poor tracking. The reaction force in the X-direction is less affected, and the tuned controllers can effectively eliminate the tracking error, so it shows a good tracking performance.

In short, the above results show that integrated control-II (fully integrated control) has better tracking performance than that of integrated control-I. Integrated control-I has better tracking performance than that of independent control.

4.1.4.2 Case Study–RMSE Estimation

To evaluate the end-effector position tracking errors, the root-mean-square error (RMSE) [121] is used to measure the differences between the desired positions in X-Z Cartesian plane and observed values. The RMSE of the end-effector trajectory is described as

$$RMSE = \sqrt{\frac{1}{N_R}\sum_{i=1}^{N_R}\left((p_{exi}-\hat{p}_{exi})^2+(p_{ezi}-\hat{p}_{ezi})^2\right)} \tag{4.9}$$

where p_{exi}, $\hat{p}_{exi}$, p_{ezi}, and $\hat{p}_{ezi}$ denote the desired and observed end-effector positions in X- and Z-directions, respectively. N_R is the total sampling number.

Using (4.9), the RMSEs of the end-effector trajectory based on the independent control, integrated control-I, and integrated control-II are shown in Figure 4.5. In Figure 4.5, RMSE in the X-direction, independent control has the smallest RMSE, i.e., the best trajectory tracking performance. RMSE in the Z-direction, integrated control-I has the best trajectory tracking performance. However, RMSE in the 2D-direction represents the overall trajectory tracking performance of the three control structures. It is clear that integrated control-II has the best trajectory tracking performance ($RMSE = 0.01889$), and independent control has the worst trajectory tracking performance ($RMSE = 0.00164$). Also, this performance matches the result shown in Figure 4.3 and Figure 4.4. Hence, integrated control-II (fully integrated control) has the best overall trajectory tracking performance for the end-effector.

In comparison with previous studies, such as PID [76], linear parameter-varying (LPV) [53], and sliding mode control (SMC) [30], the results of this chapter offer noticeable improvements in the following aspects: 1) satisfactory results are guaranteed by the optimal control inputs and constraints, and 2) the use of MPC enhances the control performance by using the future steps from the reference trajectories to generate control laws.

4.2 MPC and State Estimation for Decoupled HCDRs)[1]

Based on the decoupled in-plane and out-of-plane models presented in section 3.3, two MPCs are utilized: the first is used to control the lower-cable tensions to damp out in-plane vibrations, the second is utilized to control pendulum torques to eliminate out-of-plane moving.

4.2.1 In-Plane Control

In-plane control is performed using an MPC controller shown in Figure 4.6(a). As an optimization based control approach, the MPC cost function with constraints is defined

---

[1] Parts of this section have been published in [92]. © 2019 Elsevier B.V.: “As the author of this Elsevier article, you retain the right to include it in a thesis or dissertation, provided it is not published commercially. Permission is not required, but please ensure that you reference the journal as the original source.”

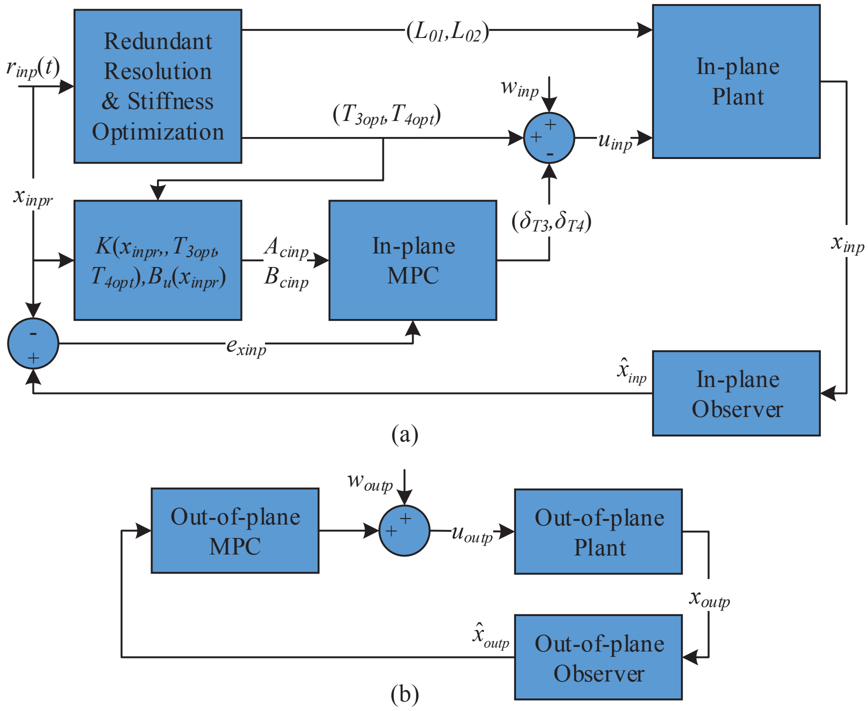

(a)

(b)

Figure 4.6: In-plane and out-of-plane control architectures. (a) in-plane control and (b) out-of-plane control.

below to minimize the vibration of the mobile platform:

$$\begin{aligned}
\min \quad & \sum_{k=0}^{N_p-1} \Big(e_{x_{inp}}(k)^T Q_p e_{x_{inp}}(k) + e_{u_{inp}}(k)^T R_p e_{u_{inp}}(k) \Big) \\
& + e_{x_{inp}}(N_p)^T P_p e_{x_{inp}}(N_p) && \text{(4.10a)} \\
\text{s. t.} \quad & \delta x_{inp}(k+\Delta T) = A_{inp}(k)\delta x_{inp}(k) + B_{inp}(k)\delta u_{inp}(k) \\
& + B_{inp}(k) w_{inp}(k) \\
& \delta y_{inp}(k) = C_{inp}(k)\delta x_{inp}(k) && \text{(4.10b)} \\
& e_{x_{inp}}(k) = x_{inpr}(k) - x_{inp}(k) \\
& e_{u_{inp}}(k) = u_{inpr}(k) - u_{inpr}(k) \\
& \delta x_{inpL}(k) \le \delta x_{inp}(k) \le \delta x_{inpU}(k) \\
& \delta u_{inpL}(k) \le \delta u_{inp}(k) \le \delta u_{inpU}(k) \\
& R_p = R_p^T \succ \mathbf{0}, R_p \in \mathbb{R}^{2\times 2} \\
& Q_p = Q_p^T \succeq \mathbf{0}, Q_p \in \mathbb{R}^{6\times 6} \\
& P_p = P_p^T \succeq \mathbf{0}, P_p \in \mathbb{R}^{6\times 6}
\end{aligned}$$

where

$$e_{x_{inp}} = x_{inpr} - x_{inp} = [p_{mxr}, \dot{p}_{mxr}, p_{myr}, \dot{p}_{myr}, \gamma_{mr}, \dot{\gamma}_{mr}]^T - [p_{mx}, \dot{p}_{mx}, p_{yz}, \dot{p}_{yz}, \gamma_m, \dot{\gamma}_m]^T \tag{4.11}$$

represents the error vector between the reference trajectory x_{inpr} and actual state vector x_{inp}. $e_{u_{inp}} = u_{inpr} - u_{inp} = [T_{3opt}, T_{4opt}]^T - [T_3, T_4]^T$ denotes the error vector between the reference input vector u_{inpr} and actual input vector u_{inp}. (4.10b) is the discrete state-space model of (3.43) with R_p, Q_p, and P_p denoting input weighting matrix, state weighting matrix, and terminal weighting matrix, respectively. It also represents the vibration model, where $\delta u_{inp} = [\delta T_3, \delta T_4]^T$ is the control input vector of lower-cable tensions. In Figure 4.6(a), the input vector $[T_3, T_4]^T = u_{inp}$ consists of nominal lower-cable tensions (T_{3opt}, T_{4opt}), control inputs $(\delta T_3, \delta T_4)$, and noise. The responses of T_3 and T_4 will be discussed in subsection 4.2.3 and subsection 5.2.1.

Additionally, δx_{inpL} and δx_{inpU} indicate the lower bound and upper bound of the state vector δx_{inp}, respectively. δu_L and δu_U represent the lower bound and upper bound of the control input vector δu, respectively.

4.2.2 Out-of-Plane Control

Out-of-plane control is also based on an MPC controller (shown in Figure 4.6(b)). The MPC cost function with constraints is defined as:

$$\begin{aligned}
\min \quad & \sum_{k=0}^{N_p-1} \Big(e_{x_{outp}}(k)^T Q_p e_{x_{outp}}(k) + u_{outp}(k)^T R_p u_{outp}(k) \Big) \\
& + e_{x_{outp}}(N_p)^T P_p e_{x_{outp}}(N_p) && (4.12a) \\
\text{s. t.} \quad & x_{outp}(k + \Delta T) = A_{outp}(k) x_{outp}(k) + B_{outp}(k) u_{outp}(k) \\
& + B_{outp}(k) w_{outp}(k) \\
& y_{outp}(k) = C_{outp}(k) x_{outp}(k) && (4.12b) \\
& e_{x_{outp}}(k) = x_{outpr}(k) - x_{outp}(k) \\
& x_{outpL}(k) \le x_{outp}(k) \le x_{outpU}(k) \\
& u_{outpL}(k) \le u_{outp}(k) \le u_{outpU}(k) \\
& R_p = R_p^T \succ \mathbf{0}, R_p \in \mathbb{R}^{2\times 2} \\
& Q_p = Q_p^T \succeq \mathbf{0}, Q_p \in \mathbb{R}^{10\times 10} \\
& P_p = P_p^T \succeq \mathbf{0}, P_p \in \mathbb{R}^{10\times 10}
\end{aligned}$$

where

$$\begin{aligned} e_{x_{outp}} = & [p_{mzr}, \dot{p}_{mzr}, \alpha_{mr}, \dot{\alpha}_{mr}, \beta_{mr}, \dot{\beta}_{mr}, \theta_{p1r}, \dot{\theta}_{p1r}, \theta_{p2r}, \dot{\theta}_{p2r}]^T \\ & - [p_{mz}, \dot{p}_{mz}, \alpha_m, \dot{\alpha}_m, \beta_m, \dot{\beta}_m, \theta_{p1}, \dot{\theta}_{p1}, \theta_{p2}, \dot{\theta}_{p2}]^T \end{aligned} \tag{4.13}$$

are the error vector between the reference trajectory x_{outpr} and actual state vector x_{outp}. $u_{outp} = [\tau_{p1}, \tau_{p2}]^T$ represent inputs of the pendulums. (4.12b) is the discrete state-space model of that shown in subsection 3.3.4. Compared with (4.10), other variables (e.g., R_p, Q_p, and P_p) are extended to different dimensions.

Furthermore, (4.10) and (4.12) are respectively rearranged as a quadratic programming (QP) problem (by substituting (4.10b) into (4.10a) and (4.12b) into (4.12a), respectively). To solve this QP problem, some alternative solvers can be used, such as qpOASES [37], CVXGEN [75], etc., and they are able to achieve the same goal.

4.2.3 Simulation Results

To evaluate the control performance, a scenario is given in Figure 4.7 to demonstrate a warehousing application, where the start operation point $P_1 : (p_{mxr1}, p_{myr1}) = (0.1, 0.05)$ m; $P_2 : (p_{mxr2}, p_{myr2}) = (0.1, 0.05)$ m; $P_3 : (p_{mxr3}, p_{myr3}) = (-0.1, 0.05)$ m; and the end point $P_4 : (p_{mxr4}, p_{myr4}) = (-0.1, -0.05)$ m. Other in-plane reference states $(\dot{p}_{mxr}, \dot{p}_{myr}, \gamma_{mr}, \dot{\gamma}_{mr}) = \mathbf{0}$. The initial out-of-plane states are also equal to zero. At each point, in-plane and out-of-plane input pulse disturbances are given.

1. In-plane control performance: Based on the scenario described in Figure 4.7, the in-plane MPC control is implemented. Point P_i $(i = 1, 2, 3, 4)$ corresponds to the time at 0.50 s, 14.75 s, 32.99 s, and 47.24 s, respectively. At these moments, input pulse disturbances are also given. Moreover, the in-plane MPC tuning parameters for simulations are given in Table 4.2. Simulation results show that the in-plane state and input responses from P_1 to P_4 are close. In this case, P_2 is considered as an example (as shown in Figure 4.8) to conduct an analysis: Clearly, when the open-loop control is implemented in-plane states vibrated (because of the inputs T_3 and T_4 with disturbances); however, when the in-plane MPC control is applied, the states are damped out in a short time, and inputs T_3 and T_4 converge to their references, i.e., the MPC controller holds a good performance. This in-plane control performance also validate the effectiveness of the control design.

Table 4.2: MPC Tuning Parameters for Simulations

Control structures	Parameters
In-plane MPC	$T_s = 0.01$ s (sampling time); $\Delta T = 0.03$ s (interval time); $N_p = 5$ (predictive horizon); $R_p = \text{diag}([0.00001, 0.00001])$ (input weighting matrix); $Q_p = \text{diag}([1, 1, 1, 1, 1, 1])$ (state weighting matrix); $P_p = \text{diag}([1, 1, 1, 1, 1, 1])$ (terminal weighting matrix); $\delta x_{inpL} = -[\infty, \infty]^T$(lower bound); $\delta x_{inpU} = [\infty, \infty]^T$(upper bound); $\delta u_{inpL} = -[10, 10]^T$(lower bound); $\delta u_{inpU} = [10, 10]^T$(upper bound).
Out-of-plane MPC	$T_s = 0.01$ s; $\Delta T = 0.02$ s; $N_p = 5$; $R_p = \text{diag}([0.1, 0.1])$; $Q_p = \text{diag}([10, 10, 1, 1, 10, 10, 1, 1, 1, 1])$; P_p is the solution of the Lyapunov equation $A_{outp} P_p A_{outp}^T - P_p = -Q_p$; $\delta x_{mL} = -[\infty, \infty]^T$; $\delta x_{mU} = [\infty, \infty]^T$; $\delta u_{mL} = -[0.92, 0.92]^T$; $\delta u_{mU} = [0.92, 0.92]^T$.

2. Out-of-plane control performance: Same as the in-plane scenario, the open-loop control and out-of-plane MPC control for the out-of-plane system are implemented. In this case, MPC is utilized to dampen undesired out-of-plane motions and keep the states at zero. The out-of-plane MPC tuning parameters are given in Table 4.2. To evaluate the control performance, state and input responses at the example point P_2 (shown in Figure 4.9) are selected. The results show that when input disturbances are given, the out-of-plane MPC controller leads the out-of-plane states to converge to zero faster than that of open-loop control. The later also results in zero states because of the damping behavior of the system. The MPC controller also shows a good control performance for out-of-plane control. In summary, the above in-plane and out-of-plane control performance validate the effectiveness of the control design.

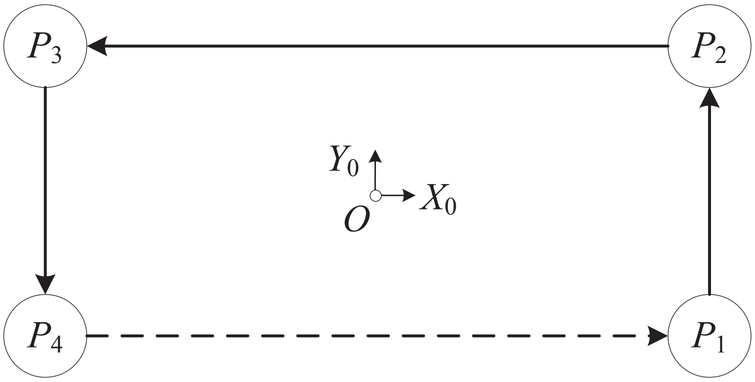

Figure 4.7: A four-point example to demonstrate warehousing application. The start point P_1 : $(0.1, -0.05)$ m, P_2 : $(0.1, 0.05)$ m, P_3 : $(-0.1, 0.05)$ m, and the end point P_4 : $(-0.1, -0.05)$ m. At each point, in-plane and out-of-plane pulse disturbances are given.

4.2.4 State Estimation and Validation

In subsection 4.2.3, the proposed control strategies is evaluated via simulations. However, in practice, the control performance is not always guaranteed if the obtained states are inaccurate. For example, in Figure 3.3, an IMU mounted on the bottom of the mobile platform (used to estimate states) has this problem. To solve it, new in-plane and out-of-plane state estimation methods (corresponding to subsection 4.2.1, subsection 5.2.2, and the system modeling (e.g., the assignment of cables and frames) in section 3.3) are proposed as follows:

4.2.4.1 In-Plane State Estimation (In-Plane Observer)

To overcome the drawbacks of IMU noise and inaccuracy problems (e.g., obtaining actual position by integrating IMU acceleration signals), a method by fusing forward kinematics and lower-cable tensions is proposed to estimate discrete in-plane states as below (the detailed implementation process is shown in Algorithm 2):

$$\begin{bmatrix} \hat{L}_3(k) \\ \hat{L}_4(k) \end{bmatrix} = \begin{bmatrix} L_{03} - \frac{1}{k_{c3}}(\underbrace{\eta_3(T_{c10}(k) + T_{c12}(k))}_{\eta_3(T_{c10}+T_{c12})\xrightarrow{\text{3-SM}}\hat{T}_3} - T_{3cal}) \\ L_{04} - \frac{1}{k_{c4}}(\underbrace{\eta_4(T_{c9}(k) + T_{c11}(k))}_{\eta_4(T_{c9}+T_{c11})\xrightarrow{\text{3-SMF}}\hat{T}_4} - T_{4cal}) \end{bmatrix} \tag{4.14}$$

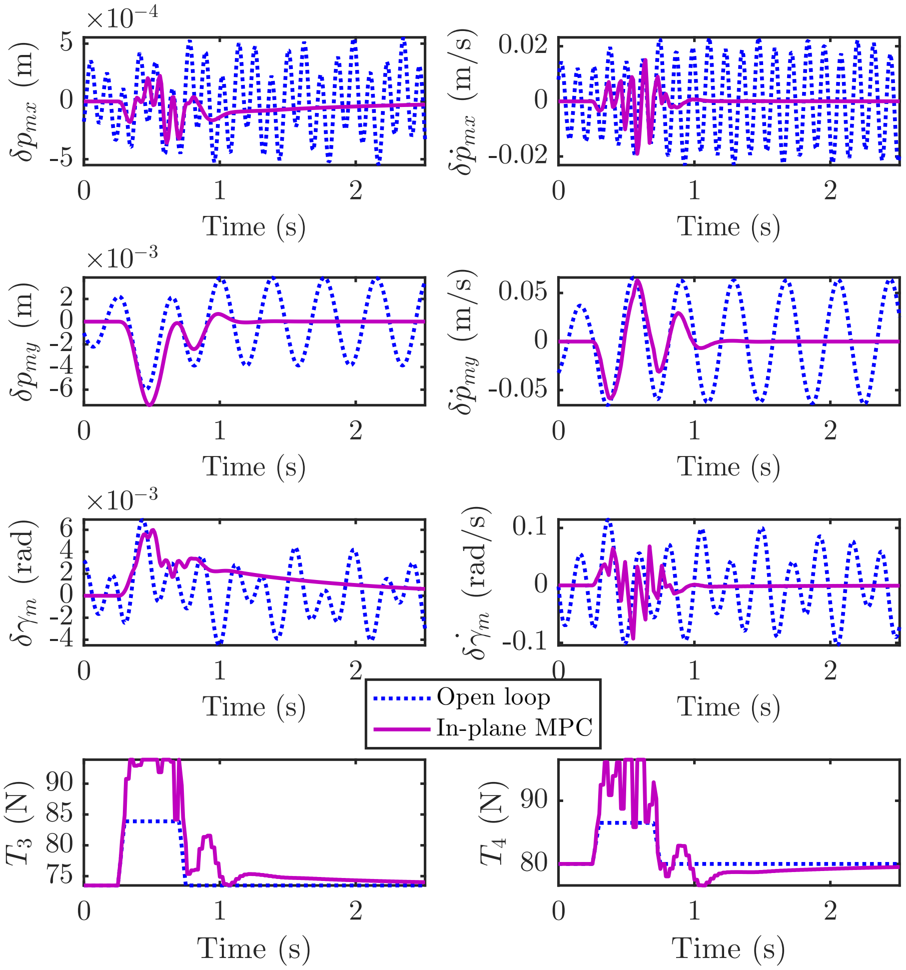

Figure 4.8: In-plane state and input responses at the example point P_2, where the open-loop control and in-plane MPC control are implemented, respectively.

where $\hat{L}_i$, k_{ci}, η_i, and T_{ical} $(i = 3, 4)$ are estimated discrete lower-cable lengths, cable stiffness, calibrated coefficients, and calibrated cable tensions, respectively. Other variables have been defined in subsection 3.3.2. $\xrightarrow{\text{3-SMF}}$ indicates the 3rd-order-sliding-mode filter.

Then, a vector $\Delta L(k) \in \mathbb{R}^2$ representing the change of cable lengths is defined as

$$\Delta L(k) = \begin{cases} L_i(k) - L_i(k-1), & \text{for } i = 1, 2 \\ \hat{L}_i(k) - L_i(k-1), & \text{for } i = 3, 4 \end{cases} \tag{4.15}$$

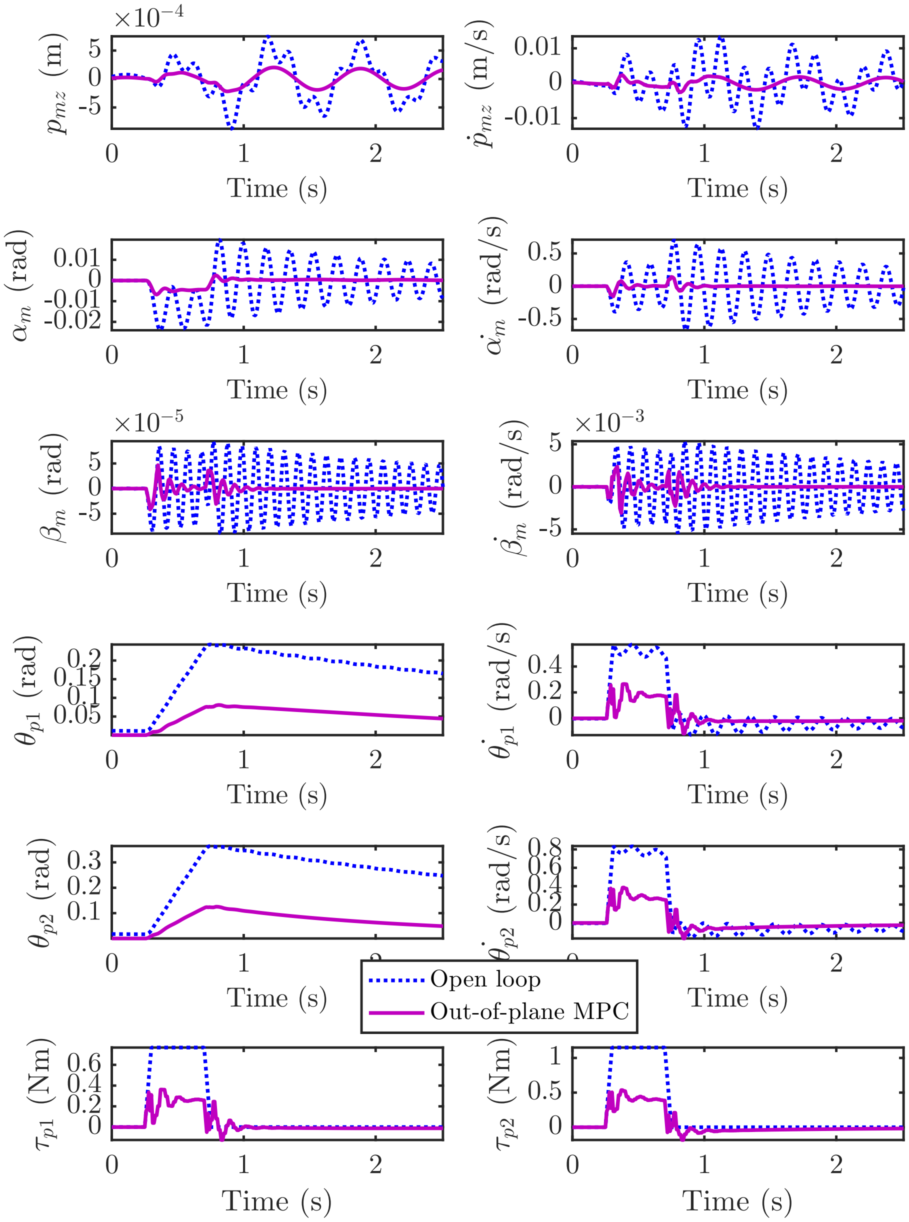

Figure 4.9: Out-of-plane state and input responses at the example point P_2, where the open-loop control and out-of-plane MPC control are respectively implemented.

where the ith cable length is computed as

$$L_i(k) = \|[a_{ix}, a_{iy}, a_{iz}]^T - [p_{mx}(k), p_{my}(k), p_{mz}(k)]^T - R_g^m[r_{ix}, r_{iy}, r_{iz}]^T\|. \tag{4.16}$$

The in-plane states can be estimated by substituting (4.15) into (4.17):

$$
\begin{aligned}
h(k) =&-[(J_{inp}(L(k))J_{inp}^T(L(k)) + \mu I)]^{-1} \\
&J_{inp}^T(L(k))\Delta L(k)
\end{aligned}
\tag{4.17a}
$$

$$
\begin{bmatrix} p_{mx}(k+1) \\ p_{my}(k+1) \\ \gamma_m(k+1) \end{bmatrix} = \begin{bmatrix} p_{mx}(k) \\ p_{my}(k) \\ \gamma_m(k) \end{bmatrix} + h(k) \tag{4.17b}
$$

$$
\begin{bmatrix} p_{mx}(k+1) \\ p_{my}(k+1) \\ \gamma_m(k+1) \end{bmatrix} \xrightarrow{\text{3-SMF}} \hat{x}_{inp}(k+1) \tag{4.17c}
$$

where h is each consecutive step, $J_{inp}(L) = \frac{\partial L}{\partial [p_{mx}, p_{my}, \gamma_m]^T}$ represents the Jacobian matrix, and μ is a damping parameter. (4.17a) is obtained using the Levenberg-Marquardt (LM) optimization algorithm [96]. $[p_{mx}, p_{my}, \gamma_m]^T$ and $\hat{x}_{inp}$ are in-plane state vector and the estimated state vector, respectively. (4.17) is forward kinematics based in-plane state estimation.

In section 5.2, the cable stiffness k_{c3}, k_{c4}, calibrated coefficients η_3, η_4, and cable tensions T_{3cal}, T_{4cal} equal 753.045 N/m, 753.045 N/m, 0.477, 0.477, 80 N, 80 N, respectively. The damping parameter μ equals 2. Additionally, the coefficients of the 3rd-order-sliding-mode filter in (4.14) and (4.17) are equal to 10000, respectively.

State estimation is vital in control design. The signals for the proposed state estimation came from accurate industrial encoders in servo motors and force sensors (Transducer Techniques, TLL-1K), respectively. In contrast, the states in [53] were estimated using IMU signals (via integrating with moving average filtering), which often resulted in error drift. Hence, the proposed state estimation is more robust than that of [53].

4.2.4.2 Out-of-Plane State Estimation (Out-of-Plane Observer)

The discrete out-of-plane state estimation shown in Algorithm 3 is proposed to illustrate the implementation process. Since the IMU signal includes real states $x_{outp}(k)$, noise $d_{outp}(k)$, and steady-state errors $e_{outp}(k)$, then the discrete state-space model of the Kalman filter is computed as

$$
\begin{aligned}
x_{eoutp}(k+1) &= A_{eoutp}(k)x_{eoutp}(k) + B_{eoutp}(k)u_{eoutp}(k) \\
y_{eoutp}(k) &= C_{eoutp}(k)x_{eoutp}(k)
\end{aligned}
\tag{4.18}
$$

Algorithm 2 Estimation of the in-plane states

```
Input: The measured lower-cable tensions (via force sensors) $T_{c9}(k)$, $T_{c10}(k)$, $T_{c11}(k)$, $T_{c12}(k)$, upper-cable lengths (via encoders in servo motors) $L_{01}(k)$, $L_{02}(k)$, and lower-cable lengths (via encoders in servo motors) $L_{03}(k)$, $L_{04}(k)$.
Output: Estimated in-plane state vector $\hat{x}_{inp}(k+1)$.
Initial state vector $[p_{mx}(0), p_{my}(0), \gamma_m(0)]^T = \mathbf{0}$;
Given $T_{c9}(k)$, $T_{c10}(k)$, $T_{c11}(k)$, and $T_{c12}(k)$ to compute the estimated lower-cable tensions $\hat{T}_3$ and $\hat{T}_4$ via $\eta_3(T_{c10}+T_{c12}) \xrightarrow{\text{3-SM}} \hat{T}_3$ and $\eta_4(T_{c9}+T_{c11}) \xrightarrow{\text{3-SMF}} \hat{T}_4$, respectively;
Given $L_{03}(k)$ and $L_{04}(k)$, and substitute $\hat{T}_3(k)$ and $\hat{T}_4(k)$ into (4.14) to calculate the estimated lower-cable lengths $\hat{L}_3(k)$ and $\hat{L}_4(k)$;
Compute $\hat{L}_3(k), \hat{L}_4(k) \rightarrow \Delta L(k)$ by using (4.15);
Resubstitute $\Delta L(k)$ into (4.17a), the consecutive step vector $h(k)$ is computed;
Substitute $\Delta L(k)$ and $[p_{mx}(k), p_{my}(k), \gamma_m(k)]^T$ into (4.17b), the new $[p_{mx}(k+1), p_{my}(k+1), \gamma_m(k+1)]^T$ is calculated;
Update $[p_{mx}(k+1), p_{my}(k+1), \gamma_m(k+1)]^T$ by using the 3rd-order-sliding-mode filter (4.17c), then the estimated $[\hat{p}_{mx}(k+1), \hat{p}_{my}(k+1), \hat{\gamma}_m(k+1)]^T$ is obtained;
Return $\hat{x}_{inp}(k+1) = [\hat{p}_{mx}(k+1), \hat{p}_{my}(k+1), \hat{\gamma}_m(k+1)]^T$.
```

with the state vector $x_{eoutp}(k) = [x_{outp}(k), d_{outp}(k), e_{outp}(k)]^T$ and input vector $u_{eoutp}(k) = [\sum_{0}^{k} \ddot{p}_{mz}^{imu}(k), \dot{\alpha}_m^{imu}(k), \dot{\beta}_m^{imu}(k)]^T$. The acceleration $\ddot{p}_{mz}^{imu}(k)$, angle velocity $\dot{\alpha}_m^{imu}(k)$, and angle velocity $\dot{\beta}_m^{imu}(k)$ signals come from IMU, respectively. In addition,

$$A_{eoutp}(k) = \begin{bmatrix} A_{outp}(k) & \mathbf{0} \\ \mathbf{0} & A_{offset}(k) \end{bmatrix}, B_{eoutp}(k) = \begin{bmatrix} B_{outp}(k) \\ \mathbf{0} \end{bmatrix}, \tag{4.19a}$$

$$C_{eoutp}(k) = \begin{bmatrix} 0,1,0,0,0,0,1,0,0,0,0,0 \\ 0,0,0,1,0,0,0,0,1,0,0,0 \\ 0,0,0,0,0,1,0,0,0,0,1,0 \end{bmatrix}, \tag{4.19b}$$

$$A_{offset}(k) = \begin{bmatrix} 0,1,0,0,0,0 \\ 0,0,0,0,0,0 \\ 0,0,0,1,0,0 \\ 0,0,0,0,0,0 \\ 0,0,0,0,0,1 \\ 0,0,0,0,0,0 \end{bmatrix} \tag{4.19c}$$

where $A_{outp}(k)$ and $B_{outp}(k)$ are obtained using (4.12b). For the experiments in section 5.2, state and input weighting matrices are equal to $Q_{eoutp} = \text{diag}([0.0001, 0.0001, 0.001, 0.001,$

Algorithm 3 Estimation of the out-of-plane states

```
Input: The measured IMU acceleration $\ddot{p}_{mz}^{imu}(k)$, angle velocity $\dot{\alpha}_m^{imu}(k)$, and angle velocity $\dot{\beta}_m^{imu}(k)$; the vector of angle and angle velocity of the pendulums $[\theta_{p1}(k), \dot{\theta}_{p1}(k), \theta_{p2}(k), \dot{\theta}_{p2}(k)]^T$.
Output: Estimated out-of-plane state vector $\hat{x}_{outp}(k+1)$.
Given $\ddot{p}_{mz}^{imu}(k)$, $\dot{\alpha}_m^{imu}(k)$, $\dot{\beta}_m^{imu}(k)$, and substitute (4.18) into the Kalman filter, then the corresponding Kalman gain is computed. Based on the obtained Kalman gain, the state vector $[\hat{p}_{mz}(k+1), \dot{\hat{p}}_{mz}(k+1), \hat{\alpha}_m(k+1), \dot{\hat{\alpha}}_m(k+1), \hat{\beta}_m(k+1), \dot{\hat{\beta}}_m(k+1)]^T = [p_{mz}(k+1), \dot{p}_{mz}(k+1), \alpha_m(k+1), \dot{\alpha}_m(k+1), \beta_m(k+1), \dot{\beta}_m(k+1)]^T$ can be estimated by updating prediction and measurement online;
Substitute $[\theta_{p1}(k), \dot{\theta}_{p1}(k), \theta_{p2}(k), \dot{\theta}_{p2}(k)]^T$ into the 3rd-order-sliding-mode filter, the state vector $[\hat{\theta}_{p1}(k+1), \dot{\hat{\theta}}_{p1}(k+1), \hat{\theta}_{p2}(k+1), \dot{\hat{\theta}}_{p2}(k+1)]^T = [\theta_{p1}(k+1), \dot{\theta}_{p1}(k+1), \theta_{p2}(k+1), \dot{\theta}_{p2}(k+1)]^T$ is estimated directly;
Return $\hat{x}_{outp}(k+1) = [\hat{p}_{mz}(k+1), \dot{\hat{p}}_{mz}(k+1), \hat{\alpha}_m(k+1), \dot{\hat{\alpha}}_m(k+1), \hat{\beta}_m(k+1), \dot{\hat{\beta}}_m(k+1), \hat{\theta}_{p1}(k+1), \dot{\hat{\theta}}_{p1}(k+1), \hat{\theta}_{p2}(k+1), \dot{\hat{\theta}}_{p2}(k+1)]^T$.
```

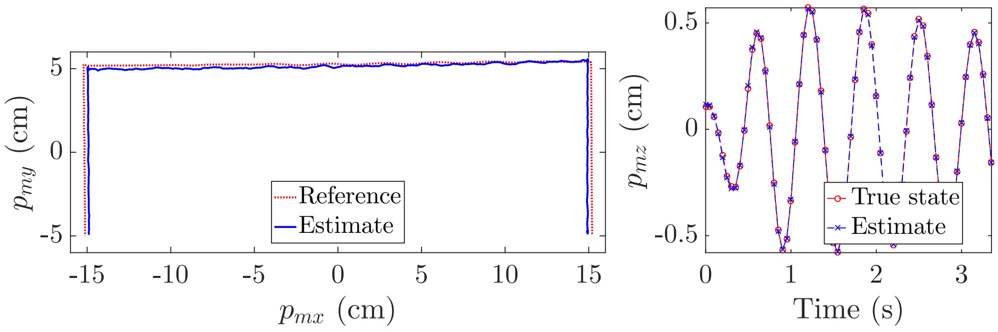

(a) (b)

Figure 4.10: An example to verify the proposed estimators. (a) In-plane trajectory (p_{mx} versus p_{my}) and (b) out-of-plane trajectory (p_{mz} versus time)

$0.0001, 0.0001, 0.2, 0.1, 0.1, 0.1, 0.1, 0.2]$) and $R_{eoutp} = \mathrm{diag}([0.00001, 0.01, 0.01])$, respectively.

By substituting (4.18) into the Kalman filter, the corresponding Kalman gain is computed. Using the obtained Kalman gain, the IMU-based out-of-plane states will be estimated by updating prediction and measurement online.

The pendulum angle signals are obtained from encoders, then states $[\hat{\theta}_{p1}(k+1), \dot{\hat{\theta}}_{p1}(k$

$+1), \hat{\theta}_{p2}(k+1), \dot{\hat{\theta}}_{p2}(k+1)]^T$ are estimated via the 3rd-order-sliding-mode filter, and the coefficient of the filter equals 1000.

To show the effectiveness of the estimators, an example including the in-plane trajectory (p_{mx} versus p_{my}) and out-of-plane trajectory (p_{mz} versus time) is given in Figure 4.10. The reference trajectory and true state are based on the measured data using a camera tracking system (Krypton RODYM [52]). Clearly, the estimates track the reference or the true state very well, i.e., the above in-plane and out-of-plane estimators are effective.

4.3 Vibration Control and Trajectory Tracking: Practical Methods

Based on the linearized model and reference variables obtained in subsection 3.4.4 and subsection 3.4.5, two control architectures are developed (shown in Figure 4.11): MPC with integral action and MPC+PI with integral action.

4.3.1 MPC with Integral Action

In Figure 4.11(a), the MPC with integral action has two control loops: an MPC-based loop and an integral compensator-based loop. MPC is used for state feedback control and the cost function with constraints is defined as

$$\begin{aligned}
\min \quad & \sum_{k=0}^{N_p-1} \left\{ x(k)^T Q_p x(k) + u(k)^T R_p u(k) \right\} \\
& + x(k)^T P_p x(k) && \text{(4.20a)} \\
\text{s. t.} \quad & x(k + \tfrac{\Delta T}{T_s}) = A(k)x(k) + B(k)u(k) \\
& y(k) = Cx(k) && \text{(4.20b)} \\
& x_L \leq x(k) \leq x_U \\
& u_L \leq u(k) \leq u_U \\
& R_p = R_p^T \succ 0, R_p \in \mathbb{R}^{3\times 3} \\
& Q_p = Q_p^T \succeq 0, Q_p \in \mathbb{R}^{12\times 12} \\
& P_p = P_p^T \succeq 0, P_p \in \mathbb{R}^{12\times 12}
\end{aligned}$$

where the state vector $x = [p_{mz}, \dot{p}_{mz}, \alpha_m, \dot{\alpha}_m, \beta_m, \dot{\beta}_m, \theta_{p1}, \dot{\theta}_{p1}, \theta_{p2}, \dot{\theta}_{p2}, p_s, \dot{p}_s]^T$ and the control input vector $u = [\tau_{p1}, \tau_{p2}, f_s]^T$. (4.20b) is the discrete state-space model of (3.58) with R_p, Q_p, and P_p denoting input weighting matrix, state weighting matrix, and terminal weighting matrix, respectively. x_L, x_U, u_L, u_U represent the lower bound and upper bound of states and control inputs, respectively.

To solve (4.21), some alternative solvers can be used, such as qpOASES [37], CVXGEN [75], etc. Due to the limitations of code generation in Beckhoff TwinCAT development environment [16], in this chapter, one can find the unconstrained optimal solution and consider the constraints in (4.20) as control saturation to avoid overshoot.

Substituting (4.20b) into (4.20a), one can obtain a quadratic programming (QP) problem as

$$\begin{aligned} J(x_k, U) = \frac{1}{2} U^T (2\bar{\Phi}^T \bar{Q}_p \bar{\Phi} + 2\bar{R}_p) U + x_k^T (2\bar{F}^T \bar{Q}_p \bar{\Phi}) U \\ + x_k^T (Q_p + \bar{F}^T \bar{Q}_p \bar{F}) x_k \end{aligned} \tag{4.21}$$

where

$$\begin{aligned} \bar{Q}_p &= \mathrm{diag}(Q_p, Q_p, \cdots, P_p), \\ \bar{R}_p &= \mathrm{diag}(R_p, R_p, \cdots, R_p), \\ U &= \begin{bmatrix} u(k) \\ u(k + \Delta T/T_s) \\ \vdots \\ u(k + (N_p - 1)\Delta T/T_s) \end{bmatrix}, \bar{F} = \begin{bmatrix} A \\ A^2 \\ \vdots \\ A^{N_p} \end{bmatrix}, \\ \bar{\Phi} &= \begin{bmatrix} B & \mathbf{0} & \cdots & \mathbf{0} \\ AB & B & \cdots & \mathbf{0} \\ \vdots & \vdots & \vdots & \vdots \\ A^{N_p-1}B & A^{N_p-2}B & \cdots & A^{N_p-N_c}B \end{bmatrix}, x_k = x(k) \end{aligned}$$

with N_p and N_c represent the predictive horizon and control horizon, respectively.

Let $\frac{\partial J(x_k, U)}{\partial U} = 0$ [114], the optimal input of (4.21) is computed as

$$u^* = -\underbrace{[I_{3\times 3}, \mathbf{0}](\bar{\Phi}^T \bar{Q} \bar{\Phi} + \bar{R})^{-1} \bar{\Phi}^T \bar{Q}^T \bar{F}}_{=:K_{mpc1}} x_k. \tag{4.22}$$

In Figure 4.11(a), the integral compensator (integral gain K_{fbi}) is included to stabilize the system, i.e., result in the tracking error $(r(k) - y(k))$ converging towards to zero

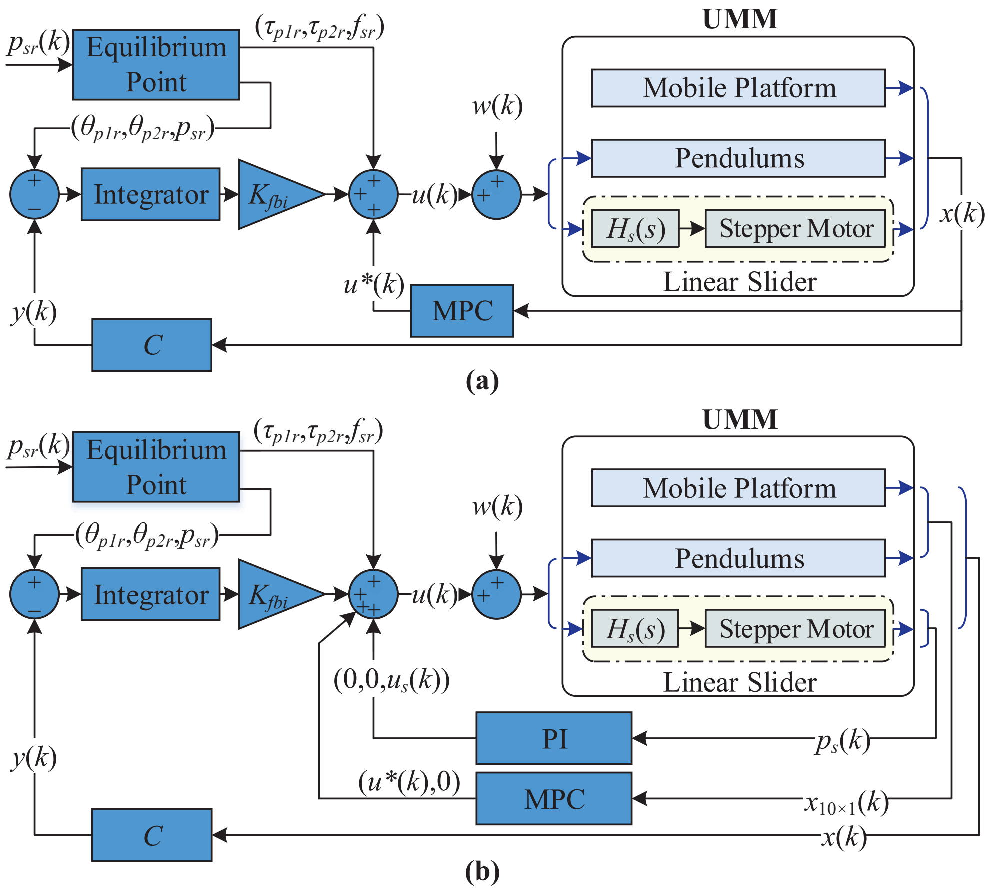

Figure 4.11: Control architectures. (a) MPC with integral action and (b) MPC+PI with integral action. The components of the UMM are illustrated as follows: 1) the mobile platform has no control input and six states $(p_{mz}, \dot{p}_{mz}, \alpha_m, \dot{\alpha}_m, \beta_m, \dot{\beta}_m)$, and the states were obtained using a Kalman-based method [92]; 2) the kth $(k = 1, 2)$ pendulum is actuated by the corresponding servo motor (Beckhoff, AM8131-0F20-0000). Each pendulum has one input (torque τ_{pk}) and two states $(\theta_{pk}, \dot{\theta}_{pk})$; 3) the linear slider is actuated by a stepper motor (Nema 17, 42 mm) with an encoder (Avago, HEDS-5540 I06), and it has one input (force f_s) and two states $(p_s, \dot{p}_s)$.

asymptotically. Finally, by combining with (4.22), the control law for the system is designed as

$$u(k) = u^* + K_{fbi}(r(k) - y(k)) + u_r \tag{4.23}$$

where the reference input vector u_r is equal to $[\tau_{p1r}, \tau_{p2r}, f_{sr}]^T$.

4.3.2 MPC+PI with Integral Action

Different with that of MPC with integral action in Figure 4.11(a), the MPC+PI with integral action shown in Figure 4.11(b) has three control loops: an MPC-based loop for the mobile platform and two pendulums, a PI controller-based loop, and an integral compensator-based loop. In this case, the MPC cost function with constraints is redefined as

$$\begin{aligned}
\min \quad & \sum_{k=0}^{N_p-1} \Big\{ x_{10\times 1}(k)^T Q_p x_{10\times 1}(k) + u_{2\times 1}(k)^T R_p \\
& u_{2\times 1}(k) \Big\} + x_{10\times 1}(k)^T P_p x_{10\times 1}(k) && (4.24a)\\
\text{s. t.} \quad & x_{10\times 1}(k + \tfrac{\Delta T}{T_s}) = A_{10\times 10}(k) x_{10\times 1}(k) + B_{10\times 2}(k) \\
& u_{2\times 1}(k) \\
& y(k) = C_{2\times 10} x_{10\times 1}(k) && (4.24b)\\
& x_L \leq x_{10\times 1}(k) \leq x_U \\
& u_L \leq u_{2\times 1}(k) \leq u_U \\
& R_p = R_p^T \succ 0, R_p \in \mathbb{R}^{2\times 2} \\
& Q_p = Q_p^T \succeq 0, Q_p \in \mathbb{R}^{10\times 10} \\
& P_p = P_p^T \succeq 0, P_p \in \mathbb{R}^{10\times 10}
\end{aligned}$$

with $x_{10\times 1} = [p_{mz}, \dot{p}_{mz}, \alpha_m, \dot{\alpha}_m, \beta_m, \dot{\beta}_m, \theta_{p1}, \dot{\theta}_{p1}, \theta_{p2}, \dot{\theta}_{p2}]^T$ and $u_{2\times 1} = [\tau_{p1}, \tau_{p2}]^T$. The reduced state and input variables $x_{10\times 1}$ and $u_{2\times 1}$ are obtained by removing the slider's states and input (in (3.57)), respectively. (4.24b) is obtained by linearizing (3.57) around the reduced reference state vector $x_{r10\times 1}$. Compared with (4.20), other variables (e.g., R_p, Q_p, and P_p) are extended to different dimensions. Then, the optimal input of (4.24) is computed as

$$u^*_{2\times 1} = -\underbrace{[I_{2\times 2}, \mathbf{0}](\bar{\Phi}^T \bar{Q} \bar{\Phi} + \bar{R})^{-1} \bar{\Phi}^T \bar{Q}^T \bar{F}}_{=:K_{mpc2}} x_{k10\times 1}. \qquad (4.25)$$

In Figure 4.11(b), the PI controller (gain K_{pi}) and the integral compensator (integral gain K_{fbi}) are also included. The PI controller is utilized to control the position of the slider. Also, the PI controller is selected since the stepper motor is under speed control mode. Hence, in this case, the control law (combining with (4.25)) for the system is described as

$$u(k) = \begin{bmatrix} u^*_{2\times 1} \\ 0 \end{bmatrix} + \left[0, 0, -K_{pi} \begin{bmatrix} \sum_0^k (p_{sr}(k) - p_s(k)) \\ p_{sr}(k) - p_s(k) \end{bmatrix} \right]^T + K_{fbi}(r(k) - y(k)) + u_r. \tag{4.26}$$

Another feature of the above control algorithms can be summarized as below: (4.23) and (4.26) are easy to be implemented in practice because one can tune the parameter K_{fbi} to reject errors when the dynamic model is not accurate enough.

4.3.3 Stability Analysis

To analyze the system stability, direct Lyapunov [69] and indirect Lyapunov approaches can be used. Since the linearized model (3.59) around the equilibrium point is known, then the indirect Lyapunov-based stability will be developed. Based on the control design shown in subsection 4.3.1 and subsection 4.3.2, two theorems are introduced to analyze the stability in the following cases:

Theorem 4.3.1. *Suppose a close-loop control law* $u = [K_{mpc1}, K_{fbi}] \begin{bmatrix} x(k) \\ z(k) \end{bmatrix} + u_r$ *with the feedback gain* $[K_{mpc1}, K_{fbi}]$ *can stabilize the augmented system* (3.59)*, then* $\lim_{k\to\infty} y(k) = r$ *for an arbitrary constant disturbance* w *and reference* r *[19].*

Proof. Substituting $u = [K_{mpc1}, K_{fbi}] \begin{bmatrix} x(k) \\ z(k) \end{bmatrix} + u_r$ into (3.59), one can get

$$\begin{aligned} \begin{bmatrix} x(k+1) \\ z(k+1) \end{bmatrix} &= \begin{bmatrix} A & \mathbf{0} \\ -C & I \end{bmatrix} \begin{bmatrix} x(k) \\ z(k) \end{bmatrix} + \begin{bmatrix} B \\ \mathbf{0} \end{bmatrix} [K_{mpc1}, K_{fbi}] \\ &\quad \begin{bmatrix} x(k) \\ z(k) \end{bmatrix} + \begin{bmatrix} B \\ \mathbf{0} \end{bmatrix} u_r + \begin{bmatrix} \mathbf{0} \\ I \end{bmatrix} r + \begin{bmatrix} B \\ \mathbf{0} \end{bmatrix} w \\ &= \begin{bmatrix} A + BK_{mpc1} & BK_{fbi} \\ -C & I \end{bmatrix} \begin{bmatrix} x(k) \\ z(k) \end{bmatrix} \\ &\quad + \begin{bmatrix} B & \mathbf{0} \\ \mathbf{0} & I \end{bmatrix} \begin{bmatrix} w + u_r \\ r \end{bmatrix}. \end{aligned} \tag{4.27}$$

The characteristic polynomial of (4.27) can be computed as

$$g(\lambda) = \det \begin{bmatrix} \lambda I - A - BK_{mpc1} & -BK_{fbi} \\ C & (\lambda - 1)I \end{bmatrix} \tag{4.28}$$

where λ is the eigenvalue. Since (4.27) is asymptotically stable via controller design and (w, r) are constant, then the roots (i.e., eigenvalue λ) of (4.28) must locate in a unit circle. Hence,

$$\begin{aligned}
&\Rightarrow \lim_{k\to\infty} \left\{ \begin{bmatrix} x(k+1) \\ z(k+1) \end{bmatrix} - \begin{bmatrix} x(k) \\ z(k) \end{bmatrix} \right\} = \mathbf{0} \\
&\Rightarrow \lim_{k\to\infty} (z(k+1) - z(k)) = \mathbf{0} \\
&\Rightarrow \lim_{k\to\infty} (z(k) + r - y(k) - z(k)) = \mathbf{0} \\
&\Rightarrow \lim_{k\to\infty} (r - y(k)) = \mathbf{0} \\
&\Rightarrow \lim_{k\to\infty} y(k) = r.
\end{aligned}$$

□

Theorem 4.3.2. *Assume another close-loop control law* $u = \left[\begin{bmatrix} K_{mpc2} & \mathbf{0} \\ \mathbf{0} & K_{pi} \end{bmatrix}, K_{fbi} \right] \begin{bmatrix} x(k) \\ z(k) \end{bmatrix} + u_r$ *with the feedback gain* $\left[\begin{bmatrix} K_{mpc2} & \mathbf{0} \\ \mathbf{0} & K_{pi} \end{bmatrix}, K_{fbi} \right]$ *can also stabilize the augmented system* (3.59), *then* $\lim_{k\to\infty} y(k) = r$ *for an arbitrary constant disturbance* w *and reference* r*.*

Proof. Using the similar proof approach as that for Theorem 4.3.1 by substituting $u = \left[\begin{bmatrix} K_{mpc2} & \mathbf{0} \\ \mathbf{0} & K_{pi} \end{bmatrix}, K_{fbi} \right] \begin{bmatrix} x(k) \\ z(k) \end{bmatrix} + u_r$ into (3.59), the corresponding characteristic polynomial is calculated as

$$g(\lambda) = \det \begin{bmatrix} \lambda I - A - B \begin{bmatrix} K_{mpc2} & \mathbf{0} \\ \mathbf{0} & K_{pi} \end{bmatrix} & -BK_{fbi} \\ C & (\lambda - 1)I \end{bmatrix}. \tag{4.29}$$

Since this closed-loop model is also asymptotically stable and (w, r) are constant, the roots of (4.29) locate in a unit circle. One can conclude as below: $\lim_{k\to\infty} (z(k+1) - z(k)) = \mathbf{0} \Rightarrow \lim_{k\to\infty} (z(k) + r - y(k) - z(k)) = \mathbf{0} \Rightarrow \lim_{k\to\infty} y(k) = r$. □

Clearly, Theorem 4.3.1 and Theorem 4.3.2 are applied to the closed-loop systems in subsection 4.3.1 and subsection 4.3.2, respectively.

Remark 4.3.1. *Theorem 4.3.2 can be generated to a multi-loop feedback gain (i.e., defined as)* $\left[diag([K_1, K_2, \dots, K_m]), K_{fbi}\right]$ $(\{\forall\ m \in \mathbb{N} : 1 \leq m \leq 12\})$ *to stabilize the augmented model* (3.59)*.*

Using the similar approach (for Theorem 4.3.2) one can easily prove Remark 4.3.1.

In this chapter, the stability around the reference point (3.60) is analyzed, which is considered as the equilibrium point. One can also derive the Lyapunov function at each time iteration using the method in [36] for other potential applications.

4.3.4 Simulation Results

4.3.4.1 Case Studies

To demonstrate a warehousing application in simulation, a step reference is given to the slider, i.e., $(p_{sr} = 0\,\mathrm{m}) \rightarrow (p_{sr} = -0.15\,\mathrm{m})$. Additionally, the initial states are equal to zero, input pulse disturbances are given, the system keeps its maximum allowable cable tensions, and the desired in-plane position (p_{mx}, p_{my}) of the mobile platform is always equal to $(0, 0)$ m.

Based on the above setup and tuning parameters shown in Table 4.3, the open-loop control, MPC with integral action, and MPC+PI with integral action are implemented, respectively. The simulated responses with these control strategies are shown in Figure 4.12 and Figure 4.13. In this case, the moving slider generates reaction forces to the mobile platform, resulting in the mobile platform vibrating. The control goal is to minimize the vibrations and increase the position accuracy of the end-effector.

For the MPC with integral action, MPC is used for state feedback control, including two objectives: 1) dampen the mobile platform's undesired out-of-plane motions and keep the states at zero; 2) to achieve the position control for the slider. While for the MPC+PI with integral action, MPC and PI controllers are used to achieve the goals 1) and 2), respectively. For both control architectures, the integral compensator (integral gain K_{fbi}) is utilized to stabilize the system, i.e., resulting in the tracking error $(r(k) - y(k))$ converging towards to zero asymptotically.

Figure 4.12 shows the state and input responses using open-loop control. Since the stepper motor is commanded in speed control mode (see subsection 3.4.1), the PI controller is still applied to the stepper motor to bring the slider to the target position p_{sr}. Clearly,

Table 4.3: Tuning Parameters for Simulations

Control structures	Parameters
MPC with Integral Action	$T_s = 0.01\,\mathrm{s}$ (sampling time); $\Delta T = 0.02\,\mathrm{s}$ (interval time); $N_p = 5$ (predictive horizon); $N_c = 5$ (control horizon); $R_p = \mathrm{diag}([0.014, 0.014, 0.0015])$ (input weighting matrix); $Q_p = \mathrm{diag}([100, 100, 1, 1, 1, 10, 1, 1, 1, 1, 150, 0])$ (state weighting matrix); P_p (terminal weighting matrix) is the solution of the Lyapunov equation $AP_pA^T - P_p = -Q_p$; $P_p = Q_p$ (terminal weighting matrix); $x_L = -\infty \in \mathbb{R}^{12\times 1}$ (lower bound); $x_U = \infty \in \mathbb{R}^{12\times 1}$ (upper bound); $u_L = -[3, 3, 10]^T$ (lower bound); $u_U = [3, 3, 10]^T$ (upper bound); $K_{fbi} = [1, 1, 22.75]^T$ (integral compensator gain).
MPC+PI with Integral Action	$T_s = 0.01\,\mathrm{s}$; $\Delta T = 0.02\,\mathrm{s}$; $N_p = N_c = 5$; $R_p = \mathrm{diag}([0.3, 0.3])$; $R_p = \mathrm{diag}([1.5\mathrm{e}^4, 1.5\mathrm{e}^4, 1\mathrm{e}^2, 1\mathrm{e}^2, 2\mathrm{e}^2, 2\mathrm{e}^2, 1, 1, 1, 1])$; P_p is the solution of the Lyapunov equation $AP_pA^T - P_p = -Q_p$; $x_L = -\infty \in \mathbb{R}^{10\times 1}$; $x_U = \infty \in \mathbb{R}^{10\times 1}$; $u_L = -[3, 3]^T$; $u_U = [3, 3]^T$; $K_{fbi} = [1, 1, 1]^T$; $K_{pi} = [30, 50]$ (PI controller gain).

in Figure 4.12(b), the actual position of the slider p_s can converge to the reference position $p_{sr} = -0.15\,\mathrm{m}$. During this process, the movement of the slider generates a reaction force resulting in the vibrations of the mobile platform (see the state responses in Figure 4.12(a)). In this case, there are no control inputs to the pendulums (in Figure 4.12(c)), and the input disturbances also contribute to the vibrations. Because of the system damping behaviors, the vibrations finally close to zero. However, when the controllers (MPC with integral action and MPC+PI with integral action) are applied, clearly, the vibrations damp out faster (shown in Figure 4.12(a)). Also, due to the in-plane kinematic constraints and high stiffness of cables, the oscillations of angle α_m and β_m are small (discussed in section 3.4), but the amplitude in the Z-direction (i.e., p_{mz}) is quite visible. Using these two controllers, the amplitude is clearly eliminated. Furthermore, the control inputs (in Figure 4.12(c)) also contribute the reference tracking (shown in Figure 4.12(b)) for the slider and pendulums.

Substituting the obtained values (in Figure 4.12) into (3.46c), the end-effector position $p_e = (x_e, y_e, z_e)$ can be computed, as shown in Figure 4.13. In Figure 4.13, x_e is small, because the X-direction is parallel with in-plane. In the Z-direction (i.e., z_e), three controllers have close performance (since in the open-loop controller, the slider is also applied the same PI controller), but MPC with Integral Action converges faster. In the Y-direction (i.e., y_e), the MPC with Integral Action and MPC+PI with Integral Action bring the UMM to the same position, which is larger than that of open-loop control. Hence, it can be concluded that two closed-loop controllers can improve the position accuracy of the end-effector.

In summary, the simulation results show that both control algorithms can achieve the objectives and have better control performance than that of open-loop control. The open-loop control also results in zero states of the mobile platform because of the damping behavior of the system. Clearly, the control performance validates the effectiveness of the control design. The results also show that when input disturbances are given, both controllers work well, i.e., excellent robust performance.

4.3.4.2 Discussion

Using (A.9) (see Appendix A.3), the performance indices results are shown in Figure 4.14 ((a) J_{mest} versus J_{md} and (b) κ_{mest} versus κ_{md}, respectively). Clearly, $J_{md} \ll J_{mest}$ and $\kappa_{md} \ll \kappa_{mest}$ for different in-plane positions (p_{mx}, p_{my}) in the feasible domain. The greater J_{mest} and stiffness magnitude κ_{mest} [124] indicate more effort to enhance system stability. Meanwhile, using the proposed control strategies in Figure 4.11, disturbance rejection is achieved.

4.4 Redundancy Resolution and Disturbance Rejection via Torque Optimization

4.4.1 Problem Definition

Consider a general second-order nonlinear system [108]:

$$\begin{aligned} \ddot{q} =& f(q, \dot{q}, u, t) = f_{\mathcal{U}}(q, \dot{q}, t) + f_{\mathcal{A}}(q, \dot{q}, t)u, \\ & \operatorname{rank}(f_{\mathcal{A}}(q, \dot{q}, t)) < n_{\mathcal{A}} + n_{\mathcal{U}} \end{aligned} \tag{4.30}$$

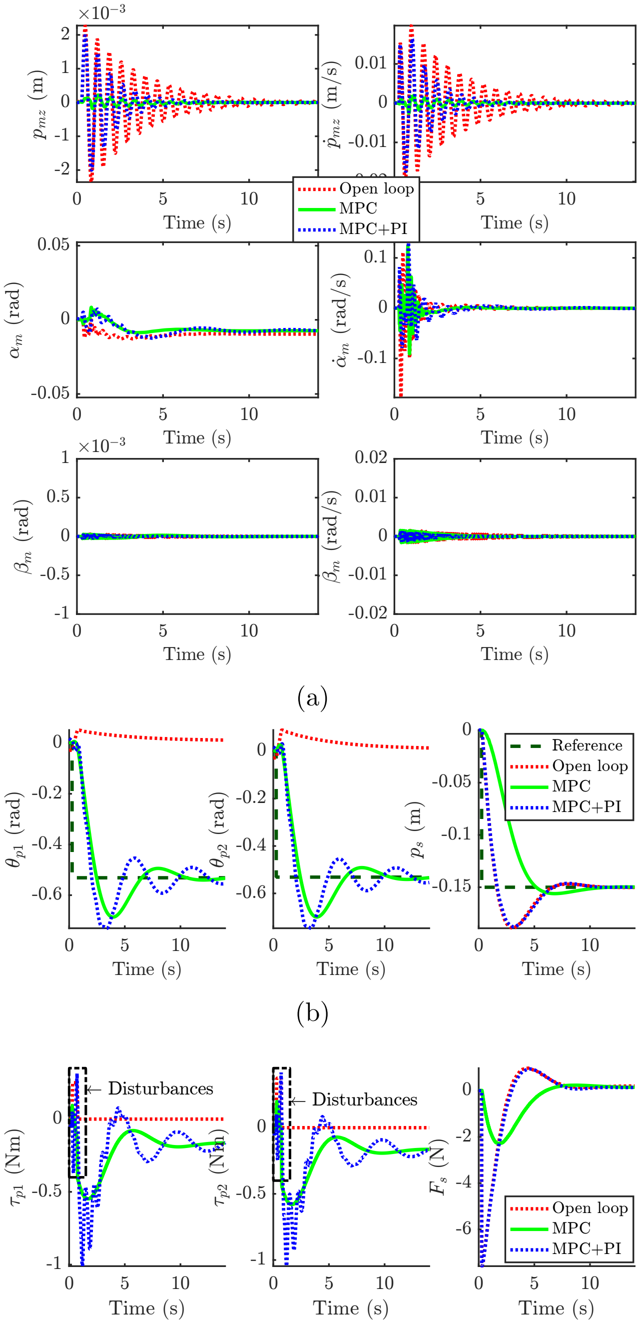

(a)

(b)

(c)

Figure 4.12: Simulated response with different control strategies. (a) State responses of the mobile platform, (b) reference tracking of the slider and pendulums, and (c) input responses of the pendulums. The open-loop control, MPC with integral action, and MPC+PI with integral action are implemented, respectively.

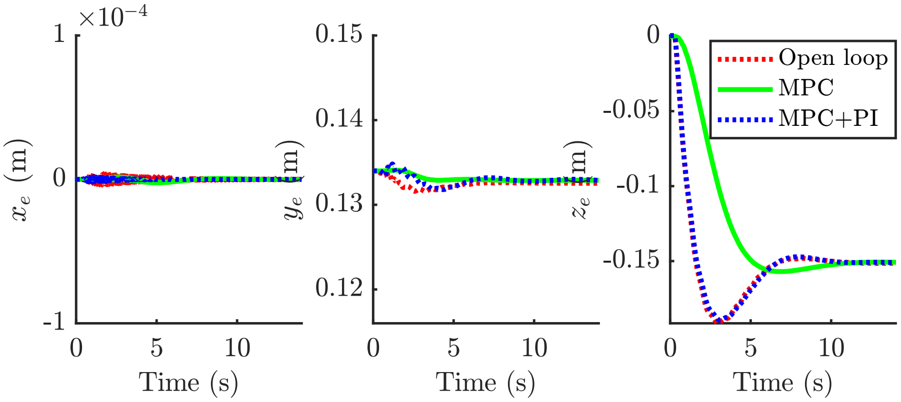

Figure 4.13: Simulated position of the end-effector with different control strategies. The open-loop control, MPC with integral action, and MPC+PI with integral action are implemented, respectively.

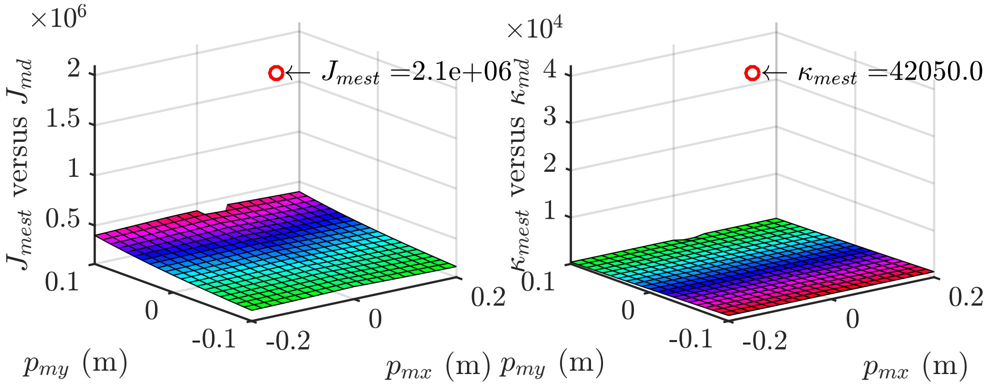

Figure 4.14: Comparison of performance indices. (a) J_{mest} versus J_{md} and (b) κ_{mest} versus κ_{md}.

where $f(q, \dot{q}, u, t)$, $f_{\mathcal{U}}(q, \dot{q}, t)$, and $f_{\mathcal{A}}(q, \dot{q}, t)$ indicate an underactuated system, an unactuated subsystem, and a fully-actuated subsystem, respectively. $q =: [q_{\mathcal{A}}^T, q_{\mathcal{U}}^T]^T \in \mathbb{R}^{n_{\mathcal{A}}+n_{\mathcal{U}}}$, $q_{\mathcal{A}} \in \mathbb{R}^{n_{\mathcal{A}}}$, and $q_{\mathcal{U}} \in \mathbb{R}^{n_{\mathcal{U}}}$ represent all generalized (joint) coordinates, actuated joint coordinates, and unactuated joint coordinates, respectively. $\dot{q} \in \mathbb{R}^{n_{\mathcal{A}}+n_{\mathcal{U}}}$, u, and t denote a vector of velocities, a vector of system inputs, and time, respectively.

When a new constraint is introduced into (4.30), i.e.,

$$\dot{p}_e = J_e \dot{q}_{\mathcal{A}}, \; n_e \leq n_{\mathcal{A}} \tag{4.31}$$

where $\dot{p}_e \in \mathbb{R}^{n_e}$ and J_e denote the velocity vector of the end-effector and task Jacobian matrix of a robot, respectively. Eq. (4.31) indicates the redundancy resolution problem (i.e., $\dot{p}_e \rightarrow \dot{q}_{\mathcal{A}}$) of a redundant actuated system by given $\dot{p}_e$.

To solve (4.30) and (4.31) at the same time when the position p_e or velocity $\dot{p}_e$ of the end-effector is given; however, the existing research focuses on actuated joints (in joint-space), unactuated joints (e.g., disturbances applied to the unactuated joints may affect the motion of a robot) are not considered. To address this problem, the redundancy resolution and disturbance rejection via torque optimization in the three-dimensional (3D) are studied by using the proposed robot shown in Figure 3.10.

In addition, in practical applications (e.g., pick-and-place), it is interesting to study the Cartesian space trajectory of the robot end-effector, which means only Cartesian position p_e, velocity $\dot{p}_e$, and/or acceleration $\ddot{p}_e$ are given. The main goal is to find joint-space commands (e.g., angles and velocities), i.e., the redundancy resolution problem. In this case, two new methods are proposed to solve it: joint-space torque optimization for actuated joints (TOAJ) and joint-space torque optimization for actuated and unactuated joints (TOAUJ).

4.4.2 Joint-Space Torque Optimization for Actuated Joints (TOAJ)

To obtain the optimal actuated-joint torque $\tau_{\mathcal{A}} \in \mathbb{R}^5$, the cost function is defined as

$$\min_{\tau_{\mathcal{A}} \in \mathscr{S}_1} \ \Lambda = \frac{1}{2}\left\| M_{\mathcal{A}}^{-1} \tau_{\mathcal{A}} \right\|_2^2 \tag{4.32a}$$

$$\text{s. t.} \ \ \mathscr{S}_1 = \Big\{ \text{argmin} \ \ddot{p}_e = J_e \ddot{q}_{\mathcal{A}} + \dot{J}_e \dot{q}_{\mathcal{A}} \tag{4.32b}$$

$$\begin{aligned} \text{s. t.} \quad & M_{\mathcal{A}}(q_{\mathcal{A}})\ddot{q}_{\mathcal{A}} + C_{\mathcal{A}}(q_{\mathcal{A}}, \dot{q}_{\mathcal{A}})\dot{q}_{\mathcal{A}} + G_{\mathcal{A}}(q_{\mathcal{A}}) \\ & + \tau_{d\mathcal{A}} = \tau_{\mathcal{A}} \end{aligned} \tag{4.32c}$$

$$\begin{aligned} & \tau_{\mathcal{A}} = [F_{mx}, F_{my}, \tau_{a1}, \tau_{a2}, \tau_{a3}]^T, \\ & F_{mx} = \tau_{m[1]}, F_{my} = \tau_{m[2]} \Big\} \end{aligned} \tag{4.32d}$$

where $q_{\mathcal{A}} := [p_{mx}, p_{my}, \theta_{a1}, \theta_{a2}, \theta_{a3}]^T$, $\dot{q}_{\mathcal{A}} := [\dot{p}_{mx}, \dot{p}_{my}, \dot{\theta}_{a1}, \dot{\theta}_{a2}, \dot{\theta}_{a3}]^T$, and $\ddot{q}_{\mathcal{A}} := [\ddot{p}_{mx}, \ddot{p}_{my}, \ddot{\theta}_{a1}, \ddot{\theta}_{a2}, \ddot{\theta}_{a3}]^T$ represent the actuated vectors of generalized coordinates, velocities, and accelerations, respectively. $J_e = \frac{\partial p_e}{\partial q_{\mathcal{A}}} \in \mathbb{R}^{3\times5}$, $\dot{J}_e \in \mathbb{R}^{3\times5}$, $p_e \in \mathbb{R}^3$, and $\ddot{p}_e \in \mathbb{R}^3$ are the task Jacobian matrix, the time-derivative of J_e, and the position and acceleration of the end-effector, respectively. The inertia matrix $M_{\mathcal{A}}(q_{\mathcal{A}}) \in \mathbb{R}^{5\times5}$, Coriolis and centripetal matrix

$C_{\mathcal{A}}(q_{\mathcal{A}}, \dot{q}_{\mathcal{A}}) \in \mathbb{R}^{5\times5}$, gravitational vector $G_{\mathcal{A}}(q_{\mathcal{A}}) \in \mathbb{R}^5$, and disturbance vector $\tau_{d\mathcal{A}} \in \mathbb{R}^5$ are obtained by choosing the corresponding actuated-joint elements in (3.69) and (3.70). Other variables (e.g., $\tau_m, \tau_a, p_{mx}, p_{my}, \theta_{a1}, \theta_{a2}, \theta_{a3}$) are also defined in (3.69).

The Lagrangian function of (4.32) is conducted as

$$\begin{aligned}
\tilde{\Lambda} &= \frac{1}{2}\left\|M_{\mathcal{A}}^{-1}\tau_{\mathcal{A}}\right\|_2^2 + \lambda^T(\ddot{p}_e - \dot{J}_e\ddot{q}_{\mathcal{A}} - J_e\dot{q}_{\mathcal{A}}) \\
&= \frac{1}{2}(M_{\mathcal{A}}\ddot{q}_{\mathcal{A}} + C_{\mathcal{A}}\dot{q}_{\mathcal{A}} + G_{\mathcal{A}} + \tau_{d\mathcal{A}})^T M_{\mathcal{A}}^{-2} \\
&\quad (M_{\mathcal{A}}\ddot{q}_{\mathcal{A}} + C_{\mathcal{A}}\dot{q}_{\mathcal{A}} + G_{\mathcal{A}} + \tau_{d\mathcal{A}}) \\
&\quad + \lambda^T(\ddot{p}_e - J_e\ddot{q}_{\mathcal{A}} - \dot{J}_e\dot{q}_{\mathcal{A}}) \\
&= \frac{1}{2}\ddot{q}_{\mathcal{A}}^T\ddot{q}_{\mathcal{A}} + (C_{\mathcal{A}}\dot{q}_{\mathcal{A}} + G_{\mathcal{A}} + \tau_{d\mathcal{A}})^T M_{\mathcal{A}}^{-1}\ddot{q}_{\mathcal{A}} \\
&\quad + \frac{1}{2}(C_{\mathcal{A}}\dot{q}_{\mathcal{A}} + G_{\mathcal{A}} + \tau_{d\mathcal{A}})^T M_{\mathcal{A}}^{-2}(C_{\mathcal{A}}\dot{q}_{\mathcal{A}} \\
&\quad + G_{\mathcal{A}} + \tau_{d\mathcal{A}}) + \lambda^T(\ddot{p}_e - J_e\ddot{q}_{\mathcal{A}} - \dot{J}_e\dot{q}_{\mathcal{A}})
\end{aligned} \tag{4.33}$$

where λ represents the Lagrange multiplier. Then, the necessary and sufficient conditions [70] for a minimum of (4.33) can be computed as

$$\begin{cases}
\frac{\partial\tilde{\Lambda}}{\partial\ddot{q}_{\mathcal{A}}} & = \ddot{q}_{\mathcal{A}} + M_{\mathcal{A}}^{-1}(C_{\mathcal{A}}\dot{q}_{\mathcal{A}} + G_{\mathcal{A}} + \tau_{d\mathcal{A}}) \\
& \quad - J_e^T\lambda = \mathbf{0} \\
\frac{\partial^2\tilde{\Lambda}}{\partial^2\ddot{q}_{\mathcal{A}}} & = I > \mathbf{0} \\
\frac{\partial\tilde{\Lambda}}{\partial\lambda} & = \ddot{p}_e - J_e\ddot{q}_{\mathcal{A}} - \dot{J}_e\dot{q}_{\mathcal{A}} = \mathbf{0}.
\end{cases} \tag{4.34}$$

By arranging (4.34), the solution is described as

$$\begin{aligned}
\ddot{q}_{\mathcal{A}} = J_e^T(J_eJ_e^T)^{-1}(\ddot{p}_e - \dot{J}_e\dot{q}_{\mathcal{A}}) - (I - J_e^T(J_eJ_e^T)^{-1}J_e) \\
M_{\mathcal{A}}^{-1}(C_{\mathcal{A}}\dot{q}_{\mathcal{A}} + G_{\mathcal{A}} + \tau_{d\mathcal{A}}).
\end{aligned} \tag{4.35}$$

Eq. (4.35) shows the solution at acceleration level (by given $\ddot{p}_e$). Alternately, it is easy to convert (4.35) into the discrete-time expression by using $\ddot{p}_e(k) = \frac{\dot{p}_e(k)-\dot{p}_e(k-1)}{T_s}$, $\ddot{q}_{\mathcal{A}}(k) = \frac{\dot{q}_{\mathcal{A}}(k)-\dot{q}_{\mathcal{A}}(k-1)}{T_s}$, and $\dot{J}_e(k) = \frac{J_e(k)-J_e(k-1)}{T_s}$, in which T_s denotes the sampling time.

Then, the recursive formula can be described as

$$\begin{aligned}\dot{q}_{\mathcal{A}}(k) = J_e^T(k)[J_e(k)J_e^T(k)]^{-1}\dot{p}_e(k) + \Big\{I - J_e^T(k)[J_e(k)\\ J_e^T(k)]^{-1}J_e(k)\Big\}\Big\{\{I - T_s[M_{\mathcal{A}}(q_{\mathcal{A}}(k))]^{-1}\\ [C_{\mathcal{A}}(q_{\mathcal{A}}(k), \dot{q}_{\mathcal{A}}(k-1))]\Big\}\dot{q}_{\mathcal{A}}(k-1) - T_s\\ [M_{\mathcal{A}}(q_{\mathcal{A}}(k))]^{-1}[G_{\mathcal{A}}(q_{\mathcal{A}}(k)) + \tau_{d\mathcal{A}}(k)]\Big\}\end{aligned} \tag{4.36}$$

where $\dot{p}_e$ is the input velocity of the end-effector. (4.35) and (4.36) can be improved by introducing a damping gain $K_{dp\mathcal{A}}$ ($K_{dp\mathcal{A}} \geq \mathbf{0}$) to stabilize self-motions:

$$\begin{aligned}\ddot{q}_{\mathcal{A}} = J_e^T(J_eJ_e^T)^{-1}(\ddot{p}_e - \dot{J}_e\dot{q}_{\mathcal{A}}) - (I - J_e^T(J_eJ_e^T)^{-1}J_e)\\ M_{\mathcal{A}}^{-1}(C_{\mathcal{A}}\dot{q}_{\mathcal{A}} + G_{\mathcal{A}} + \tau_{d\mathcal{A}} - K_{dp\mathcal{A}}\dot{q}_{\mathcal{A}})\end{aligned} \tag{4.37}$$

and

$$\begin{aligned}\dot{q}_{\mathcal{A}}(k) = J_e^T(k)[J_e(k)J_e^T(k)]^{-1}\dot{p}_e(k) + \Big\{I - J_e^T(k)[J_e(k)\\ J_e^T(k)]^{-1}J_e(k)\Big\}\Big\{\{I - T_s[M_{\mathcal{A}}(q_{\mathcal{A}}(k))]^{-1}\\ [C_{\mathcal{A}}(q_{\mathcal{A}}(k), \dot{q}_{\mathcal{A}}(k-1))] + T_sK_{dp\mathcal{A}}\Big\}\dot{q}_{\mathcal{A}}(k-1)\\ - T_s[M_{\mathcal{A}}(q_{\mathcal{A}}(k))]^{-1}[G_{\mathcal{A}}(q_{\mathcal{A}}(k)) + \tau_{d\mathcal{A}}(k)]\Big\}.\end{aligned} \tag{4.38}$$

Eqs. (4.37) and (4.38) can be extended to other redundant robots. Additionally, for the HCDR-4 shown in Figure 3.10, two types of motion ($p_e =: [p_{ex}, p_{ey}, p_{ez}]^T$) are available to the end-effector, i.e.,

$$\begin{cases} p_{ez} = 0 & \text{in-plane motion} \\ p_{ez} \neq 0 & \text{out-of-plane motion} \end{cases} \tag{4.39}$$

where p_{ex}, p_{ey}, and p_{ez} represent the positions in the X-, Y-, and Z-directions (with respect to frame $\{O\}$). When $p_{ez} = 0$, the redundancy resolution problem can be solved by using (4.37) or (4.38). However, when $p_{ez} \neq 0$, the constraints of pendulums are needed to associate with (4.32), i.e., to balance reaction forces/moments generated by the movement of the robot arm. In this case, an equilibrium condition is considered via the following method: computing the nominal angles of pendulums (θ_{p1}, θ_{p2}) using the obtained

$(\theta_{a1}, \theta_{a2}, \theta_{a3})$ in the previous step, and the problem is described as

$$\begin{bmatrix} \theta_{p1} \\ \theta_{p2} \end{bmatrix} = \underset{\theta_{a1},\theta_{a2},\theta_{a3}}{\operatorname{argmin}} \left[\sum \mathcal{M}_y, \sum \mathcal{M}_x\right] \left[\sum \mathcal{M}_y, \sum \mathcal{M}_x\right]^T \tag{4.40a}$$

$$\text{s. t.} \sum \mathcal{M}_x = \mathcal{M}_{ax} - \mathcal{M}_{p1x} - \mathcal{M}_{p2x} \tag{4.40b}$$

$$\sum \mathcal{M}_y = \mathcal{M}_{ay} - \mathcal{M}_{p1y} - \mathcal{M}_{p2y} \tag{4.40c}$$

where $\mathcal{M}_{ax}$, $\mathcal{M}_{ay}$, $\mathcal{M}_{p1x}$, $\mathcal{M}_{p1y}$, $\mathcal{M}_{p2x}$, and $\mathcal{M}_{p2y}$ denote reaction moments of the robot arm and two pendulums to the mobile platform about its X- and Y-axes, respectively. These terms can be computed as

$$\begin{cases} \mathcal{M}_{ax} = \mathcal{M}_a^T [1,0,0]^T, \\ \mathcal{M}_{ay} = \mathcal{M}_a^T [0,1,0]^T, \\ \mathcal{M}_a \ = \sum\limits_{\ell=2}^{3} \Big((p_{a\ell} - p_{a(\ell-1)}) \times \sum\limits_{j=\ell}^{3} f_{a(j+1)} \Big) + (p_{a1} - [p_{mx}, p_{my}, p_{mz}]^T) \times \sum\limits_{j=1}^{3} f_{a(j+1)} \\ \qquad + \sum\limits_{j=2}^{3} \Big((p_{acj} - p_{a(j-1)}) \times f_{aj} \Big) + (p_{ac1} - [p_{mx}, p_{my}, p_{mz}]^T) \times f_{a1} \\ \qquad + \sum\limits_{j=1}^{3} R_{aj} \left(I_{aj} \dot{\omega}_{acj} + \omega_{acj} \times (I_{aj} \omega_{acj}) \right) \end{cases} \tag{4.41}$$

and

$$\begin{cases} \mathcal{M}_{pkx} = \mathcal{M}_{pk}^T [1,0,0]^T, \\ \mathcal{M}_{pky} = \mathcal{M}_{pk}^T [0,1,0]^T, \\ \mathcal{M}_{pk} \ = (p_{pck} - [p_{mx}, p_{my}, p_{mz}]^T) \times \Big(m_{pk} (\dot{v}_{pck} + [0, g, 0]^T) \Big) \\ \qquad\quad + R_x(\theta_{pk}) \left(I_{pk} \dot{\omega}_{pck} + \omega_{pck} \times (I_{pk} \omega_{pck}) \right), \quad \text{for } k = 1, 2 \end{cases} \tag{4.42}$$

where $f_{aj} = m_{aj}(\dot{v}_{acj} + [0, g, 0]^T)$, $R_{a1} = R_y(\theta_{a1})$, $R_{a2} = R_y(\theta_{a1}) R_z(\theta_{a2})$, $R_{a3} = R_y(\theta_{a1}) R_z(\theta_{a2}) R_z(\theta_{a3})$, and $f_{a4} = \mathbf{0}$. $[p_{mx}, p_{my}, p_{mz}]^T$ is the position vector of the COM of the mobile platform. For $j = 1, 2, 3$ and $k = 1, 2$, the position, linear velocity, and angular velocity vectors $p_{aj}, p_{acj}, p_{pck}, v_{acj}, v_{pck}, \omega_{acj}$, and ω_{pck} are obtained using the equations shown in Appendix A.4. The vectors of linear acceleration and angular acceleration $\dot{v}_{acj}, \dot{v}_{pck}, \dot{\omega}_{acj}$, and $\dot{\omega}_{pck}$ are time-derivatives of $v_{acj}, v_{pck}, \omega_{acj}$, and ω_{pck}, respectively. Other parameters such as $m_{aj}, I_{aj}, m_{pk}, I_{pk}$, and g are provided in Table 3.6. Eq. (4.40) is a nonlinear optimization problem and can be solved using nonlinear solvers (e.g., MATLAB function *fmincon* which is used for case studies in subsection 4.4.6).

4.4.3 Joint-Space Torque Optimization for Actuated and Unactuated Joints (TOAUJ)

The cost function (4.32a) is used to solve the redundancy resolution problem by minimizing actuated joint torques. However, when unactuated joints exist, minimum of actuated joint torques may not be guaranteed due to the coupled actuated and unactuated joints, e.g., disturbances resulting from unactuated joints. In this case, a new cost function is proposed to address this problem:

$$
\begin{aligned}
&\min_{\tau_{\mathcal{A}},\tau_{\mathcal{U}}\in\mathscr{S}_2} \ \Lambda = \frac{1}{2}\left\|M_{\mathcal{AU}}^{-1}[\tau_{\mathcal{A}}^T,\tau_{\mathcal{U}}^T]^T\right\|_2^2 && \text{(4.43a)}\\
&\text{s. t.} \ \ \mathscr{S}_2 = \Big\{ \text{argmin} \ \ddot{p}_e = J_e\ddot{q}_{\mathcal{A}} + \dot{J}_e\dot{q}_{\mathcal{A}} && \text{(4.43b)}\\
&\qquad\qquad \text{s. t.} \ \ \tau_{\mathcal{A}} = [F_{mx}, F_{my}, \tau_{a1}, \tau_{a2}, \tau_{a3}]^T && \text{(4.43c)}\\
&\qquad\qquad\qquad \tau_{\mathcal{U}} = [F_{mz}, M_{mx}, M_{my}]^T && \text{(4.43d)}\\
&\qquad\qquad\qquad F_{mx} = \tau_{m[1]}, F_{my} = \tau_{m[2]}, F_{mz} = \tau_{m[3]}, \\
&\qquad\qquad\qquad M_{mx} = \tau_{m[4]}, M_{my} = \tau_{m[5]} \Big\} && \text{(4.43e)}
\end{aligned}
$$

where $\tau_{\mathcal{A}}$, $\tau_{\mathcal{U}}$, and $M_{\mathcal{AU}}$ denote the actuated torque vector, unactuated torque vector, and combined inertia matrix, respectively. The forces (F_{mx}, F_{my}, F_{mz}) and torques $(M_{mx}, M_{my}, \tau_{a1}, \tau_{a2}, \tau_{a3})$ in (4.43e) of the mobile platform and robot arm are obtained using (4.32c) and (4.32d). Then, the new mapping from actuated and unactuated joints to the end-effector (velocity vector $\dot{p}_e$ and acceleration vector $\ddot{p}_e$) is computed as

$$
\begin{cases}
\dot{p}_e = [J_e, \mathbf{0}][\dot{q}_{\mathcal{A}}^T, \dot{q}_{\mathcal{U}}^T]^T \\
\ddot{p}_e = [J_e, \mathbf{0}][\ddot{q}_{\mathcal{A}}^T, \ddot{q}_{\mathcal{U}}^T]^T + [\dot{J}_e, \mathbf{0}][\dot{q}_{\mathcal{A}}^T, \dot{q}_{\mathcal{U}}^T]^T
\end{cases}
\tag{4.44}
$$

where $q_{\mathcal{A}} = [p_{mx}, p_{my}, \theta_{a1}, \theta_{a2}, \theta_{a3}]^T$, $\dot{q}_{\mathcal{A}} = [\dot{p}_{mx}, \dot{p}_{my}, \dot{\theta}_{a1}, \dot{\theta}_{a2}, \dot{\theta}_{a3}]^T$, $\ddot{q}_{\mathcal{A}} = [\ddot{p}_{mx}, \ddot{p}_{my}, \ddot{\theta}_{a1}, \ddot{\theta}_{a2}, \ddot{\theta}_{a3}]^T$, $q_{\mathcal{U}} := [p_{mz}, \alpha_m, \beta_m]^T$, $\dot{q}_{\mathcal{U}} := [\dot{p}_{mz}, \dot{\alpha}_m, \dot{\beta}_m]^T$, and $\ddot{q}_{\mathcal{U}} := [\ddot{p}_{mz}, \ddot{\alpha}_m, \ddot{\beta}_m]^T$ represent the actuated and unactuated vectors of generalized coordinates, velocities, and accelerations, respectively.

One can also conduct the Lagrangian function (in the form of (4.33)) to solve (4.43) and the discrete solution is described as

$$
\begin{aligned}
\begin{bmatrix} \dot{q}_{\mathcal{A}}(k) \\ \dot{q}_{\mathcal{U}}(k) \end{bmatrix} = \begin{bmatrix} J_e^{+}\dot{p}_e(k) \\ \mathbf{0} \end{bmatrix} &+ \begin{bmatrix} \tilde{J}_e(I_{5\times5} + T_sK_{dp\mathcal{A}}) & \mathbf{0} \\ \mathbf{0} & I_{3\times3} + T_sK_{dp\mathcal{U}} \end{bmatrix} \\
&\begin{bmatrix} \dot{q}_{\mathcal{A}}(k-1) \\ \dot{q}_{\mathcal{U}}(k-1) \end{bmatrix} - \begin{bmatrix} \tilde{J}_e & \mathbf{0} \\ \mathbf{0} & I_{3\times3} \end{bmatrix} T_sM_{\mathcal{AU}}^{-1} \begin{bmatrix} F_{\mathcal{A}} \\ F_{\mathcal{U}} \end{bmatrix}
\end{aligned}
\tag{4.45}
$$

with

$$\tilde{J}_e := I_{5\times 5} - J_e^{+}(k)J_e(k) \tag{4.46a}$$

$$\begin{aligned} F_{\mathcal{A}} &:= [C(q(k),\dot{q}(k-1))]_{[1,2,9:11]}\dot{q}_{\mathcal{A}}(k-1) \\ &\quad +[G(q(k))+\tau_d(k)]_{[1,2,9:11]} \end{aligned}$$

$$F_{\mathcal{U}} := [C(q(k),\dot{q}(k-1))]_{[3:5]}\dot{q}_{\mathcal{U}}(k-1) \tag{4.46b}$$

$$\quad +[G(q(k))+\tau_d(k)]_{[3:5]} \tag{4.46c}$$

where J_e^{+} is the pseudoinverse of matrix J_e. Finally, (4.45) can be rearranged as

$$\begin{aligned} \dot{q}_{\mathcal{A}}(k) &= J_e^{+}\dot{p}_e(k) + \tilde{J}_e(I + T_s K_{dp\mathcal{A}})\dot{q}_{\mathcal{A}}(k-1) \\ &\quad -T_s(I_{5\times 5} - J_e^{+}J_e)\Xi_{\mathcal{A}} \end{aligned} \tag{4.47a}$$

$$\dot{q}_{\mathcal{U}}(k) = (I_{3\times 3} + T_s K_{dp\mathcal{U}})\dot{q}_{\mathcal{U}}(k-1) - T_s\Xi_{\mathcal{U}} \tag{4.47b}$$

with

$$\begin{bmatrix} M_{\mathcal{AU}}^{\mathcal{AA}} & M_{\mathcal{AU}}^{\mathcal{AU}} \\ M_{\mathcal{AU}}^{\mathcal{UA}} & M_{\mathcal{AU}}^{\mathcal{UU}} \end{bmatrix} := \begin{bmatrix} M_{\mathcal{AU}[1,2,6:8][1,2,6:8]}(k), & M_{\mathcal{AU}[1,2,6:8][3:5]}(k) \\ M_{\mathcal{AU}[3:5][1,2,6:8]}(k), & M_{\mathcal{AU}[3:5][3:5]}(k) \end{bmatrix} \tag{4.48a}$$

$$\begin{aligned} \Xi_{\mathcal{A}} &:= \left[M_{\mathcal{AU}}^{\mathcal{AA}} - M_{\mathcal{AU}}^{\mathcal{AU}}\left(M_{\mathcal{AU}}^{\mathcal{UU}}\right)^{-1}M_{\mathcal{AU}}^{\mathcal{UA}}\right]^{-1} \\ &\quad \left[I_{5\times 5}, -M_{\mathcal{AU}}^{\mathcal{AU}}\left(M_{\mathcal{AU}}^{\mathcal{UU}}\right)^{-1}\right]\begin{bmatrix} F_{\mathcal{A}} \\ F_{\mathcal{U}} \end{bmatrix} \end{aligned} \tag{4.48b}$$

$$\begin{aligned} \Xi_{\mathcal{U}} &:= \left[M_{\mathcal{AU}}^{\mathcal{UU}} - M_{\mathcal{AU}}^{\mathcal{UA}}\left(M_{\mathcal{AU}}^{\mathcal{AA}}\right)^{-1}M_{\mathcal{AU}}^{\mathcal{AU}}\right]^{-1} \\ &\quad \left[-M_{\mathcal{AU}}^{\mathcal{UA}}\left(M_{\mathcal{AU}}^{\mathcal{AA}}\right)^{-1}, I_{3\times 3}\right]\begin{bmatrix} F_{\mathcal{A}} \\ F_{\mathcal{U}} \end{bmatrix} \end{aligned} \tag{4.48c}$$

where (4.47) is a complete expression that can solve the redundancy resolution problem (using (4.47a) for actuated joints) as well as disturbance rejection (using (4.47b) for unactuated joints).

4.4.4 Algorithms of the TOAJ and TOAUJ

To implement the formulas (TOAJ and TOAUJ) in subsection 4.4.2 and subsection 4.4.3, here, the corresponding algorithms (shown in Algorithm 4) are proposed as follows: first, two desired end-effector points (positions $p_{er(i-1)} \rightarrow p_{eri}$ and velocities $\dot{p}_{er(i-1)} \rightarrow \dot{p}_{eri}$) and joint-space disturbances τ_d are given. The goal is to solve the redundancy resolution problem (i.e., generate an array of actuated joint-space positions/angles and velocities $q_{\mathcal{A}}(1:N+1), \dot{q}_{\mathcal{A}}(1:N+1)$) and reject disturbances. In Step 3 and Step 4, the trajectories of $\dot{p}_e(k)$ and $\ddot{p}_e(k)$ can be generated using different methods, e.g., (4.51) in subsection 4.4.6. After completing the iteration, finally, $q_{\mathcal{A}}(1:N+1), \dot{q}_{\mathcal{A}}(1:N+1)$ are obtained. The generated data also provides reference states for online control. Additionally, in Step 9, for the TOAJ, let $K_{dp\mathcal{U}}$ be $\mathbf{0}$ (indicating TOAJ mode) to compare the performance of TOAJ and TOAUJ.

4.4.5 Control Design

The joint-space states $(q_{\mathcal{A}}, \dot{q}_{\mathcal{A}}, \theta_{p1}, \theta_{p2})$ can be obtained by using Algorithm 4. One of the advantages of this process is that the state data can be generated offline to reduce the computation cost, particularly, on embedded systems. In this section, one can consider control design by applying the offline data.

The online control objective is to track the reference trajectory. To achieve this goal, the proposed nonlinear control law u is designed as

$$\begin{aligned} u = \operatorname{diag}(A^{-1}_{m[1,2][3,4]}, I_{2\times2}, I_{3\times3})\Big\{ & K_{\mathcal{A}p} e_{\mathcal{A}} + K_{\mathcal{A}d}\dot{e}_{\mathcal{A}} \\ & + K_{\mathcal{A}i}\int_0^t e_{\mathcal{A}} dt \Big\} \end{aligned} \tag{4.49}$$

where $K_{\mathcal{A}p}$, $K_{\mathcal{A}d}$, and $K_{\mathcal{A}i}$ are positive gains. The error vector between the reference and measured values is defined as

$$e_{\mathcal{A}} = [p_{mx}, p_{my}, \theta_{p1}, \theta_{p2}, \theta_{a1}, \theta_{a2}, \theta_{a3}]^T - [\hat{p}_{mx}, \hat{p}_{my}, \hat{\theta}_{p1}, \hat{\theta}_{p2}, \hat{\theta}_{a1}, \hat{\theta}_{a2}, \hat{\theta}_{a3}]^T. \tag{4.50}$$

$\dot{e}_{\mathcal{A}}$ is the time-derivative of $e_{\mathcal{A}}$ denoting velocity errors. Regarding subsection 3.5.3, one can also get $u = [\delta T_3, \delta T_4, \tau_{p1}, \tau_{p2}, \tau_{a1}, \tau_{a2}, \tau_{a3}]^T$, so the controller (4.49) has the following abilities: damp in-plane vibrations using lower cable tensions $(\delta T_3, \delta T_4)$, eliminate out-of-plane motions of the platform $q_{\mathcal{U}}$ using the torques of two pendulums (τ_{p1}, τ_{p2}), and generate joint torques $(\tau_{a1}, \tau_{a2}, \tau_{a3})$ for the rigid robot arm. In this way, the controller (4.49) attempts to minimize the tracking errors over time by adjusting u.

Algorithm 4 TOAJ and TOAUJ implementation to solve the redundancy resolution problem and disturbance rejection via joint-space torque optimization.

```
Input: $p_{er(i-1)}, \dot{p}_{er(i-1)}, p_{eri}, \dot{p}_{eri}$.
Output: $q_{\mathcal{A}}(1:N+1), \dot{q}_{\mathcal{A}}(1:N+1)$.
Initialize $q(1), \dot{q}(1), p_e(1) = p_{er(i-1)}, \dot{p}_e(1) = \dot{p}_{er(i-1)}, p_e(N+1) = p_{eri}, \dot{p}_e(N+1) = \dot{p}_{eri}$;
for $k = 1$ to $N+1$ do    ▷ Trajectory generation from point $(p_{er(i-1)}, \dot{p}_{er(i-1)})$ to point $(p_{eri}, \dot{p}_{eri})$.
    $\dot{p}_e(k) = g_v(p_{eri}, p_e(k)), p_e(1) = p_{er(i-1)}$;    ▷ $g_v(p_{eri}, p_e(k))$ is a velocity function, e.g., (4.51).
    $\ddot{p}_e(k) = g_a(\dot{p}_{eri}, \dot{p}_e(k)), \dot{p}_e(1) = \dot{p}_{er(i-1)}$;    ▷ $g_a(\dot{p}_{eri}, \dot{p}_e(k))$ is an acceleration function, e.g., (4.51).
    Compute $[M(q(k))]_{11\times 11}, [C(q(k), \dot{q}(k-1))]_{11\times 11}, [G(q(k))]_{11\times 1}$ using (3.69);
      $\rightarrow M_{\mathcal{A}\mathcal{U}} = [M(q(k))]_{[1:5,9:11][1:5,9:11]}, [C(q(k), \dot{q}(k-1))]_{[1:5,9:11][1:5,9:11]}, [G(q(k))]_{[1:5,9:11]}$ in (4.48a);
      ▷ $[p_{mx}, p_{my}, \theta_{a1}, \theta_{a2}, \theta_{a3}]^T_{5\times 1} = q_{\mathcal{A}}, [\dot{p}_{mx}, \dot{p}_{my}, \dot{\theta}_{a1}, \dot{\theta}_{a2}, \dot{\theta}_{a3}]^T_{5\times 1} = \dot{q}_{\mathcal{A}}$,
        $[p_{mz}, \alpha_m, \beta_m]^T_{3\times 1} = q_{\mathcal{U}}, [\dot{p}_{mz}, \dot{\alpha}_m, \dot{\beta}_m]^T_{3\times 1} = \dot{q}_{\mathcal{U}}$,
        $q = [p_{mx}, p_{my}, p_{mz}, \alpha_m, \beta_m, 0, \theta_{p1}, \theta_{p2}, \theta_{a1}, \theta_{a2}, \theta_{a3}]^T_{11\times 1}$,
        $\dot{q} = [\dot{p}_{mx}, \dot{p}_{my}, \dot{p}_{mz}, \dot{\alpha}_m, \dot{\beta}_m, 0, 0, 0, \dot{\theta}_{a1}, \dot{\theta}_{a2}, \dot{\theta}_{a3}]^T_{11\times 1}$.
    Calculate $J_e(q_{\mathcal{A}}(k)), J_e^{+}(q_{\mathcal{A}}(k))$ using (3.69);
    $A_m T \leftarrow (p_{mx}(k), p_{my}(k))$ using (3.70);
    $\dot{q}_{\mathcal{A}}(k) \leftarrow \dot{p}_e(k), \dot{q}_{\mathcal{A}}(k-1)$ using (4.47a);
    $\dot{q}_{\mathcal{U}}(k) \leftarrow \dot{q}_{\mathcal{U}}(k-1)$ using (4.47b);    ▷ For the TOAJ, let $K_{dp\mathcal{U}} = \mathbf{0}$.
    $\theta_{p1}(k+1), \theta_{p2}(k+1) \leftarrow \theta_{a1}(k), \theta_{a2}(k), \theta_{a3}(k)$ using (4.40);
        ▷ Compute the nominal angles of the pendulums.
    $\begin{cases} \Lambda = \frac{1}{2}\left\| M_{\mathcal{A}\mathcal{U}}^{-1}[\tau_{\mathcal{A}}^T, \tau_{\mathcal{U}}^T]^T \right\|_2^2 \leftarrow \\ \begin{cases} \ddot{q}_{\mathcal{A}}(k) = [J_e^{+}(q_{\mathcal{A}}(k))] \left\{ \ddot{p}_e(k) - [\dot{J}_e(q_{\mathcal{A}}(k), \dot{q}_{\mathcal{A}}(k-1))]\dot{q}_{\mathcal{A}}(k-1) \right\}, \\ \begin{bmatrix} \tau_{\mathcal{A}} \\ \tau_{\mathcal{U}} \end{bmatrix} = M_{\mathcal{A}\mathcal{U}}^{-1} \begin{bmatrix} \ddot{q}_{\mathcal{A}}(k) \\ \ddot{q}_{\mathcal{U}}(k) \end{bmatrix} + \begin{bmatrix} F_{\mathcal{A}} \\ F_{\mathcal{U}} \end{bmatrix} \text{ using (4.46) and (4.47);} \end{cases} \end{cases}$
    $\begin{cases} q_{\mathcal{A}}(k+1) = q_{\mathcal{A}}(k) + \dot{q}_{\mathcal{A}}(k) T_s, \\ q_{\mathcal{U}}(k+1) = q_{\mathcal{U}}(k) + \dot{q}_{\mathcal{U}}(k) T_s; \end{cases}$    ▷ Discrete integration.
    $(\cdot)_j = \begin{cases} (\cdot)_{j\,\max}, & \text{if } (\cdot)_j \geq (\cdot)_{j\,\max},\ j \in [1, 11], \\ (\cdot)_{j\,\min}, & \text{if } (\cdot)_j \leq (\cdot)_{j\,\min},\ j \in [1, 11], \end{cases}$    $(\cdot) := q(k+1),\ \dot{q}(k+1),$ or $\delta\dot{q}(k+1) = \dot{q}(k+1) - \dot{q}(k)$;
    $p_e(k+1) \leftarrow q_{\mathcal{A}}(k+1)$;    ▷ The computation of $p_e$ is shown in Appendix A.4.
    if $\|p_{eri} - p_e(k+1)\| < \varepsilon_{\mathcal{A}}$ then
        $i = i + 1$;    ▷ Switch to the next planning point $(p_{er(i+1)}, \dot{p}_{er(i+1)})$.
    end if
end for
Return $q_{\mathcal{A}}(1:N+1), \dot{q}_{\mathcal{A}}(1:N+1)$.
```

4.4.6 Simulation Results

To evaluate the performance of section 4.4 and subsection 4.4.5, the following cases will be studied. All the scenarios are implemented using MATLAB 2019a (The MathWorks, Inc.)

on a Windows 7 x64 desktop PC (Inter Core i7-4770, 3.4 GHz CPU and 8 GB RAM).

4.4.6.1 Scenario 1: Point-to-Point Trajectory

The end-effector trajectory conducted by a normalized polynomial (here, one of trajectory generation methods and constraints that have been applied in practice in [38, 82] are utilized for case studies) from Cartesian point $(p_{er(i-1)}, \dot{p}_{er(i-1)})$ to Cartesian point $(p_{eri}, \dot{p}_{eri})$ is given as follows:

$$\begin{cases} N = \frac{t_i - t_{i-1}}{t_s}, \eta = \frac{k}{N}, k \in [1, N+1] \\ \rho_r = p_{er(i-1)} + (p_{eri} - p_{er(i-1)})(6\eta^5 - 15\eta^4 + 10\eta^3) \\ \dot{\rho}_r = \frac{p_{eri} - p_{er(i-1)}}{t_i - t_{i-1}}(30\eta^4 - 60\eta^3 + 30\eta^2) \\ \ddot{\rho}_r = \frac{p_{eri} - p_{er(i-1)}}{t_i - t_{i-1}}(120\eta^3 - 180\eta^2 + 60\eta) \\ \dot{p}_e(k) = \dot{\rho}_r + 10(\rho_r - p_e(k)) \\ \ddot{p}_e(k) = \ddot{\rho}_r + 10(\dot{\rho}_r - \dot{p}_e(k)) \end{cases} \tag{4.51}$$

where the start time t_{i-1}, end time t_i, and sampling time t_s are supposed to be 0 s, 1 s, and 0.0002 s, respectively. Let the positions and velocities of Cartesian points $p_{er(i-1)} = [0, 0.334, 0]^T$ m, $p_{eri} = [0.35, 0.5, 0.1]^T$ m, $\dot{p}_{er(i-1)} = [0, 0, 0]^T$ m/s, and $\dot{p}_{eri} = [0, 0, 0]^T$ m/s, respectively. The damping gain $K_{dp\mathcal{A}} = \mathrm{diag}(500, 500, 500, 500, 500)$. Furthermore, the constraints are also given as $\dot{q}_{\mathcal{A}\max} = [3 \text{ m/s}, 3 \text{ m/s}, 25 \text{ rad/s}, 25 \text{ rad/s}, 25 \text{ rad/s}]^T$, $\dot{q}_{\mathcal{A}\min} = -[3 \text{ m/s}, 3 \text{ m/s}, 25 \text{ rad/s}, 25 \text{ rad/s}, 25 \text{ rad/s}]^T$, $\delta\dot{q}_{\mathcal{A}\max} = [30 \text{ m/s}, 30 \text{ m/s}, 250 \text{ rad/s}, 250 \text{ rad/s}, 250 \text{ rad/s}]^T$, and $\delta\dot{q}_{\mathcal{A}\min} = -[30 \text{ m/s}, 30 \text{ m/s}, 250 \text{ rad/s}, 250 \text{ rad/s}, 250 \text{ rad/s}]^T$. There are no constraints to $\dot{q}_{\mathcal{U}}$ and $\delta\dot{q}_{\mathcal{U}}$. Then, Algorithm 4 is implemented, and the following performance indices of the TOAJ and TOAUJ are compared.

The results in Figure 4.15 and Figure 4.16 show Cartesian positions and velocities of the end-effector and trajectory responses of the HCDR-4 by given the start point $p_{er(i-1)} = [0, 0.334, 0]^T$ m and the end point $p_{eri} = [0.35, 0.5, 0.1]^T$ m, respectively. The corresponding redundancy resolution of the actuated joints is shown in Figure 4.17. Clearly, using TOAJ and TOAUJ one can get smooth trajectory and redundancy resolution responses. Compared to TOAJ, TOAUJ shows a better performance in contributing to avoiding singularity, i.e., θ_{a3} is not close to zero when the HCDR-4 moves to the end point p_{eri}.

In Figure 4.18, 20 N, 2 Nm, and 2 Nm pulse disturbances (from 0.1 s to 0.3 s) are given to three unactuated joints, respectively. The results show that the force/torque responses (F_{mz}, M_{mx}, and M_{my}) of the unactuated joints TOAUJ are able to stabilize unactuated

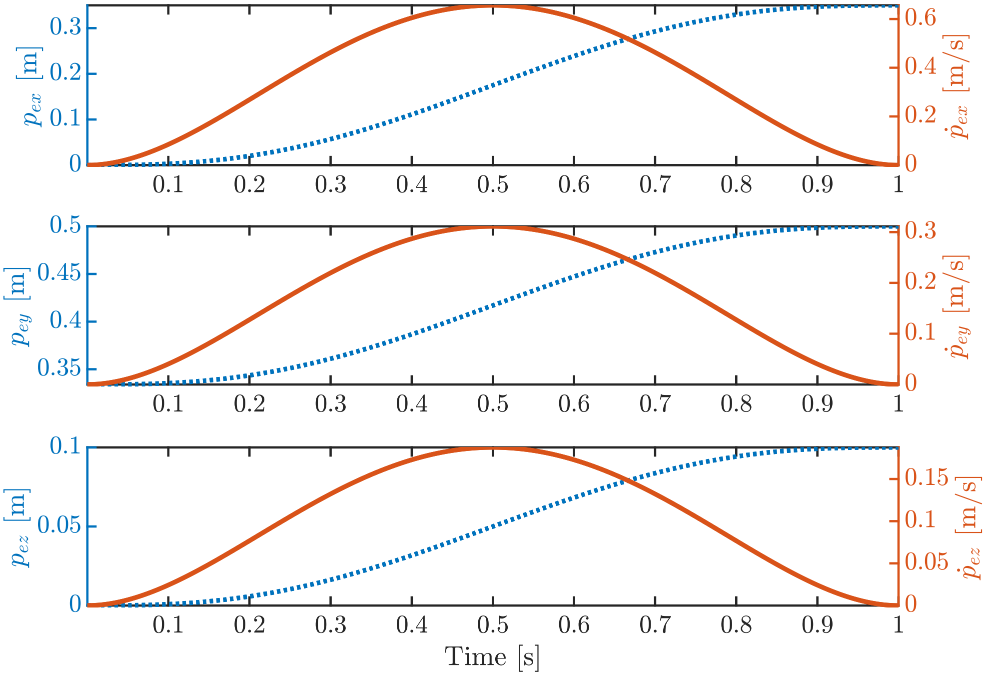

Figure 4.15: Cartesian positions and velocities of the end-effector.

joints motions, while TOAJ can not; meanwhile, these results are validated by the state responses of the unactuated joints (shown in Figure 4.19).

Additionally, to evaluate the error performance $\left(\frac{1}{N}\sum_{k=1}^{N}\|\dot{p}_e - J_e\dot{q}_{\mathcal{A}}\|_2^2\right)^{1/2}$ by using different methods (with the same setup), i.e., in comparison with the minimum weighted torque norm in [55, 71, 38] and the proposed approaches (TOAJ and TOAUJ), and the results are shown in Figure 4.20. Clearly, the errors via TOAJ and TOAUJ are much less than that of [55, 71, 38]. The results also verify the effectiveness of the proposed methods.

4.4.6.2 Scenario 2: Point-to-Point Trajectory with the Controller

In order to evaluate the performance of point-to-point trajectory with the controller, here, the generated trajectory states (as reference states) shown in Figure 4.17 are applied to the controller (4.49). In this scenario, the gains of the controller (4.49) are given as follows: $K_{\mathcal{A}p} = \mathrm{diag}(1, 1, 0.001, 0.001, 1.5, 1.8, 1.5)$, $K_{\mathcal{A}d} = \mathrm{diag}(10, 30, 0.1, 0.1, 0.05, 0.09, 0.05)$, and $K_{\mathcal{A}i} = \mathrm{diag}(1, 1, 0.1, 0.1, 2, 6.75, 5)$.

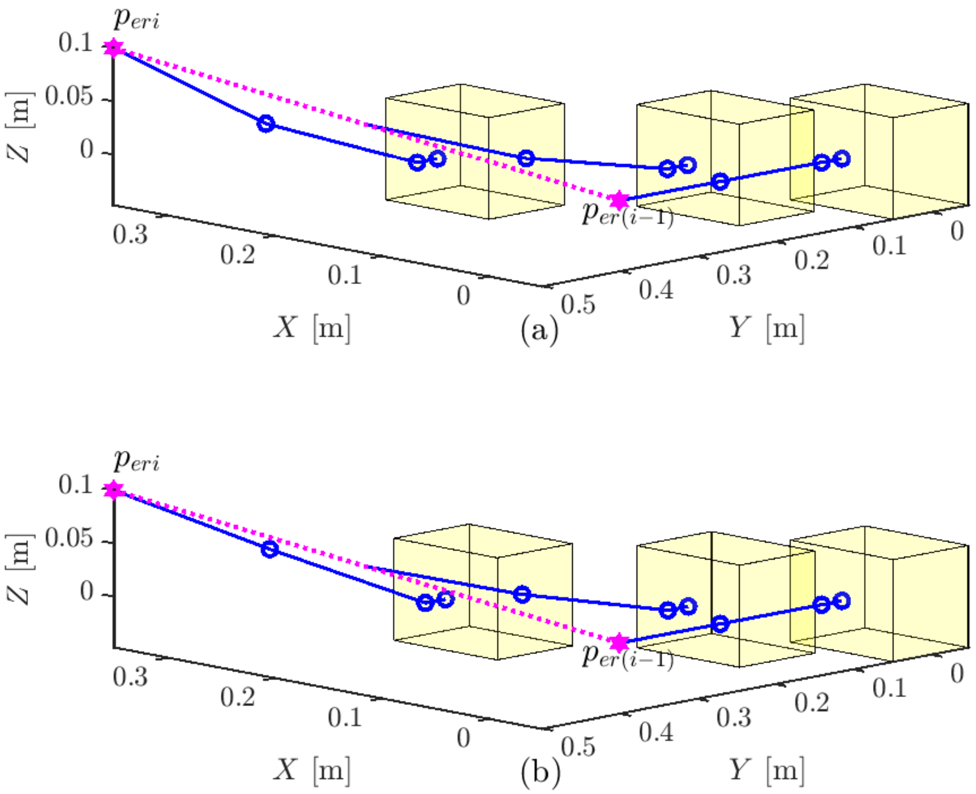

Figure 4.16: Trajectory responses of the HCDR-4 by given the start point $p_{er(i-1)} = [0, 0.334, 0]^T$ m and the end point $p_{eri} = [0.35, 0.5, 0.1]^T$ m, where the *yellow cube*, *blue lines*, *blue circles*, and *magenta dotted line* represent the mobile platform (cables are not displayed here), links of the robot arm, joints of the robot arm, and trajectory of the end-effector, respectively. (a) TOAJ and (b) TOAUJ.

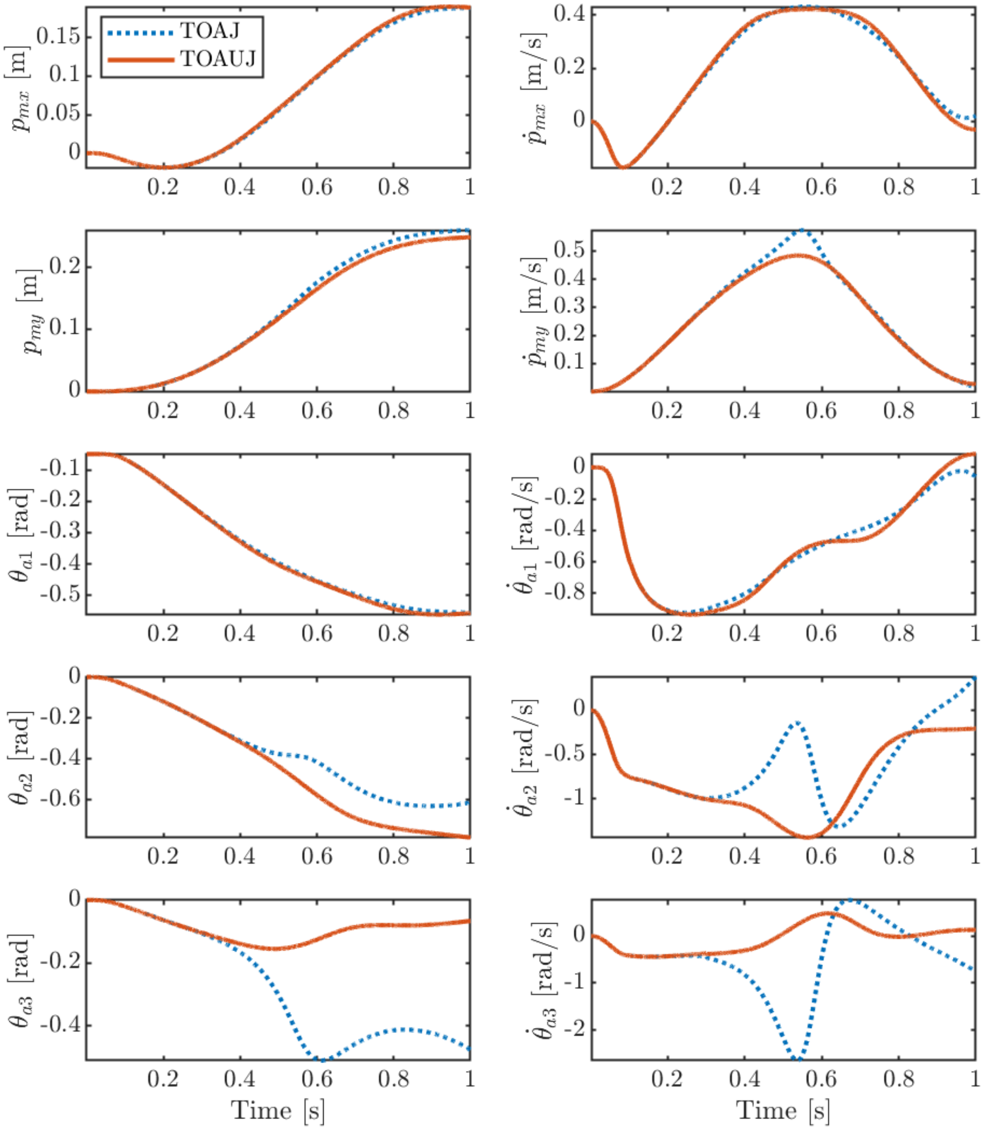

Figure 4.17: Redundancy resolution of the actuated joints.

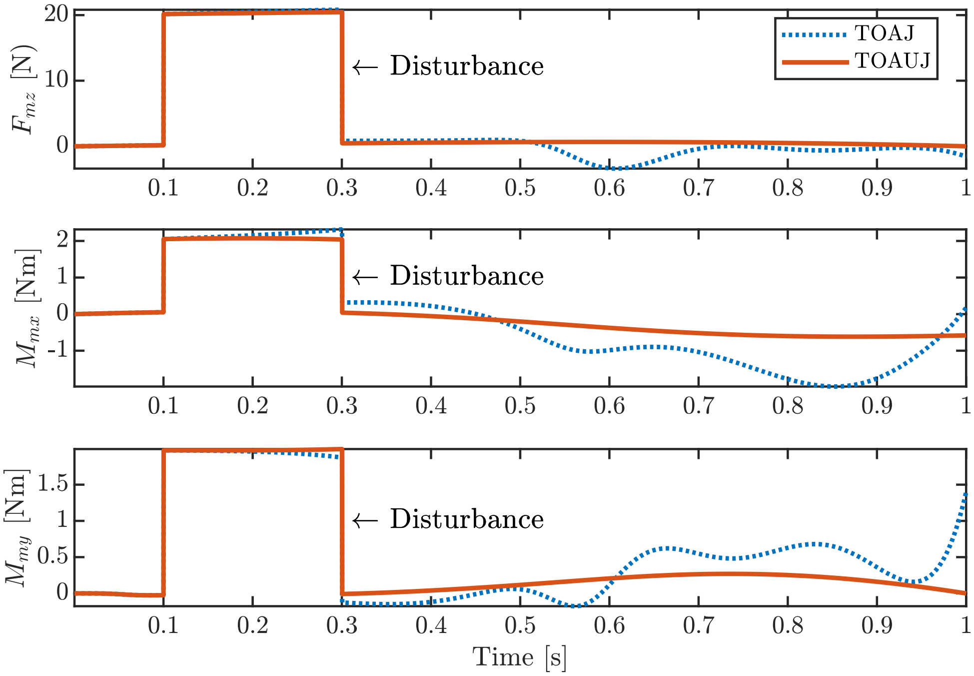

Figure 4.18: Force/torque responses of the unactuated joints.

Accordingly, the position tracking performance of the end-effector with the controller (4.49) shown in Figure 4.21 indicates the following results: the tracking errors between the reference position (p_{ex}, p_{ey}, p_{ez}) and the measured position $(\hat{p}_{ex}, \hat{p}_{ey}, \hat{p}_{ez})$ are small, while TOAUJ-based method holds a better tracking performance than that of TOAJ. Meanwhile, the controller (4.49) can also help position control by collaborating with the TOAJ-based and TOAUJ-based approaches.

4.5 Summary

To achieve the objective of reducing vibrations and improving the accuracy of the generalized HCDR, three types of control architecture are developed using HCDR-1. The proposed optimization problem (3.32) and Algorithm 1 provide an improvement over the existed stiffness optimization approaches in [57, 76, 52, 53]. Meanwhile, they can be applied to not only CDPRs but also HCDRs.

Additionally, based on the decoupled in-plane and out-of-plane models presented in section 3.3, two MPCs are utilized: the first is used to control the lower-cable tensions

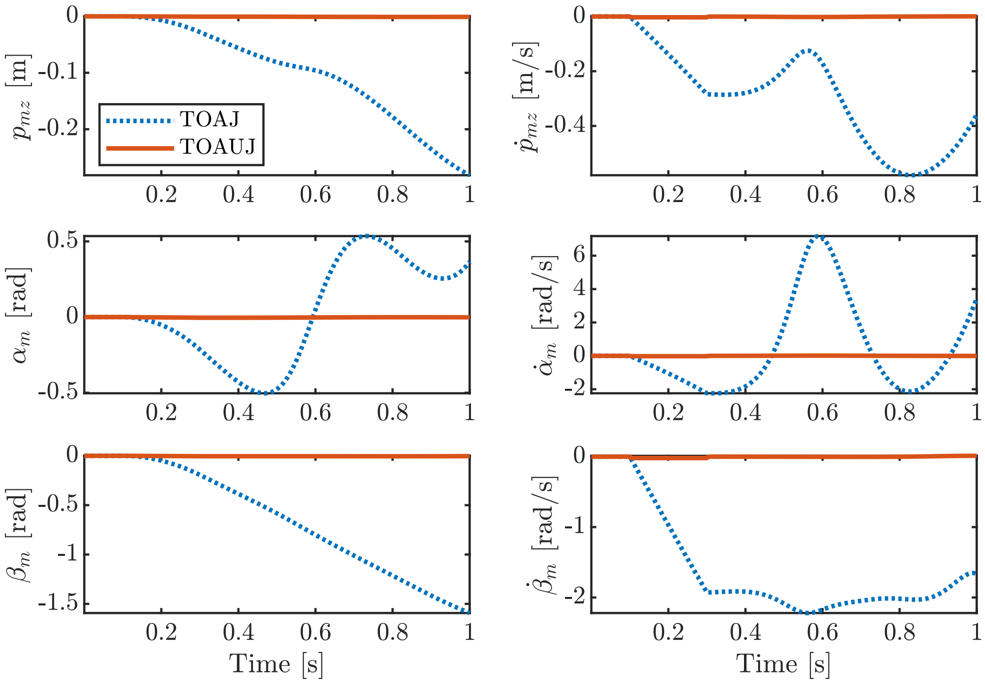

Figure 4.19: State responses of the unactuated joints.

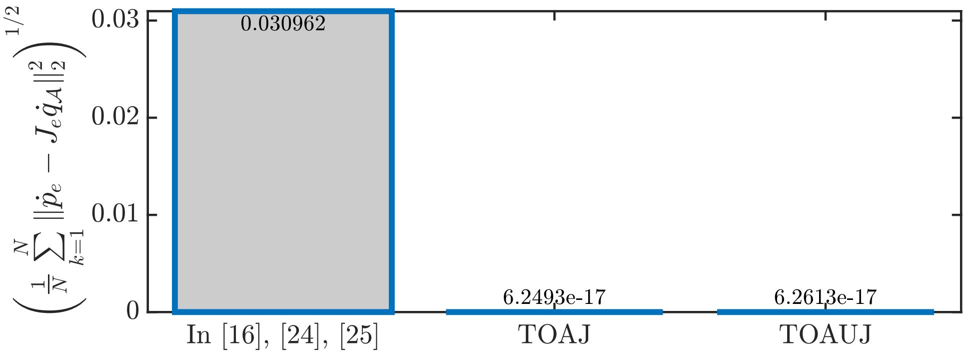

Figure 4.20: Error performance by using different methods.

to damp out in-plane vibrations, the second is utilized to control pendulum torques to eliminate out-of-plane moving. To overcome the inaccurate limitation of IMU to observe states, new in-plane and out-of-plane state estimation methods are also proposed, and results are satisfactory.

Based on the dynamic model of the UMM, two control architectures are developed:

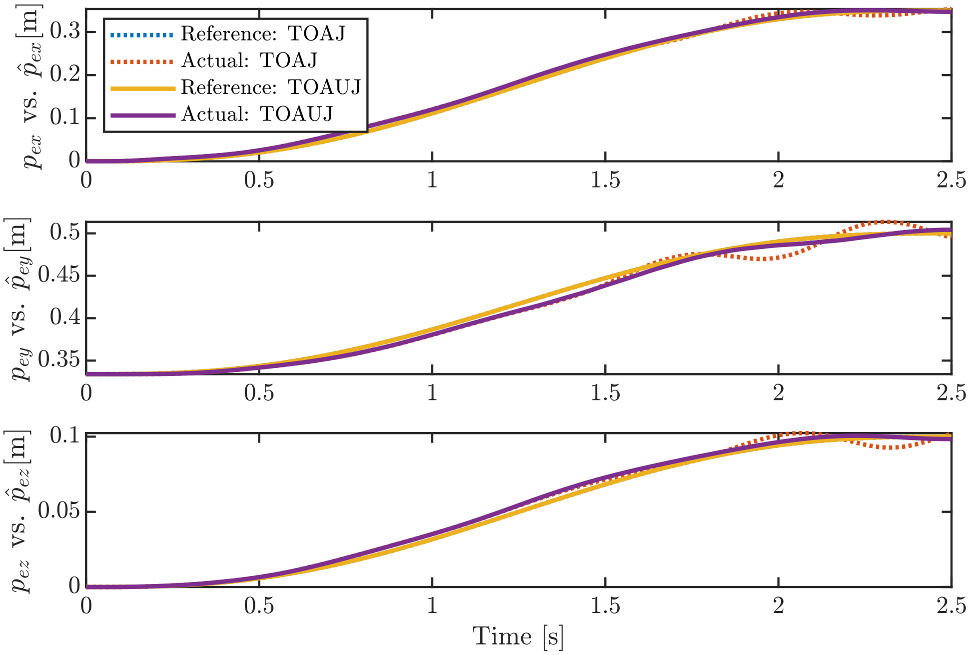

Figure 4.21: Position tracking performance of the end-effector with the controller (4.49).

MPC with integral action and MPC+PI with integral action, and they can also be applied to other recent robotic systems. Compared to other MPC-based control strategies, the proposed controllers are easier to implement in practice.

Finally, based on the reduced dynamic model of the HCDR-4, two new methods are proposed to solve redundancy resolution: joint-space TOAJ and joint-space TOAUJ. The algorithms of the TOAJ and TOAUJ are also evaluated.

Chapter 5

Experimental Results

Experiments are conducted on the platforms shown in Figure 3.3 and Figure 3.6 to evaluate the performance of the proposed control methods in Chapter 4.

5.1 Experimental Setup

As described in Chapter 3, HCDR-2 (see subsection 3.3.1) is the decoupled configuration based on the existing HCDR prototype. HCDR-3 (see subsection 3.4.1) includes an additional slider to extend out-of-plane motion and manipulation tasks. The experimental setup is provided in Figure 5.1[1], where the view of the whole setup, bottom view, and top view are shown in Figure 5.1(a)–Figure 5.1(c), respectively. A Beckhoff CX2040 controller is used to power both HCDR-2 and HCDR-3. They are connected to the control cabinet via power and fieldbus (CAN bus) cables. A camera (Logitech) is utilized to provide the absolute position reference for the mobile platform (one main reason is that the absolute positions of the top and bottom actuators will be lost when they are turned off). In addition, force sensors (Transducer Techniques, TLL-1K) are used to measure lower-cable tensions for in-plane state estimation (see subsubsection 4.2.4.1). An IMU provides acceleration and velocity signals for out-of-plane state estimation (see subsubsection 4.2.4.2). Each pendulum is actuated by a servo motor (Beckhoff, AM8131-0F20-0000). The linear slider is actuated by a stepper motor (Nema 17, 42 mm) with an encoder (Avago, HEDS-5540 I06). The actual position can be recorded using a measurement system (Krypton RODYM 6D), such as for verifying the effectiveness of estimators (shown in subsection 4.2.4).

---

[1] In Figure 5.1, the experimental setup of HCDR-3 is provided. This experimental setup can be used for HCDR-2 by removing the slider.

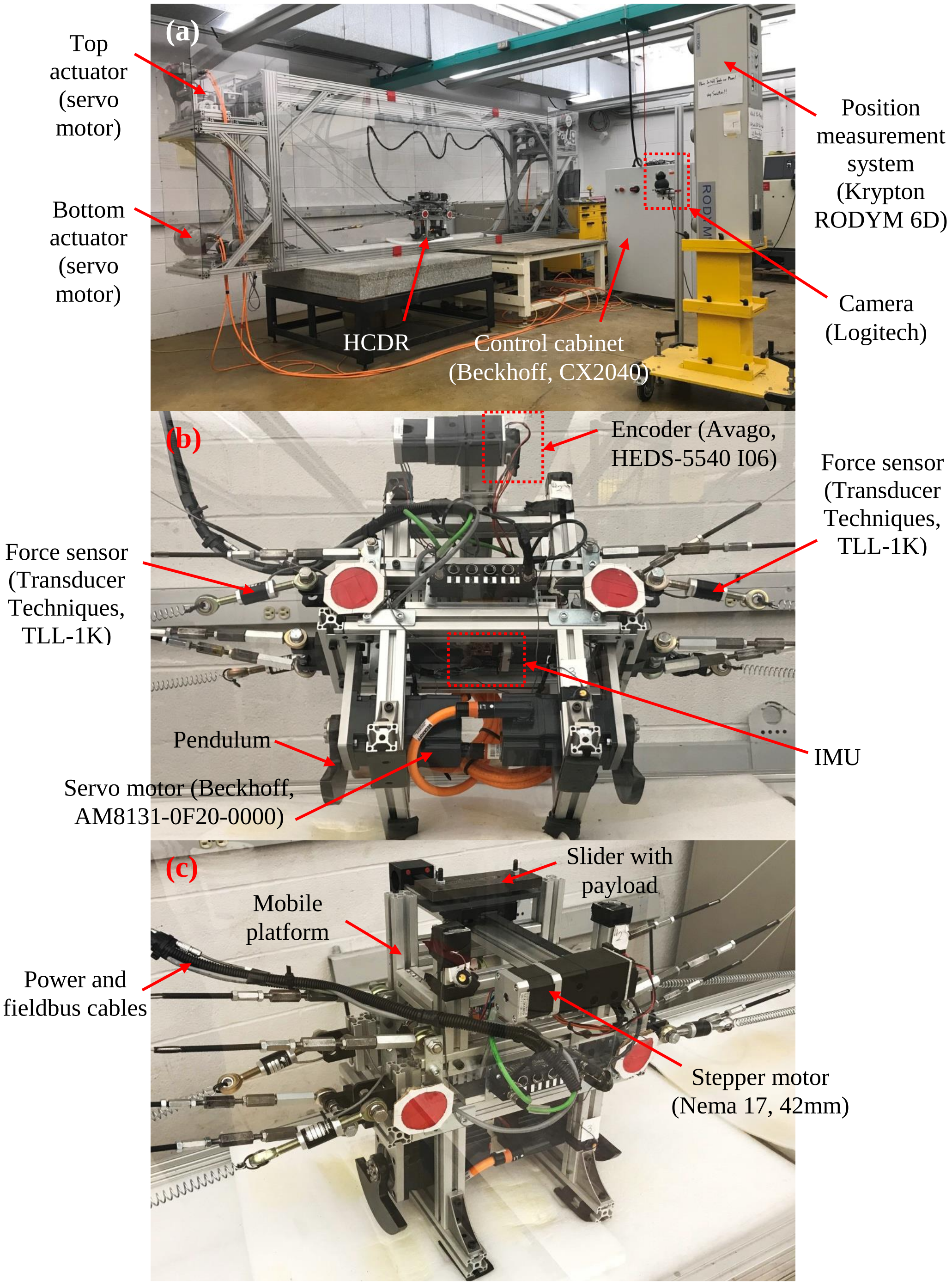

Figure 5.1: Experimental setup. (a) View of the whole experimental setup, (b) bottom view, and (c) top view.

Table 5.1: MPC Tuning Parameters for Experiments

Control structures	Parameters
In-plane MPC	$T_s = 0.01$ s (sampling time); $\Delta T = 0.03$ s (interval time); $N_p = 5$ (predictive horizon); $R_p = \text{diag}([0.0004, 0.0004])$ (input weighting matrix); $Q_p = \text{diag}([1, 1, 1, 1, 1, 1])$ (state weighting matrix); $P_p = \text{diag}([1, 1, 1, 1, 1, 1])$ (terminal weighting matrix); $\delta x_{inpL} = -[\infty, \infty]^T$(lower bound); $\delta x_{inpU} = [\infty, \infty]^T$(upper bound); $\delta u_{inpL} = -[10, 10]^T$(lower bound); $\delta u_{inpU} = [10, 10]^T$(upper bound).
Out-of-plane MPC	$T_s = 0.01$ s; $\Delta T = 0.01$ s; $N_p = 5$; $R_p = \text{diag}([10, 10])$; $Q_p = \text{diag}([0.1, 0.1, 1, 1, 1, 1, 1, 1, 1, 1])$; $P_p = \text{diag}([0.1, 0.1, 1, 1, 1, 1, 1, 1, 1, 1])$; $\delta x_{mL} = -[\infty, \infty]^T$; $\delta x_{mU} = [\infty, \infty]^T$; $\delta u_{mL} = -[0.23, 0.23]^T$; $\delta u_{mU} = [0.23, 0.23]^T$.

5.2 Experimental Results of the Decoupled System[2]

In this section, the decoupled system HCDR-2 (see Figure 3.3) is used for experiments. The operation points shown in Figure 4.7 are also utilized to evaluate the control performance in experiments.

5.2.1 In-Plane Position-Holding Performance

For the in-plane case studies, two cases are conducted: 1) with no extra load on the mobile platform and 2) with a 6 kg extra load mounted on it to show position-holding performance under disturbances. The system performance points P_2 and P_4 (given in Figure 4.7) are considered as an example for discussion.

---

[2] Parts of this section have been published in [92]. © 2019 Elsevier B.V.: "As the author of this Elsevier article, you retain the right to include it in a thesis or dissertation, provided it is not published commercially. Permission is not required, but please ensure that you reference the journal as the original source."

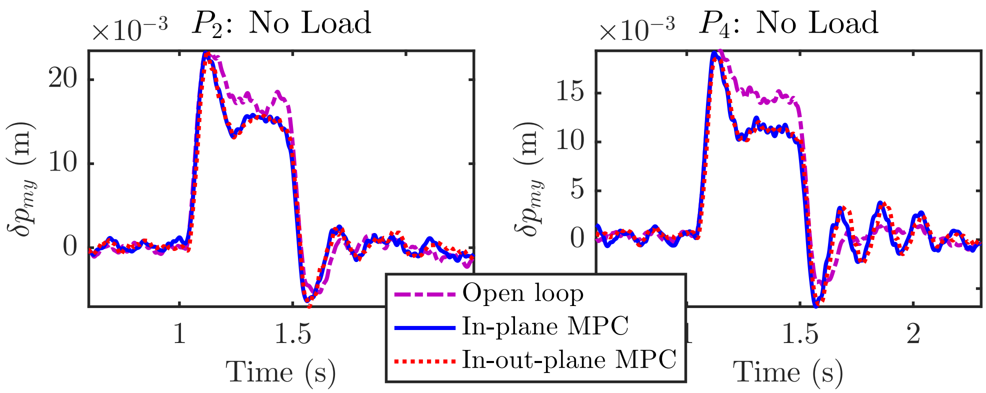

Figure 5.2: Vibration displacements in the y-direction at the points P_2 and P_4. In this case, there is no extra load on the mobile platform. The open-loop control, in-plane MPC control, and in-out-plane MPC control are implemented, respectively.

Because of the kinematic constraints (i.e., high stiffness), experimental results show that vibrations in the x-direction and rotation about the z-direction are tiny. For the in-plane experiments, more visible vibrations in the y-direction are introduced to validate the control performance. The in-plane and out-of-plane tuned MPC parameters used in experiments are shown in Table 5.1.

The vibration displacements in the y-direction at the points P_2 and P_4 are shown in Figure 5.2. In this case, there is no extra load on the mobile platform, and the open-loop control, in-plane MPC control, and in-out-plane MPC control are implemented, respectively. In-out-plane MPC means both in-plane and out-of-plane MPCs are applied. The results can be summarized as follows: compared with the open-loop control, when the in-plane MPC control and in-out-plane MPC control are implemented, vibration displacements are damped out, and the steady-state response is close to zero in 0.5 s. Correspondingly, the no-load responses of in-plane inputs T_3 and T_4 (including disturbances, control inputs, and reference inputs) in Figure 5.3 show that both in-plane and in-out-plane MPC controllers lead to inputs converge to the reference inputs (open-loop control). It can be indicated that the proposed decoupled model is considered reasonable.

In addition, when a 6 kg load is mounted on the top of the mobile platform, the corresponding vibration displacements and inputs are shown in Figure 5.4 and Figure 5.5, respectively. It can be seen from Figure 5.2, Figure 5.3, Figure 5.4, and Figure 5.5 that MPC is effective in achieving good in-plane vibration control. The no-load and load results also show that the in-plane controller has a good robust performance to suppress vibrations.

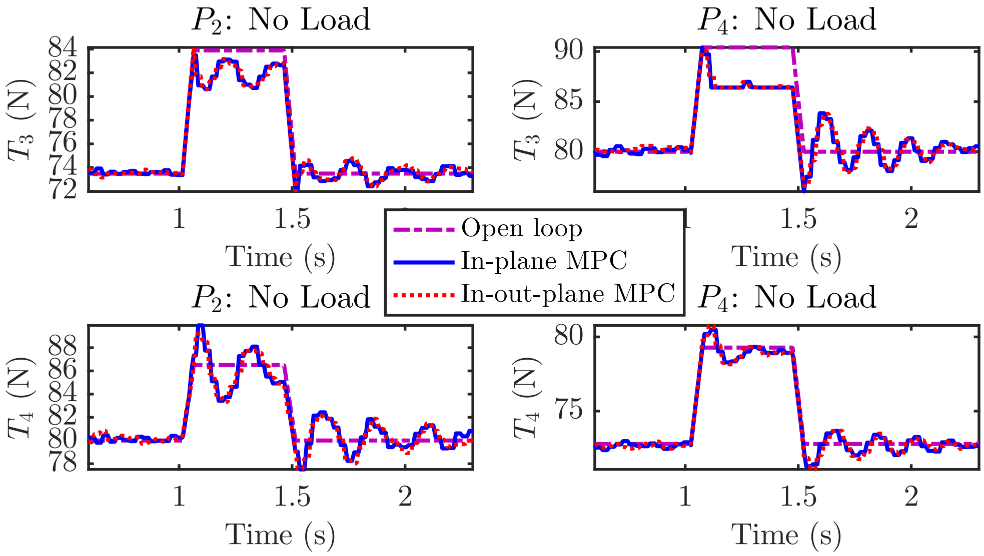

Figure 5.3: In-plane input performance at the points P_2 and P_4. There is no extra load on the mobile platform in this case. The open-loop control, in-plane MPC control, and in-out-plane MPC control are implemented, respectively.

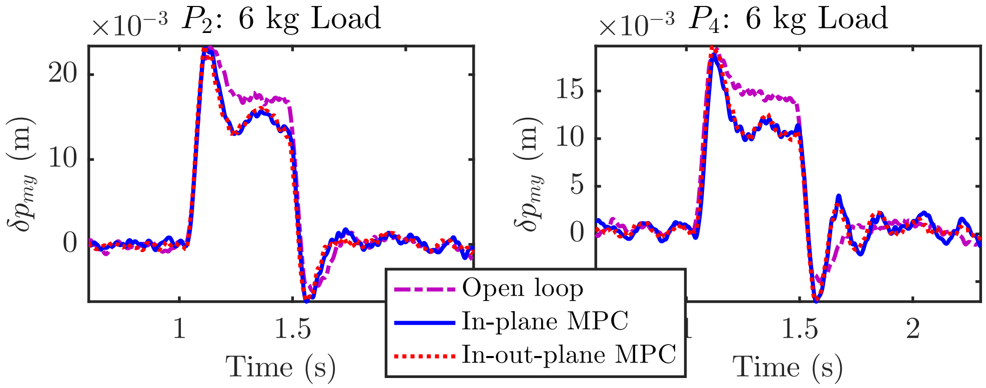

Figure 5.4: Vibration displacements in the y-direction at the points P_2 and P_4. A 6 kg extra load is mounted on the mobile platform. The open-loop control, in-plane MPC control, and in-out-plane MPC control are implemented, respectively.

5.2.2 Out-of-Plane Performance

Two pendulums (inputs τ_{p1} and τ_{p2}) are utilized to suppress the out-of-plane motions. System responses at P_2 and P_4 are selected for analysis. Meanwhile, two cases are examined:

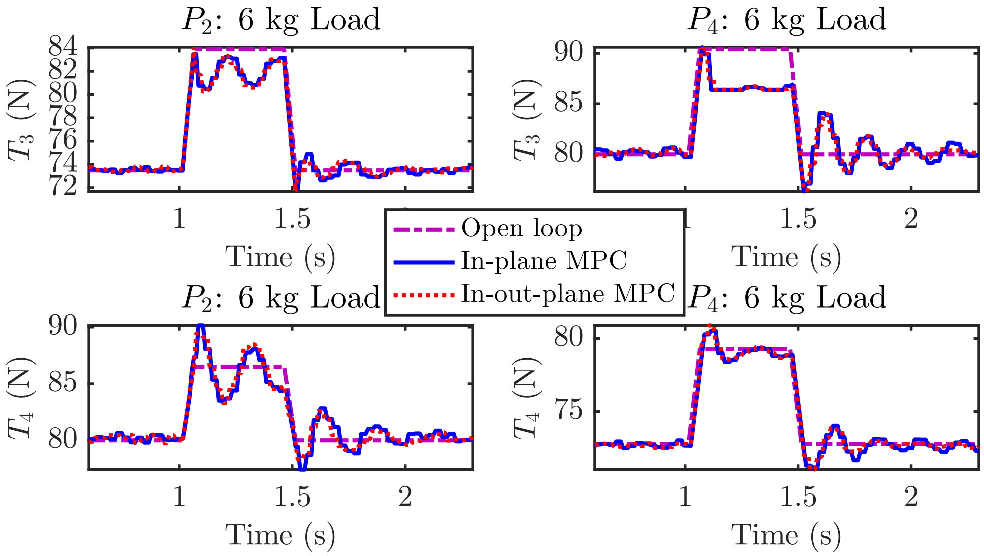

Figure 5.5: In-plane input performance at the points P_2 and P_4. A 6 kg extra load is mounted on the mobile platform. The open-loop control, in-plane MPC control, and in-out-plane MPC control are implemented, respectively.

1) no-load and 2) 6 kg load, with input disturbances.

Out-of-plane state and input performance at the points P_2 and P_4 are shown in Figure 5.6 and Figure 5.7, respectively. At these example points, open-loop control, out-of-plane MPC control, and in-out-plane MPC control are respectively implemented. Also, there is no extra load on the mobile platform. In Figure 5.6, it is clear that when the input disturbances are given, the out-of-plane MPC control and in-out-plane MPC control lead to the out-of-plane motion converging faster than that of the open-loop control. In Figure 5.7, both out-of-plane and in-out-plane MPC control lead to inputs (τ_{p1} and τ_{p2}, which include disturbances, control inputs, and reference inputs) converge to the reference inputs (open-loop control). When a 6 kg load is applied, the performance of states (in Figure 5.8) and inputs (shown in Figure 5.9) is also guaranteed.

Since the above results show that out-of-plane MPC and in-out-plane MPC lead to very close control performance, then the proposed decoupled out-of-plane model of HCDR-2 motion is considered reasonable. In short, MPC is an effective and robust approach for out-of-plane control.

In comparison with previous studies, such as [76], [53], and [30], the results in this chapter offer an improvement in the following aspects: 1) vibrations can be eliminated by

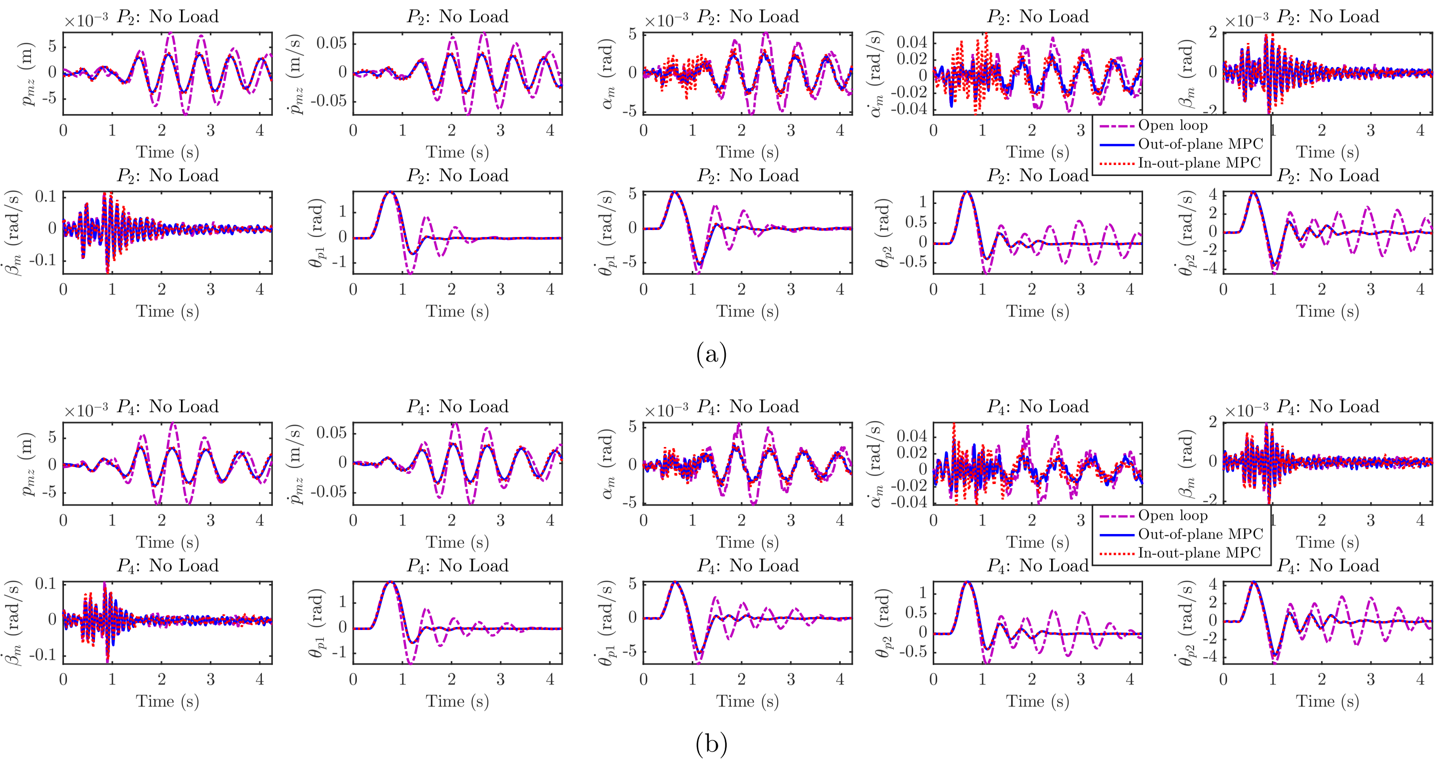

Figure 5.6: Out-of-plane state performance at the points P_2 and P_4. There is no extra load on the mobile platform. The open-loop control, out-of-plane MPC control, and in-out-plane MPC control are implemented, respectively.

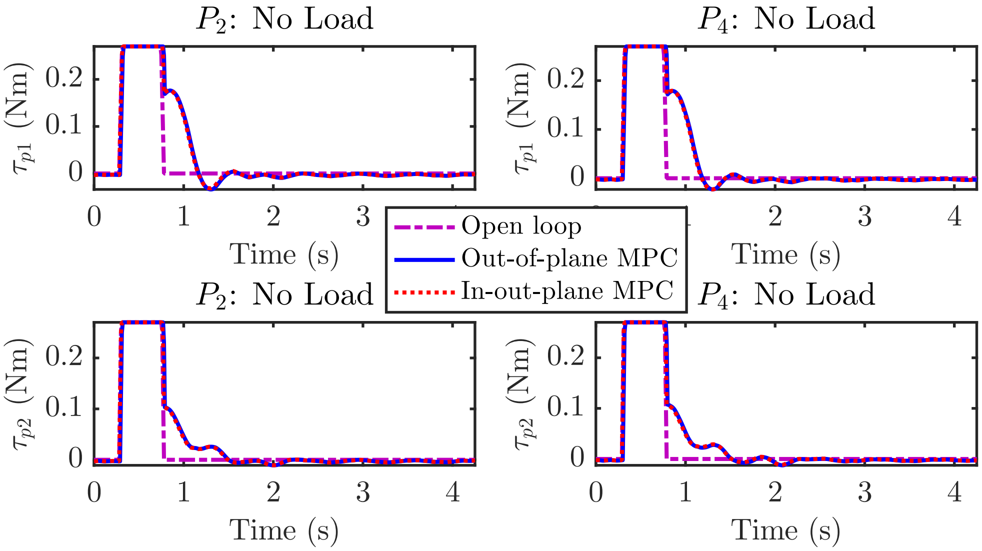

Figure 5.7: Out-of-plane input performance at the points P_2 and P_4. No extra load is mounted on the mobile platform. The open-loop control, out-of-plane MPC control, and in-out-plane MPC control are implemented, respectively.

the proposed optimal control inputs; 2) satisfactory vibration elimination results can be obtained by tuning the finite control horizon easily; 3) the predictive ability of MPC can improve the control performance by incorporating the future reference trajectories. In the experiments, the in-plane peak speed (around 0.4 m/s) is greater than that of 0.15 m/s shown in [76]. The vibration damping performance also holds for a much larger workspace than that reported in [30] (with the maximum position (p_{mx}, p_{my}) is $(0.02, 0.01)$ m).

5.3 Experiments and Robustness Verification of the Out-of-Plane System

5.3.1 Experimental Results

In this section, experiments are conducted on HCDR-3 (see Figure 3.6). Here, the experiments are focused on the out-of-plane system UMM, and the scenario is provided as follows: the slider moves fast (see the open loop response in Figure 5.10) from the initial position $p_{sr} = 0\,\text{m}$ to the pick/place position $p_{sr} = -0.15\,\text{m}$, and the top speed is around

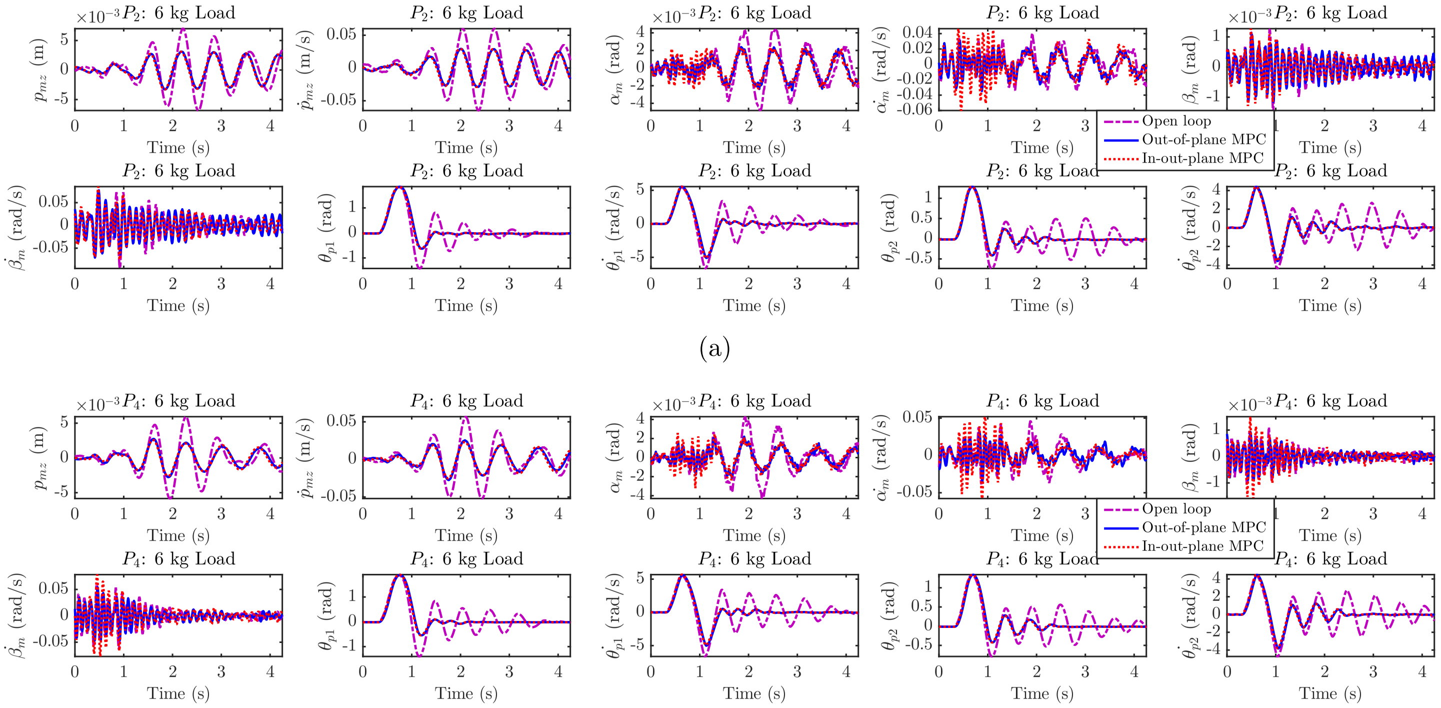

(a)

(b)

Figure 5.8: Out-of-plane state performance at the points P_2 and P_4. A 6 kg extra load is mounted on the mobile platform. The open-loop control, out-of-plane MPC control, and in-out-plane MPC control are implemented, respectively.

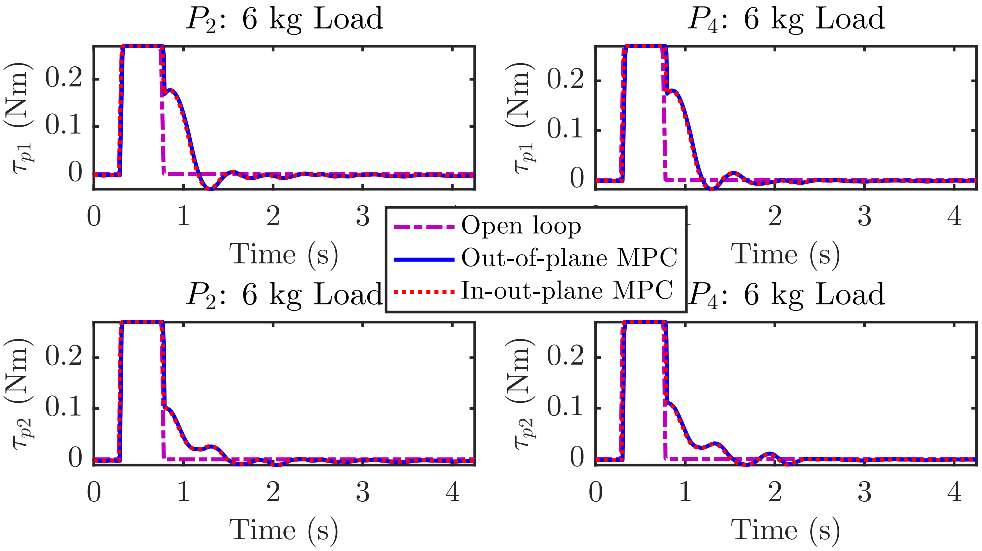

Figure 5.9: Out-of-plane input performance at the points P_2 and P_4. A 6 kg extra load is mounted on the mobile platform. The open-loop control, out-of-plane MPC control, and in-out-plane MPC control are implemented, respectively.

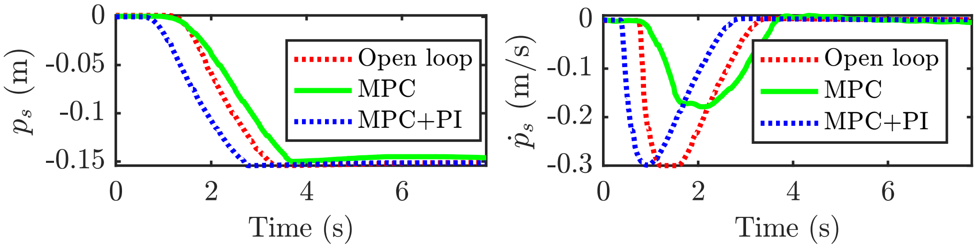

Figure 5.10: Experimental response with different control strategies (the slider). The open-loop control, MPC with integral action, and MPC+PI with integral action are implemented, respectively.

0.3 m/s. Input disturbances are given to the pendulums. Other setups are the same as simulations (see subsection 4.3.4).

The open-loop control, MPC with integral action, and MPC+PI with integral action are implemented in experiments, respectively. The experimental objectives are the same as that of simulation (in subsection 4.3.4). Using the parameters (in Table 5.2), the state and input responses are shown in Figure 5.10 and Figure 5.11, respectively.

In Figure 5.10, the slider moves from position 0 m to the set-point -0.15 m, and it

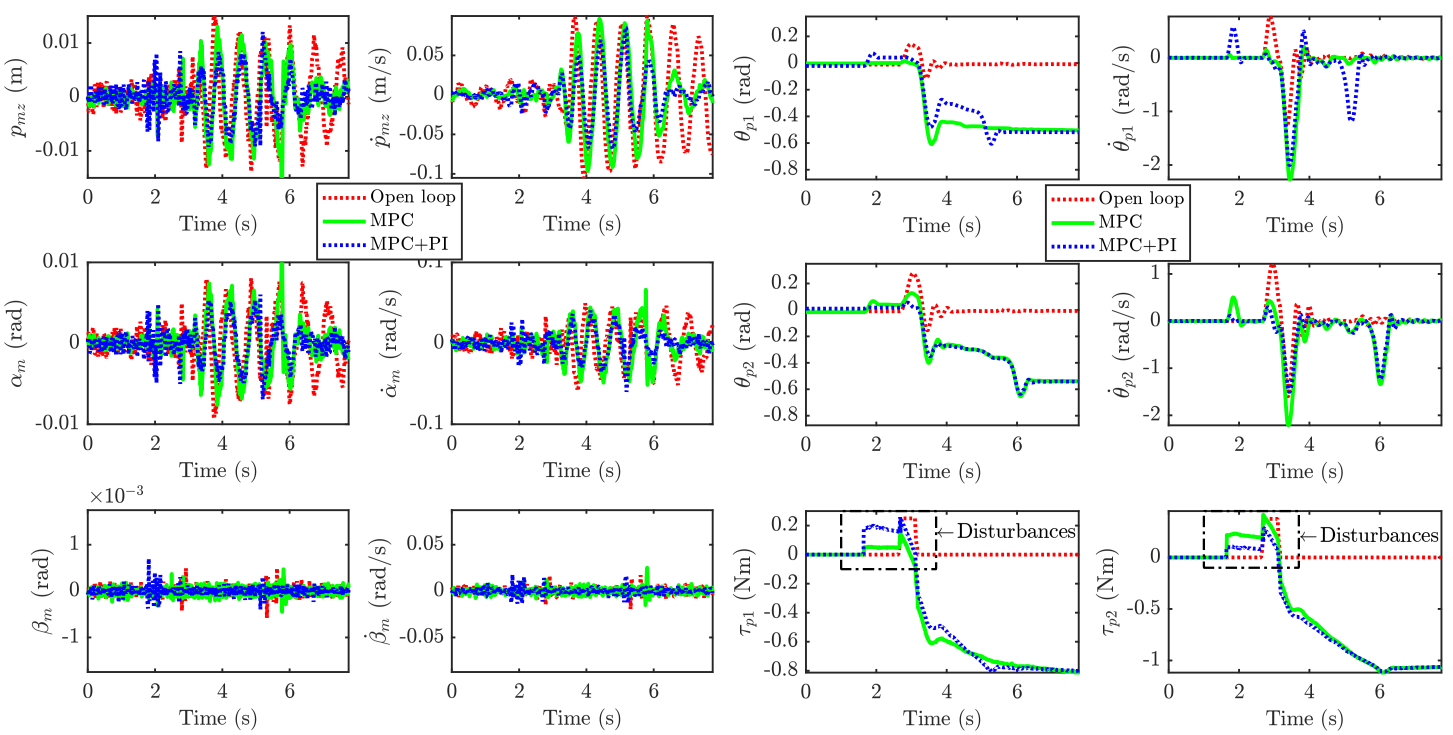

(a) (b)

Figure 5.11: Experimental response with different control strategies (the mobile platform and pendulums). (a) State responses of the mobile platform and (b) state and input responses of the pendulums. The open-loop control, MPC with integral action, and MPC+PI with integral action are implemented, respectively.

Table 5.2: Tuning Parameters for Experiments

Control structures	Parameters
MPC with Integral Action	$T_s = 0.01\,\text{s}$ (sampling time); $\Delta T = 0.02\,\text{s}$ (interval time); $N_p = 5$ (predictive horizon); $N_c = 5$ (control horizon); $R_p = \text{diag}([0.014, 0.014, 0.0015])$ (input weighting matrix); $Q_p = \text{diag}([0.01, 1, 0.5, 1, 0.5, 1, 1, 1, 1, 1, 150, 0])$ (state weighting matrix); $P_p = Q_p$ (terminal weighting matrix); $x_L = -\infty \in \mathbb{R}^{12\times 1}$ (lower bound); $x_U = \infty \in \mathbb{R}^{12\times 1}$ (upper bound); $u_L = -[3, 3, 10]^T$ (lower bound); $u_U = [3, 3, 10]^T$ (upper bound); $K_{fbi} = [1, 1, 22.75]^T$ (integral compensator gain).
MPC+PI with Integral Action	$T_s = 0.01\,\text{s}$; $\Delta T = 0.02\,\text{s}$; $N_p = N_c = 5$; $R_p = \text{diag}([0.014, 0.014])$; $R_p = Q_p = \text{diag}([0.01, 1, 0.5, 1, 0.5, 1, 1, 1, 1, 1])$; $x_L = -\infty \in \mathbb{R}^{10\times 1}$; $x_U = \infty \in \mathbb{R}^{10\times 1}$; $u_L = -[3, 3]^T$; $u_U = [3, 3]^T$; $K_{fbi} = [1, 1, 35]^T$; $K_{pi} = [0, 30]$ (PI controller gain).

generates reaction forces on the mobile platform, resulting in the mobile platform vibrating (in Figure 5.11). Meanwhile, impulse disturbances are also given to the pendulums to evaluate the controllers' robustness.

Clearly, in Figure 5.11, both controllers can eliminate vibrations and generate faster responses than that of open-loop control. When the slides stops at $p_{sr} = -0.15\,\text{m}$ (the reference angles of the pendulums are equal to $-30.45\,\text{deg}$), the tracking error of the pendulums converges towards zero asymptotically (in about 3 seconds).

In addition, by substituting the actual position and angle values (in Figure 5.10 and Figure 5.11) into (3.46c), the end-effector position p_e can also be evaluated (shown in Figure 5.12). The results show that via the proposed controllers, the position accuracy of the end-effector is improved (especially y_e). Based on the results above, it can be seen that the proposed controllers are effective to achieve the goal of tracking and vibration suppression.

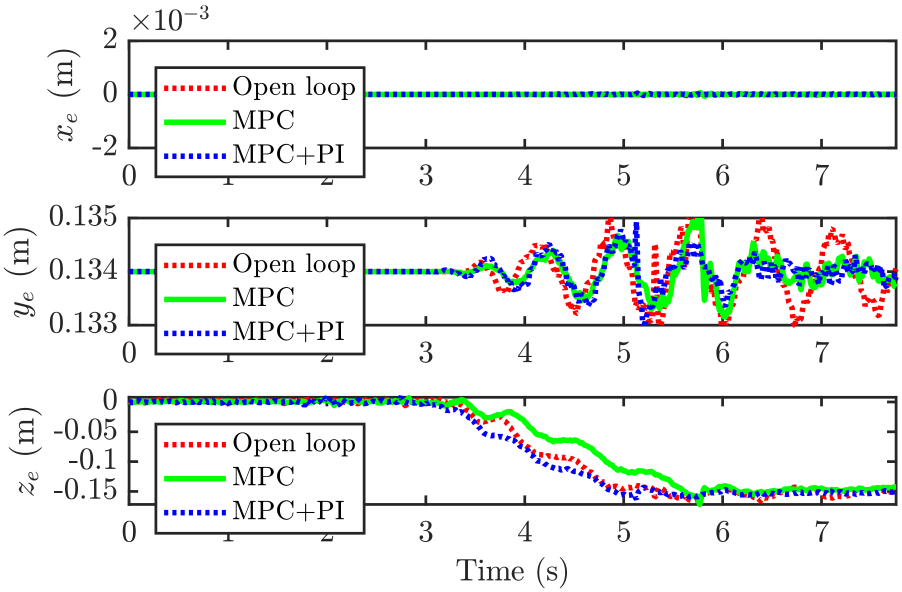

Figure 5.12: Experimental position of the end-effector with different control strategies, where the open-loop control, MPC with integral action, and MPC+PI with integral action are implemented, respectively.

5.3.2 Robustness Verification

In subsection 5.3.1, input disturbances are introduced to evaluate the controller performance. To further verify the robustness performance of the proposed strategies, three more scenarios are conducted (other experimental conditions, including the motion of the slider, input disturbances, parameters of the UMM, and tuning parameters are the same as those in subsection 5.3.1) as follows:

1. Different load masses: a reference load mass 1 (1.343 kg) and an uncertain load mass 2 (around 0.7 kg) are mounted on the slider, respectively.
2. Different in-plane positions (p_{mx}, p_{my}) of the mobile platform: the desired positions (p_{mx}, p_{my}) are equal to $(-0.1, 0.05)$ m and $(-0.1, -0.05)$ m, respectively.
3. Different load masses and in-plane positions (p_{mx}, p_{my}) of the mobile platform, i.e., the combination of two cases above.

The corresponding experimental results are shown in Figure 5.13, Figure 5.14, and Figure 5.15, respectively. Figure 5.13 shows the damping performance of the controllers with

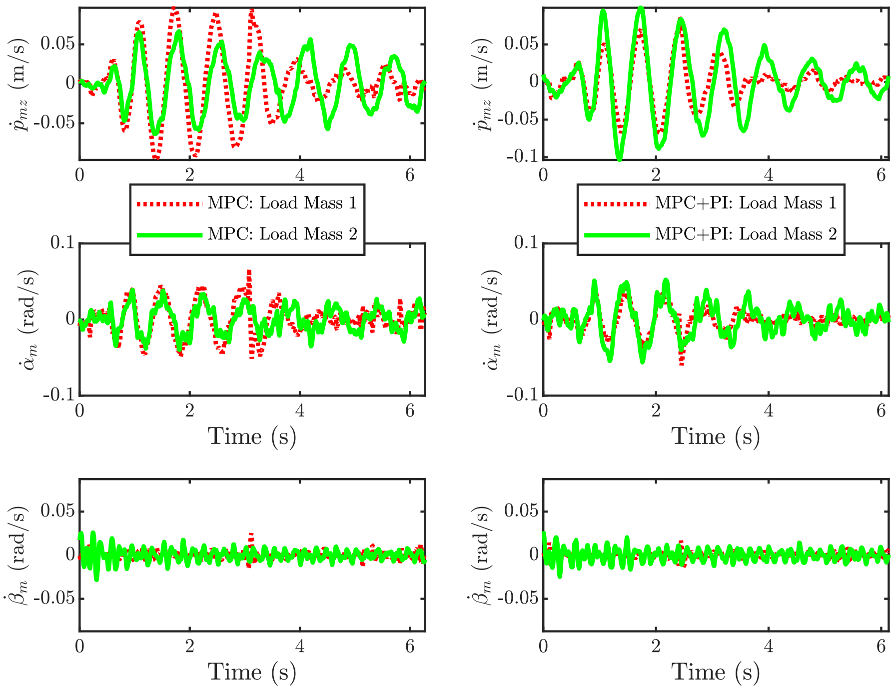

(a) (b)

Figure 5.13: Damping performance of the controllers with different load masses. (a) MPC with integral action and (b) MPC+PI with integral action.

load masses 1 and 2, where the load mass 1 is a reference (i.e., the load mass 1 is also used for experiments in subsection 5.3.1) and the load mass 2 is uncertain (around 0.7 kg). In this case, the in-plane position (p_{mx}, p_{my}) is always equal to $(0, 0)$ m and two controllers are carried out, respectively. Clearly, when the uncertain load mass 2 is mounted on the slider, vibrations can also be suppressed by using the proposed controllers. Additionally, the damping performance of the controllers with two in-plane positions (p_{mx}, p_{my}) of the mobile platform is shown in Figure 5.14, where the desired positions (p_{mx}, p_{my}) equal $(-0.1, 0.05)$ m and $(-0.1, -0.05)$ m, respectively. In this scenario, the reference load mass 1 is mounted on the slider. The experimental results also show that vibrations are damped out asymptotically by using the controllers. Figure 5.15 shows the damping performance of the controllers with the uncertain load mass 2 and in-plane positions ($(-0.1, 0.05)$ m and $(-0.1, -0.05)$ m). Clearly, in this scenario, vibrations can still be reduced.

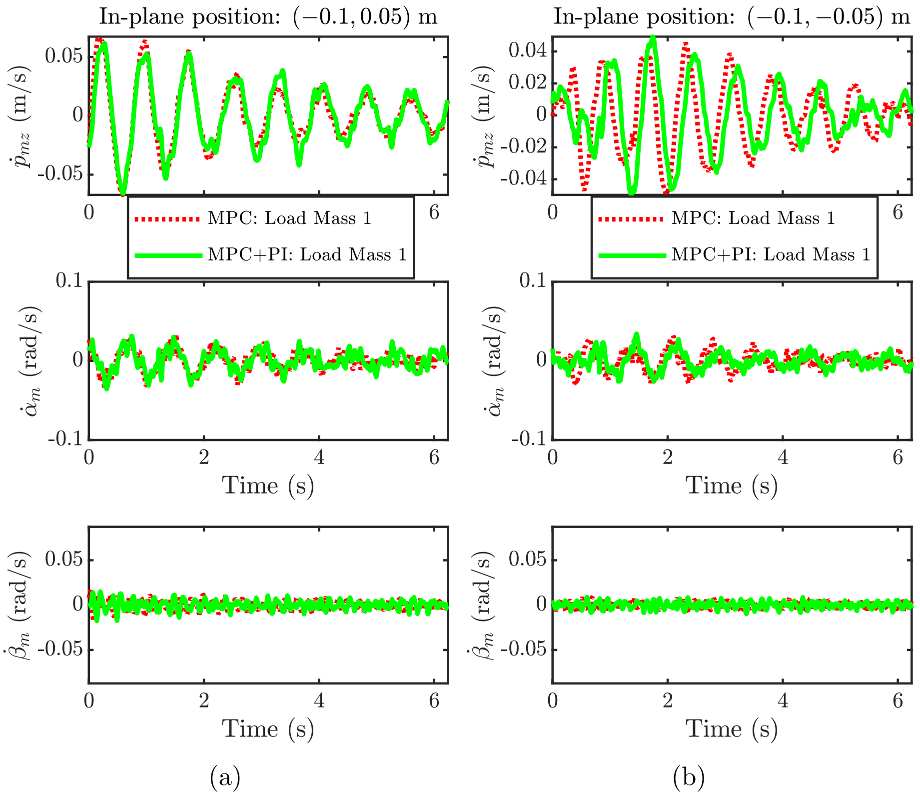

Figure 5.14: Damping performance of the controllers with different in-plane positions (p_{mx}, p_{my}) of the mobile platform. (a) $(p_{mx}, p_{my}) = (-0.1, 0.05)$ m and (b) $(p_{mx}, p_{my}) = (-0.1, -0.05)$ m.

5.4 Summary

In this chapter, experiments are conducted on HCDR-2 and HCDR-3 to evaluate the control methods proposed in Chapter 4. The results can be summarized as follows: to evaluate control performance for HCDR-2, the experiments are implemented in different aspects, including (a) open-loop control, in-plane MPC control, out-of-plane MPC control, and in-out-plane MPC control, (b) with no extra load and a 6 kg extra load, and (c) using different operation points. The experimental results are satisfactory and also validate the effectiveness of the decoupled method. Additionally, for HCDR-3, the open-loop control, MPC with integral action, and MPC+PI with integral action are implemented in experiments, respectively, and the proposed controllers prove effective and robust in handling

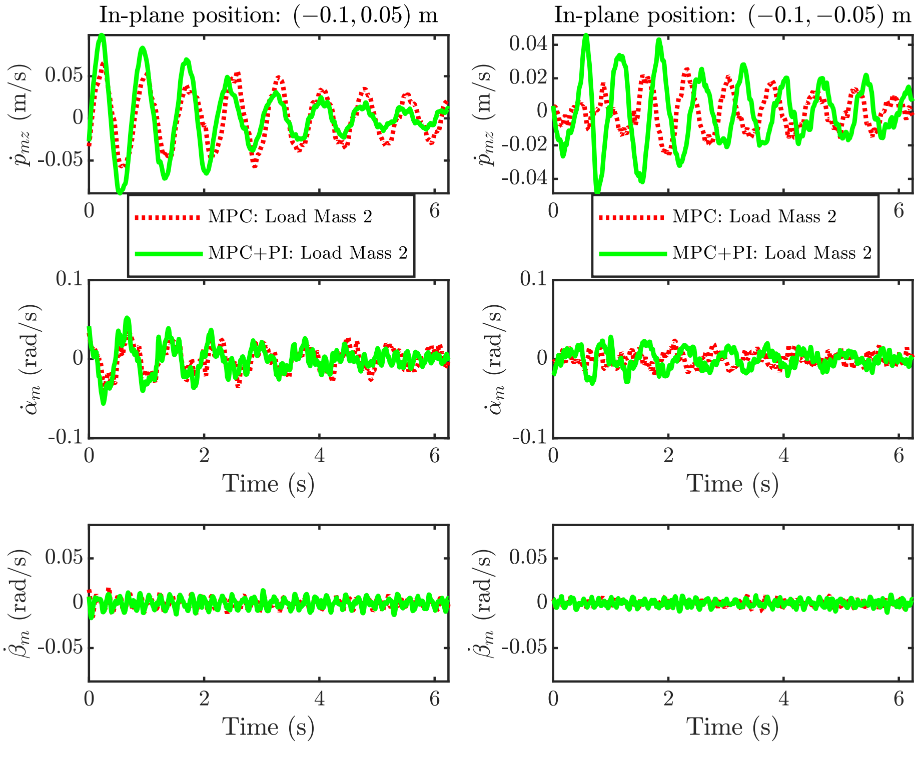

(a) (b)

Figure 5.15: Damping performance of the controllers with the uncertain load mass 2 and in-plane positions (p_{mx}, p_{my}) of the mobile platform. (a) $(p_{mx}, p_{my}) = (-0.1, 0.05)$ m and (b) $(p_{mx}, p_{my}) = (-0.1, -0.05)$ m.

the tracking and vibration suppression problems.

Chapter 6

Conclusions and Future Work

6.1 Conclusions

In this thesis, a generalized flexible Hybrid Cable-Driven Robot (HCDR) was introduced. For the proposed HCDR, generalized system modeling was developed and then extended to four types of hybrid robots: HCDR-1, HCDR-2, HCDR-3, and HCDR-4. Based on these robots, control design and optimization algorithms were proposed, and the results were evaluated using simulations and experiments. The main contributions of this thesis are as follows:

1. For modeling and control of generalized flexible HCDR: 1) The developed equations of motion (e.g., (3.10)–(3.16) and (3.21)) and the proof of (3.16) provide a very effective way to express the generalized dynamic modeling. Meanwhile, the proposed dynamic modeling approach avoids the drawback of traditional methods (e.g., Standard Denavit-Hartenberg (DH) parameters [31]), and can be easily extended to other types of hybrid robots by changing structure matrix A_m in (3.5) based on the desired configurations. 2) Three types of control architecture (shown in Figure 4.1) were developed to reduce vibrations and improve the position accuracy of the HCDR. 3) The proposed optimization problem (3.32) and Algorithm 1 provide an improvement over the existing stiffness optimization approaches in [57, 76, 52, 53]. They can be applied to not only CDPRs but also HCDRs.

2. To solve the problem of decoupled modeling and control of HCDR-2: 1) whole-body model and decoupled model were developed for the HCDR. The proposed decoupled

modeling method can be extended to other HCDRs or CDPRs based on their required configurations. 2) To achieve vibration control for the whole system in real-time (no more than 0.01s in experiments), primarily using model-based control techniques, the dynamics model was simplified for that purpose. The proposed decoupled model for the whole system can be implemented in real-time (the top CPU usage was reduced to 32%); meanwhile, it was validated via experiments. 3) Based on the decoupled dynamic model, model-based control architectures and observers were developed, and results were satisfactory in experiments (different cases were examined).

3. For the proposed UMM, modeling, tracking, and vibration- and balance-control problems were studied, and the following contributions are highlighted: 1) Compared to the modeling and control objectives in [30], this thesis extends the configuration by introducing a coupled slider on the platform to introduce more DOFs to the system. The derivation of equations of motion of the UMM, disturbance analysis, and model validation were carried out. Additionally, a simple but effective strategy was developed to solve the equilibrium point and balance problem. 2) Based on the dynamic model, two control architectures were developed: MPC with integral action and MPC+PI with integral action. Compared to other MPC-based control strategies, the proposed controllers are easier to implement in practice. The results of this thesis also offer improvements (in comparison with previous studies, such as PID [76], LPV [53], and SMC [30]) since the use of MPC enhances the control performance by using the future steps from the reference trajectories to generate control laws. 3) Simulations and experiments were carried out, and the results of tracking and vibration suppression were satisfactory.

4. Redundancy resolution and disturbance rejection via torque optimization were studied, and the following contributions are highlighted: 1) Nonlinear whole-body dynamics model of the HCDR and a model reduction approach were developed. Based on the reduced dynamics model, two new methods were proposed: TOAJ and TOAUJ. 2) The algorithms of TOAJ and TOAUJ were evaluated using case studies, and the results showed they could solve the redundancy resolution problem. Compared to TOAJ, TOAUJ can solve the redundancy resolution problem and also reject disturbances.

6.2 Future Work

The research developed in this thesis can be extended to the following directions:

1. Thus far, the 1-DOF linear slider shown in Figure 3.7 is integrated in the HCDR-3 for experiments (see section 5.3). In the future, experiments using HCDR-1 (by replacing the slide with a 3-DOF robot arm) can be implemented. In subsection 4.4.6, the algorithms of the TOAJ and TOAUJ were evaluated using simulations. The corresponding performance can also be evaluated via experiments in the future.

2. Algorithm 2 which fuses forward kinematics and lower-cable tensions was developed to estimate in-plane states, and it was shown to be more robust than that of [53] (only utilized IMU signals). This algorithm and the out-of-plane estimation algorithm (see Algorithm 3) can be improved in the future by incorporating IMU and vision-based signals, and using muti-signal fusion techniques to increase the accuracy of estimation of the system states.

3. To extend the applications (e.g., in different warehousing environments) of HCDRs, some potential topics can be studied in the future. For instance, the proposed modeling approaches and control strategies for HCDRs can also be extended to other robotic systems. New grippers (e.g., based on the previous works [91]) can be designed and affixed to the end effector of HCDRs in order to extend the range of manipulation tasks that HCDR systems can perform.

References

[1] S. Abdolshah and E. S. Barjuei. Linear quadratic optimal controller for cable-driven parallel robots. *Front. Mech. Eng.*, 10(4):344–351, Dec. 2015.

[2] S. Abdolshah, D. Zanotto, G. Rosati, and S. Agrawal. Performance evaluation of a new design of cable-suspended camera system. In *Proc. IEEE Int. Conf. Robot. Autom.*, pages 3728–3733, Singapore, May 2017.

[3] S. Aguilera-Marinovic, M. Torres-Torriti, and F. Auat-Cheein. General Dynamic Model for Skid-Steer Mobile Manipulators With Wheel-Ground Interactions. *IEEE/ASME Trans. Mechatronics*, 22(1):433–444, Feb. 2017.

[4] J. Albus, R. Bostelman, and N. Dagalakis. The NIST SPIDER, A Robot Crane. *J. Res. Natl. Inst. Stand. Technol.*, 97(3):373–385, May–June 1992.

[5] J. S. Albus. Cable Arrangement and Lifting Platform for Stabilized Load Lifting. U.S. Patent 4,883,184, Nov. 28, 1989.

[6] J. S. Albus, R. V. Bostelman, and A. S. Jacoff. Modular Suspended Manipulator. U.S. Patent 6,566,834 B1, May 20, 2003.

[7] A. Alikhani, S. Behzadipour, et al. Modeling, Control and Simulation of a New Large Scale Cable-Driven Robot. In *Proc. ASME Int. Des. Eng. Tech. Conf.*, pages 11–16, San Diego, California, USA, Aug.–Sep. 2009.

[8] A. Alikhani and M. Vali. Modeling and robust control of a new large scale suspended cable-driven robot under input constraint. In *Proc. 8th Int. Conf. Ubiquit. Robot. Ambient Intell.*, pages 238–243, Incheon, South Korea, Nov. 2011.

[9] T. Arai, S. Matsumura, et al. A proposal for a wire suspended manipulator: A kinematic analysis. *Robotica*, 17(1):3–9, 1999.

[10] M. Arsenault. Workspace and stiffness analysis of a three-degree-of-freedom spatial cable-suspended parallel mechanism while considering cable mass. *Mechan. Mach. Theory*, 66:1–13, 2013.

[11] M. Athans. The role and use of the stochastic linear-quadratic-Gaussian problem in control system design. *IEEE Trans. Autom. Control*, 16(6):529–552, Dec. 1971.

[12] M. Azadi, S. Behzadipour, and G. Faulkner. Antagonistic variable stiffness elements. *Mechan. Mach. Theory*, 44(9):1746–1758, 2009.

[13] R. Babaghasabha, M. A. Khosravi, and H. D. Taghirad. Adaptive robust control of fully-constrained cable driven parallel robots. *Mechatronics*, 25:27–36, 2015.

[14] M. Bamdad, F. Taheri, and N. Abtahi. Dynamic analysis of a hybrid cable-suspended planar manipulator. In *Proc. IEEE Int. Conf. Robot. Autom.*, pages 1621–1626, Seattle, Washington, USA, May 2015.

[15] G. Barrette and C. M. Gosselin. Determination of the dynamic workspace of cable-driven planar parallel mechanisms. *ASME. J. Mech. Des.*, 127(2):242–248, March 2005.

[16] Beckhoff Autom. Limitations. `https://infosys.beckhoff.com/english.php?content=../content/1033/tc3_c/54043196203206283.html&id=`. (accessed 23 Jan. 2019).

[17] Y. B. Bedoustani, H. D. Taghirad, and M. M. Aref. Dynamics analysis of a redundant parallel manipulator driven by elastic cables. In *Proc. 2008 10th Int. Conf. Control Autom. Robot. Vision*, pages 536–542, Hanoi, Vietnam, Dec. 2008.

[18] S. Behzadipour and A. Khajepour. Stiffness of Cable-based Parallel Manipulators With Application to Stability Analysis. *ASME J. Mech. Des.*, 128(1):303–310, Jan. 2006.

[19] A. Bemporad. Automatic Control. Class Lecture, Topic: “Integral action in state feedback control.” IMT School for Advanced Studies Lucca, Lucca, Italy, 2011.

[20] G. Boschetti and A. Trevisani. Cable Robot Performance Evaluation by Wrench Exertion Capability. *Robotics*, 7(2):15, 2018.

[21] P. Bosscher and I. Ebert-Uphoff. A stability measure for underconstrained cable-driven robots. In *Proc. IEEE Int. Conf. Robot. Autom.*, volume 5, pages 4943–4949, New Orleans, LA, USA, April 2004.

[22] T. Bruckmann, A. Pott, and M. Hiller. Calculating force distributions for redundantly actuated tendon-based stewart platforms. In Jadran Lennarčič and B. Roth, editors, *Advances in Robot Kinematics*, pages 403–412, Dordrecht, 2006. Springer Netherlands.

[23] M. Carricato and J. Merlet. Stability Analysis of Underconstrained Cable-Driven Parallel Robots. *IEEE Trans. Robot.*, 29(1):288–296, Feb. 2013.

[24] R. J. Caverly and J. R. Forbes. Dynamic Modeling and Noncollocated Control of a Flexible Planar Cable-Driven Manipulator. *IEEE Trans. Robot.*, 30(6):1386–1397, Dec. 2014.

[25] J. H. Chung, S. A. Velinsky, and R. A. Hess. Interaction control of a redundant mobile manipulator. *Int. J. Robot. Research*, 17(12):1302–1309, 1998.

[26] T. Coleman, M. Branch, and A. Grace. *Optimization Toolbox for Use with Matlab.* MathWorks, Inc., Natick, MA, 1999.

[27] P. Corke. *Robotics, Vision and Control: Fundamental Algorithms in MATLAB.* Springer, Berlin, Germany, 2011.

[28] CUHK C3 Robotics Laboratory. SpiderArm Robot: Hybrid Cable-Driven Robot with Serial Manipulator. `https://youtu.be/rf4Zpf_MxrA`, May 21, 2017. (accessed 11 June 2019).

[29] N. G. Dagalakis, J. S. Albus, et al. Stiffness Study of a Parallel Link Robot Crane for Shipbuilding Applications. *J. Offshore Mechanics Arctic Eng.*, 111:183–193, Aug. 1989.

[30] R. de Rijk, M. Rushton, and A. Khajepour. Out-of-Plane Vibration Control of a Planar Cable-Driven Parallel Robot. *IEEE/ASME Trans. Mechatronics*, 23(4):1684–1692, Aug. 2018.

[31] J. Denavit and R. S. Hartenberg. A kinematic notation for lower-pair mechanisms based on matrices. *ASME J. Appl. Mechanics*, 22:215–221, 1955.

[32] X. Diao, O. Ma, and Q. Lu. Singularity Analysis of Planar Cable-Driven Parallel Robots. In *Proc. 2008 IEEE Conf. Robot. Autom. Mechatronics*, pages 272–277, Chengdu, China, Sep. 2008.

[33] H.-D. Do and K.-S. Park. Analysis of effective vibration frequency of cable-driven parallel robot using mode tracking and quasi-static method. *Microsystem Technologies*, 23(7):2577–2585, July 2017.

[34] J. Du, H. Bao, et al. Dynamic analysis of cable-driven parallel manipulators with time-varying cable lengths. *Finite Elements in Analysis and Design*, 48(1):1392–1399, 2012.

[35] H. A. ElMaraghy, T. Lahdhiri, and F. Ciuca. Robust Linear Control of Flexible Joint Robot Systems. *J. Intell. Robotic Syst.*, 34(4):335–356, Aug. 2002.

[36] P. Falcone, F. Borrelli, et al. Linear time-varying model predictive control and its application to active steering systems: Stability analysis and experimental validation. *Int. J. Robust Nonlinear Control*, 18(8):862–875, 2008.

[37] H. J. Ferreau, C. Kirches, A. Potschka, H. G. Bock, and M. Diehl. qpOASES: a parametric active-set algorithm for quadratic programming. *Math. Prog. Comp.*, 6(4):327–63, Dec. 2014.

[38] F. Flacco and A. D. Luca. Discrete-time redundancy resolution at the velocity level with acceleration/torque optimization properties. *Robot. Auton. Syst.*, 70:191–201, 2015.

[39] G. Galuppini, L. Magni, and D. M. Raimondo. Model predictive control of systems with deadzone and saturation. *Control Eng. Practice*, 78:56–64, 2018.

[40] A. Ghasemi, M. Eghtesad, and M. Farid. Constrained model predictive control of the redundant cable robots. In *Proc. 2008 World Automa. Congress*, pages 1–6, Sep. 2008.

[41] C. Gosselin. Stiffness mapping for parallel manipulators. *IEEE Trans. Robot. Autom.*, 6(3):377–382, June 1990.

[42] C. Gosselin and J. Angeles. Singularity analysis of closed-loop kinematic chains. *IEEE Trans. Robot. Autom.*, 6(3):281–290, June 1990.

[43] M. Gouttefarde. Analysis and Synthesis of Large-Dimension Cable-Driven Parallel Robots. Habilitation À Diriger Des Recherches, Académie De Montpellier, 2016.

[44] M. Gouttefarde. Static Analysis of Planar 3-DOF Cable-Suspended Parallel Robots Carrying a Serial Manipulator. In Philippe Wenger and Paulo Flores, editors, *New*

Trends Mechanism Machine Sci., pages 363–371, Cham, 2017. Springer Int. Publishing.

[45] M. Griffis and J. Duffy. Global stiffness modeling of a class of simple compliant couplings. *Mechan. Mach. Theory*, 28(2):207–224, 1993.

[46] D. Guo and Y. Zhang. Different-level two-norm and infinity-norm minimization to remedy joint-torque instability/divergence for redundant robot manipulators. *Robot. Auton. Syst.*, 60(6):874–888, 2012.

[47] M. Hiller, S. Fang, S. Mielczarek, R. Verhoeven, and D. Franitza. Design, analysis and realization of tendon-based parallel manipulators. *Mechan. Mach. Theory*, 40(4):429–445, 2005.

[48] Y. Huang, A. Khajepour, T. Zhu, and H. Ding. A Supervisory Energy-Saving Controller for a Novel Anti-Idling System of Service Vehicles. *IEEE/ASME Trans. Mechatronics*, 22(2):1037–1046, April 2017.

[49] M. Ismail, S. Lahouar, and L. Romdhane. Collision-free and dynamically feasible trajectory of a hybrid cableserial robot with two passive links. *Robot. Auton. Syst.*, 80:24–33, 2016.

[50] H. Jamshidifar. *Integrated Trajectory-Tracking and Vibration Control of Kinematically-Constrained Warehousing Cable Robots.* PhD thesis, University of Waterloo, Waterloo, ON, Canada, 2018.

[51] H. Jamshidifar, B. Fidan, G. Gungor, and A. Khajepour. Adaptive Vibration Control of a Flexible Cable Driven Parallel Robot. *IFAC-PapersOnLine*, 48(3):1302 – 1307, 2015.

[52] H. Jamshidifar, A. Khajepour, B. Fidan, and M. Rushton. Kinematically-Constrained Redundant Cable-Driven Parallel Robots: Modeling, Redundancy Analysis, and Stiffness Optimization. *IEEE/ASME Trans. Mechatronics*, 22(2):921–930, April 2017.

[53] H. Jamshidifar, S. Khosravani, B. Fidan, and A. Khajepour. Vibration Decoupled Modeling and Robust Control of Redundant Cable-Driven Parallel Robots. *IEEE/ASME Trans. Mechatronics*, 23(2):690–701, April 2018.

[54] S. Kawamura, H. Kino, and C. Won. High-speed manipulation by using parallel wire-driven robots. *Robotica*, 18(1):13–21, 2000.

[55] K. Kazerounian and Z. Wang. Global versus local optimization in redundancy resolution of robotic manipulators. *Int. J. Robot. Research*, 7(5):3–12, 1988.

[56] L. Kevac, M. Filipovic, and A. Rakic. The trajectory generation algorithm for the cable-suspended parallel robot–The CPR Trajectory Solver. *Robot. Auton. Syst.*, 94:25–33, 2017.

[57] A. Khajepour and S. T. Méndez. Apparatus for controlling a mobile platform. U.S. Patent 14,613,450, Feb. 4, 2015.

[58] H. Kino, T. Yahiro, S. Taniguchi, and K. Tahara. Sensorless Position Control Using Feedforward Internal Force for Completely Restrained Parallel-Wire-Driven Systems. *IEEE Trans. Robot.*, 25(2):467–474, April 2009.

[59] S. Kock and W. Schumacher. A parallel x-y manipulator with actuation redundancy for high-speed and active-stiffness applications. In *Proc. IEEE Int. Conf. Robot. Autom.*, pages 2295–2300, Leuven, Belgium, May 1998.

[60] KUKA Roboter GmbH. KR 30, 60 HA with C Variants Specification, Version: Spez KR 30, 60 HA V1. https://www.kuka.com/-/media/kuka-downloads/imported/48ec812b1b2947898ac2598aff70abc0/spez_kr_30_60_ha_en.pdf, Jan. 12, 2017. (accessed 11 June 2019).

[61] H. Kwakernaak and R. Sivan. *Linear Optimal Control Systems*. John Wiley & Sons, Toronto, 4 edition, 1972.

[62] D. Lau, D. Oetomo, and S. K. Halgamuge. Generalized Modeling of Multilink Cable-Driven Manipulators With Arbitrary Routing Using the Cable-Routing Matrix. *IEEE Trans. Robot.*, 29(5):1102–1113, Oct. 2013.

[63] J. Y. Lew and W. J. Book. Dynamics of two serially connected manipulators. In *Advanced Control Issues for Robot Manipulators, ASME Winter Annual Meeting*, volume 39, pages 17–22, 1992.

[64] C. Li, Y. Ding, G. Gu, and L. Zhu. Damping Control of Piezo-Actuated Nanopositioning Stages With Recursive Delayed Position Feedback. *IEEE/ASME Trans. Mechatronics*, 22(2):855–864, April 2017.

[65] J. Li, S. Andrews, et al. Task-based Design of Cable-driven Articulated Mechanisms. In *Proc. 1st Annual ACM Sym. Comp. Fabri.*, pages 6:1–6:12, New York, NY, USA, 2017.

[66] M. Li, H. Wu, and H. Handroos. Stiffness-maximum trajectory planning of a hybrid kinematic-redundant robot machine. In *Proc. 37th An. Conf. IEEE Ind. Electron. Soc.*, pages 283–288, Melbourne, Australia, Nov. 2011.

[67] W. B. Lim, G. Yang, et al. A generic force-closure analysis algorithm for cable-driven parallel manipulators. *Mechan. Mach. Theory*, 46(9):1265 – 1275, 2011.

[68] S. Lin and A. A. Goldenberg. Neural-network control of mobile manipulators. *IEEE Trans. Neural Networks*, 12(5):1121–1133, Sep. 2001.

[69] B. Lu, Y. Fang, and N. Sun. Nonlinear control for underactuated multi-rope cranes: Modeling, theoretical design and hardware experiments. *Control Eng. Practice*, 76:123–132, 2018.

[70] D. G. Luenberger and Y. Ye. *Linear Nonlinear Programming.* Springer, New York, NY, USA, 3 edition, 2008.

[71] S. Ma. Local torque optimization of redundant manipulators in torque-based formulation. In *Proc. 20th Conf. IEEE Ind. Electron.*, volume 2, pages 697–702, Bologna, Italy, Sep. 1994.

[72] Market Research Engine. Automated Material Handling Equipment Market By Product Analysis; By System Type Analysis; By Software & Services Analysis; By Function Analysis; By Industry Analysis and By Regional Analysis–Global Forecast by 2018-2024. `https://www.marketresearchengine.com/automated-material-handling-equipment-market`, Nov. 2018. (accessed 11 June 2019).

[73] MarketWatch. Automated Material Handling Equipment Market Poised to touch US$ 50.0 Billion by 2024. `https://www.marketwatch.com/press-release/`, April 10, 2019. (accessed 11 June 2019).

[74] S. Mason, L. Righetti, and S. Schaal. Full dynamics LQR control of a humanoid robot: An experimental study on balancing and squatting. In *Proc. 14th IEEE-RAS Int. Conf. Humanoid Robot.*, pages 374–379, Nov. 2014.

[75] J. Mattingley and S. Boyd. CVXGEN: a code generator for embedded convex optimization. *Optim. Eng.*, 13(1):1–27, March 2012.

[76] S. J. T. Méndez. *Low Mobility Cable Robot with Application to Robotic Warehousing.* PhD thesis, University of Waterloo, Waterloo, ON, Canada, 2014.

[77] J. Merlet. Kinematics of the wire-driven parallel robot MARIONET using linear actuators. In *Proc. IEEE Int. Conf. Robot. Autom.*, pages 3857–3862, Pasadena, CA, USA, May 2008.

[78] G. Meunier, B. Boulet, and M. Nahon. Control of an Overactuated Cable-Driven Parallel Mechanism for a Radio Telescope Application. *IEEE Trans. Control Syst. Technol.*, 17(5):1043–1054, Sep. 2009.

[79] G. Meunier, B. Boulet, and M. Nahon. Control of an Overactuated Cable-Driven Parallel Mechanism for a Radio Telescope Application. *IEEE Trans. Control Syst. Tech.*, 17(5):1043–1054, Sep. 2009.

[80] Y. Mori and Y. Tagawa. Vibration controller for overhead cranes considering limited horizontal acceleration. *Control Eng. Practice*, 81:256–263, 2018.

[81] N. Mostashiri, J. S. Dhupia, et al. A Review of Research Aspects of Redundantly Actuated Parallel Robotsw for Enabling Further Applications. *IEEE/ASME Trans. Mechatronics*, 23(3):1259–1269, June 2018.

[82] V. Nabat, M. de la O Rodriguez, et al. Par4: very high speed parallel robot for pick-and-place. In *Proc. IEEE/RSJ Int. Conf. Intel. Robot. Syst.*, pages 553–558, Edmonton, Alta., Canada, Aug. 2005.

[83] Y. Nakamura and H. Hanafusa. Inverse kinematic solutions with singularity robustness for robot manipulator control. *ASME. J. Dyn. Sys., Meas., Control*, 108(3):163–171, Sep. 1986.

[84] D. Q. Nguyen, M. Gouttefarde, O. Company, and F. Pierrot. On the simplifications of cable model in static analysis of large-dimension cable-driven parallel robots. In *Proc. IEEE Int. Intel. Rob. Sys.*, pages 928–934, Nov. 2013.

[85] NIST. Dual Manipulator. `https://www.nist.gov/node/443271`. (accessed 23 Jan. 2019).

[86] NIST. Tetra work platform. `https://www.nist.gov/node/443196`. (accessed 23 Jan. 2019).

[87] S. Oh and S. K. Agrawal. Cable suspended planar robots with redundant cables: controllers with positive tensions. *IEEE Trans. Robot.*, 21(3):457–465, June 2005.

[88] H. Osumi, Y. Utsugi, and M. Koshikawa. Development of a manipulator suspended by parallel wire structure. In *Proc. IEEE/RSJ Int. Conf. Intell. Robots Syst.*, pages 498–503, Takamatsu, Japan, Oct. 2000.

[89] P. R. Pagilla and B. Yu. An experimental study of planar impact of a robot manipulator. *IEEE/ASME Trans. Mechatronics*, 9(1):123–128, March 2004.

[90] PRODRONE. PRODRONE Unveils the World's First Dual Robot Arm Large-Format Drone. `https://www.prodrone.com/archives/1420/`, Sep. 7, 2016. (accessed 11 June 2019).

[91] R. Qi, T. L. Lam, and Y. Xu. Design and implementation of a low-cost and lightweight inflatable robot finger. In *Proc. IEEE/RSJ Int. Conf. Intell. Robots Syst.*, pages 28–33, Chicago, IL, USA, Sep. 2014.

[92] R. Qi, M. Rushton, A. Khajepour, and W. W. Melek. Decoupled modeling and model predictive control of a hybrid cable-driven robot (HCDR). *Robot. Auton. Syst.*, 118:1–12, 2019.

[93] M. Rushton. Vibration Control in Cable Robots Using a Multi-Axis Reaction System. Master's thesis, University of Waterloo, Waterloo, ON, Canada, 2016.

[94] M. Rushton and A. Khajepour. Optimal actuator placement for vibration control of a planar cable-driven robotic manipulator. In *Proc. 2016 American Control Conf.*, pages 3020–3025, Boston, MA, USA, July 2016.

[95] M. Rushton and A. Khajepour. Transverse Vibration Control in Planar Cable-Driven Robotic Manipulators. In Clément Gosselin, Philippe Cardou, Tobias Bruckmann, and Andreas Pott, editors, *Cable-Driven Parallel Robots*, pages 243–253, Cham, 2018. Springer Int. Publishing.

[96] V. Schmidt and A. Pott. *Implementing Extended Kinematics of a Cable-Driven Parallel Robot in Real-Time*, pages 287–298. Springer Berlin Heidelberg, Berlin, Heidelberg, 2013.

[97] SKYCAM LLC. Skycam. `http://www.skycam.tv`. (accessed 23 Jan. 2019).

[98] Spidercam GmbH. Spidercam. `https://www.spidercam.tv`. (accessed 23 Jan. 2019).

[99] M. W. Spong and M. Vidyasagar. *Robot Dynamics and Control.* John Wiley & Sons, Inc., New York, NY, USA, 2008.

[100] D. Stewart. A Platform with Six Degrees of Freedom. *Proc. Institution of Mechanical Engineers*, 180(1):371–386, 1965.

[101] M. M. Svinin, S. Hosoe, and M. Uchiyama. On the stiffness and stability of Gough-Stewart platforms. In *Proc. IEEE Int. Conf. Robot. Autom.*, volume 4, pages 3268–3273, Seoul, South Korea, May 2001.

[102] H. D. Taghirad and Y. B. Bedoustani. An Analytic-Iterative Redundancy Resolution Scheme for Cable-Driven Redundant Parallel Manipulators. *IEEE Trans. Robot.*, 27(6):1137–1143, Dec. 2011.

[103] H. D. Taghirad and M. A. Nahon. Dynamic Analysis of a MacroMicro Redundantly Actuated Parallel Manipulator. *Advanced Robotics*, 22(9):949–981, 2008.

[104] W. S. Tang and J. Wang. A recurrent neural network for minimum infinity-norm kinematic control of redundant manipulators with an improved problem formulation and reduced architecture complexity. *IEEE Trans. Syst., Man, Cybern. B*, 31(1):98–105, Feb. 2001.

[105] W. S. Tang, J. Wang, and Y. Xu. Infinity-norm torque minimization for redundant manipulators using a recurrent neural network. In *Proc. 38th IEEE Conf. Decision Control*, volume 3, pages 2168–2173, Phoenix, Arizona, USA, Dec. 1999.

[106] N. Tardella. Earthbound Robots Today Need to Take Flight. `https://spectrum.ieee.org/automaton/robotics/industrial-robots/earthbound-robots-today-need-to-take-flight`, Feb. 9, 2016. (accessed 11 June 2019).

[107] Tecnalia. Parallel Cable Robotics: Best solution for optimizing operations in large spaces. `https://www.tecnalia.com`. (accessed 23 Jan. 2019).

[108] R. Tedrake. Underactuated Robotics: Algorithms for Walking, Running, Swimming, Flying, and Manipulation (Course Notes for MIT 6.832). (accessed 15 May 2019).

[109] F. Ullmann. FiOrdOs: A Matlab Toolbox for C-Code Generation for First Order Methods. Master's thesis, ETH Zurich, Switzerland, 2011.

[110] A. Vafaei, M. A. Khosravi, and H. D. Taghirad. Modeling and Control of Cable Driven Parallel Manipulators with Elastic Cables: Singular Perturbation Theory. In S. Jeschke, H. Liu, and D. Schilberg, editors, *Intelligent Robotics and Applications*, pages 455–464, Berlin, Heidelberg, 2011. Springer Berlin Heidelberg.

[111] R. Verhoeven, M. Hiller, and S. Tadokoro. Workspace, Stiffness, Singularities and Classification of Tendon-Driven Stewart Platforms. *Advances in Robot Kinematics: Analysis and Control*, pages 105–114, 2013.

[112] C. Viegas, M. Tavakoli, et al. SCALA–A Scalable Rail-based Multirobot System for Large Space Automation: Design and Development. *IEEE/ASME Trans. Mechatronics*, 22(5):2208–2217, Oct. 2017.

[113] C. W. Wampler. Manipulator inverse kinematic solutions based on vector formulations and damped least-squares methods. *IEEE Trans. Syst., Man, Cybern.*, 16(1):93–101, Jan. 1986.

[114] L. Wang. *Model Predictive Control System Design and Implementation Using MATLAB*. Springer-Verlag, London, U.K., 2009.

[115] L. T. Wang and C. C. Chen. A combined optimization method for solving the inverse kinematics problems of mechanical manipulators. *IEEE Trans. Robot. Autom.*, 7(4):489–499, Aug. 1991.

[116] Z. Wang, G. Li, H. Jiang, Q. Chen, and H. Zhang. Collision-Free Navigation of Autonomous Vehicles Using Convex Quadratic Programming-Based Model Predictive Control. *IEEE/ASME Trans. Mechatronics*, 23(3):1103–1113, June 2018.

[117] H. Wei, Y. Qiu, and J. Yang. An Approach to Evaluate Stability for Cable-Based Parallel Camera Robots with Hybrid Tension-Stiffness Properties. *Int. J. Adv. Robot. Syst.*, 12(12):185:1–185:12, 2015.

[118] S. Widnall, 2009. Dynamics. Lecture Notes, Topic: "Lecture L19–Vibration, Normal Modes, Natural Frequencies, Instability." Massachusetts Institute of Technology, Cambridge, MA, USA.

[119] S. Widnall and J. Peraire, 2008. Dynamics. Lecture Notes, Topic: "Lecture L12–Work and Energy." Massachusetts Institute of Technology, Cambridge, MA, USA.

[120] W. A. Wolovich and H. Elliott. A computational technique for inverse kinematics. In *Proc. 23rd IEEE Conf. Decision Control*, pages 1359–1363, Las Vegas, Nevada, USA, Dec. 1984.

[121] F. Y. Wu, S. Foong, and Z. Sun. A hybrid field model for enhanced magnetic localization and position control. *IEEE/ASME Trans. Mechatronics*, 20(3):1278–1287, June 2015.

[122] W. Xu, T. Liu, and Y. Li. Kinematics, Dynamics, and Control of a Cable-Driven Hyper-Redundant Manipulator. *IEEE/ASME Trans. Mechatronics*, 23(4):1693–1704, Aug. 2018.

[123] Y. Yamamoto and X. Yun. Effect of the dynamic interaction on coordinated control of mobile manipulators. *IEEE Trans. Robot. Autom.*, 12(5):816–824, Oct. 1996.

[124] S. H. Yeo, G. Yang, and W. B. Lim. Design and analysis of cable-driven manipulators with variable stiffness. *Mech. Mach. Theory*, 69:230–244, 2013.

[125] K. Yu, L. Lee, C. P. Tang, and V. N. Krovi. Enhanced trajectory tracking control with active lower bounded stiffness control for cable robot. In *Proc. IEEE Int. Conf. Robot. Autom.*, pages 669–674, Anchorage, AK, USA, May 2010.

[126] M. Zeinali and A. Khajepour. Design and Application of Chattering-Free Sliding Mode Controller to Cable-Driven Parallel Robot Manipulator: Theory and Experiment. In *Proc. ASME 2010 Int. Design Eng. Tech. Conf. and Computers and Inf. in Eng. Conf.*, pages 319–327, Montreal, Quebec, Canada, Aug. 2010.

[127] Y. Zhang. Inverse-free computation for infinity-norm torque minimization of robot manipulators. *Mechatronics*, 16(3):177–184, 2006.

[128] Y. Zhang. A set of nonlinear equations and inequalities arising in robotics and its online solution via a primal neural network. *Neurocomputing*, 70(1):513–524, 2006.

[129] Y. Zhang, S. S. Ge, and T. H. Lee. A unified quadratic-programming-based dynamical system approach to joint torque optimization of physically constrained redundant manipulators. *IEEE Trans. Syst., Man, Cybern. B*, 34(5):2126–2132, Oct. 2004.

[130] Y. Zhang and S. Ma. Minimum-energy redundancy resolution of robot manipulators unified by quadratic programming and its online solution. In *Proc. Int. Conf. Mechatronics Autom.*, pages 3232–3237, Harbin, China, Aug. 2007.

[131] Z. Zhang, Y. Lin, et al. Tricriteria optimization-coordination motion of dual-redundant-robot manipulators for complex path planning. *IEEE Trans. Control Syst. Technol.*, 26(4):1345–1357, July 2018.

[132] J. Zhao and N. I. Badler. Inverse kinematics positioning using nonlinear programming for highly articulated figures. *ACM Trans. Graph.*, 13(4):313–336, Oct. 1994.

[133] B. Zi, Z. Zhu, and J. Du. Analysis and control of the cable-supporting system including actuator dynamics. *Control Eng. Practice*, 19(5):491–501, 2011.

[134] D. Zlatanov, R. G. Fenton, and B. Benhabib. Singularity analysis of mechanisms and robots via a velocity-equation model of the instantaneous kinematics. In *Proc. IEEE Int. Conf. Robot. Autom.*, pages 986–991, San Diego, CA, USA, May 1994.

[135] C. Zou, C. Manzie, and D. Nei. Model Predictive Control for Lithium-Ion Battery Optimal Charging. *IEEE/ASME Trans. Mechatronics*, 23(2):947–957, April 2018.

APPENDICES

Appendix A

Derivations and Analysis

A.1 Derivation of the Equations of Motion of HCDR-1

For the specific 9-DOF HCDR-1, the COM (of the links) positions are computed as $p_{ac1} = p_{a0} + R_g^m R_z(\theta_{a1})[x_{ac01}, y_{ac01}, z_{ac01}]^T$, $p_{ac2} = p_{a1} + R_g^m R_z(\theta_{a1}) R_y(\theta_{a2})[x_{ac02}, y_{ac02}, z_{ac02}]^T$, and $p_{ac3} = p_{a2} + R_g^m R_z(\theta_{a1}) R_y(\theta_{a2}) R_y(\theta_{a3})[x_{ac03}, y_{ac03}, z_{ac03}]^T$ where the joint position vectors are described as $p_{a0} = [p_{mx}, p_{my}, p_{mz}]^T + R_g^m l_m$, $p_{a1} = p_{a0} + R_g^m R_z(\theta_{a1})[x_{a01}, y_{a01}, z_{a01}]^T$, $p_{a2} = p_{a1} + R_g^m R_z(\theta_{a1}) R_y(\theta_{a2})[x_{a02}, y_{a02}, z_{a02}]^T$, and $p_e = p_{a3} = p_{a2} + R_g^m R_z(\theta_{a1}) R_y(\theta_{a2}) R_y(\theta_{a3})$ $[x_{a03}, y_{a03}, z_{a03}]^T$. Additionally, the COM linear velocities and angle velocities (of the links) are calculated as $v_{ac1} = \dot{p}_{ac1}$, $v_{ac2} = \dot{p}_{ac2}$, $v_{ac3} = \dot{p}_{ac3}$, $\omega_{ac1} = (R_z(\theta_{a1}))^T \omega_m + [0, 0, \dot{\theta}_{a1}]^T$, $\omega_{ac2} = (R_z(\theta_{a1}) R_y(\theta_{a2}))^T (\omega_m + [0, 0, \dot{\theta}_{a1}]^T) + [0, \dot{\theta}_{a2}, 0]^T$, and $\omega_{ac3} = (R_z(\theta_{a1}) R_y(\theta_{a2}) R_y(\theta_{a3}))^T$ $(\omega_m + [0, 0, \dot{\theta}_{a1}]^T) + (R_y(\theta_{a2}) R_y(\theta_{a3}))^T [0, \dot{\theta}_{a2}, 0]^T + [0, \dot{\theta}_{a3}, 0]^T$, where the corresponding parameters are shown in Figure 3.2 and Table 3.2. By substituting these corresponding equations into (3.16) and (3.17), respectively, the dynamic equation of the 9-DOF HCDR-1 can be derived (in forms of (3.22) and (3.23)).

A.2 Derivation of the Equations of Motion of HCDR-2[1]

For the HCDR shown in Figure 3.4, the COM (of the pendulums' links) positions are computed as

$$p_{pc1} = p_{p1_0} + R_g^m R_x(\theta_{p1})[x_{pc01}, y_{pc01}, z_{pc01}]^T \tag{A.1a}$$

$$p_{pc2} = p_{p2_0} + R_g^m R_x(\theta_{p2})[x_{pc02}, y_{pc02}, z_{pc02}]^T \tag{A.1b}$$

where the joint position vectors are described as $p_{p1_0} = [p_{mx}, p_{my}, p_{mz}]^T + R_g^m[x_{p01}, y_{p01}, z_{p01}]^T$ and $p_{p2_0} = [p_{mx}, p_{my}, p_{mz}]^T + R_g^m[x_{p02}, y_{p02}, z_{p02}]^T$.

The COM linear velocities and angle velocities (of the pendulums' links) are calculated as

$$v_{pc1} = \dot{p}_{pc1} \tag{A.2a}$$

$$v_{pc2} = \dot{p}_{pc2} \tag{A.2b}$$

$$\omega_{pc1} = (R_x(\theta_{p1}))^T \omega_m + [\dot{\theta}_{p1}, 0, 0]^T \tag{A.2c}$$

$$\omega_{pc2} = (R_x(\theta_{p2}))^T \omega_m + [\dot{\theta}_{p2}, 0, 0]^T \tag{A.2d}$$

with $\omega_m = [R_g^m]^T[\dot{\alpha}_m, 0, 0]^T + [R_{m\beta}^{m\gamma}]^T[R_{m\alpha}^{m\beta}]^T[0, \dot{\beta}_m, 0]^T + [R_{m\beta}^{m\gamma}]^T[0, 0, \dot{\gamma}_m]^T$ and the corresponding parameters are shown in Figure 3.4 and Table 3.4.

Substituting the corresponding results in (A.1)–(A.2), the total kinetic energy K_E and potential energy V_E are calculated as

$$\begin{aligned} K_E = {} & \frac{1}{2} m_m [\dot{p}_{mx}, \dot{p}_{my}, \dot{p}_{mz}][\dot{p}_{mx}, \dot{p}_{my}, \dot{p}_{mz}]^T + \frac{1}{2}\omega_m^T I_m \omega_m \\ & + \frac{1}{2}\sum_{k=1}^{2} \left\{ m_{pk} v_{pck}^T v_{pck} + \omega_{pck}^T I_{pk} \omega_{pck} \right\}. \end{aligned} \tag{A.3}$$

and

$$\begin{aligned} V_E = {} & m_m g p_{my} + \sum_{k=1}^{2} \left\{ m_{pk} g p_{pck}^T [0, 1, 0]^T \right\} \\ & + \frac{1}{2} \sum_{i \in \{1,2,5,6,7,8,11,12\}} \left\{ \frac{EA_i}{L_{0i}} \left(L_i - L_{0i}\right)^2 \right\} \end{aligned} \tag{A.4}$$

---

[1] Parts of this section have been published in [92]. © 2019 Elsevier B.V.: "As the author of this Elsevier article, you retain the right to include it in a thesis or dissertation, provided it is not published commercially. Permission is not required, but please ensure that you reference the journal as the original source."

where g represents the gravity acceleration. Then, the Lagrangian dynamic equation is computed as

$$L_E = K_E - V_E. \tag{A.5}$$

Finally, (3.35) can be derived by rearranging (A.5).

A.3 HCDR-3 Disturbance Analysis

Using the elastic force vector F_K (in (3.52)), one can get

$$\begin{bmatrix} K_z & 0 & 0 \\ K_{z\alpha_m} & K_{\alpha_m} & 0 \\ 0 & 0 & K_{\beta_m} \end{bmatrix} \begin{bmatrix} p_{mz} \\ \alpha_m \\ \beta_m \end{bmatrix} =: K_{mest} \begin{bmatrix} p_{mz} \\ \alpha_m \\ \beta_m \end{bmatrix} \tag{A.6}$$

where $K_{mest} \in \mathbb{R}^3$ represents the estimated out-of-plane stiffness matrix of the actual cable-driven mobile platform. In practice, this stiffness matrix might be affected by the in-plane locations of the mobile platform and other unknown disturbances, so it is challenging or impossible to obtain its exact value. In this case, the following scenario analysis can be conducted even though the above uncertainties exist:

In (3.52), the disturbances $\{\tau_{md} \in \mathbb{R}^3 : \tau_{md} \subset \tau_d\}$ to the mobile platform can be divided into a new form:

$$\tau_{md} = \tau_{md_{unknown}} \pm K_{md}(p_{mx}, p_{my})[p_{mz}, \alpha_m, \beta_m]^T \tag{A.7}$$

where $\tau_{md_{unknown}} \in \mathbb{R}^3$ and $K_{md}(p_{mx}, p_{my}) \in \mathbb{R}^3$ are unknown bounded disturbances and the out-of-plane disturbance stiffness matrix of the mobile platform that effected by in-plane locations (p_{mx}, p_{my}), respectively.

Combining (A.6) and (A.7), then

$$\begin{aligned} K_{mest}[p_{mz}, \alpha_m, \beta_m]^T + \tau_{md} = &\big\{K_{mest} \pm K_{md}(p_{mx}, p_{my})\big\} \\ &[p_{mz}, \alpha_m, \beta_m]^T + \tau_{md_{unknown}} \end{aligned} \tag{A.8}$$

where $K_{md} = K_{[3,4,5][3,4,5]}$ with $K \in \mathbb{R}^{6\times 6}$ denoting the stiffness matrix of the 6-DOF cable-driven mobile platform using the four-spring model proposed by Behzadipour and Khajepour [18]. The corresponding items in (3.52) are equivalent to that of (A.8).

Additionally, K_{mest} and $K_{md}(p_{mx}, p_{my})$ in (A.8) can be evaluated using the following performance indices:

$$J_{mest} = \lambda^T \lambda, \qquad \kappa_{mest} = \frac{\lambda_{\max}^2 \lambda_{\min}^2}{\lambda_{\max}^2 + \lambda_{\min}^2}, \qquad \text{for } K_{mest} \tag{A.9a}$$

$$J_{md} = \lambda^T \lambda, \qquad \kappa_{md} = \frac{\lambda_{\max}^2 \lambda_{\min}^2}{\lambda_{\max}^2 + \lambda_{\min}^2}, \qquad \text{for } K_{md} \tag{A.9b}$$

where $\lambda \in \mathbb{R}^3$ represents the eigenvalues of K_{mest} or $K_{md}(p_{mx}, p_{my})$.

A.4 Derivation of the Dynamics of HCDR-4

The corresponding terms in (3.67) and (3.68) are computed as follows: the rotation matrix $R_g^m = R_x(\alpha_m)R_{y'}(\beta_m)R_{z''}(\gamma_m) \in \mathcal{SO}(3)$ and the angular velocity ω_m of the frame $\{O_m\}$ is calculated as $\omega_m = [R_g^m]^T[\dot{\alpha}_m, 0, 0]^T + [R_{m\beta}^{m\gamma}]^T[R_{m\alpha}^{m\beta}]^T[0, \dot{\beta}_m, 0]^T + [R_{m\beta}^{m\gamma}]^T[0, 0, \dot{\gamma}_m]^T$ with the rotation matrices $R_{m\alpha}^{m\beta} = R_{y'}(\beta_m) \in \mathcal{SO}(3)$ and $R_{m\beta}^{m\gamma} = R_{z''}(\gamma_m) \in \mathcal{SO}(3)$. Then, the COM (of the pendulums' links) positions are computed as $p_{pc1} = p_{p1_0} + R_g^m R_x(\theta_{p1})[x_{pc01}, y_{pc01}, z_{pc01}]^T$ and $p_{pc2} = p_{p2_0} + R_g^m R_x(\theta_{p2})[x_{pc02}, y_{pc02}, z_{pc02}]^T$ where the joint position vectors are described as $p_{p1_0} = [p_{mx}, p_{my}, p_{mz}]^T + R_g^m[x_{p01}, y_{p01}, z_{p01}]^T$ and $p_{p2_0} = [p_{mx}, p_{my}, p_{mz}]^T + R_g^m[x_{p02}, y_{p02}, z_{p02}]^T$. The COM linear velocities and angle velocities (of the pendulums' links) are calculated as $v_{pc1} = \dot{p}_{pc1}$, $v_{pc2} = \dot{p}_{pc2}$, $\omega_{pc1} = (R_x(\theta_{p1}))^T\omega_m + [\dot{\theta}_{p1}, 0, 0]^T$, $\omega_{pc2} = (R_x(\theta_{p2}))^T\omega_m + [\dot{\theta}_{p2}, 0, 0]^T$ with the corresponding parameters are shown in Figure 3.10 and Table 3.6. Then, the COM (of the links) positions are computed as $p_{ac1} = p_{a0} + R_g^m R_y(\theta_{a1})[x_{ac01}, y_{ac01}, z_{ac01}]^T$, $p_{ac2} = p_{a1} + R_g^m R_y(\theta_{a1})R_z(\theta_{a2})[x_{ac02}, y_{ac02}, z_{ac02}]^T$, $p_{ac3} = p_{a2} + R_g^m R_y(\theta_{a1})R_z(\theta_{a2})R_z(\theta_{a3})[x_{ac03}, y_{ac03}, z_{ac03}]^T$ where the joint position vectors are calculated as $p_{a0} = [p_{mx}, p_{my}, p_{mz}]^T + R_g^m[x_{a0}, y_{a0}, z_{a0}]^T$, $p_{a1} = p_{a0} + R_g^m R_y(\theta_{a1})[x_{a01}, y_{a01}, z_{a01}]^T$, $p_{a2} = p_{a1} + R_g^m R_y(\theta_{a1})R_z(\theta_{a2})[x_{a02}, y_{a02}, z_{a02}]^T$, and $p_e = p_{a3} = p_{a2} + R_g^m R_y(\theta_{a1})R_z(\theta_{a2}) R_z(\theta_{a3})[x_{a03}, y_{a03}, z_{a03}]^T$. Additionally, the COM linear velocities and angle velocities (of the links) are calculated as $v_{ac1} = \dot{p}_{ac1}$, $v_{ac2} = \dot{p}_{ac2}$, $v_{ac3} = \dot{p}_{ac3}$, $\omega_{ac1} = (R_y(\theta_{a1}))^T\omega_m + [0, \dot{\theta}_{a1}, 0]^T$, $\omega_{ac2} = (R_y(\theta_{a1})R_z(\theta_{a2}))^T(\omega_m + [0, \dot{\theta}_{a1}, 0]^T) + [0, 0, \dot{\theta}_{a2}]^T$, $\omega_{ac3} = (R_y(\theta_{a1})R_z(\theta_{a2}) R_z(\theta_{a3}))^T(\omega_m + [0, \dot{\theta}_{a1}, 0]^T) + (R_z(\theta_{a2})R_z(\theta_{a3}))^T[0, 0, \dot{\theta}_{a2}]^T + [0, 0, \dot{\theta}_{a3}]^T$, where the corresponding parameters are also shown in Figure 3.10 and Table 3.6.

In (3.68), the cable stiffness matrix is $K_c = \operatorname{diag}\left(\frac{EA_1}{L_{01}}, \frac{EA_2}{L_{02}}, \cdots, \frac{EA_{12}}{L_{012}}\right) \in \mathbb{R}^{12\times 12}$, where $\frac{EA_i}{L_{0i}}$ represents the ith cable stiffness, EA_i is the product of the modulus of elasticity and cross-sectional area of the ith cable. L_{0i} and L_i denote the ith input unstretched cable length and actual cable length, respectively. $L_0 = [L_{01}, L_{02}, \cdots, L_{012}]^T \in \mathbb{R}^{12}$ and $L = [L_1, L_2, \cdots, L_{12}]^T \in \mathbb{R}^{12}$.

To obtain the matrix A_m in (3.69), the terms in A_m are computed as follows: let the ith cable-length vector $\vec{L}_i = [a_{ix}, a_{iy}, a_{iz}]^T - [p_{mx}, p_{my}, p_{mz}]^T - R_g^m[r_{ix}, r_{iy}, r_{iz}]^T$, $\{\forall\, i \in \mathbb{N} : 1 \leq i \leq 12\}$, with $\vec{L}_i \in \mathbb{R}^3$ denotes the position vector from the ith cable anchor point on the robot static frame to the ith cable anchor point on the mobile platform. Then, one can get the ith cable length $L_i = \|[a_{ix}, a_{iy}, a_{iz}]^T - [p_{mx}, p_{my}, p_{mz}]^T - R_g^m[r_{ix}, r_{iy}, r_{iz}]^T\|$ and the ith unit cable-length vector $\hat{L}_i = \frac{\vec{L}_i}{L_i} = [\hat{L}_{ix}, \hat{L}_{iy}, \hat{L}_{iz}]^T \in \mathbb{R}^3$. Furthermore, $[r_{ix}, r_{iy}, r_{iz}]^T \in \mathbb{R}^3$ denotes the position vector of the ith cable anchor point on the mobile platform with respect to the frame $\{O_m\}$, $[a_{ix}, a_{iy}, a_{iz}]^T \in \mathbb{R}^3$ represents the position vector of the ith cable anchor point on the robot static frame with respect to the frame $\{O\}$, and the parameters $[r_{ix}, r_{iy}, r_{iz}]^T, [a_{ix}, a_{iy}, a_{iz}]^T$ are provided in Table 3.3.